SLAC – 322
UC – 34D
(E/I)

DESIGN AND CONSTRUCTION OF A VERTEX CHAMBER AND MEASUREMEMENT OF THE AVERAGE B-HADRON LIFETIME*

Harry Norman Nelson

Stanford Linear Accelerator Center
Stanford University
Stanford, California 94305

October 1987

Prepared for the Department of Energy
under contract number DE-AC03-76SF00515

Printed in the United States of America. Available from the National Technical Information Service, U.S. Department of Commerce, 5285 Port Royal Road, Springfield, Virginia 22161. Price: Printed Copy A09, Microfiche A01.

* Ph.D. Dissertation

ABSTRACT

Four parameters describe the mixing of the three quark generations in the Standard Model of the weak charged current interaction. These four parameters are experimental inputs to the model. A measurement of the mean lifetime of hadrons containing b-quarks, or B-Hadrons, constrains the magnitudes of two of these parameters.

Measurement of the B-Hadron lifetime requires a device that can measure the locations of the stable particles that result from B-Hadron decay. This device must function reliably in an inaccessible location, and survive high radiation levels. We describe the design and construction of such a device, a gaseous drift chamber. Tubes of 6.9 mm diameter, having aluminized mylar walls of 100 μm thickness are utilized in this Vertex Chamber. It achieves a spatial resolution of $45\mu m$, and a resolution in extrapolation to the B-Hadron decay location of $87\mu m$. Its inner layer is 4.6 cm from e^+e^- colliding beams.

The Vertex Chamber is situated within the MAC detector at PEP. We have analyzed both the $94\,\mathrm{pb}^{-1}$ of integrated luminosity accumulated at $\sqrt{s} = 29\,\mathrm{GeV}$ with the Vertex Chamber in place as well as the $210\,\mathrm{pb}^{-1}$ accumulated previously. We require a lepton with large momentum transverse to the event thrust axis to obtain a sample of events enriched in B-Hadron decays. The distribution of signed impact parameters of all tracks in these events is used to measure the B-Hadron flight distance, and hence lifetime.

The trimmed mean signed impact parameters are $130 \pm 19\mu m$ for data accumulated with the Vertex Chamber, and $162 \pm 25\mu m$ for previous data. Together these indicate an average B-Hadron lifetime of

$$\tau_b = \left[1.37\,^{+0.22}_{-0.19}\ \text{stat.}\pm 0.11\ \text{sys.}\right] \times (1 \pm 0.15\ \text{sys.})\ \text{psec.}$$

We separate additive and multiplicative systematic errors because the second does not degrade the statistical significance of the difference of the result from 0.

If b–c dominates b-quark decay the corresponding weak mixing matrix element $|V_{cb}| = 0.047 \pm 0.006 \pm 0.005$, where the first error is from this experiment, and the second theoretical uncertainty. If b–u dominates, $|V_{ub}| = 0.033 \pm 0.004 \pm 0.12$.

ACKNOWLEDGEMENTS

I would like to thank my advisor, Dave Ritson, for taking me as his student. It has been a very long way from the monopole experiments to this dissertation, and along that way Dave's ability to discern the heart of whatever matter at hand, and maintain progress, has inspired and impressed me.

The MAC Vertex Chamber project consisted of a relatively small number of physicists, engineers, and technicians, and very much belies the conception that High Energy Physics suffers from over-large collaborations. I would like to thank the MAC collaborators who contributed their help at the various stages of this project. Most monumental, however, were the contributions of Tiziano Camporesi, without whom the chamber never would have been integrated into the MAC software system. Tiziano's can-do attitude also has inspired me.

Tom Pulliam contributed greatly to the engineering involved in building and installing the chamber, and the acquisition of the extruded beryllium central column exhibited his characteristic creative spirit. It is a tragedy he did not live to see these results.

The enthusiasm and commitment of the Group F technicians, Jack Schroeder and Justin Escalera, probably exceeded that of any other participants in the project. I cannot remember Jack hesitating even once before plunging in to each of the many of prototypes and mock-ups we built. Justin not only stayed until the job was done, period, but exercised foresight, creativity, and ingenuity at all times. And his wit kept me going when those times were stressful.

The later stages of this research had their own peculiar pressures. I would like to thank my office-mate, Leslie Rosenberg, for his answers to many of my naive questions about the MAC analysis software, and his generally irrelevant attitude. Roger Hurst and Bob Messner always stopped by to attempt to lighten the darker hours, and Maureen Richards always brightened up the scene.

Discussions with fellow students and scientists are an important part of graduate school and science, although they usually go from the cynical to the ridiculous to the inane. These discussions stimulate the creative intellect. It has been my pleasure to enjoy such discussions with Gary Godfrey, Karl Van Bibber, Elliott Bloom, Steve Leffler, Steve Lowe, John Bartelt, Fred Bird, Chris

Wendt, Kent Hornbostel, John Butler, Jim Smith, Steve Wagner, Tricia Rankin, Jeremy Margulies, John Price, Dan Coffman, and others too numerous to name. Thank you for your time and patience.

The graphics in this thesis would have suffered immeasurably if Bruce LeClaire had not committed countless hours to the REXX program SKETCH. The same can be said about the typesetting, which is due to the arduous efforts of Ray Cowan.

I thank my family for tolerance and understanding over the past eleven years of my education. Two friends have been especially close over the past few years. Mark Carter, thank you for putting up with my constant gripes and frustrations. The strong and committed friendship of René Ong carried me through some crucial periods, particularly at the end.

To my dearest wife Rosemary Dunn, I wish this had not been so difficult. It's over now.

I dedicate this thesis to my father: it is the fulfillment of his last words to me; and to our two budgerigars, Newton and Galileo.

Table of Contents

Figure Captions

List of Tables

Chapter 1

Introduction

1.1 General Discussion

Elementary Particle Physics is the search for the most fundamental constituents of matter and energy, and the study of their interactions. At the present, we believe these constituents to be: quarks, the fermions that constitute neutrons and protons; leptons, fermions such as the electron; and gauge bosons, such as the photon. The rules for the interactions of these constituents have come to be known as the *Standard Model.* The Standard Model consists of the recently unified theories of electromagnetism and the weak interaction, now referred to as the single *electroweak* theory, and a similar theory that describes the strong interaction between quarks, Quantum Chromo-Dynamics (QCD). Gravity is not usually considered part of the Standard Model, because a generally accepted quantum theory of gravitation has not yet emerged.

The existing Standard Model contains some 18 parameters which are not predicted by the model, and are determined entirely by experiment. This dissertation concerns the measurement of the mean lifetime of hadrons containing b-quarks, or B-hadrons. From this measurement, we can derive boundaries on two of the 18 parameters of the Standard Model. The Standard Model states interrelationships between the B-hadron lifetime and other physical measurements; if these interrelationships prove to be false, we may infer new phenomena *outside* the Standard Model.

1.1.1 *The Standard Model*[2]

Some information about the fermions of the Standard Model is given in

Table 1.1, while Table 1.2 describes the gauge bosons. Fermions interact with one another via the gauge bosons, implying that the gauge bosons can mediate the decay of fermions, and in particular, the b-quark. The form of the interaction is intimately connected with a mathematical property of the equations that describe the interaction, local gauge invariance. It is in the past twenty years that importance of local gauge invariance has been appreciated: the property also seems, in a beautiful and subtle manner, to guarantee that an acceptable *quantum* field theory can be developed from the *classical* field equations, The electroweak theory and QCD are constructed around local gauge invariance, giving the gauge bosons their name.

It is the massive W gauge boson of the electroweak interaction that mediates b-quark decay. On the surface, a *massive* gauge boson is directly incompatible with local gauge invariance. This impediment has been overcome through the introduction of a symmetry in the field equations that is not respected by the ground state of the fields, a so called spontaneously broken symmetry. The manner in which this spontaneously broken symmetry has been introduced into the Standard Model not only allows a locally gauge invariant description of the W, but also links electromagnetism and the weak interaction into the unified electroweak interaction, and predicts the existence of the Z^0 gauge boson at approximately the same mass as the W.

A schematic of how the W allows the b-quark to decay appears in Figure 1.1. The W provides the means for the b to transmute into a charge $+2/3$ quark, either a c or a u, with the accompaniment of debris from the W. This process does not occur instantaneously after the production of the b. The time elapsed is related to the strength with which the W couples to the $(b\bar{c})$ and $(b\bar{u})$ quark pairs. These two coupling strengths are not predicted by the Standard Model, and are the two parameters which can be limited by measurement of the B-hadron lifetime.

In fact, the rules of the electroweak theory allow *any* of the charge $-1/3$ quarks to transmute into *any* charge $2/3$ quark via the emission of a W. We know of (or strongly suspect there to exist) three types of each charge quark, allowing $3 \times 3 = 9$ possible transitions. The coupling strength for each transition can be described by one complex number; therefore at most $9 \times 2 = 18$ parameters are needed to describe all of these. These 18 parameters are not the 18 fun-

		Leptons		Quarks	
	Charge	0	-1	$-1/3$	$2/3$
'First Generation'	Symbol	ν_e	e	d	u
	Name	electron neutrino	electron	down	up
	Mass	< 46 eV	0.511 MeV	0.34 GeV	0.34 GeV
'Second Generation'	Symbol	ν_μ	μ	c	s
	Name	muon neutrino	muon	strange	charm
	Mass	< 250 keV	105.7 MeV	0.51 GeV	1.5 GeV
'Third Generation'	Symbol	ν_τ	τ	b	t
	Name	tau neutrino	tau	bottom	top
	Mass	< 70 MeV	1.784 GeV	4.9 GeV	> 23 GeV

Table 1.1 The Fundamental Fermions[3] The leptons interact exclusively via the electroweak interaction; the quarks interact also via the strong interaction. We have not conclusively observed a quark in isolation, so we believe the strong force confines quarks to the inside of hadrons. The horisontal arrangement of certain pairs of leptons with other pairs of quarks, *e.g.*(ν_e, e) with (d, u), into 'generations' is somewhat arbitrary and historical. There is a theoretical argument that for each lepton pair such as (ν_e, e) there should exist a combination of charge $-1/3$ and $2/3$ quarks, such as (d, u). The neutrinos listed may be massless; the experimental upper limits on their masses are shown. Most matter consists of the massive fermions in the First Generation. All but the neutrinos in the Second and Third Generations are known to be unstable; they transmute into combinations of d and u-quarks, electrons, and neutrinos. The τ lepton and the b-quark were discovered in the 1970's; no evidence for the t-quark has been conclusively found, but we anticipate it on theoretical grounds. For each type of fermion there exists an anti-fermion as well.

damental parameters of the Standard Model, and the current Standard Model states that *only four* are necessary to describe all of the nine possible quark transmutations. The B-hadron lifetime puts limits on two of the four 'quark mixing' parameters, but when considered along with other measurements, can test whether the Standard Model's reduction from 18 to four is correct.

Name	Symbol	Charge	Mass	Force
Photon	γ	0	$< 3 \times 10^{-27}$ eV	Electroweak
Charged Intermediate Vector Boson	W	± 1	~ 82 GeV	Electroweak
Neutral Intermediate Vector Boson	Z^0	0	~ 93 GeV	Electroweak
Gluon	g	0	~ 0	Strong

Table 1.2 The Fundamental Gauge Bosons. The bosons are associated with certain forces between quarks; these are shown. The photon is the carrier of the electromagnetic force; electromagnetism has been mathematically unified with the weak interaction into the electroweak force. The W boson enables the transmutation of the heavy fermions in Table 1.1 to the lighter fermions.

1.2 Theoretical Discussion

The rate of decay of B-hadrons can, in principle, be completely calculated from the Lagrangean of the Standard Model, up to the two unknown Kobayashi-Maskawa (KM) matrix elements. In practice, QCD proves a major obstacle to the calculation. At the present, calculations of the B-hadron lifetime are uncertain to at least the 25% level. Calculations of the B semileptonic rate alone are less uncertain, and probably can be trusted at the 25% level.

1.2.1 *Formalism*

In the Standard Model, quarks couple to W-bosons via the current

$$J^\mu = \frac{g}{2\sqrt{2}} V_{ij} J^\mu_{ij}$$

where

$$J^\mu = \overline{u_i} \gamma^\mu (1 - \gamma_5) d_j$$

and the mass eigenstates of the i^{th} generation quark doublet are (u_i, d_i). The expression $g/(2\sqrt{2}) = G_F^{1/2} M_W 2^{-1/4}$. The V_{ij} are the elements of the KM quark mixing matrix[4] often expressed for three generations as

$$V = \begin{pmatrix} V_{ud} & V_{us} & V_{ub} \\ V_{cd} & V_{cs} & V_{cb} \\ V_{td} & V_{ts} & V_{tb} \end{pmatrix}. \qquad [1.1]$$

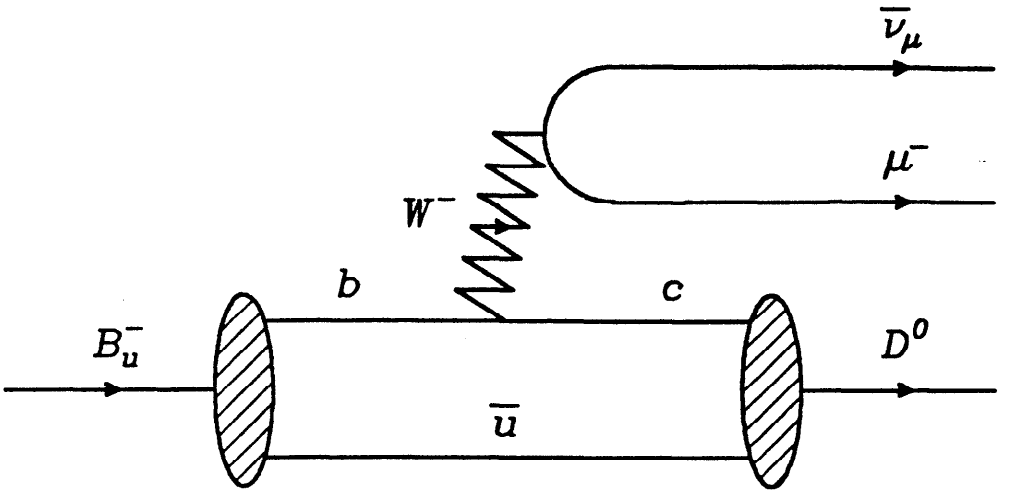

Figure 1.1 Diagram of B-hadron Decay. The B-hadron in this case is a B_u^- meson, which contains inside a b-quark and a $\overline{u}$-antiquark. The b-quark emits a W boson, and transmutes into a c-quark. Charge is conserved in this process; the initial b has charge $-1/3$; the subsequent W and c have a net charge of $-1 + 2/3 = -1/3$. The W transmutes to a negative muon and a muon antineutrino; the c and remaining $\overline{u}$ emerge as a D^0 meson.

For N quark generations, the V_{ij} can be described by N^2 complex or $2N^2$ real numbers. Such a description is always phenomenologically correct, but if there is no new physics hidden in V, and merely the mixing of N generations within the Standard Model, a substantial reduction in parameters can be effected. Unitarity provides N^2 independent constraints. The remaining degrees of freedom describe one common phase and $2(N-1)$ relative phases of the quark fields that alter no physics, so are irrelevant. This allows $N^2 - 1 - 2(N-1) = (N-1)^2$ real numbers to specify all the V_{ij}. If V were real, it would be analogous to a rotation matrix in N-dimensional space. A number of real angles equal to the number of unique axis pairs, or $\frac{1}{2}N(N-1)$, would be sufficient to describe V. This implies $(N-1)^2 - \frac{1}{2}N(N-1) = \frac{1}{2}(N-1)(N-2)$ phases are needed, in addition, to describe complex V.

For two generations, only one real angle is sufficient to describe V; this is just the Cabibbo angle. For three generations, three real angles and one phase are sufficient. This phase *might* be sufficient to describe the observed CP violation in the K^0 system. However, it is possible that three real angles and one phase are not sufficient to describe measurements of quark mixing and CP violation. Then new physics outside the Standard Model, such as a fourth generation of

quarks and leptons, would be implied.

A convenient parameterization[5] of V for N generations can be built from simple rotation matrices

$$V = \Omega_{(N-1)N}...\Omega_{2N}\Omega_{1N}...\Omega_{23}\Omega_{13}\Omega_{12}$$

where the $N \times N$ matrices (Ω_{ij}) are nearly the identity matrix, except for the i^{th} and j^{th} columns and rows

$$\Omega_{ij} = \begin{array}{c} \\ i \\ j \end{array} \begin{array}{c} \begin{array}{cc} i & \quad j \end{array} \\ \begin{pmatrix} c_{ij} & s_{ij}e^{-i\delta_{ij}} \\ -s_{ij}e^{i\delta_{ij}} & c_{ij} \end{pmatrix} \end{array}$$

$$c_{ij} = \cos(\theta_{ij})$$

$$s_{ij} = \sin(\theta_{ij})$$

$$\delta_{ij} \begin{cases} = 0, & \text{if j=i-1;} \\ \neq 0, & \text{otherwise.} \end{cases}$$

The $(\theta_{12}, \ldots, \theta_{(N-1)N})$ are the $\frac{1}{2}N(N-1)$ real angles, and the $(\delta_{13}, \ldots, \delta_{(N-2)})$ the $\frac{1}{2}(N-1)(N-2)$ phases. This parameterization keeps V simple above the diagonal. For three generations

$$V = \begin{pmatrix} c_{12}c_{13} & s_{12}c_{13} & s_{13}e^{-i\delta_{13}} \\ -s_{12}c_{23} - c_{12}s_{23}s_{13}e^{i\delta_{13}} & c_{12}c_{23} - s_{12}s_{23}s_{13}e^{i\delta_{13}} & s_{23}c_{13} \\ s_{12}s_{23} - c_{12}c_{23}s_{13}e^{i\delta_{13}} & -c_{12}s_{23} - s_{12}s_{23}s_{13}e^{i\delta_{13}} & c_{23}c_{13} \end{pmatrix}. \quad [1.2]$$

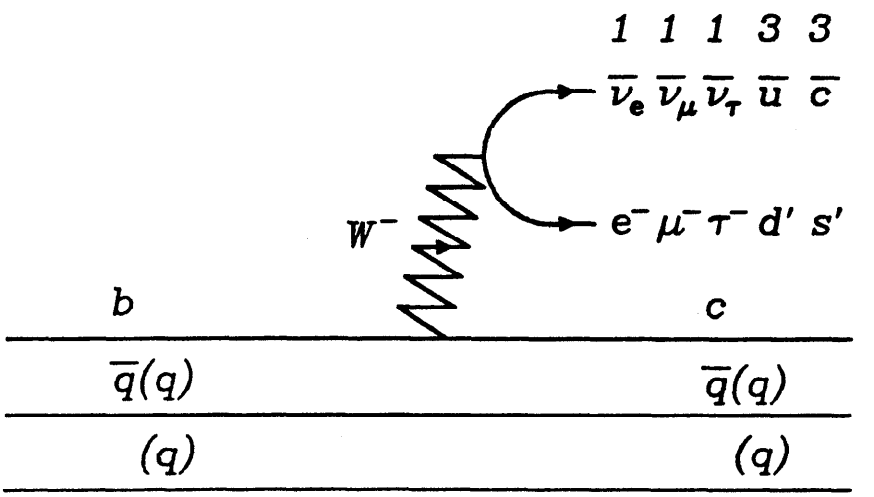

Figure 1.2 Spectator Approximation of B-hadron Decay. The B-hadron is assumed to consist entirely of its valence quark state, either $b\bar{q}$ if a meson or bqq if a baryon. The decay is considered equivalent to free quark decay of the b; any effect of interaction between the W products and the c or other quarks is ignored. Without phase space effects, the leptons would enter with weight 1, the quarks 3 from color. d' and s' represent the KM rotation of the mass eigenstates u, d.

1.2.2 *Naive Spectator Model*

In the Naive Spectator Model[6] the effects of gluons and of non-b quarks in B-hadrons are ignored. The only relevant process is exhibited in Figure 1.2. The b-quark lifetime differs from the muon lifetime only because 1)the mass of the b-quark is greater than that of the muon; 2) more final states are kinematically accessible; and 3)the 3 degrees of freedom of color are available when the W hadronizes.

For the moment ignoring phase space factors, one estimates

$$\frac{1}{\tau_b} = \Gamma_b = 9\left(\frac{m_b}{m_\mu}\right)^5 \frac{1}{\tau_\mu}(|V_{cb}|^2 + |V_{ub}|^2) = 9\frac{G_F^2 m_b^5}{192\pi^3}(|V_{cb}|^2 + |V_{ub}|^2)$$
$$= 9 \times 10^{14}\left(\frac{m_b}{4.9\,\mathrm{GeV}}\right)^5 (|V_{cb}|^2 + |V_{ub}|^2)\ \mathrm{s}^{-1}$$

In this crude approximation, the B semileptonic branching ratio is $1/9 = 11\%$.

Available phase space[7] reduces the partial decay rate for the process $b \to q p_1 p_2$

by a factor

$$I(x,y,z) = 12\int_{(x+y)^2}^{(1-z)^2} \frac{d\xi}{\xi}(\xi - x^2 - y^2)(1 - z^2 - \xi)W(\xi, x^2, y^2)W(1, z^2, \xi)$$

$$W(a,b,c) = \left(a - (\sqrt{b} + \sqrt{c})^2\right)^{\frac{1}{2}} \left(a - (\sqrt{b} - \sqrt{c})^2\right)^{\frac{1}{2}}$$

$$x = \frac{m_q}{m_b},\ y = \frac{m_1}{m_b},\ z = \frac{m_2}{m_b}$$

The familiar case of $m_1 = m_2 = 0$, applicable to the electron and muon partial decay rates, is

$$I(x,0,0) = 1 - 8x^2 - 24x^4 \ln x + 8x^6 - x^8$$

The effects of phase space on the leptonic and non-leptonic partial decay rates are shown in Table 1.3. One sees that phase space reduces $b \to c$ partial rates by a factor of 2-3.

	Crude		Phase Space +K-M		Short Distance QCD		QCD Rad. Cor.		Wirbel, Stech, and Bauer[8]		Grinstein, Wise, and Isgur[9]		Altomari and Wolfenstein[10]	
	a_c	a_u	a_c	a_u	a_c	a_u	a_c	a_u	a_c	a_u	a_c	a_u	a_c	a_u
$\Gamma_{e,\mu}$	1	1	0.51	0.96	0.51	0.96	0.46	0.84	0.33	(0.34)	0.58	(0.57)	0.39	
Γ_τ	1	1	0.11	0.36	0.11	0.36	0.10	0.31						
Γ_{NL}	6	6	1.79	3.93	2.09	4.59	2.15	4.72						
Γ_b	9	9	2.92	6.21	3.22	6.87	3.17	6.71						
$B_{e,\mu}$	11%		18%		16%		15%							

Table 1.3 Calculated Decay Rates. The (partial) decay rate is $10^{14}(a_c V_{cb}^2 + a_u V_{ub}^2)\ s^{-1}$; $m_b = 4.9$ GeV. The first column gives results from the Naive Spectator Model and merely counting final states; the second column includes phase space effects, and K-M matrix elements for the non-leptonic (NL) final states. The progressive effect of two QCD corrections is in the next two columns. The remaining columns give the results of several calculations for the semileptonic rate using quark model wave functions; in all three cases a_c has been calculated from the $1.1 \times (\Gamma(B \to DX) + \Gamma(B \to D^*X))$, to incorporate other final states. Wirbel, Stech and Bauer[8] include only π and ρ final states in their estimate of a_u; Grinstein, Wise, and Isgur[9] include $1P$ and $2S$ quark states as well.

1.2.3 *QCD Corrections to the Naive Spectator Model*

QCD alters the Naive Spectator Model in several ways, broadly categorized as short distance effects, radiative corrections, and long distance effects.

Short distance QCD effects leave semileptonic decays unchanged, but enhance non-leptonic channels.[11,12] Hard-gluon exchange renormalizes and destroys the color-blindness of the charged current interaction between quarks. These effects are normally described by two numbers, denoted c_+ and c_-. The color degree of freedom normally enhances the non-leptonic channels by a factor of three; short distance effects replace this by the expression $2c_+^2 + c_-^2$. At the mass scale of the b-quark, typical estimates are $c_+ \approx 0.85$, $c_- \approx 1.4$[6], yielding an enhancement of 14%.

Radiative corrections afflict both semileptonic and non-leptonic channels. In the semileptonic case,[13] the situation is similar to the QED correction to muon decay.[14] The semileptonic rate is reduced by $\approx 9\%$ for $b \to c$ and $\approx 13\%$ for $b \to u$. In the non-leptonic case, the interaction of radiative corrections with short distance effects must be carefully considered.[12] The result is an additional enhancement of only $\approx 3\%$.[6]

Long distance QCD effects include any process involving the quarks other than the b in B-hadrons, as well as the hadronization process that describes the evolution of final state quarks to hadrons. The experimental consequences of such effects include: 1) further enhancement of the non-leptonic decay rate, leading to a smaller semileptonic branching ratio; 2) $\tau(B^0) \neq \tau(B^+)$, or equivalently, $\Gamma_e(B^0) \neq \Gamma_e(B^+)$; 3) uncertainty in the non-leptonic partial rates as well as a_u in the semileptonic partial rate in Table 1.3, due to fragmentation phenomena; and 4) B^0-$\overline{B^0}$ mixing. The measured B semileptonic branching ratio is $12 \pm 1\%$, lower than the QCD-corrected spectator model in Table 1.3 estimate of 14%. Imperfect quark masses, or long distance effects, could produce this discrepancy.

The CLEO experiment has set the limits $0.44 < (\tau_{B_d^0}/\tau_{B_u^-}) < 2.05$ at 90% confidence.[15] Two distinct physical processes could lead to $\tau_{B^0} \neq \tau_{B^-}$. In the first, τ_{B^-} is *lengthened* by destructive interference among the amplitudes of identical final states.[16] In the second, τ_{B^0} is *shortened* due to a W exchange diagram.[17] The first process is probably more operative in non-leptonic D decays, which

are predominantly two-body; the higher multiplicity in B decays is liable to destroy coherence. Normally, the second process is helicity suppressed, and grows only as m_b, so is small compared to the spectator process, which grows as m_b^5. However, gluon emission can remove the helicity suppression, and lead to a rate like $\alpha_s m_b^5$. There is some controversy the importance of this process; Soni[18] suggests $\tau_{B^+}/\tau_{B^0} \approx 1.4 - 1.6$; Bigi[19] dissents, and argues from the D system that $\tau_{B^+}/\tau_{B^0} < 1.2$. Only future experiment will decide. However, the statistical error of CLEO's existing technique, which does not require tagging of B^0 or B^-, will only improve as $1/\mathcal{L}^{1/4}$, where $\mathcal{L}$ is their integrated luminosity. Therefore B^0-B^- tagging must be performed, either for direct branching ratio or lifetime measurements, to get a substantial improvement.

The soft fragmentation of final state quarks into hadrons can probably bring uncertainty to all of the entries in Table 1.3 except the semileptonic $b - c$ transition. For the semileptonic $b \to c$ transition, quark model estimates (see below) for the exclusive transitions sum to near the spectator estimate. For $b \to u$, this is not true, possibly indicating the importance of non-resonant fragmentation.

1.2.4 *Estimates from the use of Quark Model Wave Functions*

Several researchers have estimated B-decay rates to exclusive semileptonic final states with use of meson wave functions from the constituent quark model[8-10] Their motivation is to avoid the b-quark mass uncertainty, and to derive expressions for the lepton energy spectrum. The phenomenological Lorentz structure of the transition matrix elements is developed, and then the wave functions are used to estimate the unknown form factors. Only the B-hadron mass, which is well known, appears in the leading m^5 factor. The results of three of these estimates are shown in Table 1.3.

There is a large discrepancy between the calculations. Recently, this discrepancy has been traced to one form factor that disappears in the non-relativistic limit. Most of the discrepancy appears in the exclusive channel $B \to D^* l \overline{\nu_l}$.

1.2.5 *Discussion Concerning Calculated Decay Rates*

The result from the QCD corrected Naive Spectator Model is:

$$\frac{1}{\tau_b} = \Gamma_b \approx 3.2 \times 10^{14} \left(\frac{m_b}{4.9\,\mathrm{GeV}}\right)^5 (|V_{cb}|^2 + 2.1|V_{ub}|^2)\ \mathrm{s}^{-1} \qquad [1.3].$$

Long-distance effects are totally ignored in this model, and could substantially alter the non-leptonic decay rates used in this result. The decay rate is heavily dependent on the value of m_b used; at least $m_b = 4.9 \pm 0.2\,\mathrm{GeV}$[21] is allowed by existing data. If one considers only the semileptonic decay rate, QCD uncertainties are reduced. Use of the quark-model approach reduces the decay rate uncertainty caused by the b-quark mass uncertainty, at the price of new ignorance over form factors. However, both spectator and quark model approaches yield

$$\frac{B_e}{\tau_b} = \Gamma_e = \approx 0.4 \times 10^{14}(|V_{cb}|^2 + 2|V_{ub}|^2)\ \mathrm{s}^{-1} \qquad [1.4].$$

Probably the uncertainty in the factor multiplying $|V_{cb}|^2$ is $\pm 0.1 \times 10^{14}$ in either approach. The factor multiplying $|V_{ub}|^2$ is uncertain to $O(50\%)$.

1.3 B-lifetime Measurement

Before 1983, the use of [1.3] and the assumption that $|V_{bc}| \approx \sin(\theta_c)$, where θ_c is the Cabibbo angle, led to the general belief that $\tau_b \approx 0.08\,\mathrm{ps}$. On the one hand, this rate is too slow to compete with $b\bar{b}$ annihilation at the Υ; on the other hand, the B flight path corresponding to $\tau_b = 0.08\,\mathrm{ps}$ is only $2\mu m$ at the $\Upsilon(4s)$, where $\gamma\beta \approx 0.08$, and $60\mu m$ at PEP or PETRA, where $\gamma\beta \approx 2.5$. These flight paths were considered too small to be measured. It came as a great surprise, therefore, when the MAC collaboration, followed by the Mark-II collaboration, reported in 1982-83 that $\tau_b \approx$ 1-2 ps.[22–24] These measurements had large errors, however, and history has shown, for example for the π^0 lifetime,[25] that the first measurements of short lifetimes are systematically long. For this reason, the research for this dissertation, which consisted of the design and installation of an improvement to the MAC detector to better measure the B-lifetime, was undertaken. It is somewhat humorous that it is now considered 'natural' to take $|V_{bc}| \approx \sin^2(\theta_c)$, which leads to B-lifetimes in the picosecond range.

The measurement of the B-lifetime at a high energy e^+e^- collider involves two steps: first, a sample of events enriched in B-hadrons must be selected, and second, a measurement of the non-zero B flight path must be made in these events. The most reliable enrichment technique is to require high transverse momentum electrons and/or muons from the B semileptonic decay. Using this technique purities of $\approx 60\%$ and yields of 2 pb can be achieved, compared with

the $\approx$ 9% purity and $\approx$ 500 pb yield of inclusive continuum multihadron production.

A typical example of B production and decay at PEP is portrayed in Figure 1.3. The $b\bar{b}$ pair is produced, each with beam energy, modulo QED and QCD radiative corrections. The b and $\bar{b}$ subsequently pull light quarks from the vacuum and hadronize into B-hadrons. In this process, most of the beam energy is retained by each B, although typically 15% is lost to $\approx$ 5 charged, and $\approx$ 3 neutral, light hadrons, such as πs and Ks. The B hadrons and these light hadrons are referred to as primaries, and their origin as the primary vertex. The Bs travel a short distance, then decay at the secondary vertex; the lepton used to tag the events comes from this decay. Usually a charmed particle is emitted from this decay as well, decaying at a subsequent vertex. Typically four charged particles result from a semileptonic B decay, and six from a non-leptonic decay.

A measurement of the event portrayed in Figure 1.3 might appear as in Figure 1.4. The primary vertex is *a priori* unknown, but should be consistent with the beam envelope, which is typically $100 \times 700 \mu m$ at PEP. The centroid of the envelope can be measured to $25 \mu m$ with the use of Bhabha scattering events. The common B and $\overline{B}$ direction is estimated using the thrust axis, a direction that maximizes projected momenta of particles in the event. The trajectories of charged particles, or tracks, in the plane perpendicular to beams, or x-y plane, are extrapolated back to the interaction region, with some error. The distance of closest approach, or impact parameter δ, of these tracks is measured with respect to an estimate of the primary vertex, for example the beam centroid. A positive sign is attributed to δ if it appears the B flew forward along the thrust axis into the hemisphere containing the track. A net positive impact parameter, when averaged over many tracks in many events, is used to measure the B-lifetime.

The primary goal of the research undertaken for this dissertation was the reduction of the error in impact parameter error, or σ_δ. This goal was pursued by the construction and installation of a high precision drift chamber, or vertex chamber (VC), placed as close as possible to the interaction point. With this chamber, a reduction of σ_δ from $390 \mu m$, as in the 1983 MAC B-lifetime measurement, to $90 \mu m$, as measured with Bhabha scattering events, has been achieved. Secondary goals of improved muon identification efficiency and primary vertex

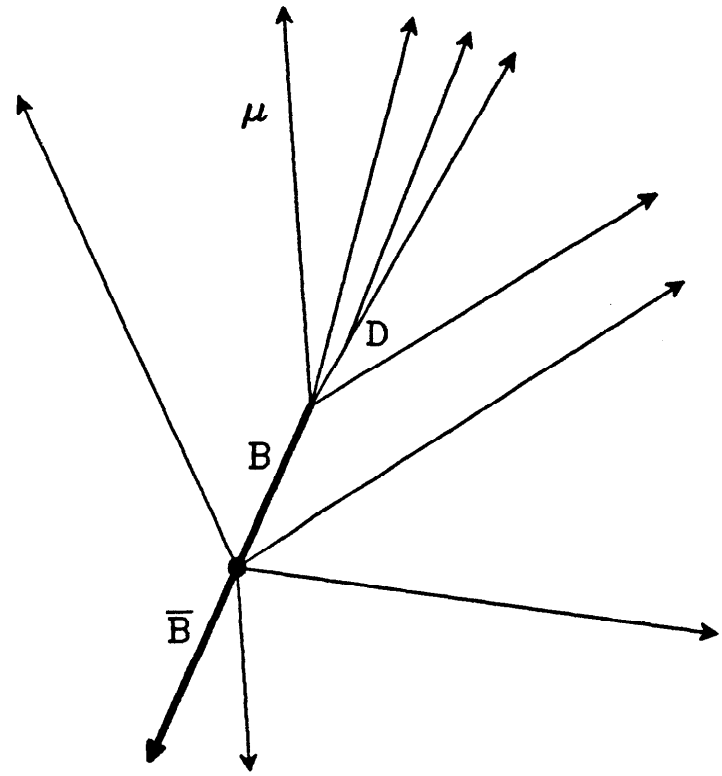

Figure 1.3 B Production and Decay at PEP. The $b\bar{b}$ pair is produced at the primary vertex, then hadronizes into the $B\overline{B}$ pair, as well as $\approx 4-5$ light hadrons. The decay of the $\overline{B}$ is not portrayed, but the B goes on to decay at the secondary vertex into a D-hadron and some light particles. The D decays, and ultimately some five charged tracks result from the B decay. A muon comes from B semileptonic decay with a $\approx$ 12% branching ratio, and is used to tag events at PEP.

estimation have been achieved. In addition, in the 1983 measurement, the impact parameters of only lepton tracks were employed; in this dissertation, all tracks in lepton tagged events are employed, to statistical advantage. The result, as described in subsequent chapters, is a B-life with a statistical error less than 1/3 of that published by MAC in 1983.

1.3.1 *Relationship to Other Measurements*

A measurement of the B-lifetime can be used to constrain the magnitude of $|V_{cb}|^2 + 2|V_{ub}|^2$, as discussed above. The ratio $|V_{ub}|/|V_{cb}|$ can be constrained via studies of B decay final states. At the present time, there is no direct

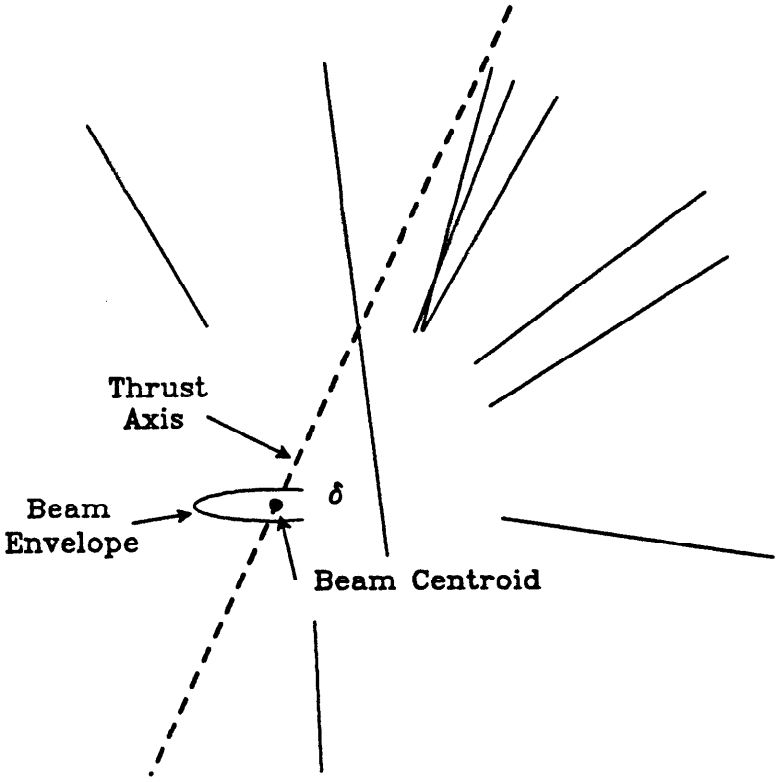

Figure 1.4 Measurement of B life at PEP. This might be the appearance of the event in Figure 1.3 after reconstruction from the detector. The beam centroid might be used to estimate the primary vertex, the thrust axis is used to estimate the $B\overline{B}$ direction, and the impact parameter δ to measure the non-zero B flight path. A positive sign is attributed to δ if it appears the B flew along the thrust axis into the hemisphere containing the reconstructed track.

evidence that $V_{ub} \neq 0$, † but upper limits on $|V_{ub}|/|V_{cb}|$ have been obtained from studies of the lepton energy spectrum from semileptonic decay, and from searches for charmless final states. The technique is limited by theoretical uncertainty over the shape of the spectrum near the endpoint; $|V_{ub}|/|V_{cb}| < 0.11$-0.23 at 90% confidence has been derived, depending on which theoretical model is employed?[27] A search for $B^- \to \rho^0 l^- \overline{\nu_l}$ implies $|V_{ub}|/|V_{cb}| < 0.15$-0.26 at 90% confidence?[27] Indirect evidence for $|V_{ub}| \neq 0$ has been implied because only 0.6-0.7 D's per B decay have been measured. However, this measurement depended on outdated D branching ratios;[28] and probably updates to 0.7-0.9 D's per B. In light of the difficulty of estimating absolute reconstruction efficiencies in

† Since we wrote this, the ARGUS collaboration has given evidence that $|V_{ub}|/|V_{cb}| > 0.07$, from observation of the decays $B \to p\bar{p}\pi(\pi)$.[26]

the high multiplicity environment of B decay, this measurement may in fact be consistent with $V_{ub} \approx 0$.

The K^0 CP violation parameter

$$\epsilon \propto m_t^2 \mathrm{Im}(V_{ts}^* V_{td})^2 \qquad [1.5]$$

from consideration of the 'box' diagram in the Standard Model?[29] It is surprising that ϵ *increases* with the mass of the top quark, m_t. The reason is the helicity suppression of the transition of a pseudoscalar to a spin non-zero pair via the left-handed Lagrangean of the Standard Model. The magnitude of $\mathrm{Im}(V_{ts}^* V_{td})^2$ can be related via [1.2] to the B-lifetime. As the lifetime grows, this magnitude shrinks, requiring larger m_t to keep ϵ fixed. Unfortunately, the constant of proportionality in [1.5] is theoretically uncertain;[30] due to our inability to calculate in QCD. Without this uncertainty, one would be able to make a solid prediction for m_t, or provide a basis for rejection of the Standard Model when m_t is measured.

Two other measurements in the kaon system are sensitive to KM matrix parameters: the measurement of the direct, or $\Delta S = 1$, CP violation parameter ϵ' and the measurement of the branching ratio $K^- \to \pi^- \nu\overline{\nu}$. $\epsilon' \propto \mathrm{Im}(V_{ts}^* V_{td})$, and only weakly increases with m_t. The branching ratio $K^- \to \pi^- \nu\overline{\nu}$ is $\propto m_t^2 |V_{ts}^* V_{td}|^2$. The relation between ϵ' and KM matrix elements has a large theoretical uncertainty from QCD, while the relationship for $K^- \to \pi^- \nu\overline{\nu}$ is less uncertain. In a sense these measurements are complementary; if m_t is very large, s_{13} and hence ϵ' can be small, but $K^- \to \pi^- \nu\overline{\nu}$ will be large. Typical predicted values[31] of $|\epsilon'/\epsilon|$ are 0.001-0.01 and of $K^- \to \pi^- \nu\overline{\nu}$ are[32] 1-10 $\times 10^{-10}$; experiments[33] with sensitivities at the low end of these ranges are taking data now, with results expected in 1-2 years.

The mixing of B^0 mesons is another measurement related to KM parameters. $B^0_{d(s)}$-$\overline{B^0_{d(s)}}$ mixing is $\propto m_t^2 |V_{tb}^* V_{td(ts)}|^2 / \tau_b$. Evidence for mixing in both systems has recently been reported.[34] Most surprising is the report of B^0_d-$\overline{B^0_d}$ mixing; the smallness of V_{bu} (from the B-lifetime and $|V_{bu}|/|V_{bc}|$) implies that V_{td} should be small as well. However;[35] large m_t ($\approx 70\,\mathrm{GeV}$) and/or $\delta_{13} \approx \pi$ can explain B^0_d-$\overline{B^0_d}$ mixing within the constraints of [1.2].

For the present, the simple mixing of three generations via [1.2] is sufficient to describe the measurements just reviewed. This may be because of our uncertainty in the QCD calculations that enter in the evaluation of every effect, or because the Standard Model with three mixed quark generations may be all the physics there is. If so, it remains unexplained *why any* quark mixing occurs, and even more, why this mixing violates CP. It is clearly important to refine all of these measurements and calculations.

1.4 Outline

In the remainder of this dissertation, we describe the measurement of the B-hadron lifetime at the PEP Storage Ring with the MAC Detector. Chapter 2 is devoted to the MAC Detector; in Chapter 3 the MAC Vertex Chamber is described, a high precision tracking chamber designed and built specially for the B-lifetime measurement. Chapter 4 contains a discussion of the selection of the data sample used for the measurement; Chapter 5 contains the description of the measurement itself. In Chapter 6 we summarize and state conclusions, and make comparisons with other B-lifetime measurements.

Chapter 2

Apparatus

In this chapter, the apparatus that existed prior to the undertaking of the research for this dissertation is described. The PEP e^+e^- storage ring is briefly described, and then the MAC detector is described in somewhat more detail. The offline processing of data, including selection of the multihadron data sample is discussed, as is the Monte-Carlo simulation of multihadron data.

2.1 The PEP Storage Ring

The concept for a large e^+e^- storage ring at SLAC was developed in a 1971 summer study at SLAC. The idea started as an e^+e^- storage ring in the same tunnel as a proton ring; PEP stood originally for Positron- Electron-Proton. The proton ring lost favor, and the final P now stands for Project.[36]

A map of the PEP ring on the SLAC site appears in Figure 2.1. The PEP ring is some 5 meters underground, 700 meters in diameter, and 2200 meters in circumference. Electrons and positrons are injected from the Linear Accelerator into PEP. Each circulates the ring grouped in three bunches, typically containing 7×10^{11} particles, with a current of ≈ 15 mA of both positrons and electrons. A bunch is usually 1.5 cm in length. For all the data used in this dissertation, the beam energy was 14.5 GeV.

The electron and positron beams cross at six interaction regions (IRs) around the ring. Typically the beam cross-section at each interaction point is 0.014 cm high and 0.7 cm wide. One of the bunches traverses the entire ring in $2200/c = 2200/(3 \times 10^8) = 7.3\mu s$; since there are three pairs of electron-positron bunches, collisions occur at each IR every $7.3/3 = 2.4\mu s$. The design luminosity of

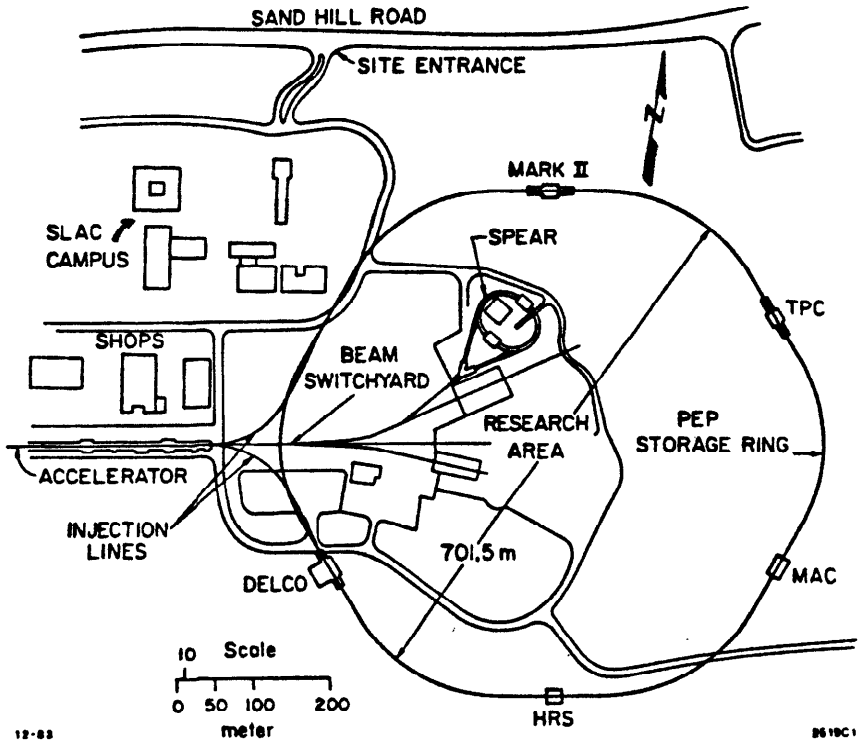

Figure 2.1 A Map Showing the PEP Ring. Electrons and positrons from the Linear Accelerator are transferred through the injection lines into the hexagonal PEP storage ring. Positrons travel clockwise, electrons counterclockwise. Five of the six experimental stations are shown; the MAC detector is at IR-4, approximately at 4 o'clock on this plot.

PEP was $1 \times 10^{32}\,\mathrm{cm}^{-2}\mathrm{s}^{-1}$, but the ring has never achieved more than $0.3 \times 10^{32}\,\mathrm{cm}^{-2}\mathrm{s}^{-1}$, and typically has operated at $0.1 \times 10^{32}\,\mathrm{cm}^{-2}\mathrm{s}^{-1}$.

2.2 The MAC Detector

MAC stands for MAgnetic Calorimeter. Contemporary particle detectors used at colliders are built to perform the following functions: 1) hermetic measurement of energy flow over all 4π of solid angle; 2) identification of leptons; 3) accurate tracking of charged particles back to the interaction point; 4) momentum measurement and 5) identification of hadrons. MAC is the first collider detector to pursue 1), and was designed to excel at 2) and 3). MAC also does well at 4) but was not designed to perform 5), hadron identification.[37] The durability of the MAC design is manifest by the similarity of many new detectors to MAC.

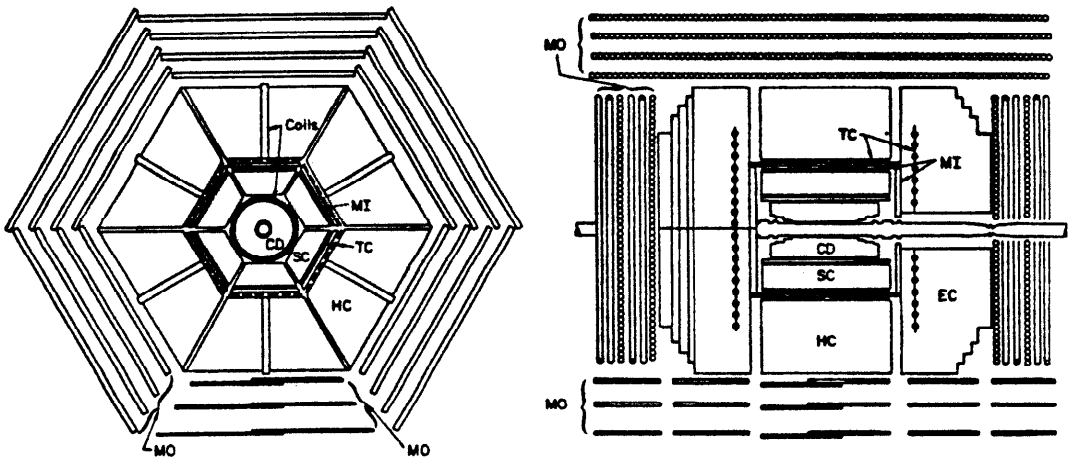

Figure 2.2 The MAC Detector. On the right is side view, with the beam pipe shown penetrating the center of the detector. The detector consists of a central section and two endcaps, surrounded by the muon system. On the left is an end view of the center section; the beam pipe would go in and out of the page. Subsystems are labeled: CD, the Central Drift chamber; SC, the central electromagnetic Shower Chamber; MI, the Inner Muon chambers; TC, the scintillation Trigger Counters; HC, the central Hadronic Calorimeter; EC, the Endcap Calorimeters; and MO, the Outer Muon drift chambers, usually labelled the OD.

The MAC detector is shown in Figure 2.2. A perspective illustration of the detector is exhibited in Figure 2.3. The central tracking chamber, the Central Drift chamber (CD), is surrounded by layers of lead or steel interspersed with proportional wire chambers, that form the MAC calorimeters. The CD is inside a solenoid that allows the momenta of charged particles to be measured. The calorimeters are surrounded by drift chambers for the measurement of muons. The steel in the outer calorimetry is toroidally magnetized, which enables a second momentum measurement to made for muons. A high precision drift chamber, the Vertex Chamber (VC), was added inside the CD in 1984 specifically for the B-lifetime measurement, and will be described in the next chapter. A detailed description of the various subsystems follows:[38]

2.3 Calorimeters

Sampling gas calorimetry was pioneered by the MAC detector[39] ; all the calorimeters are of this type. The calorimeters are split into three segments: the central electromagnetic shower chamber (SC); the central hadron calorime-

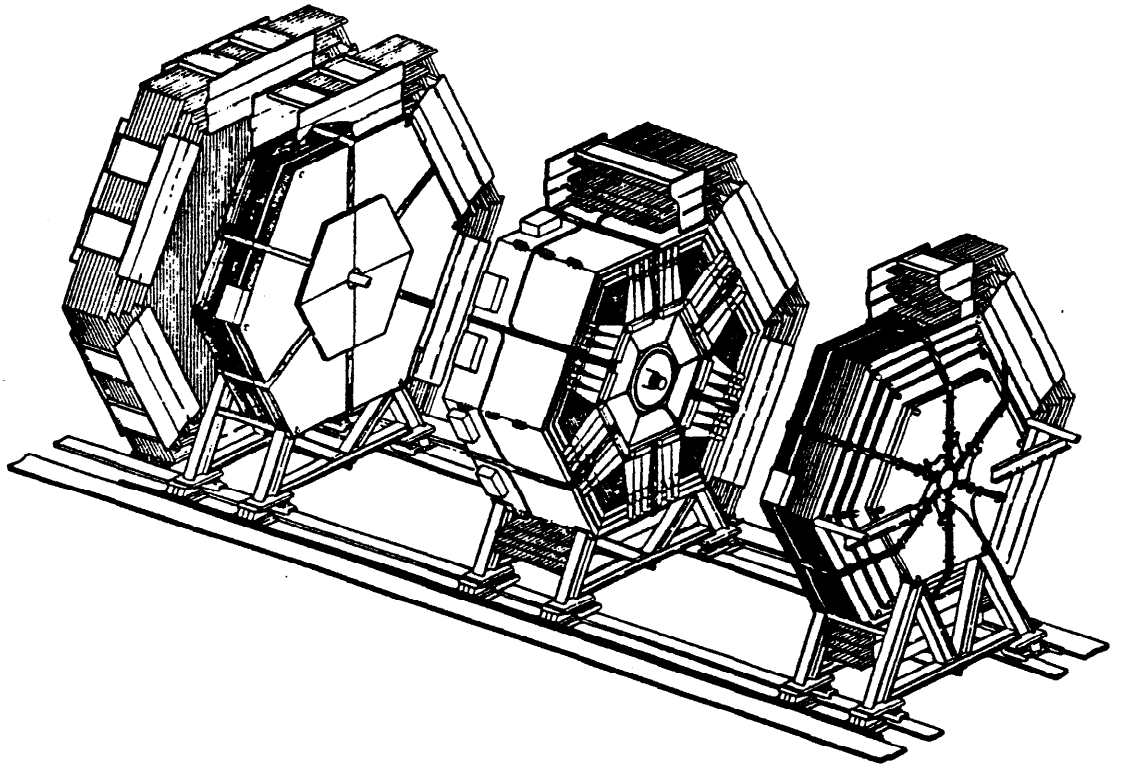

Figure 2.3 A Perspective View of the MAC Detector. Here the endcaps are shown pulled back off the central section, and cutaways of the muon system are made. The hexagonal structure is evident.

ter (HC); and the endcap calorimeters (EC). Small angle chambers (SA) were installed in 1983 to add veto power for a supersymmetry search. Figure 2.4 gives an overview of the arrangement and segmentation of the calorimeters. All the calorimeters use a gas mixture of 85% Argon-15% Methane at atmospheric pressure.

2.3.1 *Central Electromagnetic Shower Chamber*

The central electromagnetic shower chamber, or SC, consists of six sextants in azimuth, apparent in Figure 2.3. The inner face of each sextant is 60 cm in radius from the beam axis, outside the MAC solenoid. Within the sextant are 32 layers of 0.254 cm thick printer's type-metal (83% Lead, 12% Antimony, 5% Tin, radiation length $X_0 = 0.656$ cm) alternated with proportional wire chambers. The chambers consist of extruded aluminum channel, of channel width 1.7 cm and height 1.3 cm, with a $40\mu m$ diameter stainless steel sense wire, which runs

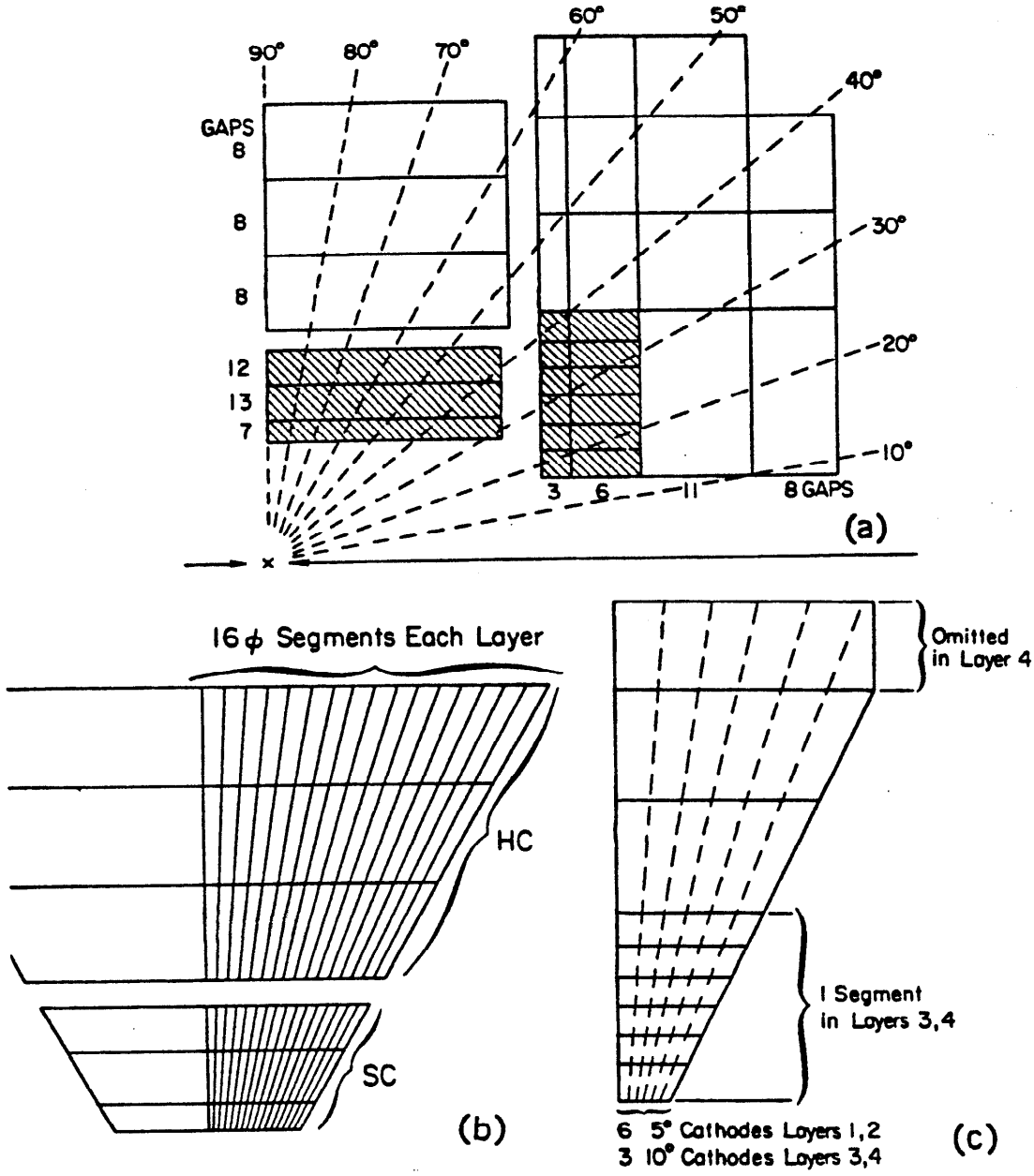

Figure 2.4 Segmentation of the Various Calorimeters. (a) Side view of the calorimetry. The electromagnetic shower systems are shown shaded. The number of wire planes in each radial layer is also indicated. (b) End view of the central section calorimetry. Each sextant of the SC and HC is divided into 62 azimuthal wedges of anode wires. These are further subdivided into 3 radial layers. (c) End view of the endcap calorimeter.

parallel to the beam. The chamber is 230 cm long parallel to the beam. The total number of sense wires is $\approx$ 9000.

The sense wires within a sextant are ganged into 62 groups in azimuth and 3 groups in radius, as shown in Figure 2.4. The total $12.4X_0$(0.5 nuclear absorption lengths, λ) is segmented radially into $2.7X_0$, $5.0X_0$, and $4.7X_0$ from in to out. The sense wires are read out from both ends and charge division employed to measure the z position of ionization. The wires are connected to low input impedance preamplifiers, which output to Sample and Hold Modules[40] (SHAMs), which in turn are read out by Brilliant Analog to Digital Converters[41] (BADCs) that perform pedestal subtraction. The MAC online computer, a DEC VAX 11/780, then reads out the BADCs via a CAMAC system.

Gas gain is monitored with Bhabha scattering events. The energy resolution for electromagnetic showers, measured with Bhabhas, is $\approx 24\%/\sqrt{E(\mathrm{GeV})}$. The resolution in azimuth is $\sigma_\phi \approx 0.6°$ for Bhabhas, and $\sigma_\theta \approx 1.2°$ in polar angle.

The SC is the detector element used to identify electrons in multihadron events. A sample of events with electrons at high $p_\perp$ relative to the thrust axis is used to measure the B-lifetime, and will be described in Chapter 4.

2.3.2 *Central Hadronic Calorimeter*

The central hadronic calorimeter, or HC, is segmented into sextants much like those of the SC. The construction is similar as well, consisting of iron plates alternating with proportional chambers. The iron is magnetized to $\approx$ 17 kG toroidally about the beam axis, and is used as a muon spectrometer. Each sextant starts 114 cm from the beam axis, and contains 24 layers of 2.5 cm thick plates followed by three 10 cm thick plates. The 2 cm gaps between the plates contain square extruded aluminum proportional tubes of inner dimension 1.2 cm x 2.4 cm. The $40\mu m$ stainless steel sense wires run parallel to the beam. Charge division is used to measure the location of ionization along their 230 cm length.

The sense wires within a sextant are grouped into 62 azimuthal segments, like those in the SC, and into five radial segments. The first three radial segments contain 8 layers, each 1.2λ. The two outer segments contain one layer of proportional chamber each between the 10 cm, or 0.6λ, iron pieces. Charge division is performed only for the inner two and outermost radial segments. There is a total of 5.4λ of iron in the HC. The preamplifiers and read out system of the inner four HC segments are very similar to the SC. A clever arrangement

of the inexpensive 733 video amplifier and a different readout system is used for the fifth layer.[42]

Calibration is performed with cosmic rays. The resolution for hadronic showers is typically $\approx 75\%/\sqrt{E(\mathrm{GeV})}$.

The HC is crucial to the measurement of energy flow in multihadron events. The thrust axis derived from measurements in the calorimeters is central to the B-lifetime measurement, as discussed in Chapter 5. The HC is also used to trace muons and to prevent pions from being misidentified as electrons.

2.3.3 *Endcap Calorimeter*

The construction of the endcap calorimeters, or ECs, differs considerably from that of the central calorimeters. Only iron plates are used. The iron is arranged perpendicular to the beam line, starting 128 cm from the interaction point, and is toroidally magnetized. There are 28 2.54 cm thick layers, followed by two 10 cm thick layers. The first 21 layers are hexagons of width 517 cm; the outer 9 layers narrow gradually to 351 cm. Twelve planar wire chambers are placed in each 2.54 cm gap in the pattern shown in Figure 2.5. The wire chambers consist of a plastic frame with walls of 0.32 cm fiberglass. Sense wires of $50\mu m$ Be-Cu are strung across the narrow width of the chambers, such that the wires end up at approximately at constant radius about the beam axis. The sense wires are spaced 1.9 cm apart. The cathodes are copper layers glued to the fiberglass walls. They are in segments that are perpendicular to the wires and pulses are read out from them. With the beam axis taken as the z-axis, the sense wires measure polar angle; the cathodes and chamber segmentation measure azimuth.

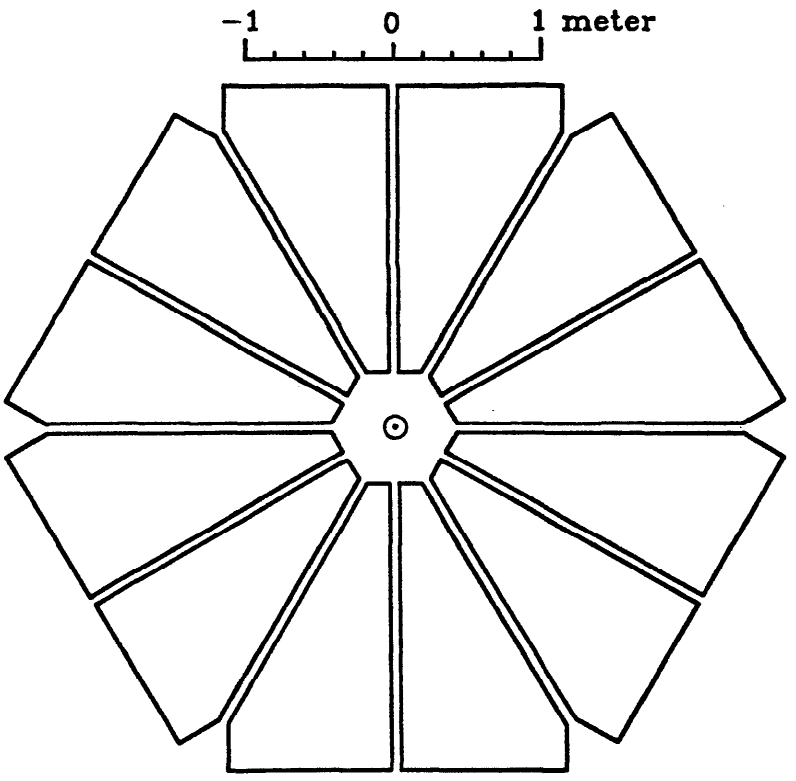

Figure 2.5 Azimuthal Arrangement of Endcap Wire Chambers. Twelve chambers are arranged about the beam axis. Wires are strung across the narrow width of the chambers, and the cathodes are azimuthally segmented.

Groups of chambers are ganged together in five segments in distance from the interaction point, with 3 layers in the first segment, 6 in the second, 11 in the third, 8 in the fourth, and 1 in the fifth. This segmentation is $4.3X_0$, $8.7X_0$, $15.9X_0$, $11.5X_0$, and $4.5X_0$ or 0.45λ, 0.91λ, 1.7λ, 1.2λ, and 0.6λ. The two inner segments have their sense wires ganged into 9 groups perpendicular to the beam line. These start at 40 cm from the beam, and are 2 @ 18 cm, 4 @ 12 cm, and 3 @ 43 cm across. The third segment has four groups of sense wires, 84 cm, and 3 @ 43 cm across. The fourth and fifth segments have only the first three wire groups of the third. The grouping of cathodes in azimuth is also finer for the inner two layers: 72 divisions are made, while only 36 are made for the third and fourth layers and just 12 for the fifth. Wires and cathodes were read out with SHAMs and BADCs.

Typical energy resolutions in the endcap calorimetry are $45\%/\sqrt{E(\mathrm{GeV})}$ for electromagnetic showers and $100\%/\sqrt{E(\mathrm{GeV})}$ for hadronic showers. Angular

resolutions are typically 1-2°.

The endcap calorimeters allow vetoing against low angle particles that produce electromagnetic or hadronic showers. They help measure energy flow in multihadron events, and are useful for tracing muons. However, the Be-Cu wires broke nearly daily during operation. These shorted the cathodes and compromised azimuthal segmentation. Cracks in the wire chambers, but not in the iron absorber, lined up as well, leading to inefficiency for muon tracing and azimuth dependent energy calibrations.

2.3.4 *Small Angle Chambers*

A sandwich of two pairs of wire chambers and two layers of lead, $6.3X_0$ and $2.3X_0$, form an annulus about the beam pipe just outside the CD. These small angle, or (SA), chambers were installed in 1983 to provide veto power for a supersymmetry search. The are placed ± 115 cm from the interaction point and subtend $0.951 < |\cos(\theta)| < 0.998$.

2.4 Drift Chambers

Gaseous drift chambers are used in the MAC detector for the vertex chamber (VC), the Central Drift chamber (CD), the inner muon chambers (MI), and the outer muon chambers (OD). The vertex chamber is described in Chapter 3. The CD starts close to the beam line and covers 95% of the solid angle. It has a small outer radius, so allows little distance for decay in flight of pions and kaons. The CD is used in conjunction with the axial magnetic field of the solenoid to measure the momenta of charged particles. The outer muon drift chambers perform precision tracking of muons for linkage with the CD and measurement of muon momentum in conjunction with the toroidal field in the steel calorimeters.

2.4.1 *Central Drift Chamber*

The MAC Central Drift chamber starts close to the beam axis, with an inner radius of 9.9 cm and the first active layer at 11.9 cm. The outer radius is 47.4 cm and the tenth and last active layer is 45.4 cm from the beam line. Six of the ten layers are stereo; details about all ten layers can be found in Table 2.1.

Layer	# Cells	Radius (cm)	Length (cm)	Stereo angle (mrad)
1	48	11.930	112.56	0
2	63	15.659	112.56	+50
3	78	19.938	140.42	-50
4	62	23.114	168.32	0
5	72	26.843	187.96	+50
6	82	30.571	187.96	-50
7	92	34.300	187.96	0
8	102	38.026	187.96	+50
9	112	41.755	187.96	-50
10	122	45.484	187.96	0

Table 2.1 Physical parameters of the Central Drift. Each cell contains a double sense wire to resolve the left-right ambiguity.

The six inner layers of the chamber cover $\cos(\theta) < 0.95$, where θ is the polar angle from the beam line. The ends of the chamber are stepped, to avoid very low angle noise. Figure 2.6 exhibits a side view of the chamber. The inner wall of the chamber contains 1.7% of a radiation length. For most of the data taken with the CD alone, an aluminum beam pipe of inner radius 8.26 cm and a thickness of 2.0% of a radiation length was employed.

There are a total of 833 cells. The cell structure employed in the Central Drift is shown in Figure 2.7. Cells in the inner three layers have a full width of 1.57 cm, and in the outer seven a full width of 2.35 cm. All cells are 1.10 cm high and layers are separated by 3.73 cm. For the first $\approx 2/3$ of MAC data taking, 90% Argon-10% Methane, or P-10, at atmospheric pressure was the sensitive medium, and gave maximum drift time of $\approx$ 300 ns in the inner three and $\approx$ 500 ns in the outer seven layers. In the final $\approx 1/3$ of MAC data, when the vertex chamber was present, 89% Argon-10% CO_2-1%Methane, or HRS gas, was used to suppress the Malter effect. This gas was faster, giving maximum drift times of $\approx$ 150 ns and $\approx$ 250 ns.

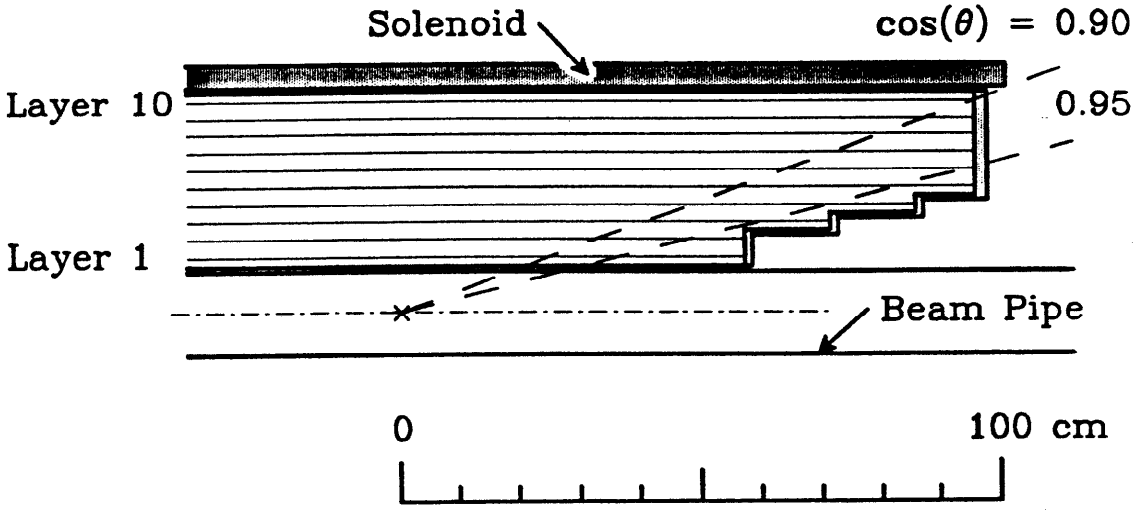

Figure 2.6 Side View of the Central Drift Chamber. The beam line, beam pipe, and solenoid are shown as well. Thin lines inside the chamber represent the ten layers of sense wires. The end walls are stepped for the first four layers.

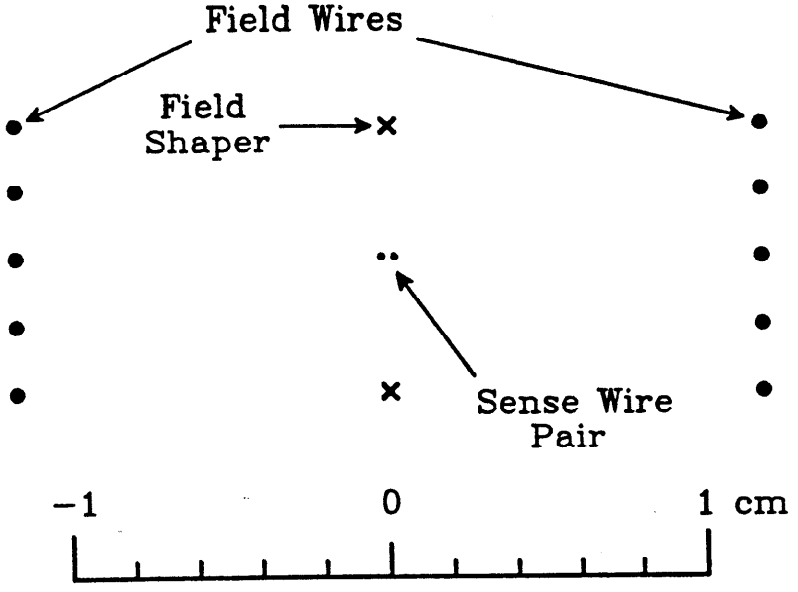

Figure 2.7 Cell structure in Central Drift. The field and field shaper wires are 200μm copper-beryllium, with a tension of 700 g. The double sense wires are 20μm gold plated tungsten, strung to 55 g tension, and spaced by epoxy bead. Negative high voltages of typically 1850 kV and 1400 kV were applied to the field and field shaper wires, respectively. The dimensions correspond to cells in the outer seven layers; those in the inner three layers are narrower by 0.75 cm

Novel double sense wires, at ground potential, are used to resolve the left-right ambiguity. Negative high voltage is applied to the field wires. Each sense wire pair is led to the ubiquitious differential 733 video amplifier, mounted on the chamber end wall. The sign of the output pulse thereby determines the side of the sense pair that the track passed. The drift chamber discriminators (DCDs) and drift time to voltage converters (TVCs) are differential throughout to maintain this sign. The start pulse for drift time measurements is derived electronically from the PEP master oscillator, although the time of the beam crossing, as determined from beam pickups, is monitored. The TVCs are read out by a smart unit known as a scanner, which performs null suppression, digitization, and buffering until the data is transferred to the online computer.

The chamber is calibrated in software with Bhabhas on two time scales: the average drift velocity and timing offset is calibrated every few hours (on a run-by-run basis), while channel by channel constants are determined several times per year. The typical spatial resolution measured with Bhabhas is $140\mu m$ for data taken with P-10 and $160\mu m$ for data taken with HRS gas. Resolutions for track parameters are shown in Table 2.2.

parameter	resolution
hit position	$140 - 160\mu m$
momentum, p	$\sigma_{\frac{1}{p}}/\frac{1}{p} = 0.052\, p(\mathrm{GeV}/c)\, \sin\theta$
phi, ϕ	$\sigma_\phi = 0.2°$
theta, θ	$\sigma_\theta = 0.7°$
impact parameter, d_0	$\sigma_{d_0} = 390\mu m$
vertex z-position, z_0	$\sigma_{z_0} = 0.6\,\mathrm{cm}$

Table 2.2 Central Drift Resolutions.

Without the CD, no B-lifetime measurement could have been performed. We use the tracking parameters determined from the CD to extrapolate back to the B production point, and look for non-zero B flight paths. In data for which the VC is present, linkage of VC and CD is essential to obtain the best

vertex resolution. The CD tracking parameters are linked with those determined in the outer muon drift system to identify muons, which we use to tag events containing B hadrons. These parameters are used to identify electrons in the central shower chamber for the same purpose.

2.4.2 *Inner Muon Drift Chambers*

Planar drift chambers are placed between the central shower chamber and the central hadron calorimeter, and just prior to the endcap calorimeter. Each cell has a 10 cm full width and a height of 2.5 cm. Twin sense wires of $50\mu m$ gold plated tungsten run toroidally about the beam. One layer is in the central calorimeter, and three are used in the endcap. These chambers are not used in the B-lifetime measurement.

2.4.3 *Outer Muon Drift Chambers*

The MAC calorimeters are surrounded by drift chambers with 5 cm maximum drift distance. Figures 2.2 and 2.3 show their positions and orientations. Everywhere but below the calorimeters these chambers are constructed of 10 cm diameter extruded aluminum tubes; planar chambers are used on the bottom. The aluminum tubes are grouped into two sections, known respectively as the hex boxes and the endplugs. The hex boxes surround five of the six faces of MAC, and consist of four active layers. The first layer is 285 cm from the beam axis, and the layers are 30 cm apart. The hex boxes extend ± 450 cm along the beam line on either side of the interaction region, so they cover $|\cos(\theta)| < 0.81$. The hex box tubes are typically 330 cm in length. The bottom chambers are outside the sixth face, have three layers separated by 35 cm that begin 285 cm from the beam, continue ± 420 cm along the beam line, and cover $|\cos(\theta)| < 0.79$, with some holes for calorimeter supports. The bottom chambers are 170 cm by 170 cm. The endplugs are outside the endcaps, consist of six layers spaced 18 cm apart, start 325 cm along the beam line from the interaction point, and extend from 45 to 253 cm outward from the beam, so cover $0.82 < |\cos(\theta)| < 0.99$. The endplug tubes vary in length from 180 cm to 570 cm. There are some 1720 tubes in the hex boxes, 348 in each of the endplugs, and 360 bottom chamber channels.

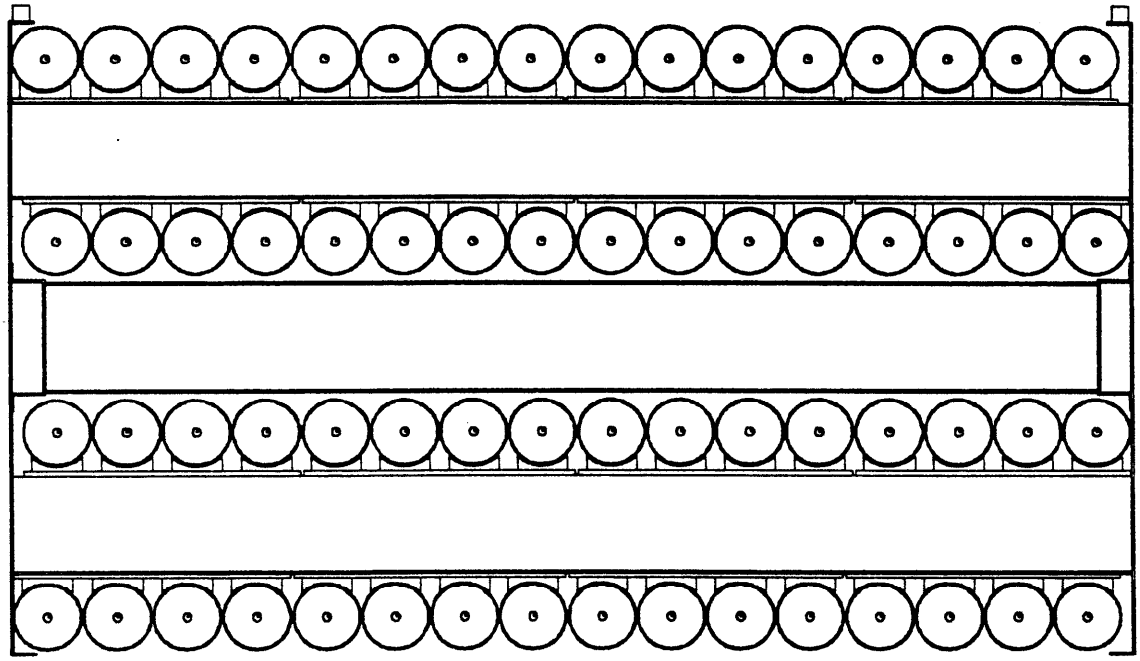

Figure 2.8 Cross Section of Hex Boxes. The aluminum tubes are 10 cm in diameter; the sense wire and wire insulator, as well as the support structure are shown. Note that the inner two layers are offset 1 cm with respect to the outer two, to aid in ambiguity resolution. This cross section is in the plane of the beam, the same plane in which muons bend due to the toroidal field in steel of the calorimeters.

The aluminum tubes all contain a $50\mu m$ gold plated tungsten sense wire, and the bottom chambers have a double sense wire to resolve the left-right ambiguity. In the hex boxes and bottom chambers, the wires run toroidally around the beam axis. This allows direct measurement of the bending angle of the muon in the toroidal magnetic field of the magnetized iron of the calorimeters. A cross section of the hex boxes is shown in Figure 2.8. The sense wires in the endplug chambers are perpendicular to the beam axis. Pairs of endplug layers have parallel sense wires; the three pairs are rotated in azimuth 60° relative to one another. A gas mixture of 85% Argon-15% Methane at atmospheric pressure is used, with a positive operating voltage of 2.7 kV and a maximum drift time of $\approx 1\mu s$. Outputs amplified by 733's are fed to DCDs and then to TVCs, read out by scanners and passed to the online computer.

The typical spatial resolution was 0.2 cm. Resolutions for reconstructed quantities for muons were dominated by multiple scattering for momenta up to $\approx$ 10 GeV. Typically, $\sigma_p/p \approx 25\%$, independent of p, below 10 GeV. The amount of matter between the interaction point and the muon system, critical for hadron rejection, is shown in Figure 2.9.

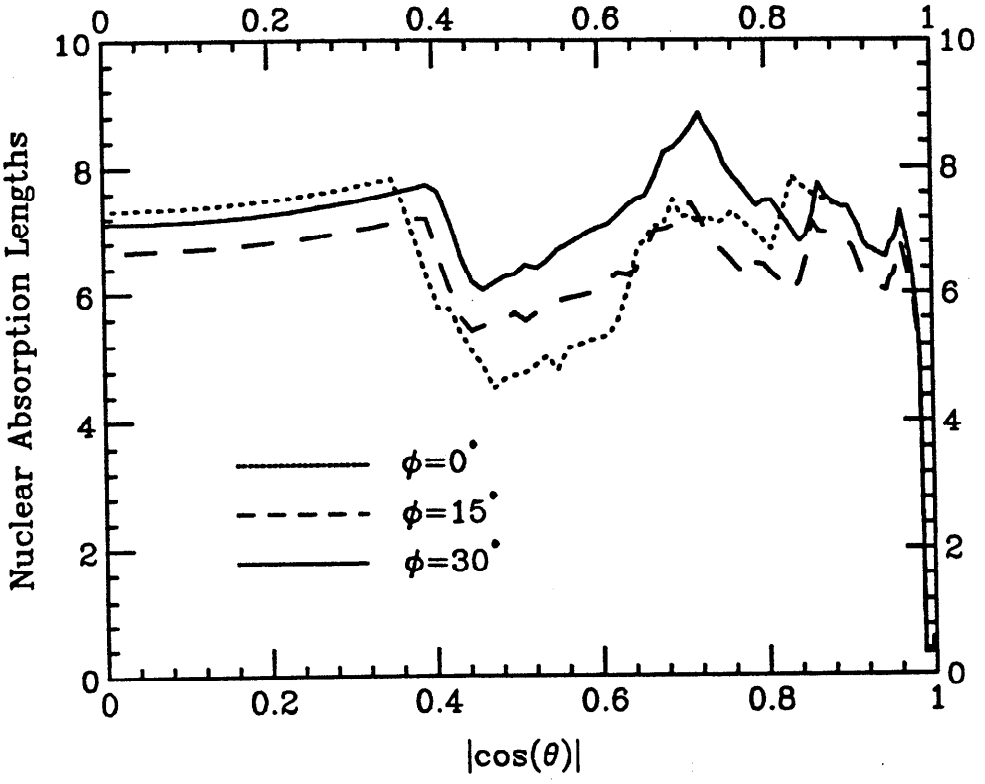

Figure 2.9 Matter Between Interaction Point and Muon System. Typically 6-7λ separates the interaction point and the muon system. Evident is the transition between the central section and endcap at $|cos(\theta) \approx 0.4$, and the endcap corner at $|cos(\theta)| \approx 0.75$.

The muon system is absolutely crucial for selection of the sample used for the B-lifetime measurement. It is noteworthy that the muon system, when used with the calorimetry, measures the muon direction and momentum independently of the central drift chamber, providing redundancy for cross checks. No other e^+e^- detector features a muon system with both the acceptance and the redundancy of the MAC system.

2.5 Scintillators

MAC features three scintillator systems. The trigger counters (TC) cover some 97% of 4π. Two systems are used to tag low angle electromagnetic showers: an annulus of plastic scintillator and another of BGO.

2.5.1 *Trigger Counters*

The locations of the MAC trigger counters can be seen in Figures 2.2 and 2.3. The arrangement can be seen in more detail in Figure 2.10. There are 72 counters in the central section, consisting of 36 azimuthal segments broken into two groups along the beam line. The scintillators are 128 cm from the beam axis, between the SC and the HC, 1.3 cm thick, 24 cm wide and 112 cm long. Lucite light guides lead to phototubes placed outside the central sections. There are 36 counters in each endcap, 159 cm from the interaction region. These are grouped into four quadrants, and consist of scintillators 20 cm wide, 1.3 cm thick, and between 106 cm and 189 cm in length.

The phototube output is split, 1/3 going to LeCroy Analog to Digital Converters (ADC's) and 2/3 going to LeCroy discriminators and Time to Digital Converters (TDC's). The typical time resolution is 1.0 ns.

The trigger counters enter solely in the B-lifetime measurement as the fast hardware trigger.

2.5.2 *Low Angle Taggers*

Two pairs of annular scintillators were placed at ± 1.6 m and ± 4.4 m, and cover $2.5° < \theta < 6.2°$ and $2.3° < \theta < 3.8°$, respectively. These detectors are primarily used in the MAC search for supersymmetric (SUSY) final states, and are not used in the B-lifetime measurement.

2.5.3 *BGO*

A pair of annular arrays of BGO crystals surround the beam pipe ± 40 cm from the interaction points. These crystals cover $4.8° < \theta < 7.2°$, and have a depth of $10.7 X_0$ which corresponds to only 12 cm. The BGO is read out by photodiodes. This novel application of new technology was also primarily used for the MAC SUSY search, and is not used in the B-lifetime measurement.

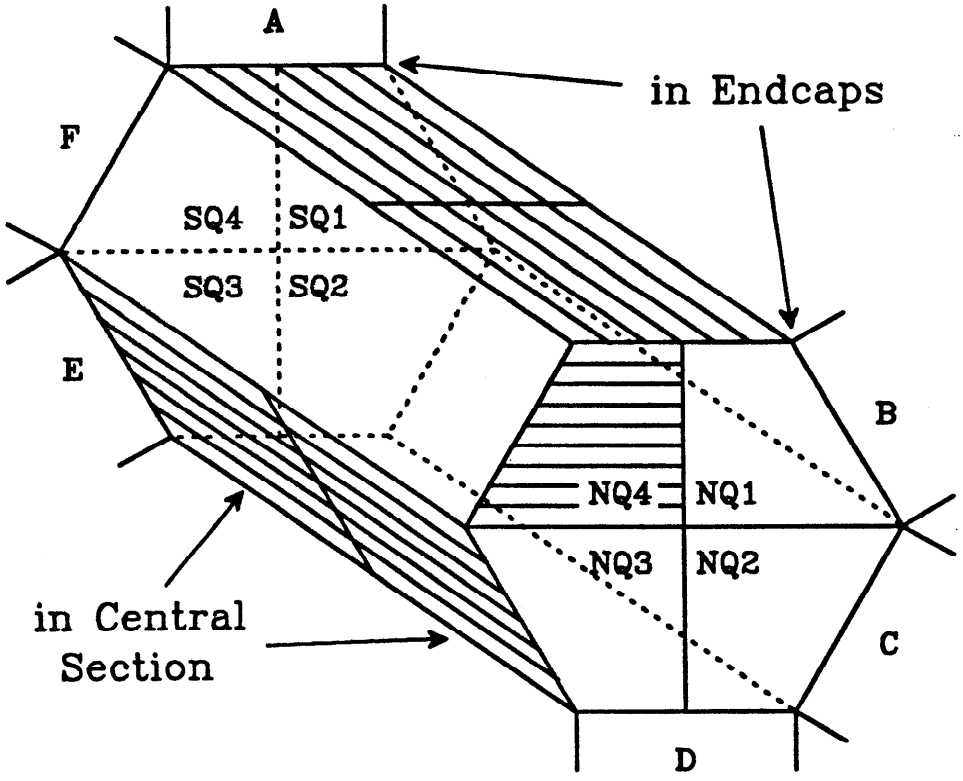

Figure 2.10 Arrangement and Segmentation of Trigger Counters. The trigger counters occupy the faces of a hexagonal prism. The beam runs along the axis of this prism and the interaction point is at the center. The counters in the central section are 112 cm, and those in the endcaps are 159 cm, from the interaction point.

2.6 Other Detector Elements

2.6.1 *Magnets*

The MAC solenoid is inside the central shower chamber, with an inner radius of 49 cm, a thickness of $0.85X_0$, and a length of 215 cm. Typically 6000 A is run through the windings, giving a field of 5.7 kG. The magnetic flux was returned in the inner layers of the HC. The solenoid's water cooling system set and maintained the temperature of the central tracking system at $\approx 30°$ C.

The MAC toroid is formed by the iron in the HC and EC iron. eighteen 700 A coils enclose the central section and each endcaps. The field in the iron is $\approx$ 18 kG, and $\approx$ 1.5 Tesla-Meter is traversed by muons.

2.6.2 *Luminosity Monitors*

Two pairs of detectors formed by a lead-scintillator sandwich are located at $\theta = 1.7°$. They subtend $\approx 1°$ at 470 cm from the interaction point. These are useful for a fast approximation of the luminosity.

2.7 Trigger

As discussed previously, beams cross every $2.4\mu s$ in PEP, or at a rate of 420 kHz. However, the time to transfer data from the 8000-odd channels of the MAC detector to the online computer limits the recording of events to several Hertz. Therefore, a fast decision must be reached whether to accept an event. This fast decision is known as the trigger. To make this decision, the 8000 channels are electronically combined into at most $\approx$ 250 segments, although most triggers utilize even coarser combinations of only 10-20 segments.

The MAC electronics of SHAM's, BADC's, TVC's, discussed previously, is usually reset after each beam crossing. However, if some of the MAC segments show sufficient activity, a *Pause* is made, meaning the reset after the beam crossing is inhibited. The pause buys time for a more complex decision. If more of the segments, possibly in proper geometric patterns, show activity, a *Trigger* is made, which inhibits all subsequent clears until data is read out. The trigger signals the BADC's and scanners to digitize the information in the SHAM's and TVC's, respectively. Then, the BADC's and TVC's are read into the VAX, and the detector returns to a quiescent state. Once in the VAX, the data is briefly examined by the *Software Trigger*, and the event rejected if it fails to meet even more stringent criteria. If the event passes, it is written to disk on the VAX. The time sequence of these events is shown in Figure 2.11.

2.7.1 *Segmentation*

Some 5213 channels of MAC are grouped into segments that are subsequently used in the trigger. Not included are the muon systems or luminosity monitors. Table 2.3 describes how the systems used are segmented. For the TC, CD, and VC the digital outputs of discriminators are combined into segments electronically. The calorimeter systems are actually summed at the analog level on the preamp boards and using special summing amplifiers before finally being discriminated. Typical discriminator levels appear in Table 2.4.

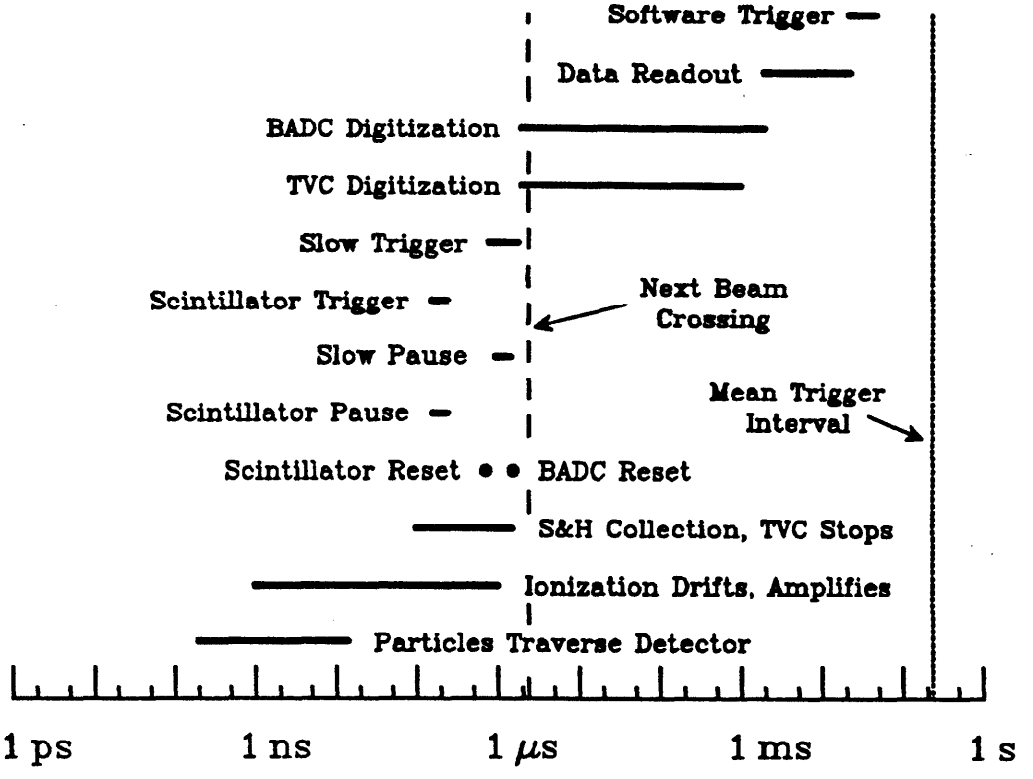

Figure 2.11 Time Sequence After Beam Crossing. The physical effect of particles traversing the detector, ionization, showering, and scintillation tends to be over $\approx$ 10 ns after the crossing. Drift in gases, phototubes, and transport of signals to the electronic sensors such as the TVC's and SHAM's takes another microsecond. These signals are combined and used for pauses and triggers, which are activated $0.2 - 2\mu s$ later. The triggers initiate digitization of analog signals, which consumes $1 - 3$ ms. Digitization is followed by readout to the computer and software examination.

2.7.2 *Pauses*

Pauses, also called pretriggers, suppress clearing of the data acquisition system for one beam crossing. They are simpler than triggers, and occur at a total rate of approximately 1 kHz. There is a fast pause, formed from only scintillator information, and a slow pause, which uses CD and calorimeter information as well. The fast pause occurs within 200 ns of the beam crossing, in time to prevent the scintillator data acquisition from being cleared. The slow pause occurs typically $1.2\mu s$ after the beam, but never occurs later than $1.7\mu s$, when the BADC clear occurs. Table 2.5 summarizes the pauses and their characteristics. Note that if a slow pause occurs in absence of a fast pause, scintillator information is not lost, because the fast pause occurs when *any* scintillator fires.

Detector Element	Total Channels	Finest (A) # Seg.	Finest (A) $\theta \times \phi \times d$	Finer (B) # Seg.	Finer (B) $\theta \times \phi \times d$	Coarse (C) # Seg.	Coarse (C) $\theta \times \phi \times d$
TC c	72	36	$2 \times 18 \times 1$	6	$1 \times 6 \times 1$	1	1
TC e	72	8	$2 \times 4 \times 1$	8	$2 \times 4 \times 1$	2	$2 \times 1 \times 1$
SC	1152	36	$1 \times 12 \times 3$	-	-	6	$1 \times 6 \times 1$
HC	1536	30	$1 \times 12 \times 2$ $1 \times 6 \times 1$ d	6	$1 \times 6 \times 1$	1	1
EC	1128	96	$2 \times 12 \times 4$	20	$2 \times 6 \times 1$ $2 \times 4 \times 1$ d	2	$2 \times 1 \times 1$
SA	96	16	$2 \times 4 \times 2$	-	-	2	$2 \times 1 \times 1$
CD	833	22	$1 \times 18 \times 1$ $1 \times 4 \times 1$ $\theta = d$	-	-	-	-
VC	324	18	$1 \times 18 \times 1$	-	-	-	-

Table 2.3 Segmentation of Detector Elements Used in the Trigger. Approximately three levels of segmentation are employed, denoted here (A), (B), and (C). d stands for depth from the interaction point. The trigger counters (TC) are segmented very differently in the central (c) and endcap (e) sections of MAC; this can be seen in Figure 2.10. The HC, EC, and CD are segmented differently in angle for different depths.

Detector Element	Finest (A) # Seg.	Finest (A) Threshold	Finer (B) # Seg.	Finer (B) Threshold	Coarse (C) # Seg.	Coarse (C) Threshold
SC	36	0.25 GeV	-	-	6	1 GeV
HC	30	not disc.	6	0.5 GeV	1	4 GeV
EC	96	not disc.	20	0.5 GeV	1	3 GeV
SA	16	not disc.	-	-	2	3 GeV

Table 2.4 Discriminator Thresholds for Calorimeter Segments. The analog sums from some segments are not discriminated, but only used for further sums. The characterization in GeV is approximate.

Name	Delay	Rate	Condition	Target
P_{TC}	$0.2\mu s$	0.2-1 kHz	*Any* of 144 Scintillators	Charged Final State
P_{neut}	$1.2\mu s$	3 Hz	$\overline{P_{TC}}(\geq 2$ of 9 calor. (C))	Neutral Final State
P_{CD}	$1.2\mu s$	30-50 Hz	≥ 2 of CD (A)	2γ, cracks
P_{SC}	$1.2\mu s$	130 Hz	≥ 1 SD (C)	e, γ
P_{SA}	$1.2\mu s$	30 Hz	≥ 1 SA (C)	e, γ

Table 2.5 Pauses Used in MAC The delay from the beam crossing and typical rate are shown. $\overline{P_{TC}}$ means lack of the P_{TC} pause. The segmentation of detector elements from Table 2.3 that is used is shown.

2.7.3 *Triggers*

More complex combinations of detector segments are used to generate triggers. There is one fast trigger, available $0.2\mu s$ after beam crossing, that relies on either back to back scintillators or a multiplicity of scintillators to fire. Slower triggers that require several segments from different detector elements are also used. These triggers are typically available $1.3\mu s$ after beam crossing, but may fluctuate to later times, such that they arrive after the BADC reset. Table 2.6 describes the various triggers. These triggers varied somewhat over the history of the experiment, but their typical characteristics are shown.

All of the hardware triggers are efficient for the multihadrons used in the B-lifetime. For the first $\approx 40\%$ of MAC data taking, $\approx 99\%$ of multihadrons logged fired the CD Shower trigger, $\approx 98\%$ fired the Energy trigger, and $\approx 96\%$ fired the Muon trigger. For the remainder of the data the Energy trigger's threshold was raised, such that $\approx 70\%$ of logged multihadrons fired it. At this point the Shower trigger was installed, which fired for $\approx 93\%$ of multihadrons. The Scintillator trigger fired for $\approx 85\%$ of multihadrons. These triggers were redundant and predominantly uncorrelated, with measured non-random correlations of only $\approx 10\%$. The detector simulation reproduced efficiencies and correlations very well, and indicates the hardware trigger efficiency for multihadrons exceeds 99.5%.

Name	Delay	Rate	Condition	Target
Scintillator	$0.2\mu s$	1.7 Hz	[Back to Back Scintillators (B)] or [$\geq$ 3 of 14 Scintillators (B)]	$\mu^+\mu^-, q\bar{q}$
Energy	$1.3\mu s$	0.2 Hz	$\geq$ 2 of {SC (C); [TCc (C)] and [HC (C)]; [TCe (C)] and [EC (C)]}	inclusive
Muon	$1.3\mu s$	0.7 Hz	$\geq$ 1 of {[CD (A)] and [TCc (A)] and [HC (B)]; [CD (A)] and [TCe (A)] and [outer EC (B)]}	$\mu^+\mu^-, \tau^+\tau^-$
CD Shower	$1.3\mu s$	1 Hz	[$\geq$ 2 of CD (A), separated by 90°] and [$\geq$ 2 of (SC (C); inner EC (B))]	2γ
Shower	$1.3\mu s$	1.5 Hz	[SC (C)] and [$\geq$ 2 of adjacent SC (A)]	e, γ
SA Shower	$1.3\mu s$	0.4 Hz	[SA (C)] and [$\geq$ 2 of adjacent SC (A)]	$ee\gamma$

Table 2.6 Triggers Used in MAC The required detector segments with letters giving the detector segmentation from Table 2.3are shown. The primary physics targets of these triggers is also given.

2.7.4 *Software Trigger*

A fast computer program evaluates each event read into the VAX. This program assigns the event to one of $\approx$ 20 categories, or throws it away. Some of the 20 categories, or 'software triggers,' are refined versions of the 'hardware' triggers listed in Table 2.6. For example, the software Scintillator trigger requires not only back to back scintillators, but also CD (A) segments, or 'wedges,' in coincidence. The software Energy trigger also requires CD wedges in addition to the hardware requirements. New triggers are invoked in software as well, such as one that passes events with back to back energy in the calorimeters. Typically the software trigger passes 40-60% of events with a hardware trigger.

2.8 Data Processing

MAC features a very good data processing and management system. Data is transferred from the online VAX to the computer for offline processing, an IBM 3081, electronically, without the use of tape. At the IBM, processing starts

as soon as data arrives, in an automated fashion. Critical constants for the calorimeters and the drift chambers are determined either online with bhabhas, or in the first short IBM job, called PASS0. Subsequently, a second IBM job is automatically executed called PASS1. PASS1, also called the offline filter, does full event reconstruction and filters out $\approx 90\%$ of the data. The surviving 10% is intended to include all events from one-photon annihilation, and is kept on disk for typically several weeks, and is also stored on tape. Subsequent jobs to select samples of special interest, such as the multihadrons used for the B-life measurement, $\mu^+\mu^-$, or $\tau^+\tau^-$ are run while the data resides on disk. It is usual for all PASS1 processing to be complete within one day of the end of a PEP running cycle, and all special interest samples to be complete a few weeks later. This data flow is shown in Figure 2.12.

2.8.1 *Online Management*

After an event passes the software filter, it is logged to disk on the VAX. Typically it is $\approx$ 1600 bytes long after suppression of zeroes in the calorimeter information. Data is grouped into 'Runs' that correspond to fills of the PEP ring. Runs typically last 2 hours, contain 10,000 events, and accumulate 50 nb^{-1} of integrated luminosity. Runs are then automatically transferred to the IBM disks over a high speed ($\approx$ 50 kbaud) line.

2.8.2 *Offline Management*

Subsequent processing of events occurs while runs remain on an IBM disk. After each run arrives, a batch job, known as PASS0, is automatically submitted which determines drift chamber constants. After PASS0 is complete, a second batch job, PASS1, is submitted. PASS1 reconstructs events, uses the reconstructed information to assign *attributes* to each event, then rejects or retains events depending upon on whether they have combinations of attributes called *masks*. Reconstruction is performed in order or time needed, from the least time consuming detector element to the most, the CD+VC. The examination of attributes is performed during reconstruction, so if an event fails an early mask, reconstruction ceases, thereby saving computer time. Typically 150 ms is spent on each event that survives to full reconstruction.

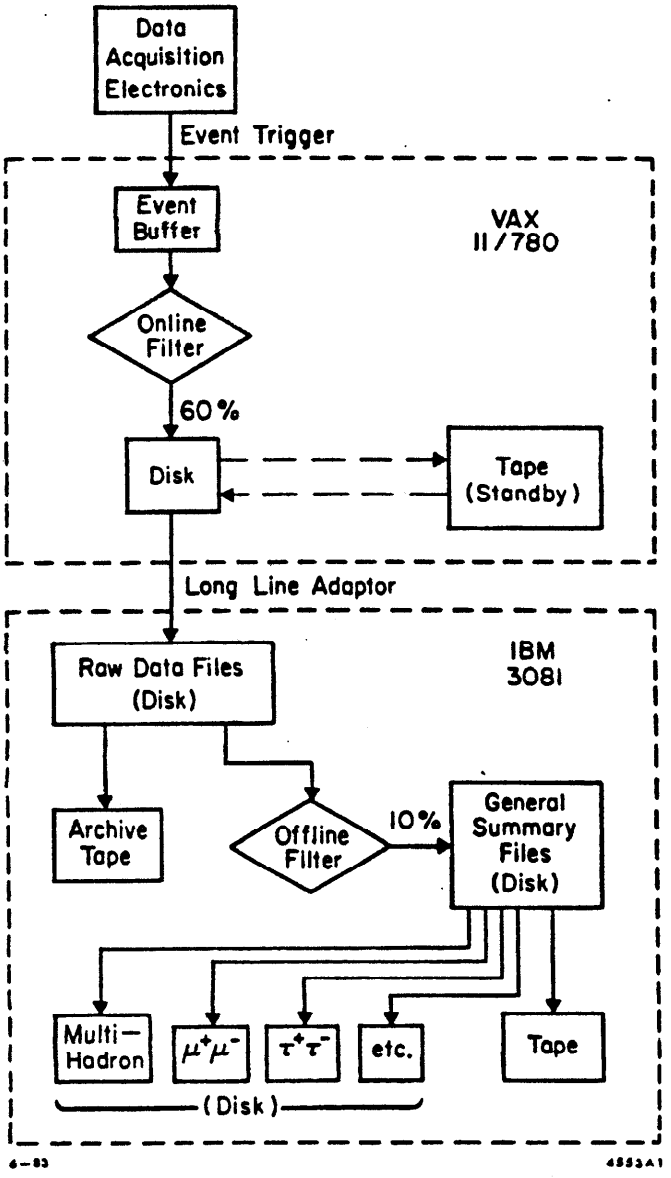

Figure 2.12 Data Flow Structure. Data is read in when a hardware trigger occurs, and proceeds in an automated fashion to the 'General Disk Summary Files.' These files are then used to produce subsamples, of which the multihadron subsample is used for the B-lifetime measurement.

Some attributes are: amount of energy in the HC, number of CD tracks, number of TC scintillators hit. Up to 18 attributes can be examined with a mask. The mask specifies an allowed range that each attribute can take. In the PASS1 analysis, some 43 masks in two 'levels' are employed. The 17 first level

masks require only a fast CD reconstruction, while the 26 second level masks require full CD+VC reconstruction. Typically $30-50\%$ of input events survive the first level, and 10% survive the second level or masks. These survivors are logged into disk files, and remain on disk for several weeks. During this time multihadron, as well as other subsample, selection, is performed. Monte-Carlo studies indicate that PASS1 passes multihadrons with $\approx 95\%$ efficiency.

In contemporary jargon, MAC's hardware trigger is the 'Level I' trigger: it makes a decision in a time limited only by analog, not digital, timing. The software trigger is a crude 'Level II' trigger: it uses the results of digitization, and does some simple reconstruction. Finally, PASS1 is the 'Level III' trigger: it performs full reconstruction. PASS1 could be implemented in emulators resident at the experiment.

2.8.3 *Multihadron Selection*

Events surviving PASS1 are subjected to further filtering to select multihadrons. The following quantities are used in this filter:

- $E_{vis} = \sum_{i=1}^{N} |\vec{E}_i|$, where N, 2-ended calorimeter hits are used in the summation;
- $E_{\perp} = \sum_{i=1}^{N} |E_{i\perp}|$ is the transverse energy;
- $I = |\sum_{i=1}^{N} \vec{E}_i|/E_{vis}$ is the energy imbalance;
- $\rho_{sum} = \sum_{i=1}^{M_{ch}} |\vec{P}_i|$, where M_{ch} charged tracks are used in the summation;
- Z_v is the z-position of the event vertex;
- H_{cd} = (number of CD hits)$/M_{ch}$ is the average number of drift chamber hits;
- $\rho_{cal} = \frac{1}{N} \sum_{i=1}^{N} |\vec{E}_i|$ is the average energy per calorimeter hit; and
- E_{had} is the sum the energy in the hadron part of the calorimetry.

Loose and tight cuts are constructed for these quantities; these are detailed in Table 2.7. Any event passing all the tight cuts is accepted; any event failing any loose cut is rejected. Events that pass some loose cuts but fail tight cuts are either rejected or hand scanned. The purpose of the hand scanning is to reject very obvious background from cosmic rays or Bhabhas. Typically $< 0.1\%$ of

Cut	Loose	Tight
E_{vis}	> 12 GeV	> 15 GeV
$E_{\perp}$	> 7.5 GeV	> 9.1 GeV
I	< 0.65	< 0.55
M_{ch}	≥ 3	≥ 5
P_{sum}	> 2.0 GeV/c	> 4.5 GeV/c
$\|Z_v\|$	< 5 cm	< 5 cm
H_{cd}	> 5.75	> 6.30
ρ_{cal}	< 1.1 GeV	< 0.7 GeV
E_{had}	no cut	> 1.5 GeV

Table 2.7 **Cuts Used to Select Multihadrons. Event failing loose cuts are rejected, those passing loose cuts are accepted. Some of those that fall between the cuts are rejected, and others are scanned to remove obvious background.**

Monte-Carlo generated hadronic events, from either one-photon annihilation or two-photon processes, are rejected by the scan.

Based on Monte-Carlo studies, we estimate the efficiency of the of the multihadron cuts to be 78%, with 2% background from 2γ processes, and 1% from $\tau^+\tau^-$. These cuts select 150,845 events from the $320\,\mathrm{pb}^{-1}$ collected by the MAC detector. Approximately the last one third of these data, or $107\,\mathrm{pb}^{-1}$, were taken with the Vertex Chamber installed, and yield 49778 events. The accumulation of events as a function of integrated luminosity is shown in Figure 2.13.

2.9 Monte-Carlo

A number of Monte-Carlo programs are used to simulate a sample of multihadron events. Specific to multihadrons is the event generation. First, we model $e^+e^- \rightarrow q\bar{q}(\gamma)$ with a slightly modified version of the Berends-Kleiss-Jadach generator, which includes QED effects to $O(\alpha^3)$ and virtual Z^0 exchange.[43] Next, additional quarks and gluons are added using *2*, *3*, and *4-jet* matrix elements.[44] The quarks and gluons are then evolved into hadrons, and the decay of short-lived hadrons are modeled, by a modified Lund Monte-Carlo, using

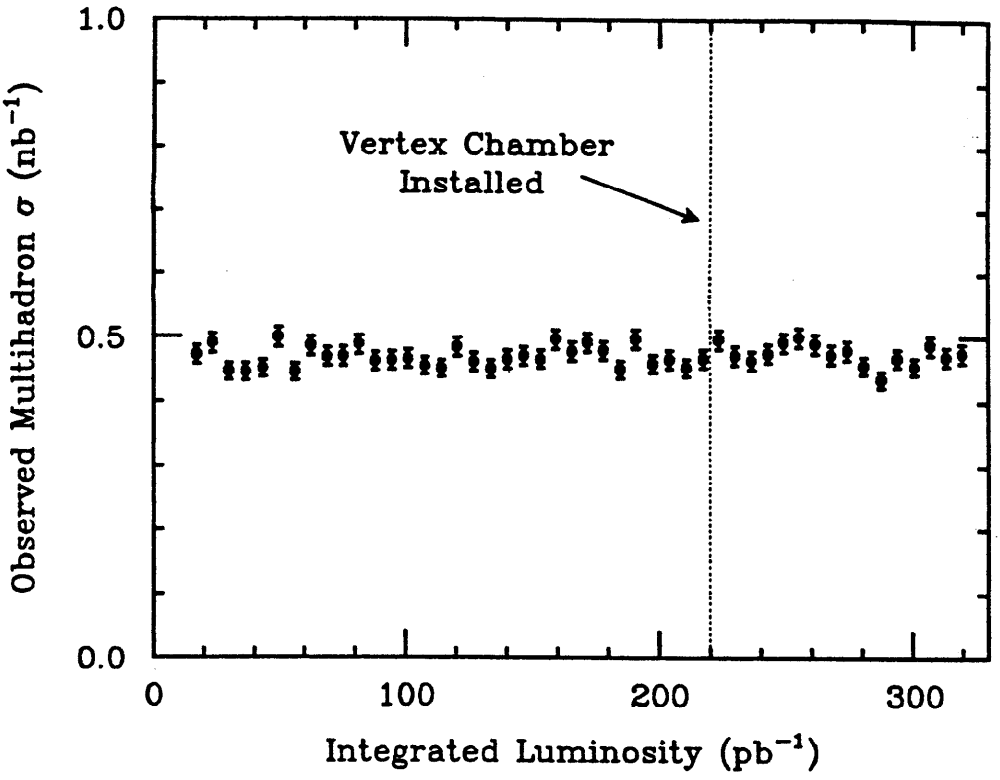

Figure 2.13 Observed Multihadron Production. The observed cross section, σ, as a function of integrated luminosity; no efficiency correction is made. 3000 events comprise each point. The Vertex Chamber was present for the final 107 pb^{-1}.

string fragmentation.[45] The primary modification is in c and b-quark fragmentation, where we employ the Peterson form.[46] Particles with non-zero lifetimes are given pathlengths using our own code. At this point the event generation is complete.

In the next stage, the signals these events would make in our detector is simulated. The same detector simulation is used, no matter what the event generator. The propagation of electrons and photons through the detector, including their development into electromagnetic showers, is performed using the EGS code. The propagation of hadrons is modeled using the HETC code. Decays in flight of primary pions and kaons, as well as secondary pions and kaons generated inside hadronic showers, is performed by modified HETC subroutines. Ultimately, the ionization and scintillation of particles in MAC is modeled, including Landau fluctuations and δ-rays, and TVC and BADC outputs computed.

After detector simulation, events are processed through PASS1 and the mul-

tihadron event selection.

Chapter 3

Vertex Chamber

In the summer of 1983, the MAC and Mark-II collaborations gave evidence for bottom hadron lifetimes of 1-2 ps[22-24] accumulated at the PEP e^+e^- storage ring at SLAC. The importance and fundamental nature of this measurement[4,29] prompted the MAC collaboration to propose, in autumn 1983, the addition of a high precision vertex chamber to the MAC detector. There was insufficient time available to either develop a typical drift chamber, or to employ solid state technology, so a device that utilized thin walled cylindrical drift tubes made of aluminized mylar was designed. Aluminized mylar drift tubes had first been used by the HRS collaboration at PEP.[51] The MAC Vertex Chamber was installed in autumn 1984 and immediately provided useful data. It continued to operate until March, 1986, when MAC data taking ceased. It has achieved the highest spatial resolution $-35\mu m-$ of any drift chamber used at colliders for physics results.

Following the successful operation of this Vertex Chamber, many collaborations, including the Mark-III at SPEAR, CLEO at CESR, the upgraded TPC at PEP, AMY at TRISTAN, and JETSET at LEAR have built or proposed similar devices. Indeed several features of this type of chamber are well matched to the probable conditions at future accelerators such as the SSC or LHC: the small cell size is suited to the high rate and dense tracking environment anticipated; the simplicity and ruggedness make a system of 10^5 channels credible. The Multidrift-Tube, intended primarily for SSC or LHC use,[52] is in some ways the evolutionary descendant of the MAC-type Vertex Chamber It should be noted that the MAC Vertex Chamber has operated only 4.6 cm from colliding beams, and has suffered *no* degradation due to radiation damage; this augurs well for

survival in the more extreme conditions of the SSC or LHC.

3.1 Design Choices

Our initial motivation for using the thin walled mylar tubes[51,54] (often referred to as 'straws' because they are made in a spiral wrap, much like paper drinking straws) was simplicity and robustness. Field wires and problems of drift field mapping are eliminated. If a sense wire breaks, it is physically and electronically isolated from the other sense wires, so does not harm the rest of the chamber. However, there are other advantages to the use of straws. We have obtained $20\mu m$ spatial resolution in beam tests with them, and $35\mu m$ in our Vertex Chamber for physics results. Their small size is not only useful for the high rate environment, but aids pattern recognition in the dense regions of multitrack events. Their large, flat cathode makes straws less susceptible to some ills of radiation damage, including whisker growth and cathode coating.

Our Monte Carlo studies[55] indicated that the spacing of ionization clusters, and not diffusion, dominates the spatial resolution for drift distances as short as those in straws. This is in contrast to jet type cells, and indicates that the best strategy for high spatial resolution is to trigger the timing discriminator at the least possible ionization, instead of using the centroid in time of ionization arriving at the sense wire. To achieve a low threshold, we decided to operate the chamber at the highest possible gas gain, even in the 'self quenching streamer' mode if possible. We also decided to operate the chamber at high pressure, to reduce the spacing between ionization clusters.

Of course, a disadvantage of high gas gain is that the chamber might age quickly from beam-related radiation. We carefully designed our shielding, and performed a number of gas lifetime studies, so we avoided this problem. Other disadvantages of straw chambers include: 1) the drift region close to the wire makes up a larger fraction of the active region than in jet type cells; this region *can*, but by no means *must*, have poor spatial resolution; 2) high gas gain is not linear with ionization, possibly impeding dE/dx measurements; 3) the radial drift field makes multihit resolution difficult; 4) the matter in the straw walls causes photon conversion and multiple coulomb scattering; and 5) very long straws are hard to keep straight. None if these disadvantages appear insurmountable.

We took great care in the machining of the endplates and the placement of our sense wires, but our strategy was always to survey the positions of the wires *in situ* with tracks from Bhabha scattering events. This has proved very successful. We have established the wire positions to $10\mu m$ in this manner.

3.2 Research, Development, and Design

3.2.1 *Gas Gain*

We observed that the straw walls were photosensitive. When visible light from an incandescent bulb was shined on the straw, single electrons were ejected. These proved useful for the study of gas gain, and were complementary to the Fe^{55} source, which provides some 240 initial electrons per pulse. Battistoni *et al.* have also observed photosensitivity in aluminum-walled streamer tubes.[53] We found that the photo-efficiency of the wall depended greatly on the history of the straw; higher efficiencies could be induced by several seconds of high voltage discharge in the straw.

We noticed that signals from the large amount of primary ionization from the 5.9 keV X-ray of an Fe^{55} source never went through the characteristic 'jump' from proportional to streamer mode. It is possible that electrostatic saturation limited the gain. In contrast, the signals from single electrons *did* go through the characteristic jump, as shown in Figure 3.1. In the streamer mode, single electron pulses were nearly as large as those from 5.9 keV X-rays. The stable streamer 'plateau' for single electrons lasted for 500 V in 4 atm absolute 50% Argon-50% Ethane. We found similar behavior in two gas mixtures with little organic additive: 49.5% Argon-49.5% CO_2-1.0% CH_4, with a 200 V plateau; and 50% Argon-40% CO_2-10% Xenon, with a very nice 900 V plateau. The limiting behavior at the high end of the plateau was photoelectric feedback from the cathode. Stable, large pulses from single electrons have been achieved in Magic Gas;[56] where the addition of freon suppresses feedback from the cathode; similar gas gains have been achieved in Dimethylether.[57]

Operation at high voltages where single electrons produce streamers would lead to the best spatial resolution for short drift distances, as mentioned in the previous section. The noise requirements on the preamplifiers would not be stringent.

3.2.2 *Radiation Damage*

The primary obstacle to operation at high gas gain near colliding beams is damage induced by background radiation. We conducted studies of radiation

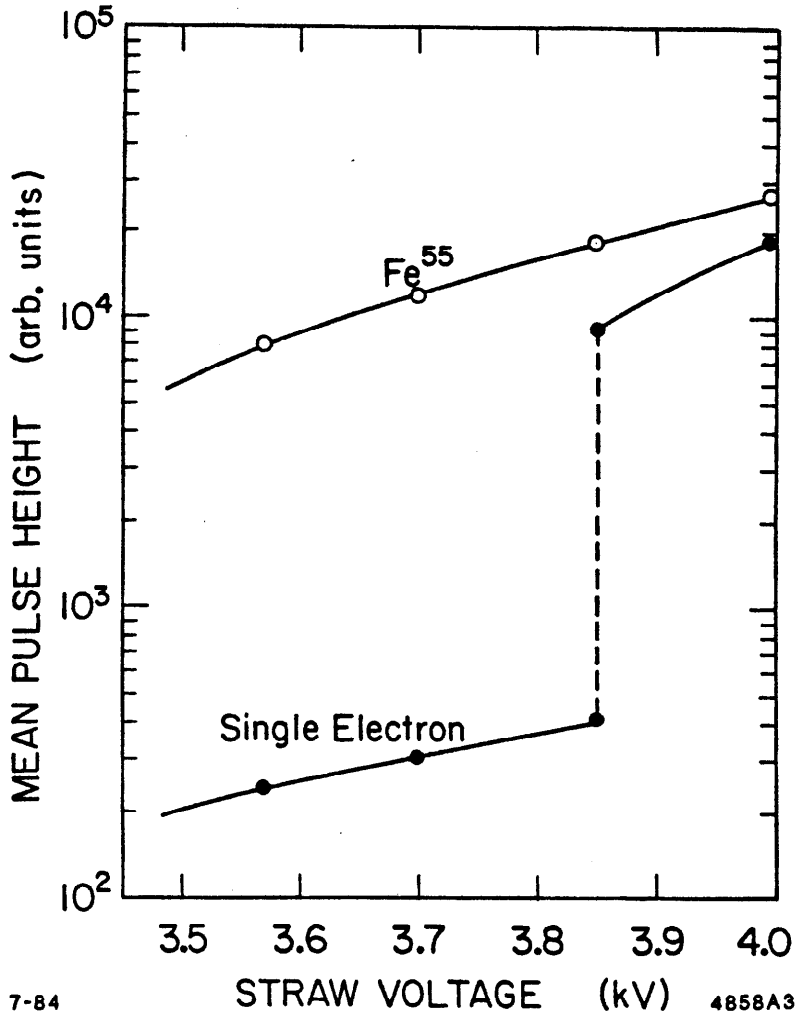

Figure 3.1 Gas Gain for 5.9 keV X-rays and single electrons. Data taken with 50% Argon- 50% Ethane at 4 atm. absolute, with a 20μm sense wire and a straw of radius 6.9 mm. The signal from Fe^{55} X-rays never underwent the characteristic 'jump' into streamer mode, but the single electron signal did.

damage in a test apparatus as similar as possible to our proposed Vertex Chamber. In particular, we conducted the tests at 4 atm absolute pressure, and did not circulate the gas; plastics such as teflon, PVC, and epoxy were used in the test vessel. More details of our tests appear in Ref. (58).

We found a variety of Argon-Hydrocarbon mixtures, including 50% Argon-50% C_2H_6, 70% Argon-30% C_4H_{10}, and 49.5% Argon-49.5% C_2H_6-1.0% H_2 failed reproducibly at 0.05 C/cm of accumulated charge. The straw would go into continuous discharge; replacement of the anode wire restored performance.

We concluded that a whisker had grown on the anode wire. We did not add alcohol, as this damaged the glue in the straw. Constraints of time prevented us from searching for a more resilient glue.

We estimated that 0.05 C/cm was unacceptable, so we turned to a non-organic quencher, CO_2. 50% Argon- 50% CO_2 showed no anode damage; in fact, study of the Fe^{55} X-ray spectrum indicated the anode wire became cleaner up to 0.05 C/cm accumulated charge. However, the straw failed at 0.25 C/cm accumulated charge due to the disappearance of aluminum from the cathode. We hypothesized that positively charged CO_2 fragments attacked the cathode. We added a small amount of CH_4 hoping charge transfer would occur, and that CH_4 species would cause less damage to the cathode. Only a slight improvement was observed; we settled on 49.5% Argon-49.5% CO_2-1.0% CH_4 as our operating gas. Use of Xenon rather than CH_4 led to a similar slight improvement in lifetime.

The aluminum layer on our mylar had a surface resistivity of 0.8Ω/square, indicating a thickness of $\approx$ 30 nm. A thicker layer of aluminum, or use of a different metal, may extend the liftime of straws. In fact we had obtained aluminized mylar with a resistivity of 0.4Ω/square, but time constraints precluded its use.

The choice of 49.5% Argon-49.5% CO_2-1.0% CH_4 brought with it certain benefits and compromises. A definite benefit was the slow drift velocity: the maximum drift time was some 240 ns, whereas the maximum drift time was 70 ns for 50% Argon-50% Ethane. The slow drift velocity made the spatial resolution fairly insensitive to timing errors, in particular for large drift distances. On the other hand, in a high rate hadronic environment, this long drift time is a disadvantage. Further, the drift velocity is not constant as a function of drift distance (see Figure 3.14). This presented no problem in our application, but space charge could well render the drift velocity unstable in a high rate environment, such as the SSC. This is not the case for 50% Argon-50% Ethane, which has a nearly constant drift velocity.

A compromise involved in using 49.5% Argon-49.5% CO_2-1.0% CH_4 is its gas gain properties. Carbon Dioxide does not absorb hard UV as well as Ethane. At the highest gas gains, where single electrons are capable of initiating streamers, 49.5% Argon-49.5% CO_2-1.0% CH_4 produced a much broader pulse height spectrum than 50% Argon-50%Ethane. We suspect this broad pulse height spec-

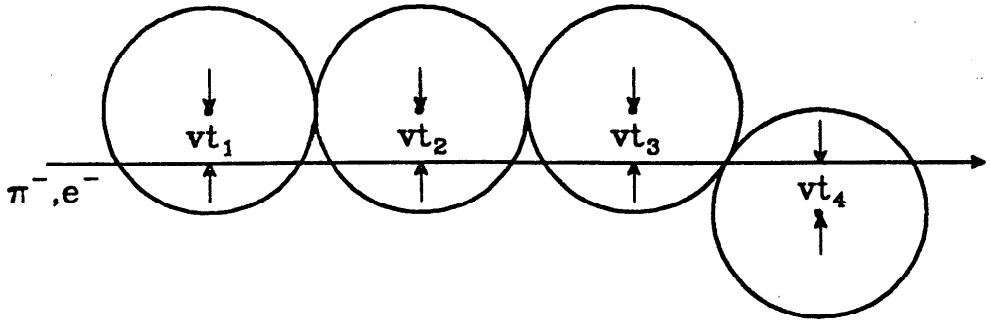

Spatial Resolution: $\Delta = t_2 - \frac{1}{2}(t_1 + t_3)$

$\sigma_w = \sqrt{\frac{2}{3}} v \sigma_\Delta$

Drift Velocity: $v = 50\ \mu m/ns$

Figure 3.2 Straw Arrangement in Test Beam. Electrons and pions were supplied by the SLAC Research Yard. v is the drift velocity, which was typically a constant $50\mu m/$ ns for the Argon-Hydrocarbon gases used. The spatial resolution, σ_W, was determined from the drift times in the first three straws. The fourth, staggered straw was useful for determining the time to distance relationship.

trum might be the cause of a deterioration of spatial resolution near the wire, as discussed in section 3.7.2. We note that the use of Xenon as a quencher, which absorbs hard UV,[59] in addition to CO_2, resulted in a more satisfactory gas gain, and did not cause a reduction in radiation lifetime.

3.3 Beam Test

We conducted a beam test[54] to determine the resolutions possible with a drift chamber made of straws. A variety of high voltages, discriminator thresholds, gases, and pressures were used. An unseparated beam of 8 GeV/c electrons and pions in the SLAC Research Yard was used. Four straws were arranged as shown in Figure 3.2. The simple geometry allowed a straightforward and systematic free determination of the spatial resolution. For example, Figure 3.3exhibits the simple scatter plot of drift time in the first straw versus that in the last, offset straw. The cases where the track passed above both sense wires, between the sense wires, and below both are clearly visible. The lack of degradation of

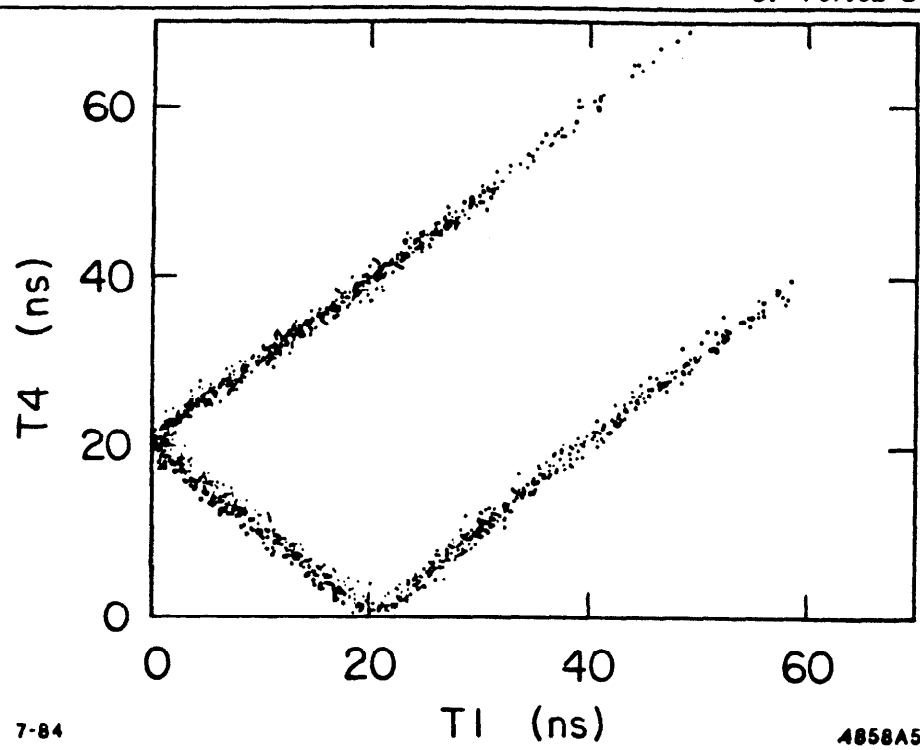

Figure 3.3 Drift Time Correlation in Offset Straws. The drift times are in straws 1 and 4 of Figure 3.2. The regimes of the track passing above both sense wires, between the sense wires, and below both are distinct. Note the lack of degradation in resolution for tracks passing very close to the sense wire.

spatial resolution for tracks passing near the wire is clarly visible. The spatial resolution as a function of drift distance is given in Figure 3.4, for a variety of discriminator thresholds. In the streamer mode at 4 kV, the spatial resolution was an average of 25 μm, *and did not degrade near the sense wire.* The data agree quite well with Monte-Carlo calculation. Figure 3.5 shows the spatial resolution measured for a variety of high voltages and gas pressures. Based on these test beam results, one sees that straws obtain spatial resolutions in the $25\mu m$ regime.

3.4 Design

3.4.1 *Radiation Shielding*

At the beginning of PEP operation, the MAC detector ran for a short time with a 3.15 cm radius beam pipe, and minimal shielding was employed. From this experience, we deduced that the primary radiation background came from off-energy electrons that were overfocussed by the 'low-beta' quadrupoles into

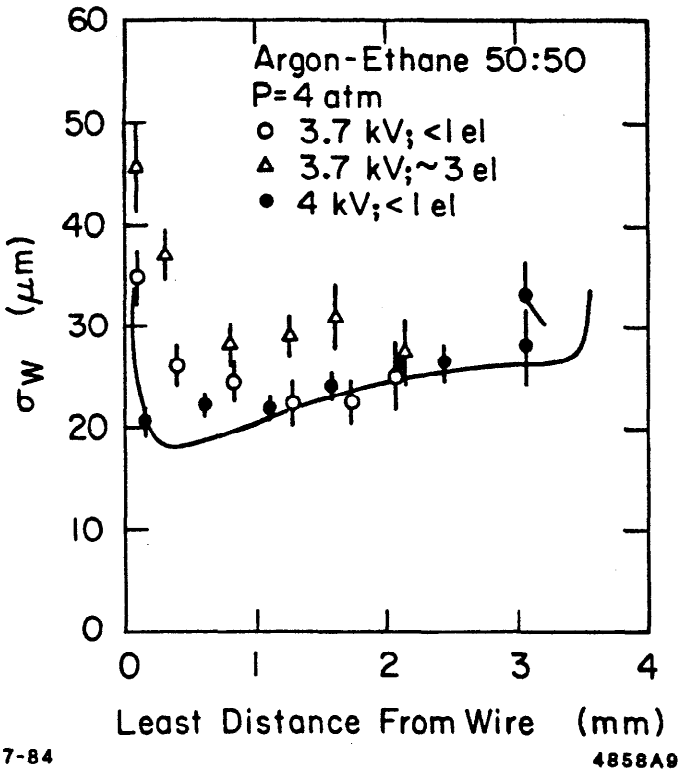

Figure 3.4 Spatial Resolution in Test Beam vs. Drift Distance for a Variety of Thresholds. Absolute calibration of the thresholds were performed with a source of single electrons produced via the photoelectric effect on the straw cathode. The streamer mode was fully efficient at 4 kV for single electrons. Our Monte-Carlo calculation is shown as well.

the beam pipe and tracking chamber. Another important background source was synchrotron radiation, both from the 'soft bend' dipole and the low-beta quad.

We designed a close-in collimator to suppress these backgrounds. The collimator was a tantalum annulus of 2.8 cm inner radius and 0.8 cm thickness, placed 60 cm from the interaction region. Shielding of heavimet, a sintered tungsten material, surrounded the collimator to absorb electromagnetic showers. The location and dimensions of the collimator were chosen to allow sufficient room for this shielding, and to shield the Vertex Chamber from direct particle and photons originating from the soft bend and low-beta quad magnets. Figure 3.6 shows the shielding and these trajectories. A $75\mu m$ titanium liner, placed inside the beam-pipe to attenuate the $\approx$ 10 keV fluorescence from tantalum by a factor of $\approx$ 30, completed the shielding.

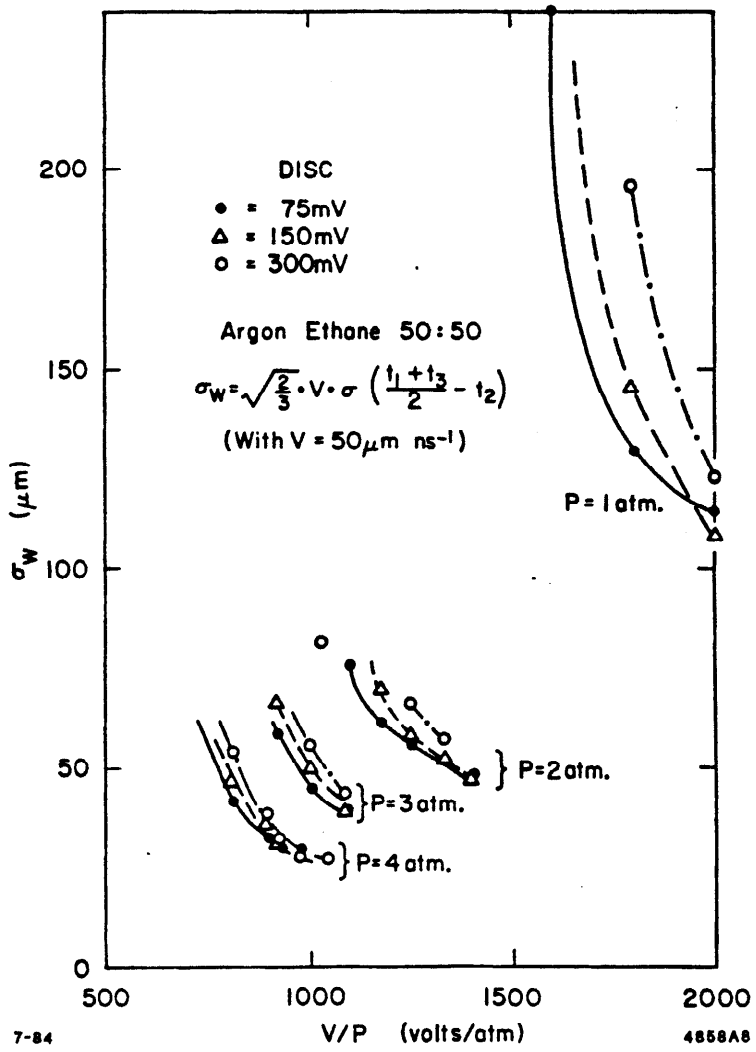

Figure 3.5 Spatial Resolution in Test Beam For a Variety of High Voltages, Pressures, and Discriminator Thresholds.

The heavimet occluded the low angle electron veto counters previously installed for the MAC search for $e^+e^- \rightarrow \gamma +$ *weakly interacting particles*.[60] To maintain this search, an annulus of BGO was placed between the heavimet and the interaction region. The dense BGO was read out with compact photodiodes,[61] a well matched combination for such a cramped situation. This was the first application of this technology in an operating colliding beam experiment.

3.4.2 *Beampipe and Pressure Vessel*

The beampipe was 0.11 cm thick beryllium, brazed to aluminum tubes at its

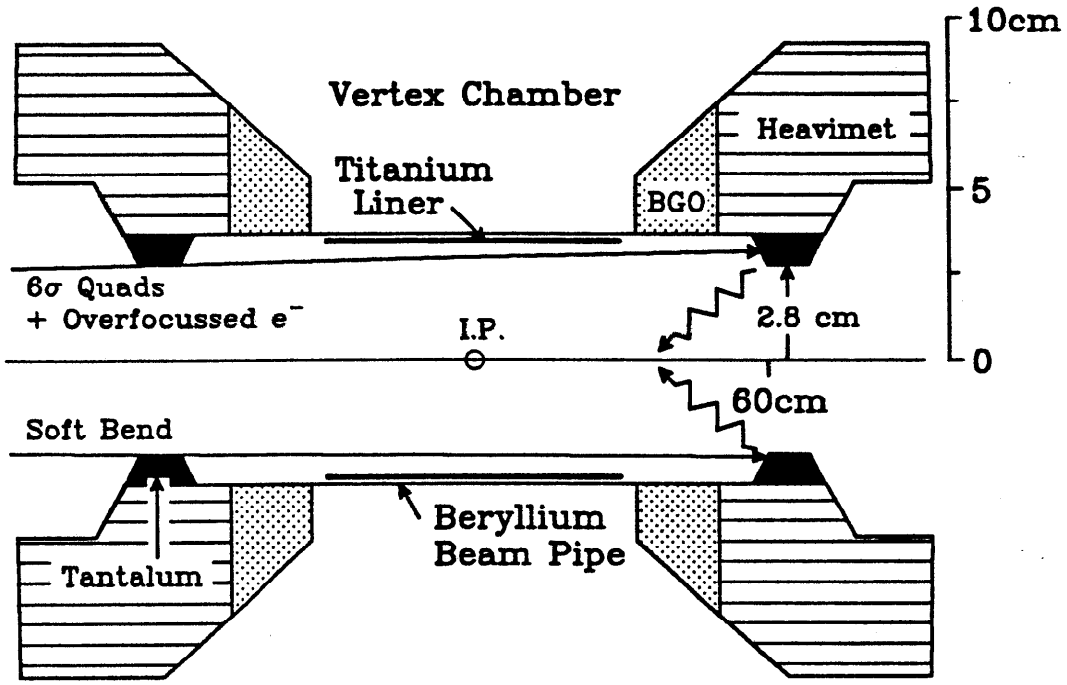

Figure 3.6 Shielding Configuration. The tantalum close-in collimators and surrounding heavimet shielding protected the Vertex Chamber from off-axis electrons, and off-energy electrons overfocussed by the nearby low-beta quadrupoles. The collimators also shadowed the Vertex Chamber from direct synchrotron radiation from the soft bend and low-beta quad. The titanium liner absorbed the $\approx$ 10 keV fluorescence from the tantalum. The remaining background was $\approx$ 25 keV synchrotron light from the low-beta quad, which scattered off the tantalum.

ends. The aluminum tubes were in turn welded to the pressure vessel endplates, which were an explosion welded bimetal of aluminum and stainless steel. The remainder of the pipe was stainless steel. The outer wall of the pressure vessel was a 2.54 mm aluminum tube, also welded to the aluminum side of the bimetal endplates. The outer wall carried the mechanical load of the beampipe and shielding. I-beams placed vertically above and below the beampipe carried the load on either side of the vessel.

The pressure vessel was distinct from the Vertex Chamber. The coaxial signal cables from the chamber were potted in epoxy plugs that were captured in the endplates and sealed with O-rings.

3.4.3 *Chamber*

The straws were strung on a spool that consisted of a 0.076 cm thick, ex-

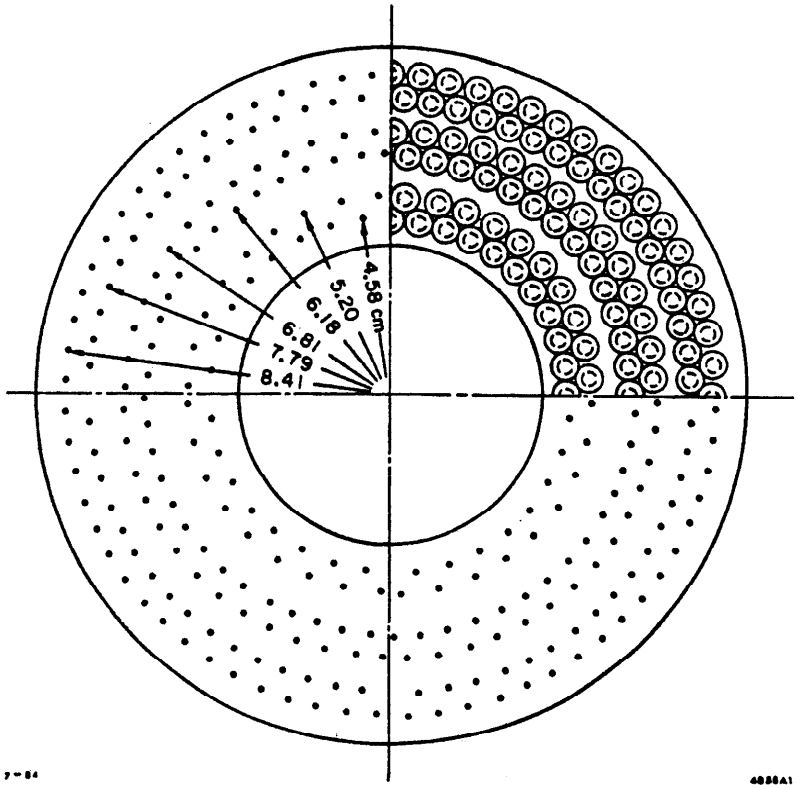

Figure 3.7 Spool Endplate Layout, Showing Placement of Straws in Radius and Azimuth.

truded beryllium tube, to which 1.6 cm thick aluminum endplates were glued. Holes were precision reamed in these endplates to accept the endplugs of the straws. The endplate layout is shown in Figure 3.7. There are six radial straw layers, arranged in three pairs. The inner layer of each pair is close packed in azimuth. The outer layer contains the same number of straws as the inner, but is staggered one half cell in azimuth. The stagger resolves the left-right ambiguity in the straws.

The straws themselves had an inner diameter of 6.9 mm. The wall consisted of a double wrap of 50μm mylar, each layer coated on one side with 0.8Ω/square. surface resistivity aluminum. The conductive layers faced inward and outward. The pitch angle of the spiral wraps was 28°.

The end-fitting design is shown in Figure 3.8. An aluminum collar was glued with conductive epoxy to the straw inner face, trapping a Delrin (acetal) plastic plug. The plug performed several functions. First, it insulated the high voltage

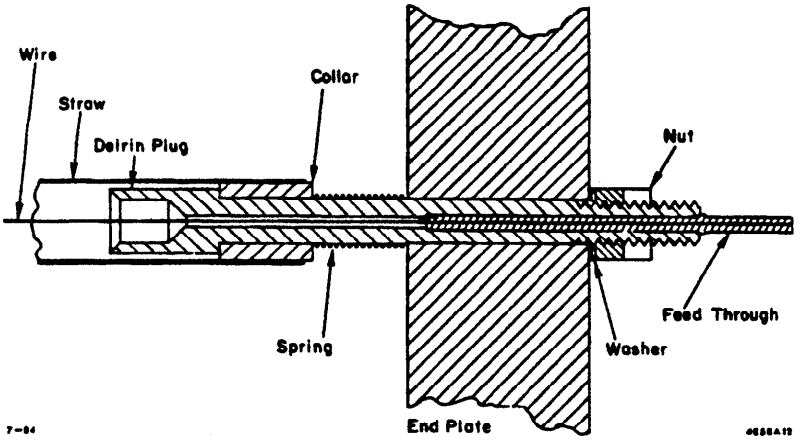

Figure 3.8 End-fitting Design for Straws. See text for more details. The collar contacted the endplate on one end of the straw; on the other, the spring made electrical contact.

on the sense wire from the ground of the endplate and straws. For this reason, virgin Delrin (Delrin that was not reformed from old pieces, was used) to avoid cracks and crevices that lead to high voltage breakdown. Considerable trial and error lead to the shape of the plug inside the straw, in order to avoid edge breakdown at extremely high voltages. Second, the plug provided a means to apply tension once the straw was mounted between the endplates. The threaded tip of the plug allowed a nut to apply tension when tightened. Third, the plug provided a seat for the feedthrough that held and positioned the sense wire. Last, the plug provided a conduit for gas flow through the straw, via two channels cut lengthwise on its outer radius. The $30\mu m$ gold-tungsten sense wire was threaded through the $100\mu m$ hole of a the feed through, a tempered stainless steel tube, which was crimped to capture the wire.

3.4.4 *Signal Processing*

Figure 3.9 shows the electronic layout of the Vertex Chamber and associated electronics. The sense wires were operated at positive high voltage, and one end was terminated through a standoff capacitor and a resistor. The other end was connected to 19 meters of RG179B, a 75Ω, teflon insulated, miniature coaxial cable. This coaxial cable provided high voltage, and carried signals to preamps that were located away from the detector.

We used the LABEN 5242 preamplifier, a hybrid optimized for fast rise time

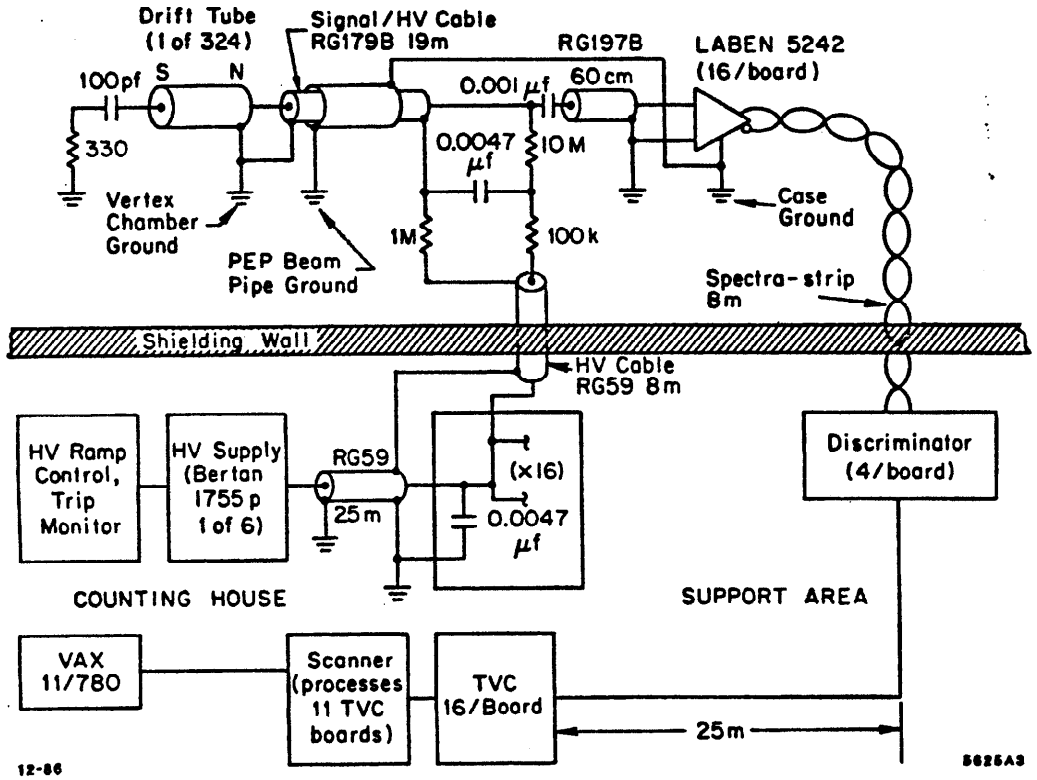

Figure 3.9 Electronic Layout of the Vertex Chamber. Straws are terminated in approximately their characteristic impedance at one end; signals go from the straw's other end, through 19 meters of coaxial cables to the preamplifiers, then to the discriminators and finally the TVC (time to voltage) drift time measuring system.

and low noise. This preamp can achieve a white noise of 0.6 fC when used with a low capacitance source. As discussed in section 3.6.1, the low impedance source provided by the long cables resulted in an increase of approximately a factor of three in white noise. It may be that an input transistor can be obtained, and transistor biasing can be developed, that would result in less white noise for the low impedance source. However, the long cables also made the system susceptible to electromagnetic interference, as also discussed in section 3.6.1. Good grounding practice can eliminate this interference completely; in practice we only suppressed it to approximately the same level of the white noise.

Our discriminator circuit utilized the Plessey SP9687 dual comparator. Each discriminator channel used two comparators, one set to a low threshold, and one high, as shown in Figure 3.10. The discriminator output was fed to our time-

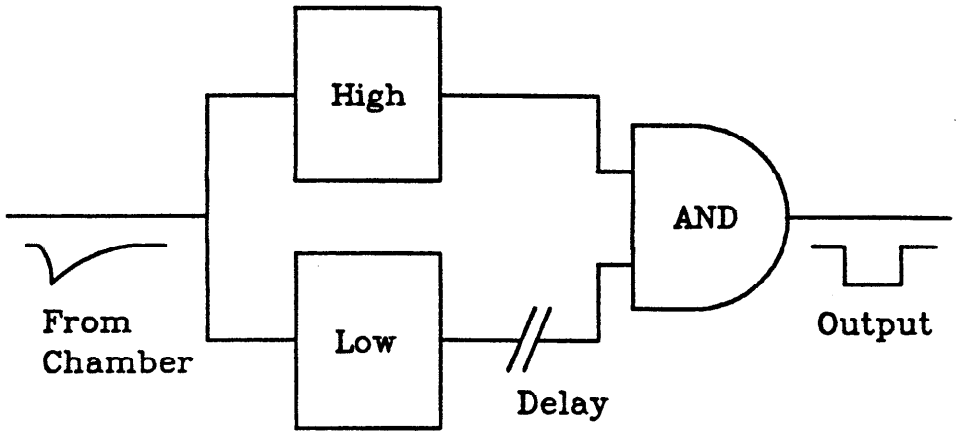

Figure 3.10 Principle of Discriminator Circuit. The low level output was delayed, so typically they reached the AND gate after the high level. Hence, the low level comparator controlled the timing of the output, but small pulses that did not fire the high level comparator were suppressed.

to-voltage converters, or TVC's. These circuits demonstrated $< 300ps$ timing resolution in bench tests.

3.4.5 *Gas System*

The gas system was designed to maintain constant density in the chamber while allowing gas flow. Figure 3.11 shows the gas circuit of the final design. The gas pressure was maintained by mechanical regulators. These proved quite reliable, but were sensitive to ambient thermal variations, necessitating thermal isolation. Flow was maintained by a vacuum pump on the output of the system, which eliminated flow variations due to atmospheric pressure fluctuation. The temperature of the chamber was maintained nearly constant by the cooling system of our solenoid; no effect of heating from the beam was observed.

This system maintained the gas density constant with an rms density variation of 0.8% over one week. The rms variation of the time to distance relationship contributed by this was a maximum of only $14\mu m$, at the straw wall. An electrical control system would seize control of the pressure if the density wandered outside $\pm 0.75\%$; this only occurred once in the operation of the chamber. Adjustment of the mechanical regulators for long term drift was made several times per week.

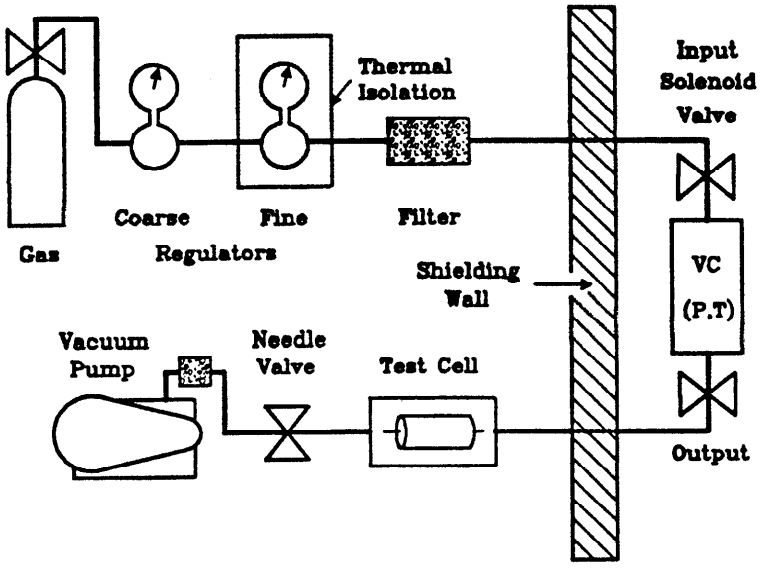

Figure 3.11 Gas System Circuit. Pressurised gas from cylinders flowed through Poly-Flo tubing to the Vertex Chamber, then back through a test chamber and a vacuum pump, which vented to the atmosphere. Absolute pressure was maintained by a pair of mechanical regulators on the cylinder output, and a needle valve on the output controlled the flow rate. Pressure and temperature were monitored in the Vertex Chamber (VC); if the density in the chamber drifted outside limits an electrical circuit could regulate the density via the solenoid valves.

3.5 Practical Matters

3.5.1 *Schedule*

The preliminary studies for the MAC Vertex Chamber were begun in November 1983, and the goal was set to take data useful for physics results when PEP resumed operations in the Fall of 1984. An intensive period of prototyping and of study of beam related backgrounds led to a complete set of detailed engineering drawings for the chamber by mid-March 1984. By necessity some items, such as the extruded beryllium central column of the chamber spool and the stainless steel feed throughs shown in Figure 3.8, had been decided upon and ordered much earlier. The remainder of March 1984 and most of April 1984 were devoted to the beam test. All items for construction of the chamber were on hand by early May, 1984, and after some development of procedures for stringing the chamber, stringing began near the end of May, and was complete within four weeks. Two weeks were then spent cabling the chamber. The chamber was

taken to the PEP Vacuum Group for mounting on the beam pipe assembly in early July. This was completed by August. The combined assembly was then removed to the MAC interaction hall, tested, and mounted on the PEP beam line on August 20, 1984. Assembly of the chamber electronics ensued, and data was taken from the chamber when PEP was filled on November 4, 1984. Some refinement of the gas and high voltage systems occurred during the remainder of 1984, and by 1985 the chamber was fully integrated into the MAC online system.

The integration of the VC into the MAC offline system was accomplished during the first half of 1985. By July, 1985, this task was substantially complete, and physics analysis began.

3.5.2 *Construction Details*

The spool upon which the straws and wires were strung, consisting of two aluminum endplates, shown in Figure 3.7, and the central beryllium column, was glued together with epoxy. The spool assembly was performed on a precision granite table. Measurements after gluing showed that twist between the endplates was less than $12\mu m$, although the endplates were not parallel by $\approx 0.02°$. Before stringing, six weak Fe^{55} sources were placed on the beryllium column. These sources were useful for checkout of the chamber, and provided maximum counting rates of ≈ 100 Hz in the inner layer.

Straws were selected for lack of defects and checked for electrical continuity along both inner and outer faces. Approximately half the straws had obvious defects, such as dents or ragged mylar edges. A small number had scratches across their aluminization that broke electrical continuity. Acceptable straws were then cut to 432 mm length with very sharp scissors, and the aluminum collars (see Figure 3.8) were glued inside each straw end with Eccobond 25, a very smooth and creamy conductive epoxy. The straws were heated in an oven for several hours at $\approx 48°$ C to cure the epoxy. Distortion of the straws by this heating, and subsequent cooling, was avoided by keeping the straws in grooved trays. Nevertheless, a very few straws warped, and all were rolled down an incline to test for straightness.

The Delrin plugs were trapped in the straw by the collars. To mount the straw in the VC spool, the plugs were pushed into the collars so that only

≈ 0.05 cm was exposed. The straws were ≈ 0.2 cm shorter than the distance between the spool endplates, so the straw could be positioned with Delrin plugs directly in front of the holes in the endplates. A narrow set of tweezers was used to pull the threaded tip of the each Delrin plug through its endplate hole. Nuts were attached to the tips and tightened. One end of the straw contacted the endplate. The ≈ 0.2 cm gap on the other end of the straw was bridged by a spring that made electrical contact, as portrayed in Figure 3.8. A wave washer was used on this end of the straw to provide some measure of the tension applied to the straw, typically ≈ 500 g.

A piece of welding stock, with a small hook filed in one end, was used to draw the wire through the straw. The stock was threaded one way through the straw, the wire attached to the hook, and the wire drawn back through the straw. A taper in the Delrin plug facilitated the threading of the rod. A stainless feed through was then slipped over one end of the wire, and crimped with a tool that ran on compressed air. A second feed through was then slipped over the other wire end, and a 100 g weight hung on that end, and the second feed through was crimped. Approximately 30 straws and wires per day were strung in this manner, although the time involved in checking the wires and straws limited output to 15 per day.

After a group of straws and wires were installed, the tension of each wire was checked. A magnet was placed near the wire, and an oscillating current was driven through the wire. The frequency of oscillation was varied, and resonance was searched for via the induced voltage caused by motion of the wire in the field. Typically, the resonant frequency was 290 Hz, with a width of 0.5 Hz, implying a tension of 120 g. Wires were restrung if they were outside the range $275 - 305$ Hz. We found that our initial crimping technique allowed a slippage of 5 g per week, which we viewed as unacceptable. We arrested the slippage by recrimping each wire after reducing the distance between the jaws of the crimping tool, and achieved a slippage of < 0.1 g per week.

After checking the tension, we placed the chamber inside a pressure vessel containing 4 atm of 50%-Argon 50%-Ethane, and examined the output of each channel with 4.7 kV applied to the sense wire. This voltage is well into the limited streamer regime for a single electron signal. Initially, $\approx 25\%$ of the channels drew substantial current at this high voltage, and were replaced. This effect was

traced to small Delrin flakes present on the sense wire, and was substantially eliminated by careful cleaning of the Delrin plugs.

Attaching cables and termination resistors and capacitors to the chamber proved to be a painstaking task. Half of the signal cables were attached on each end of the chamber. The center conductor of each signal cable was soldered to a small cap, which contained a transverse spring. The cap was then slid over the exposed end of the feed through. Layers of teflon tubing were used to insulate the cap; finally a piece of heat shrink tubing that contained a conductive inner layer was shrunk over the straw tension nut and the shield of the signal cable, making the ground connection. In this manner, the signal was always coaxial. The epoxy plugs in which the cables were potted were held in a jig which provided stress relief.

The Vertex Chamber was then mounted on the beam pipe assembly. The beam pipe assembly consisted of two sections which were mirror images; these two sections were linked by the central beryllium pipe. The two sections were made of stainless steel, and contained the tantalum masks shown in Figure 3.6; the central beryllium pipe had aluminum tubes brazed on at either end. Each section was joined to the beryllium pipe through the endplate of the Vertex Chamber pressure vessel, that is the explosion welded composite of steel and aluminum. One section and one end of the beryllium pipe were both welded to an endplate; then the pipe was inserted through the central column of the Vertex Chamber. Then, the free end of the beryllium was welded to the other pressure vessel endplate, *with the Vertex Chamber present.* Special care was taken not to heat the VC. Finally, the second stainless beam pipe section was also welded to the endplate, and the outer cylindrical vessel wall was slid over the entire assembly and welded. Care was taken to keep the Vertex Chamber electrically insulated from beam pipe with a kapton insulator on the beam pipe, and a mylar insulator on the outer wall. Table 3.1 contains a list of the matter in the Vertex Chamber. The final assembly was rugged and easy to move onto the beam line.

Inner Radius	Thickness			
cm	cm	X_0, %	Material	Name
3.564	0.0075	0.21	Titanium	X-ray Absorber
3.571	0.1118	0.32	Beryllium	Beam Pipe
3.683	0.0050	0.02	Kapton	Electrical Insulator
3.843	0.0762	0.22	Beryllium	VC Spool Column
4.582-8.405	-	0.76	Mylar, Tungsten,Straws,Wires,Gas Argon, CO_2, CH_4	
9.024	0.0064	0.02	Mylar	Electrical Insulator
9.035	0.254	2.85	Aluminum	Pressure Vessel Wall

Table 3.1 Matter in the Vertex Chamber Assembly.

3.6 Vertex Chamber

3.6.1 *Vertex Chamber Performance*

Electronics

Refer to Figure 3.9 for the electronic layout of the Vertex Chamber and associated electronics. The electrical ground of the Vertex Chamber was insulated from the ground formed by the PEP beam pipe, to suppress pickup from the image currents of the beam itself. No pickup from this source was observed at the level of white noise from the preamplifiers. However, the long signal cables between the chamber and the preamplifiers proved susceptible to electromagnetic interference in the 1-100 MHz regime. Their susceptibility was reduced substantially by isolating both their center conductor and shield with 1-10 MΩ resistors from the high voltage supply cables. The dominant source of interference was the system for measuring drift times in the Vertex Chamber (VC), the time to voltage converters (TVCs). Moving these from 10 meters to 30 meters from the preamplifiers reduced the total pickup to approximately the level of the white noise of the preamps. The long cables limited the 10-90% rise time at their output to 4 ns, and attenuated signals from the chamber by 15%. The output

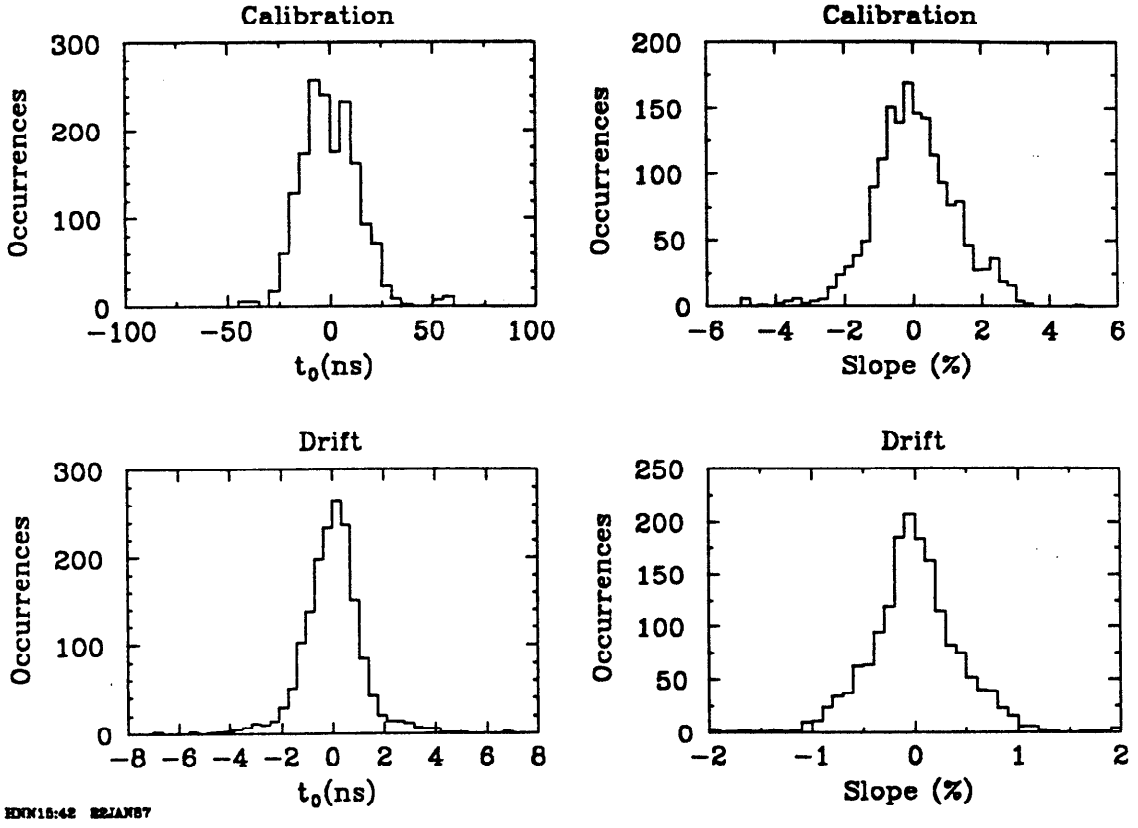

Figure 3.12 Fitted constants in the TVC system. The top plots are distributions of the timing pedestals and slopes. The bottom plots give the variability of these constants over the 8 recalibrations done during the 17 months of data taking.

slew rate of the preamps was 90 mV/ns, yielding a 10-90% rise time of 8.0 ns for pulses from Fe^{55} sources in the chamber. The white noise of the preamps was 2.0 fC at their input with cables attached, 0.6 fC without. The low level of our discriminators was set at 6 fC input to the preamps, which corresponded to 30 mV at their output. Slewing and noise contributed less than 0.15 ns to our timing resolution. TVC channels were calibrated with a CAMAC controlled delay generator. The delayed calibration pulse was injected at the preamplifier input, into half the channels at a time. For each channel, the delay was fit as a quadratic function of the voltage output from the TVC. The non-linearity contributed only 0.5% to the calibration. This calibration was performed 8 times over the 17 months of data taking.

The channel by channel pedestals had a standard deviation of 15 ns; this was governed by the variability of a CMOS switch in the TVC circuit. Over the

data taking period these pedestals were stable to 1.3 ns. The slope term in the quadratic fit was far more reproducible from channel to channel, varying only 1.3%; this was governed by one resistor and one charging capacitor. The drift was only 0.5% in these slopes. Figure 3.12 shows the actual distributions of the offsets and slopes.

The calibration reproduced input delays to better than 0.5 ns. During data taking, four spare channels were fed fixed delays; these indicated that the system achieved a timing resolution over a typical two hour data taking run of 250 ps.

The combined effect of 1)slewing in the signal cables; 2)noise in the preamplifiers; and 3)resolution of the TVC system produces a timing resolution of < 300 ps. The maximum drift velocity in the Vertex Chamber itself was $100\mu m/ns$. Therefore the degradation in spatial resolution from purely electronic sources was $< 30\mu m$.

Operating Point

The high voltage and threshold at which the chamber was operated was a compromise between spatial resolution and radiation damage considerations. As discussed in earlier, for the short drift distances in our cells, triggering on the first arriving electron was desirable. The observed charge for various high voltages appears in Figure 3.13. At 3900 V, our threshold of 6 fC was very near the most probable signal for a single electron. Synchrotron X-rays were the dominant source of current drawn in the chamber. Approximately two random hits per beam crossing occurred in the chamber, causing a current of 3-5 nA/cm to be drawn in the innermost layer, for a high voltage of 3900 V. Higher voltages put the chamber in danger of accumulating more than 0.2 C/cm charge in the innermost layer, so we operated at 3900 V. In retrospect, we were slightly conservative; the innermost layer accumulated only 0.03 C/cm over the entire data taking period.

The two random hits per beam crossing in no way interfered with our track finding procedure. Electronic cross talk did not limit our ability to maintain a low threshold: studies with Bhabha events indicated that electronic cross talk produced $< 0.1\%$ of the hits in five of the six layers. However, knock-on electrons did produce hits in the cells immediately neighboring a cell penetrated by a track 1-2% of the time.

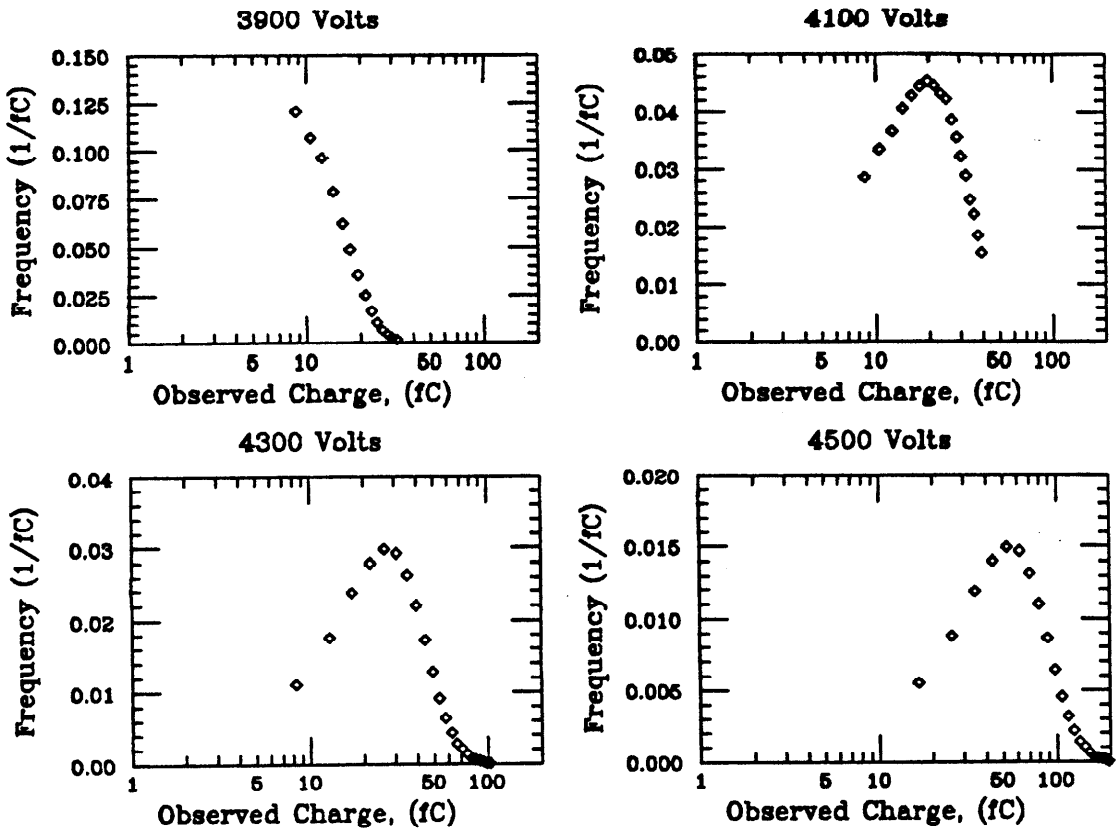

Figure 3.13 Single Electron Gain. The four plots are for different high voltages applied to the sense wire. These data were obtained with a test straw identical to those used in the Vertex Chamber. An incandescent light produced single electrons via the photoelectric effect on the straw cathode. Not shown are the very large charges due to self quenching streamer formation which were approximately 500 fC. Few single electrons initiated streamers at 3900 Volts, but most did at 4500 Volts. The spectra are not shown below 8 fC where amplifier noise begins to dominate. The gas mixture was 49.5% Argon, 49.5%CO_2, 1.0%CH_4, at an absolute pressure of 4 atm.

3.7 Off–line calibrations

We performed off–line calibrations of wire positions, drift timing constants, the time to distance relationship, and drifts in these quantities. Bhabha scattering events proved very useful for this purpose due to their simple topology. The use of Bhabha scattering events is by no means mandatory. Any sample of tracks free of bias from pattern recognition could have been utilized. Bias can occur, for example, in dense regions of multihadron events, when two tracks pass through the same cell but only one is recorded.

Our calibration techniques require existing programs to link hits into tracks

and to fit the track parameters. The programs used to do this are described in reference (62).

Global Alignment

For a description of our tracking parameterization, see the appendix. The VC measured only the three parameters that describe the track in the x-y plane. Of these three, only two were well measured, δ_{0vc} and ϕ_{0vc}. Our existing central drift (CD) chamber extended from 12 cm to 45 cm in radius, and had stereo layers, so it measured all five helix parameters. Systematic comparison of δ_{0vc} and ϕ_{0vc} with δ_{0cd} and ϕ_{0cd} as a function of ϕ_{0cd}, θ, and z_0 allowed determination of the five relevant parameters that describe the relative global orientation of the VC and the central drift chamber.

These five parameters were measured 13 times over the course of data taking. Figure 3.14 shows the stability of the three most important over these measurements. The horizontal and vertical translations were stable to 10 μm.

Time to Distance Calibration

The gas used in the Vertex Chamber, 49.5% Argon, 49.5%CO_2, 1%CH_4, has a drift velocity approximately proportional to the applied electric field. In a cylindrical geometry, this implies the drift distance r and the drift time t are related by $r \approx \sqrt{t}$. This simple relationship provided an initial guess for our time to distance function.

We improved the initial guess with the following procedure. Tracks in Bhabha scattering events with 4-6 hits in the VC and 7-10 out of 10 possible hits in the CD were chosen. A VC hit waseliminated, and the remaining VC and CD hits were used in a new track fit. This new fit was used to predict the drift distance, r_{pred}, in the eliminated VC cell. Errors in the initial time to distance relationship tend to cancel in r_{pred}. We give a scatter plot of r_{pred} as a function of the measured drift time, t_{meas} in Figure 3.15. The $r_{pred} \propto \sqrt{t_{meas}}$ character is evident. We fit data such as that in Figure 3.15 to obtain the improved time to distance relationship, $r(t)$, or its inverse, $t(r)$. Fitting r_{pred} as a function of t_{meas} or vice versa yield systematically different results for short drift distances, because no drift distances are defined as negative. Furthermore, the large slope of $\sqrt{t}$ near $t_{meas} = 0$ makes fitting r_{pred} as a function of t_{meas}

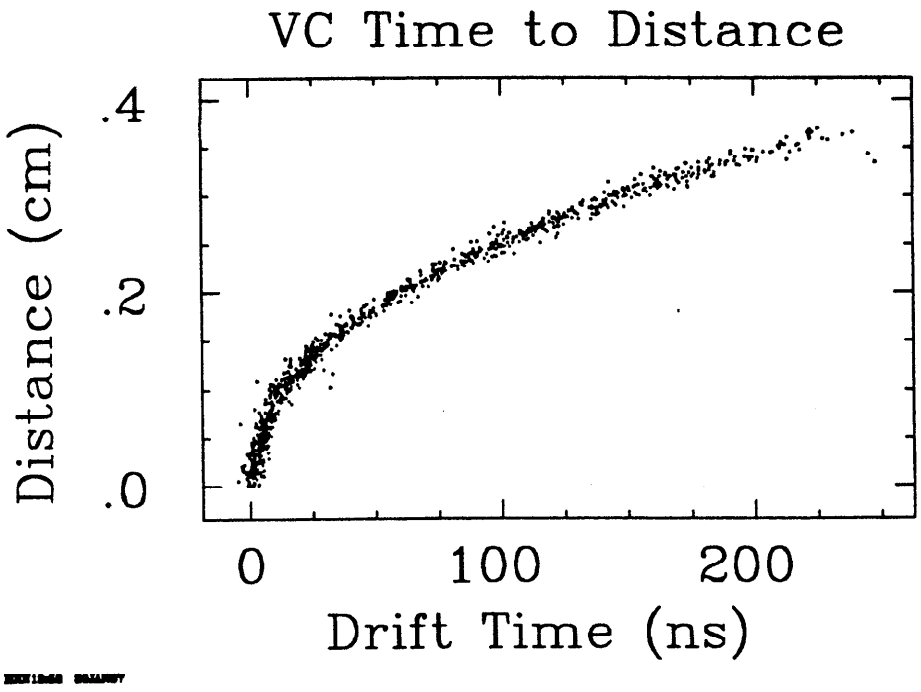

Figure 8.15 Time to Distance Relationship. The drift time is that measured in a cell of the VC, t_{meas}. The drift distance is obtained by dropping that cell from the track fit, then predicting the drift distance in the missing cell. In this manner the cell's 'pull' in the track fit is avoided. A fit is made to data like that above to obtain the functional time to distance relationship.

where t_{0rr} and s_{rr} are the run by run timing offset and slope. These are found using a procedure very similar to that used to extract the time to distance relationship. Typically t_{0rr} could be measured to an accuracy of .2 ns and s_{rr} to 2 %. t_{0rr} remained stable for weeks, then would suddenly shift, usually due to a power failure or changes in PEP timing. The slope term was very stable, reflecting the stability of the gas density.

Channel by Channel Calibration

The timing constants and physical positions of each cell were calibrated offline. The procedure was similar to that used to obtain the time to distance calibration. The residuals $\delta r = r_{pred} - r(t_{meas})$ and $\delta t = t(r_{pred}) - t_{meas}$ were fit for each cell with four constants:

1. An offset in time, t_0.
2. An offset in distance, in the azimuthal direction, d_0.
3. A slope in time, s.

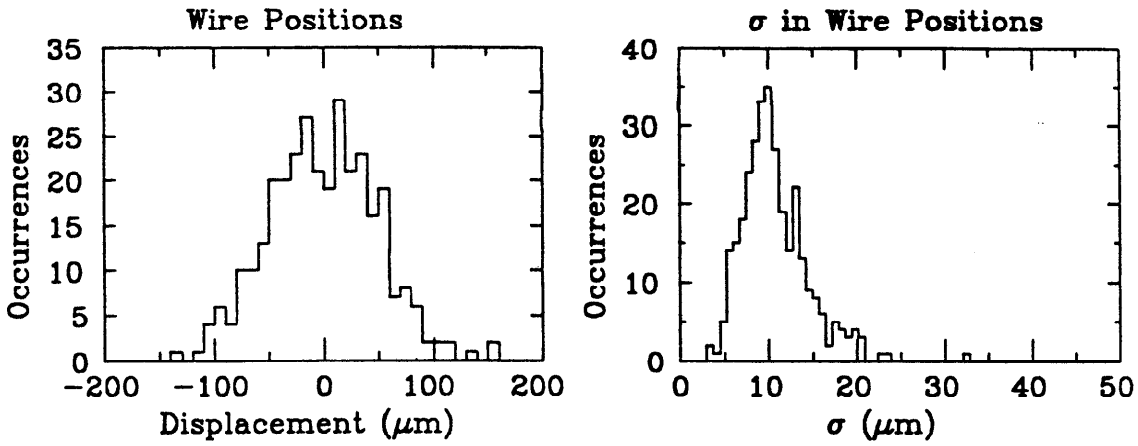

Figure 3.16 Sense Wire Positions. The histogram on the left gives the wire offsets in azimuth as obtained in the channel by channel calibration. The accuracy of wire placement was controlled by the size of the hole in the crimp pins that capture the sense wire, and the pins' tendency to bend slightly. This calibration was repeated 13 times; the histogram on the right is the standard deviation of each wire's offsets among the 13 calibrations. It indicates that the calibration procedure found the wire positions to $\approx 10\mu m$ accuracy.

4. A tilt in z, the axial direction.

d_0 and t_0 affect δr with opposite signs on opposite sides of the sense wire. In a typical calibration, 100 runs were used, corresponding to $6\,\mathrm{pb}^{-1}$ of integrated luminosity. This yielded approximately 150 residuals in each of the 324 cells. The largest correction was d_0, appearing in Figure 3.16. The calibration was performed 13 times. The standard deviations of d_0 for each cell over the 13 measurements also appear in Figure 3.16, indicating a reproducibility of 10 μm.

The channel by channel calibrations were made in a single pass through Bhabha scattering data. The improvement in spatial resolution due to the calibration was then immediately known via the multivariate analog of the relationship:

$$\sum_{i=1}^{N}(x_i-\overline{x})^2=\sum_{i=1}^{N}x_i^2-N\overline{x}^2$$

Use of orthogonal polynomials as fitting functions allowed straightforward isolation of the contribution of the various constants. Table 3.2 gives the importance of each of the constants.

3.7.1 *Pattern Recognition*

Algorithm

Track segments were obtained by independent pattern recognition programs in the CD and the VC. The CD algorithm was complex, due to the presence of stereo layers and non-negligible track curvature.[62] The VC algorithm was simpler, because tracks are approximately straight lines in the VC.

We regard the six layers of the VC as three double layers for the first step of pattern recognition. Because of the overlapping, regular geometry of the VC double layers, the drift distances r_1 and r_2 for hits produced by a radial track are related by:

$$r_1 + \frac{R_1}{R_2} r_2 \approx r_0 \qquad [3.1]$$

Here R_1 is the radius of layer 1 or the double layer, R_2 that of layer 2, and r_0 the straw radius. Pairs of hits in double layers were associated if they met [3.1] within 200 μm. Random associations were thereby suppressed, with little loss of real tracks. Most loss of real tracks occurred for very low momentum tracks or tracks from very long lived species, such as K^0s and Λs. The ambiguity concerning by which side of the sense wire the track passed is resolved by [3.1] in most cases.

Associated pairs in the three double layers were then linked based on their agreement in azimuth. A straight line fit was made to the resulting set of hits and drift distances. The straight lines found in the VC were then compared to and matched with tracks found in the CD. Unmatched CD tracks were extrapolated into the VC and a search made for VC hits. A weighted, least squares fit was performed to both the VC and CD hits and drift distances. VC hits were assigned weights based on the measured resolution as a function of drift distance (Figure 19). Multiple scattering was accounted for by allowing partially constrained kinks at the beam pipe, the boundary between the VC and CD, and at fixed locations within the chambers. A final search was made for hits along the track fit, and .1% of the VC and CD hits were dropped due to large residuals.

Considerable effort was expended on scanning graphical representations of events and interrogating the pattern recognition programs to tune their deci-

Events	VC Efficiency
Bhabhas	0.994 ± 0.001
Taus	0.982 ± 0.003
Multihadrons	0.939 ± 0.001

Table 3.3 Vertex Chamber Efficiency.

sions. After some optimization of cuts, results at least as good as those from scanning were achieved.

Efficiency

Since the CD and VC are in one sense redundant devices, it was possible to measure the efficiency of the VC by using a sample of tracks well measured in the CD. Sources of inefficiency include dead cells, overlap of particle trajectories, and inadequacy of the track finding algorithm for particles with low momentum or very large impact parameter.

We define well measured tracks in the CD by four requirements: 1)ten hits from the CD must be linked to the track, 2)$z_{0cd} \leq 5$ cm., 3)$\theta \leq 20°$, and 4)$\hat{\chi} \equiv \sqrt{2\chi^2} - \sqrt{2n_D - 1} \leq 4$. Table 3.3 gives the efficiency for well measured CD tracks to link to ≥ 3 VC hits. The Bhabha efficiency was determined from $2\,\mathrm{pb}^{-1}$ of integrated luminosity, tau lepton and multihadron efficiencies from $94\,\mathrm{pb}^{-1}$.

Track overlap was a source of inefficiency in the VC in multihadron events. If two tracks were separated by less than the diameter of a straw, 6.9 mm, they could leave only one hit in a layer of the VC. The staggering of VC layers usually prevented this phenomenon from happening in every layer. Double-hit electronics probably would not eliminate it, because the drift field for straws is radial. Figure 3.17 shows the efficiency for well measured CD tracks to link to ≥ 3 VC hits as a function of VC track separation. The VC track separation is the minimum distance in the azimuthal direction from the well measured track to the nearest CD track, within the VC boundary. The efficiency was near 50% for small separation, indicating one track of the overlapping pair was found in the VC. For large separations, the efficiency was better than 96%.

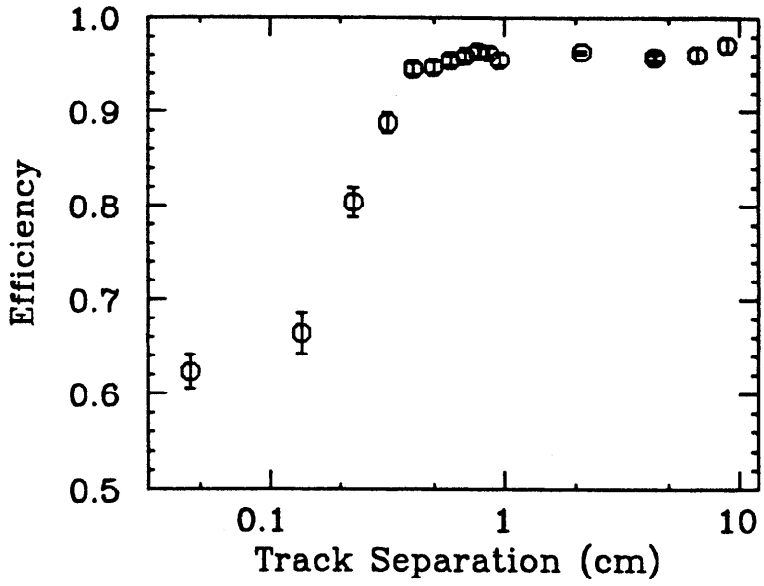

Figure 3.17 Effect of Track Overlap on VC Efficiency.

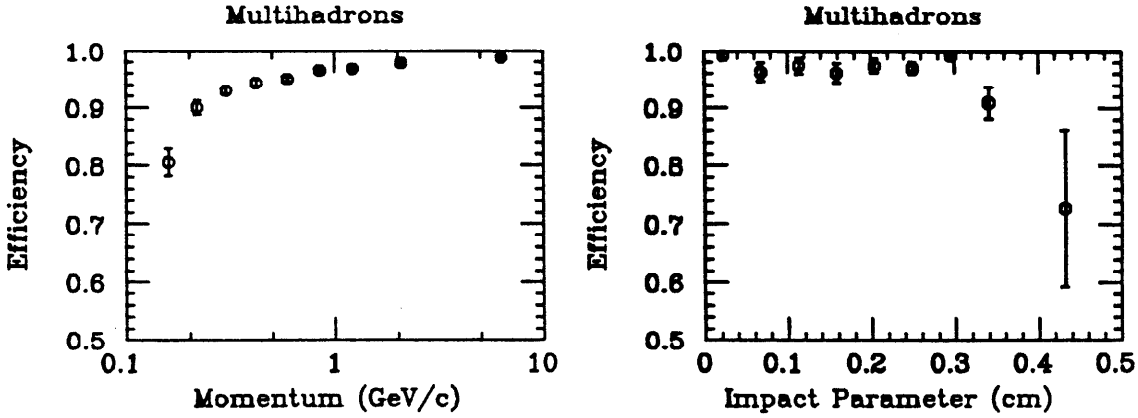

Figure 3.18 VC Efficiency for Various Momenta and Impact Parameters.

The VC track finding algorithm was most efficient for straight tracks coming from the beam centroid. The efficiency for CD tracks with VC track separation greater than one straw diameter is shown versus momentum in Figure 3.18. The efficiency was $\geq 90\%$ above 200 MeV/c. Tracks softer than 500 MeV/c had an error in impact parameter due to multiple scattering in the beam pipe equal to their error due to chamber resolution. Since the multiple scattering error scales as $1/p$, tracks with $p < 200$ MeV/c contribute little information to lifetime

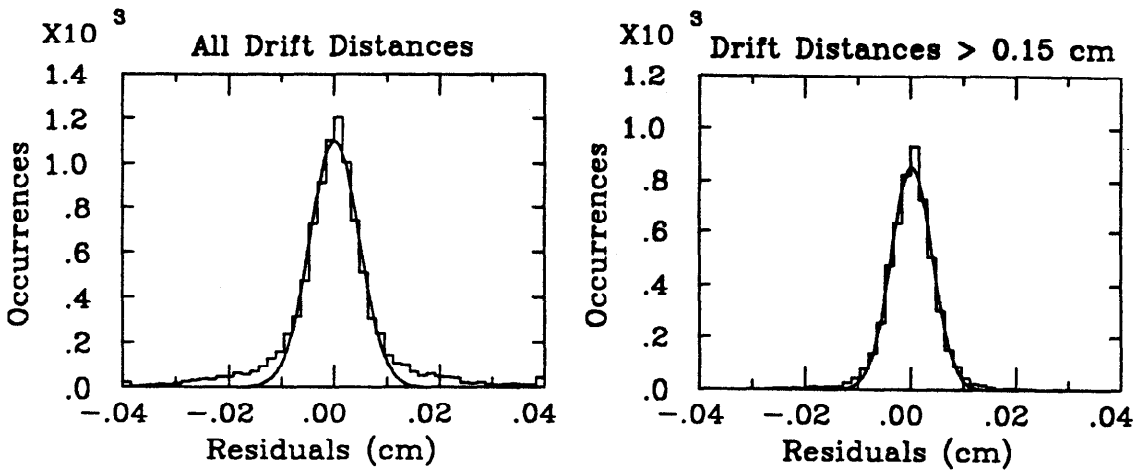

Figure 3.19 VC Residuals. The hit was *removed* from the track fit in these data. Residuals for all drift distances are on the left, where the fitted gaussian has $\sigma = 45\mu m$. On the right, only data from distances > 0.15 cm; the fitted gaussian has $\sigma = 38\mu m$. As discussed in the text, these data the true σ is actually smaller than these data indicate.

measurements. Figure 3.18 also exhibits the efficiency for the same tracks versus the impact parameter itself. Typical impact parameters of particles from B-meson decay are $300\mu m$, and the VC efficiency is flat and $\geq 96\%$ to some ten times this value, (3 mm). We conclude that linking efficiency effects lifetime measurements very little.

Well measured tracks in the VC can be used to measure the efficiency of the CD. Defining a well measured track as one with six hits in the VC, 0.932 ± 0.001 are matched with tracks having six or more hits in the CD, and 0.798 ± 0.001 are matched to tracks having seven hits or more.

3.7.2 *Observed Resolutions*

Spatial resolutions were measured using residuals from the track fit. If the VC hit used to measure the residual is left in the track fit, the resulting residual distribution is systematically narrower than the true residual distribution, due to the pull of the hit in the fit.[63] Conversely, if the hit is removed from the fit the distribution is wider than the true distribution, due to interpolation error in the track fit. The size of the bias is almost equal in these two cases, but opposite in sign. Figure 3.19 displays the residuals from Bhabha scattering events, where VC hits were removed from the fit. The non-gaussian tails arise

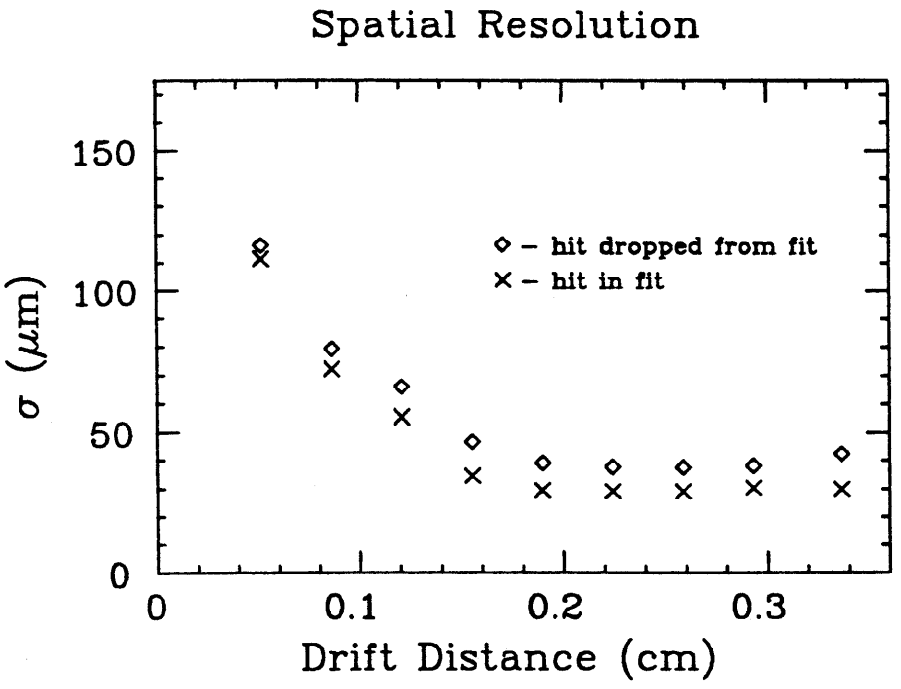

Figure 3.20 VC Spatial Resolution. The fitted σ of the residual distribution is shown as a function of drift distance. Both cases of hit left in the track fit and removed are shown. The true σ is approximately half way between these two extremes.

from the variation of resolution with drift distance. The resolution (σ) as a function of drift distance is shown in Figure 3.20. σ as a function of drift distance both for the hit left in the fit, and for the hit removed. For most drift distances, the resolution is 35 μm. Near the wire the resolution degrades, most probably due to the dispersion in pulse heights in our gas mixture, which is underquenched. Estimates of degradation due to spacing of ionization clusters, and due to timing resolution, indicate that these do not provide the degradation of resolution near the wire. The mean resolution is 45 μm.

The figure of merit for lifetime measurements is σ_v, the resolution in extrapolated distance of closest approach to the geometric center of the chamber. σ_v depends on the position resolutions of both the VC and the CD, the radii from the beam of their sense wires, and the amount of matter that causes multiple scattering in the beam pipe:

$$\sigma_v^2 \approx \frac{\overline{\sigma}^2}{N}(1. + f_1^2(\overline{\rho}) + f_2^2(\overline{\rho})) + \frac{\sigma_p^2}{p^2} \qquad [3.2]$$

The first term arises from the non-zero measurement resolution in the drift chambers, the second from multiple coulomb scattering. Here $f_1(x)$ and $f_2(x)$ represent the errors in extrapolation due to the slope and curvature in the fit, and are polynomials of order 1 and 2 respectively:

$$f_1(x) = x$$

$$f_2(x) = \frac{x^2 + \gamma_{1r}x + 1}{\gamma_{2r} + \gamma_{1r}^2 + 2}$$

$\overline{\rho}$, the dimensionless mean extrapolation distance, is $\overline{\rho} \equiv \overline{r}/\sigma_r$; given the radii $\{r_1, \ldots, r_N\}$ of the sensing layers, and their spatial resolutions $\{\sigma_1, \ldots, \sigma_N\}$,

$$\overline{r} \equiv \frac{\overline{\sigma}^2}{N}\sum_{i=1}^{N}\frac{r_i}{\sigma_i^2} \quad , \quad \frac{1}{\overline{\sigma}^2} \equiv \frac{1}{N}\sum_{i=1}^{N}\frac{1}{\sigma_i^2} \quad , \quad \sigma_r^2 \equiv \frac{\overline{\sigma}^2}{N}\sum_{i=1}^{N}\frac{1}{\sigma_i^2}(r_i - \overline{r})^2 \quad ,$$

and γ_{1r} and γ_{2r} are the coefficients of skew and curtosis defined in analogy with σ_r. For the combination of CD and VC, $\overline{r} = 8.6\,\text{cm}, \sigma_r = 7.4\,\text{cm}, \gamma_{1r} = 3.5, \text{and} \gamma_{2r} = 15$. $f_1^2(\overline{\rho}) = 1.4$, while $f_2^2(\overline{\rho}) = 12$, indicating that uncertainty in the curvature in the fit dominates the extrapolation error. This uncertainty arises primarily from the small maximum radius, 45 cm, of the MAC CD; the vertex resolution decreases as the *square* of this radius. The first term in [3.2] predicts a vertex resolution of $72\mu m$ for $45\mu m$ resolution in the VC. In the second term, σ_p depends on the angle of the track with respect to the beam axis, but was typically $65\mu m$- GeV/c.

The resolution in impact parameter was measured with Bhabha scattering events. Ideally, the opposing electron tracks would have equal and opposite impact parameters. Figure 3.21 shows the sum of the measured impact parameters. The distribution is very gaussian, with fitted σ of 124μm. This indicates a resolution $\sigma_v = 124/\sqrt{2} = 87\mu m$ in impact parameter. Constraint of the momentum leads to $\sigma_v = 52\mu m$.

The effective spatial resolution in the VC degraded to $\approx 70\mu m$ in multihadron events. The primary source of this degradation was the misassociation of hits with tracks in the dense environment of a multihadron event. Hits in adjacent cells due to knock-on electrons probably caused some confusion as well.

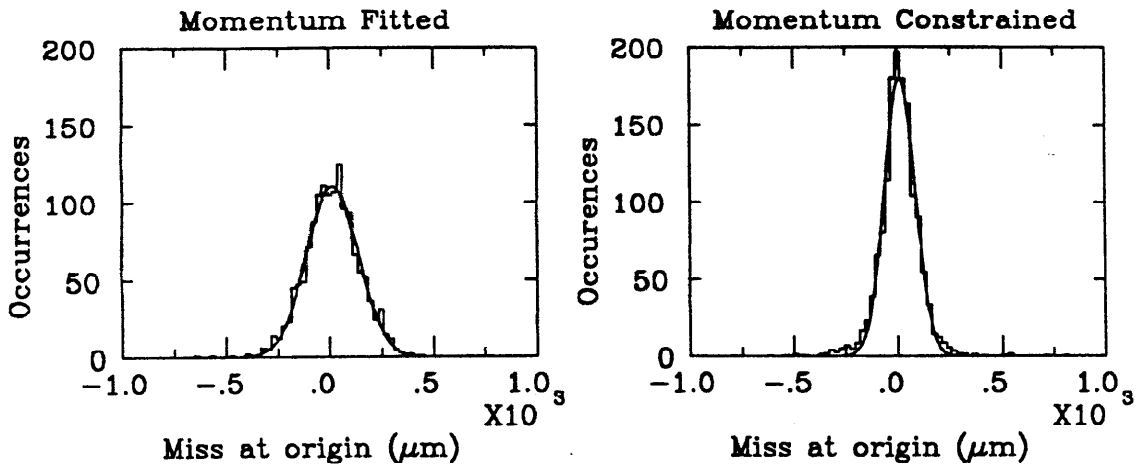

Figure 3.21 'Miss' distance in Bhabha Scattering Events. These data show the sum of the δ_0s for the two tracks in Bhabha events. On the left, the momenta were allowed to vary in the track fit. The distribution is very gaussian, with $\sigma = 124\mu m$. On the right, the track momenta were constrained to equal beam energy, and the distribution narrowed to $\sigma = 74\mu m$. This indicates the importance of the term arising from track *curvature* in [3.2].

The resolution in extrapolated distance of closest approach, or impact parameter, in multihadron events is given in Figure 3.22. Tracks with: 1) 3 or more hits in the VC; 2)7 or more hits in the CD; and 3) momenta > 500 MeV/c were used. The first plot makes use of the beam centroid, as determined from Bhabha scattering events on a run-by-run basis. The resolution in this case is dominated by the size of the beam itself, which we measured to have $\sigma_x = 350\mu m$ and $\sigma_y = 70\mu m$. For the second plot, an improved estimate of the e^+e^- annihilation location, the 'average vertex,' was made on an event by event basis. These data indicate a vertex resolution of $210\mu m$, of which $110\mu m$ was due to multiple coulomb scattering.

Figure 3.23 exhibits the tracks and VC hits in a typical multihadron event. This event is in no way unusual in complexity or lack of noise.

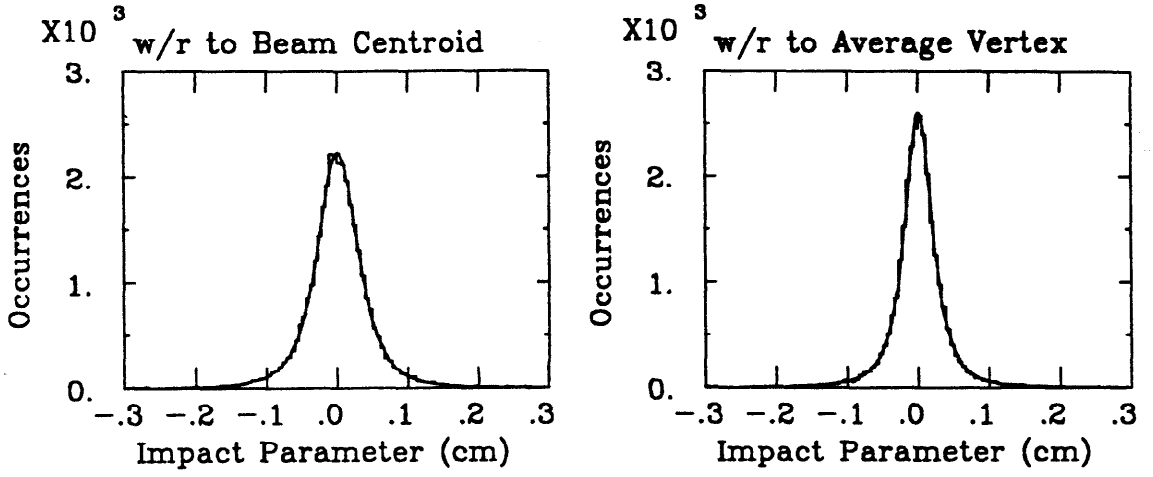

Figure 3.22 Vertex Resolution in Multihadron Events. These data show the distance of closest approach of tracks with respect to two estimates of the e^+e^- annihilation point. In the plot on the left, the estimate is the beam centroid, as determined in Bhabha scattering events. The fit is to a Student's t distribution, with $\sigma = 306\mu m$ and asymptotic power 1.9 describing the tails. In the plot on the right, the 'average vertex' was used; the fit yields $\sigma = 210\mu m$ and power 1.5.

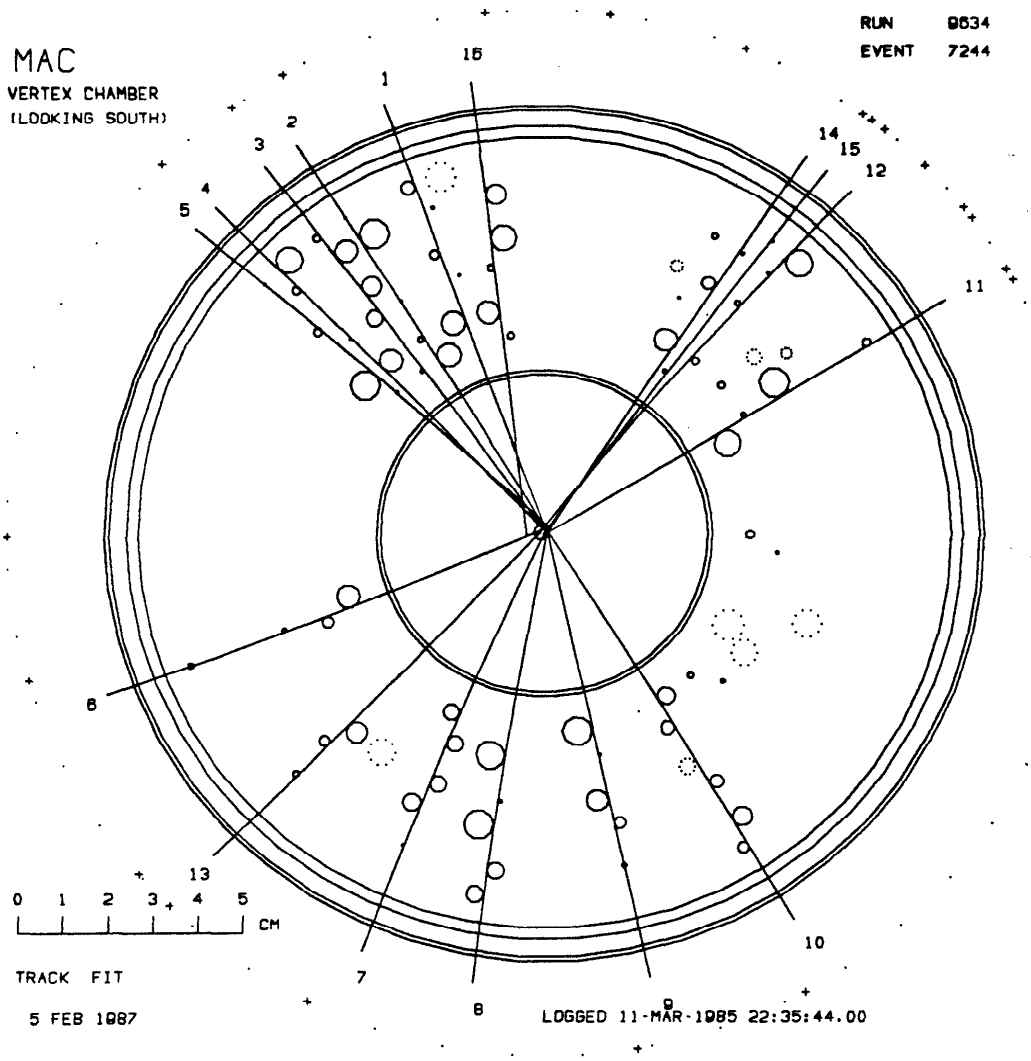

Figure 3.23 A Typical Multihadron Event in the VC. Each small circle is the contour of constant drift distance found from the drift time measured in that cell. Solid circles indicate the hit was linked to a track; dotted indicate it was not. Tracks should be tangent to the small circles. The innermost small circles represent the beam pipe, the outermost the outer chamber wall and inner wall of the CD.

Chapter 4

Event Selection

In this chapter, we discuss the selection and some attributes of the sample of events that are enriched in $e^+e^- \to b\bar{b}$. As discussed in the introduction, $b\bar{b}$ production constitutes only 9% of the $\approx$ 500pb of inclusive multihadron production at PEP We demand a muon or electron with high momentum transverse to the event thrust axis to obtain an enriched sample of 60% $e^+e^- \to b\bar{b}$ purity and yield $\approx$ 1.5pb. We have rejected other methods of enrichment because they depend on untested b-quark hadronization calculations[64] Use of the total inclusive multihadron sample, with no enrichment, leads to such a small sensitivity to the B-hadron lifetime that systematic errors swamp its measurement.

We begin with a very brief discussion of the hadronization of b-quarks, and their subsequent decay. Beyond providing orientation, this serves to define a number of parameters that are ultimately varied for systematic error estimates. Next we discuss the measurement of the thrust axis, important both for the event selection and later for the lifetime measurement itself. A discussion of muon identification with the MAC detector follows, and the estimation of the purity of the muon sample. A similar but shorter discussion of the electron sample completes the chapter.

4.1 Physics in Flavor Enrichment

4.1.1 *Fragmentation*

The reaction $e^+e^- \to q\bar{q}$ is followed by the spontaneous creation of many quark pairs from the vacuum, which combine with the original pair and one

another to form hadrons. In the reaction $q \rightarrow (q\bar{q}')q'$, the fragmentation function describes the distribution function of the fraction of the quarks (q's) initial energy retained by the meson ($q\bar{q}'$). Mesons containing c and b quarks tend to retain most of the initial quark's energy, because only light quark pairs (u, d, and s) are pulled from the vacuum in the fragmentation process.[65] A popular parameterization of the fragmentation function $f(\varsigma)$ is due to Peterson,[66]

$$f(\varsigma) = \frac{1}{\varsigma \left[1 - \frac{1}{\varsigma} - \frac{\epsilon_q}{(1-\varsigma)}\right]^2}.$$

The precise definition of ς was meant to be $z = \frac{(E+p_{\parallel})_{\text{hadron}}}{(E+p)_{\text{quark}}}$, but unfortunately this variable cannot be directly determined by experiment. The variable most simply accessible to experiment is $\frac{E_{\text{hadron}}}{E_{\text{beam}}}$, particularly when exclusive reconstruction of heavy mesons is performed. In fact, a clade of variables to describe fragmentation has formed, whose study is not particularly enlightening, but must be performed to compare the world data on heavy quark fragmentation.[68] The result of our study for $\varsigma = z$, is $\epsilon_c = 0.063^{+0.014}_{-0.023}$, while $\epsilon_b = 0.012^{+0.019}_{-0.009}$.

Heavy quark fragmentation effects the B-hadron lifetime in several ways. First, the harder the B-hadron energy spectrum, the harder the subsequent lepton momentum spectrum, and the more leptons from B hadron decay pass our minimum momentum cut of 2 GeV, to be described later this chapter. The same is clearly true for charmed hadrons. Hence fragmentation effects the purity of our sample. Second, the harder the B-hadron energy spectrum, the less energy is left available for the hadronization of light quarks into light mesons. This means that a larger fraction of tracks in a $b\bar{b}$ event originate from B-hadron decay. Finally, at PEP energies, the mean impact parameter for a given B lifetime depends on the B momentum.

4.1.2 *Lepton Tagging*

B-hadrons have large mass, so their decays produce particles with large momentum transverse to the B-direction. Unfortunately, light quark $e^+e^- \rightarrow q\bar{q}$ events are sufficiently broadened by the emission of gluons to produce particles

with large transverse momentum as well. However, as discussed in the Chapter 1, B-hadrons decay $12\pm1\%$ of the time to muons or electrons.[68] The rejection obtained by demanding both high transverse momentum and lepton identification strongly suppresses light quark background. The shape of the lepton momentum spectrum from B hadron decay tends to peak toward the kinematic maximum, because the associated antineutrino is right handed; this is in contrast to the situation for charmed hadron decay. Hence, lepton transverse momentum also gives good separation between $b\bar{b}$ and $c\bar{c}$ production. In fact, based on our Monte Carlo studies, most $c\bar{c}$ events enter the high transverse momentum sample via gluon emission.

Lepton tagging as a method of $b\bar{b}$ enrichment has been extensively studied, both by MAC and other PEP and PETRA detectors.[68] It is fair to say that this method of flavor enrichment is very well understood. Unfortunately, the yield is somewhat low, only $\approx 1-2$pb out of a total b-quark production cross section of 90pb at PEP. One would hope the high mass of the b-quark could be exploited to distinguish $b\bar{b}$ production without paying the price in efficiency of lepton identification. A number of variables, such as the jet mass and the boosted sphericity product, which depend on $b\bar{b}$ events being more spherical than lighter quark events have been used, but in general the same level of experimental verification that exists for lepton tagging has been absent.[69] Further, the effect of quark masses in perturbative computations of $e^+e^- \rightarrow 2,3,4$ *jets* is currently unclear.[70] It is possible to argue, for example, that $e^+e^- \rightarrow b\bar{b}$ is dominantly *2 jet*, and thus that the jet mass and sphericity product methods are less effective than current calculations indicate. Hence, for a result of such fundamental importance as the B-hadron lifetime, we have chosen lepton tagging as the most effective method of $b\bar{b}$ enrichment.

4.2 Estimation of B-Hadron Direction

Estimation of the B-hadron direction is important both for selection of the sample of events enriched in B-hadron decays, and for the measurement of the lifetime. Leptons with a large component of momentum transverse to the estimated B-hadron direction are used to select the enriched sample. The projection of the B-hadron direction in the plane transverse to the beam, or x–y plane, is used to determine the sign of the impact parameters used to measure the

lifetime.

We use the thrust axis, $\hat{t}$, as our estimate of the B-hadron direction?[1] The thrust axis is found by maximizing the quantity known as thrust,

$$T = \frac{\sum_{i=1}^{N} |\vec{v}_i \cdot \hat{t}|}{\sum_{i=1}^{N} |\vec{v}_i|},$$

where $\{v_1, \ldots, v_N\}$ are a set of vectors that describe the N particles in the event. As originally formulated, these were the momenta of the particles. In MAC, we use instead vectors composed from the magnitude and direction from the interaction point of pulses in the segmented calorimeters. Separate weights are assigned for electromagnetic and hadronic showers. A muon leaves small pulses characteristic of a minimum ionizing particle, so a correction based on the measured muon momentum is made. Figure 4.1a shows the distribution of the thrust axis in polar angle for a sample of multihadron events. We also make a second, redundant measurement of the thrust axis using the momentum vectors of charged particles, as determined by our CD. This estimate neglects neutrals, and is less accurate then the calorimetric thrust axis.

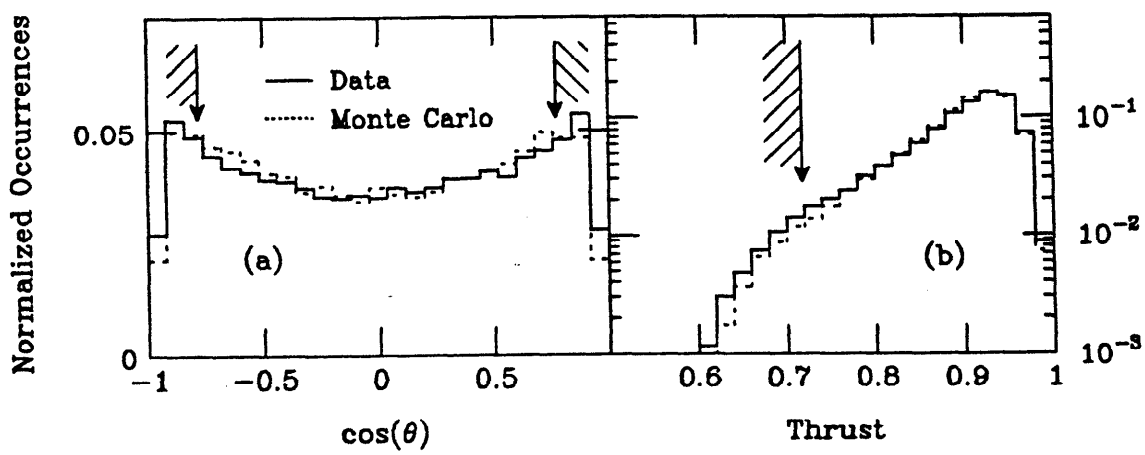

Figure 4.1 Thrust Axis and Thrust Distributions. (a) Distribution of thrust axis $\hat{t}$ in polar angle in multihadron events. Events having the thrust axis within 30° of the beam are cut. (b) Distribution of thrust, T, in multihadron events. Events having $T < 0.72$ are eliminated, due to error in thrust axis reconstruction. The excellent agreement with the MAC Monte Carlo is to be noted.

The thrust T can vary from $\frac{1}{2}$ to 1. A thrust of $\frac{1}{2}$ corresponds to an isotropic distribution of particles, and 1 to a completely back to back distribution. In practice, for $e^+e^- \rightarrow q\bar{q}$ at PEP, T is on the average ≈ 0.9, and rarely lower than 0.7. Figure 4.1b shows the measured distribution. Two-jet events tend to have high thrust, while three-jet events caused by radiation of a hard gluon tend to have low thrust. Two jet B-hadron events have slightly lower thrust than two jet light quark events, because of the large b-quark mass. However, it is somewhat unclear how the quark mass affects the emission of gluons and subsequent hadronization, and therefore unclear whether B-hadron events have on average lower thrust than light quark events.

It is impossible to directly measure how well the thrust axis estimates the B-hadron direction. One expects that the estimate is best for high thrust events, and deteriorates for low thrust events. For this reason, we cut events having $T < 0.72$ from the sample used to measure the B-hadron lifetime. Further, errors in the B-direction estimate are amplified in the x–y projection when the thrust axis is at very small angles with respect to the beam. The error in thrust axis azimuth, $\sigma_\phi \propto (1/\sin(\theta))\sqrt{1+\cos^2(\theta)}$, where θ is the polar angle with respect to the beam. For this reason, we eliminate events with $\hat{t}$ less than 30° from the beam axis. The B-hadron flight path appears foreshortened for these events, providing a second motivation for their removal. The location of the thrust and θ cuts are shown in Figure 4.1.

We must rely on our Monte Carlo to model how closely the thrust axis estimates the B-hadron direction. However, we perform a powerful check on the Monte Carlo's ability to model the thrust axis. Multihadron events from both data and Monte Carlo are split into hemispheres based upon the calorimetric thrust axis. Two new thrust axes, found using only calorimeter hits in either hemisphere, are then found. The difference in azimuth, $\delta\phi$, and polar angle, $\delta\theta$, between these hemispheric thrust axes are shown in Figure 4.2a and b, respectively. Both distributions are well fit by a Student's t-distribution[72], with argument $\sin(\delta\phi)$ or $\sin(\delta\theta)$, $s_\phi = 0.106$ or $\approx 6.1°$, and $\nu = 1.3$. Agreement between data and Monte Carlo is excellent, even in the tails. One can conclude that the thrust axis is reproducible to $\approx 6.1°/\sqrt{2} = 4.3°$, in both ϕ and θ. The same study shows that the thrust axis reconstructed from CD momentum vectors is has a reproducibility of 9.9°.

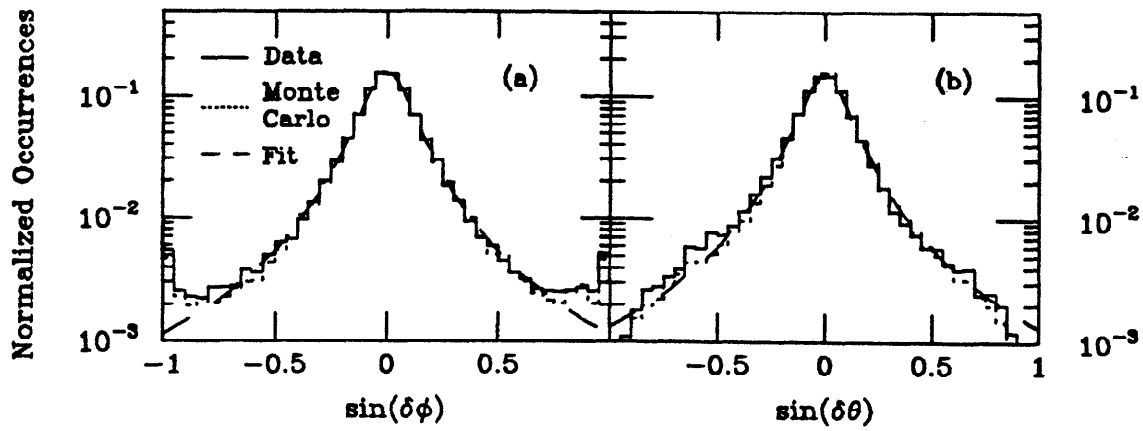

Figure 4.2 Azimuthal and Polar Differences of Hemispheric Thrust Axes. Multihadron events are split into two hemispheres, based upon the calorimetric thrust axis, and two independent thrust axes are found using only calorimeter hits in either hemisphere. (a) Distribution of $\sin(\delta\phi)$, where $\delta\phi$ is the difference in azimuth between these axes. (b) Distribution of $\sin(\delta\theta)$, the difference in polar angle. Agreement is excellent between data and Monte Carlo, even for the tails. The fit is described in the text.

We employ the same technique to measure the thrust axis resolution as a function of thrust axis polar angle and thrust itself. The results for the resolution in ϕ, as determined in a Student's t fit, are shown in Figure 4.3. The close agreement of the Monte Carlo with the data is evident from this figure. One sees that the thrust axis is reproducible to $s_\phi \approx (3.1°/\sin(\theta))\sqrt{1+\cos^2(\theta)}$. We conclude that the Monte Carlo models thrust axis reconstruction exceedingly well.

The Monte Carlo predicts that the thrust axis estimates the direction of the B-hadron involved in semileptonic decay to $s = 5.6°$, for a Student fit in either $\sin(\delta\phi)$ or $\sin(\delta\theta)$, with $\nu = 1.4$. Physics effects presumably keep s larger than the reproducibility of the thrust axis. The equivalent numbers in $c\bar{c}$-production are $s = 5.1°$ and $\nu = 1.7$, reflecting the higher mean thrust of charm events. The Monte Carlo shows a slight correlation of thrust axis with lepton direction, resulting in a systematic change in the shape of the muon and electron $p_\perp$ distributions.

4.3 Selection of Muon Sample

As discussed in Chapter 2, the MAC calorimeters are surrounded by drift

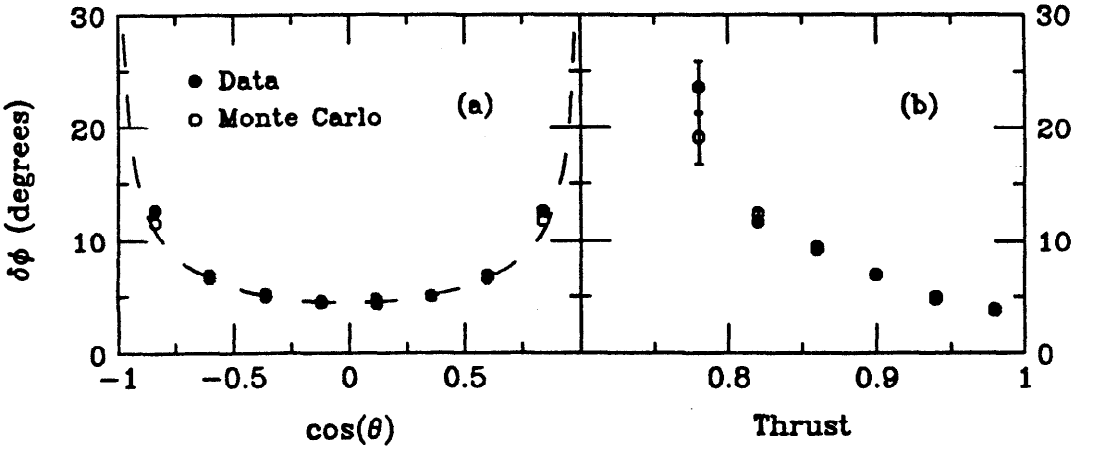

Figure 4.3 Azimuthal Difference of Hemispheric Thrust Axes. The azimuthal difference of the hemispheric thrust axes is with a Student's t-distribution for various thrust polar angles (a) θ and thrusts (b). $\delta\phi$ is the scale parameter s of the student fit. In (a), the function $1/\sin(\theta)\sqrt{1+\cos^2(\theta)}$ is plotted as well. The agreement between data and Monte Carlo is excellent.

chambers that reconstruct muon tracks over nearly the entire solid angle. The steel in the calorimeters is toroidally magnetized, allowing a measurement of the muon momentum that is completely independent of the momentum measurement made in the CD. The techniques we use to identify muons in hadronic events for the purpose of this dissertation are substantially different than in previous MAC analyses.[73] On one hand, the previous analyses of muon and tau final states allowed use of much looser cuts, because of the much smaller background from hadron misidentification and decay in flight. On the other hand, previous analyses of muons in hadronic events did not fully exploit the redundancy of the MAC system. The techniques developed for this dissertation have allowed both higher efficiency, less background, and better understanding of both.

4.3.1 *General Discussion*

The MAC calorimeters and solenoid present typically 60 radiation lengths and 7 nuclear absorption lengths (see Figure 2.10) to particles exiting from the interaction region. Therefore photons and electrons are extremely well absorbed, as are hadrons, although $\approx e^{-7} = 9 \times 10^{-4}$ of the time a hadron can 'punch-through' to the muon drift chambers. Bremmstrahlung in the nuclear field, which causes electrons to shower, is enormously suppressed for muons because of their larger mass. Muons usually penetrate to the outer drift system, or OD,

if they have enough energy to overcome energy loss to ionization and atomic excitation of the calorimeters. Typically 1.8 GeV is lost to these processes.

Muons that do penetrate execute curved trajectories due to the toroidal magnetic field in the iron calorimeter segments. The toroidal field gives muons a 'kick' parallel to the beam axis, or z-direction. The muon drift tubes are aligned to measure this kick, and therefore measure the muon polar angle θ as well. However, the muon azimuth ϕ is found by linking to a clean track in the hadron calorimeter, which measures both θ and ϕ. Thus the muon momentum, polar angle, and azimuth are measured by the linked track, referred to as an OD-HD track.

The uncertainty in the momentum measurement, or more naturally inverse momentum, is dominated by multiple coulomb scattering for most momenta at PEP, although the outer drift chamber resolution contributes slightly important for momenta near beam energy. Then

$$\sigma^2_{\frac{1}{p}} \approx \left(\frac{1}{0.3BL}\right)^2 \left[\left(\frac{0.015\sqrt{X_0}}{p}\right)^2 + \sigma^2_{OD}\right]. \qquad [4.1]$$

Here B is the magnetic induction in the iron, $= 1.7$T, L the magnetized iron thickness, typically .9m, X_0 the number of radiation lengths in the iron, typically 45, p the muon momentum in GeV, and σ_{OD} the error caused by the non zero resolution of the outer drift chambers, ≈ 0.0188. Then [4.1] gives

$$\sigma^2_{\frac{1}{p}} \approx \left(\frac{0.22}{p}\right)^2 + (0.039)^2. \qquad [4.2]$$

The resolution in polar angle θ extrapolated back into the CD, calculated similarly, is $\sigma_\theta \approx \sqrt{(0.02/p)^2 + (0.013)^2}$, but at least in the central section multiple scattering in the shower chamber degrades this by a factor of three. The resolution in extrapolated ϕ is dominated by calorimeter segmentation, except for the endplugs.

We further demand the OD-HD track to link to a track in the central tracking system. At all but the highest momenta the central tracking system makes more precise measurements of θ, ϕ, and $1/p$, as quantified in Chapter 2. The redundancy of the OD-HD and central tracking systems in *three* variables makes

it possible to study backgrounds independently of the Monte Carlo, and perform meaningful tests of the Monte Carlo.

The dominant background comes from punch-through, mentioned previously, and from leakage from hadronic showers. These two processes are not strictly distinct, with a continuum of possibilities between them. Decays of pions and kaons, although truly muons, are regarded as 'background' because they do not come from prompt heavy quark decay. The short distance between the interaction region and the start of the MAC calorimeter limits the flight path available for decay of pions and kaons before they interact in the calorimeters.

4.3.2 *Specific Implementation*

Tracks in the OD system are reconstructed and fit by independent computer programs in the hex boxes, bottom chambers, and endplugs. These tracks must include hits from at least 3, 2, and 5 layers of the respective systems. Among the sample of 150,845 multihadron events discussed in Chapter 2, 16313 have reconstructed OD stubs. A momentum, p_{OD}, is determined for each stub, taking into account energy loss in the calorimeters and variations in $\int Bdx$. It is assumed that the muon originated from the mean vertex of the event, although the momentum determination is sensitive only to the z position of this vertex. The polar angle, θ_{OD}, at the muon's exit from the CD, is similarly determined.

An expected pattern of struck layers in the central hadronic and/or endcap calorimeters is constructed based upon θ_{OD}. The tracks found by independent reconstruction programs in the central hadronic and endcap calorimeters are inspected for matches to the pattern, and those that match with at most one discrepancy are considered further. The polar angles of each of these tracks, θ_{HD}, are compared to θ_{OD}, and those that match within 0.2 radians are accepted as part of the combined OD-HD track. If the OD stub came from the hex boxes or bottom chambers, the precise azimuth of the stub is determined from the calorimeter track, and a correction to the momentum is made. If the OD stub came from the endplug, its azimuth, ϕ_{OD}, is actually determined by the OD reconstruction programs. For such stubs, an additional match to within 0.4 radians of ϕ_{HD} is required, and a weighted mean of ϕ_{OD} and ϕ_{HD} is used for the OD-HD track. No correction is made to p_{OD} in this case. For ease in comparison with the Monte Carlo, we will quote the raw cross section, uncorrected for

efficiency and acceptance, of OD-HD track production in the 311 pb^{-1} of utilized integrated luminosity. We measure a raw cross section, after the thrust cuts discussed in Section 4.2, of 36.2 ± 0.3pb, in agreement with the Monte Carlo prediction of 35.5 ± 0.3pb.

The OD-HD tracks are then examined for evidence of hadronic shower activity. The number of OD and calorimeter hits in the neighborhood of the track is considered, as are the pulse heights of the calorimeter hits. A minimum number of struck layers in the calorimeters is required. The exact cuts used were determined from a large amount of scanning, as well as from consideration of clean muon events from $e^+e^- \rightarrow \mu^+\mu^-$ and $e^+e^- \rightarrow e^+e^-\mu^+\mu^-$. We refer to these cuts as the 'punch' cuts, although technically they are intended to remove background from hadronic shower leakage, and not clean punch-through of hadrons. After these cuts, we measure a raw cross section of 21.4 ± 0.3pb, in slight discrepancy with the Monte Carlo prediction of 24.5 ± 0.3pb. Detailed study reveals that most of the discrepancy is in the region $0.4 < |cos(\theta)| < 0.6$, and is due to the requirement that a minimum number of layers be struck in the calorimeters. The Monte Carlo is slightly over-efficient in this region. This discrepancy has no consequence for the measurement of the B-hadron lifetime, other than a slight loss of statistics.

Comparison is then made between tracks found in the central tracking system (CD alone for the first 217 pb^{-1} of integrated luminosity, and CD+VC for the final 94 pb^{-1}) and the OD-HD tracks. The central and OD-HD polar angle, azimuth, and inverse momentum are compared. The inverse momentum is given the sign of the muon it describes. Central and OD-HD tracks are associated 1) if their azimuth agrees to within 0.2 radians 2) if a chi-squared, χ^2_m, made from the mismatch in polar angle, azimuth, and signed inverse momentum is ≤ 25. The errors used in the computation of the χ^2_m are determined empirically from the study of clean $e^+e^- \rightarrow \mu^+\mu^-$ and $e^+e^- \rightarrow e^+e^-\mu^+\mu^-$ events. For example, Figure 4.4 displays a scatterplot of the mismatch in θ between central and OD-HD tracks as a function of signed inverse momentum. From such scatterplots, we determine

$$\sigma^2_\theta = \left(\frac{0.065}{p}\right)^2 + (0.013)^2$$

$$\sigma^2_{\frac{1}{p}} = \left(\frac{0.22}{p}\right)^2 + (0.034)^2$$

in excellent agreement with the estimates in the previous section. The effective error in phi is determined primarily by calorimeter segmentation, and is typically 0.014 radians in the central section of MAC and 0.060 radians in the endcaps. The θ and ϕ for linked tracks is taken from the central tracking system, while a weighted mean of the central and OD-HD momenta is taken for the momentum.

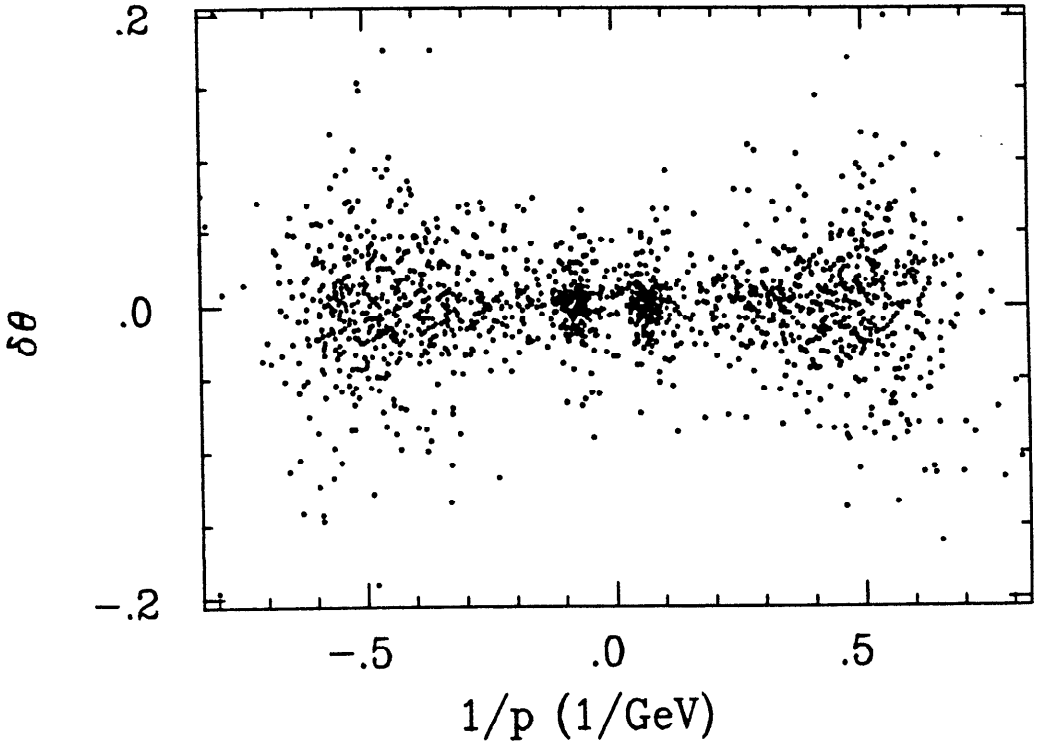

Figure 4.4 Central OD-HD Polar Angle Difference in $e^+e^- \rightarrow \mu^+\mu^-$ and $e^+e^- \rightarrow e^+e^-\mu^+\mu^-$. The inverse momentum is given the sign of the muon. Muons from $e^+e^- \rightarrow \mu^+\mu^-$ occupy the center of the plot. We determine from such plots the errors for the match χ^2_m used to link central and OD-HD tracks.

There is no reason to expect the mismatches in θ, ϕ, and inverse momentum to be distributed in a gaussian, and hence no reason for the match χ^2_m to follow a chi-square distribution function. This is true for clean $\mu^+\mu^-$ events, but even more so in multihadron events, where leakage from hadronic showers, decay in flight and central tracking confusion degrade the mismatch distribution. For

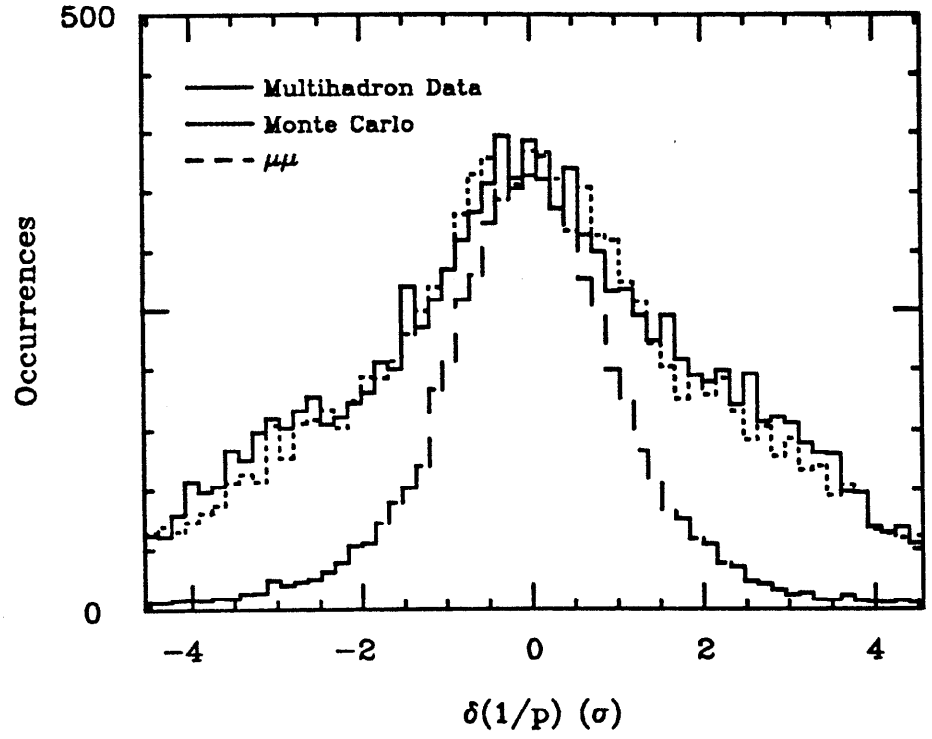

Figure 4.5 Mismatch in Inverse Momentum between Central and OD-HD Tracking. In 'standard deviations' as computed in this section of the text. The distribution is broader in multihadron events than in $e^+e^- \rightarrow \mu^+\mu^-$ and $e^+e^- \rightarrow e^+e^-\mu^+\mu^-$ events because of the effect of hadronic showers, decay in flight, and central tracking confusion. These phenomena are quite clearly well represented by the Monte Carlo multihadron simulation.

example, Figure 4.5 shows the mismatch distribution in inverse momentum for both multihadron and clean muon events. Neither distribution is gaussian, and that for multihadron events is considerably wider than for clean muons, but is very well modeled by the Monte Carlo. The same is true of the match χ^2_m distribution itself, exhibited in Figure 4.6. The χ^2_m cut for linking central and OD-HD tracks of 25 can be seen from Figure 4.6 to be somewhat loose. We vary the value of this cut down to 5 and up to 100 to study systematic errors, but the excellent agreement of the Monte Carlo and data is already evident.

Requiring a match to a central track brings the raw cross section measured in the data to 13.8 ± 0.2pb, and the Monte Carlo prediction to 15.6 ± 0.2pb. In fact discrepancy introduced by the punch cut has remained in proportion, and the efficiency for OD-HD tracks to link to central tracks has been modelled very well by the Monte Carlo, as discussed in the next section. The number of events

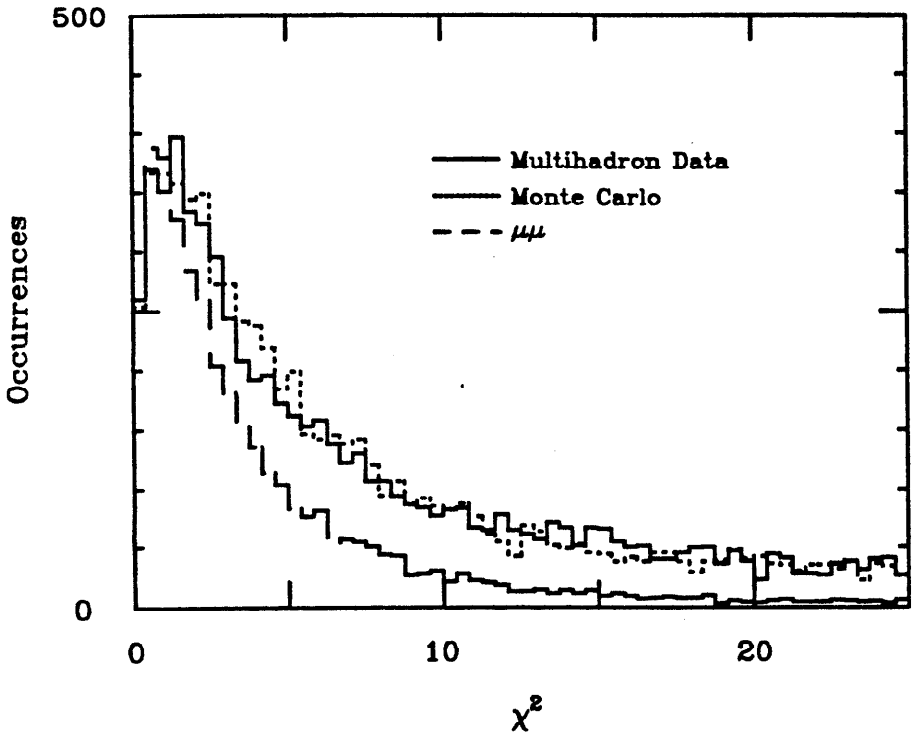

Figure 4.6 Distributions of Match χ^2_m. The difference between low multiplicity muons and multihadrons is again evident, as is the excellent modeling of the Monte Carlo.

with linked OD-HD-central tracks is 4205, and these events contain 4306 tracks.

4.3.3 *Efficiency*

As already mentioned, knowledge of the precise efficiency for finding muons is not critical for the B-lifetime measurement, except that it determines the number of events in the final sample. In this section we present a brief study of the muon reconstruction efficiency, to be used later to check the number of B-enriched events in the sample.

We select events with exactly two tracks in the central tracking system, and require these tracks to match scintillator pulses that occur within 1 ns of the beam crossing. We further require the two tracks to enter sensitive areas of the calorimeters, and demand < 8 GeV in all the calorimeters. These requirements produce a sample of events highly enriched in $e^+e^- \rightarrow \mu^+\mu^-$ and $e^+e^- \rightarrow e^+e^-\mu^+\mu^-$, selected independently of the OD-HD system. The efficiencies through the various stages of muon identification are given in Table 4.1.

ID Stage	Efficiency
OD-HD	72%
and punch	68%
and $\chi^2_m < 100$	65%
and $\chi^2_m < 25$	62%
and $\chi^2_m < 5$	47%

Table 4.1 OD-HD and Linkage Muon Efficiency. Determined with a sample of $e^+e^- \rightarrow \mu^+\mu^-$ and $e^+e^- \rightarrow e^+e^-\mu^+\mu^-$ events selected only with the inner portions of the detector. The efficiency of the central tracking has not been included.

No fiducial region has been selected, although the CD covers $|cos(\theta)| < 0.95$. Figure 4.7 shows the inefficient regions, which occur at boundaries and physical supports. The measured efficiency varies less than 2% as a function of momentum between 2 and 14.5 GeV.

A similar study was made of the central tracking reconstruction efficiency. Events with at least two OD-HD tracks that passed the punch cuts and linked to scintillator hits that occurred within 1 ns of the beam crossing were selected; no requirement was made on the central tracking. The results are given in Table 4.2. We conclude the absolute efficiency for muon detection is 59% in the

# of Layers	Efficiency
5 CD, 0 VC	98.9%
7 CD, 3 VC	95%
9 CD, 5 VC	59%

Table 4.2 Central Tracking Efficiency. Determined with a sample of $e^+e^- \rightarrow \mu^+\mu^-$ and $e^+e^- \rightarrow e^+e^-\mu^+\mu^-$ events selected only with the outer portions of the detector. A fiducial region of $\cos(\theta) < 0.95$ has been used.

region $|cos(\theta)| < 0.95$. This is somewhat lower than the $80 - 90\%$ efficiencies quoted for MAC studies of the τ lepton and the $\mu^+\mu^-$ final state. The difference can be traced to: 1) tracks with only 2 hits in the outer drift system are allowed

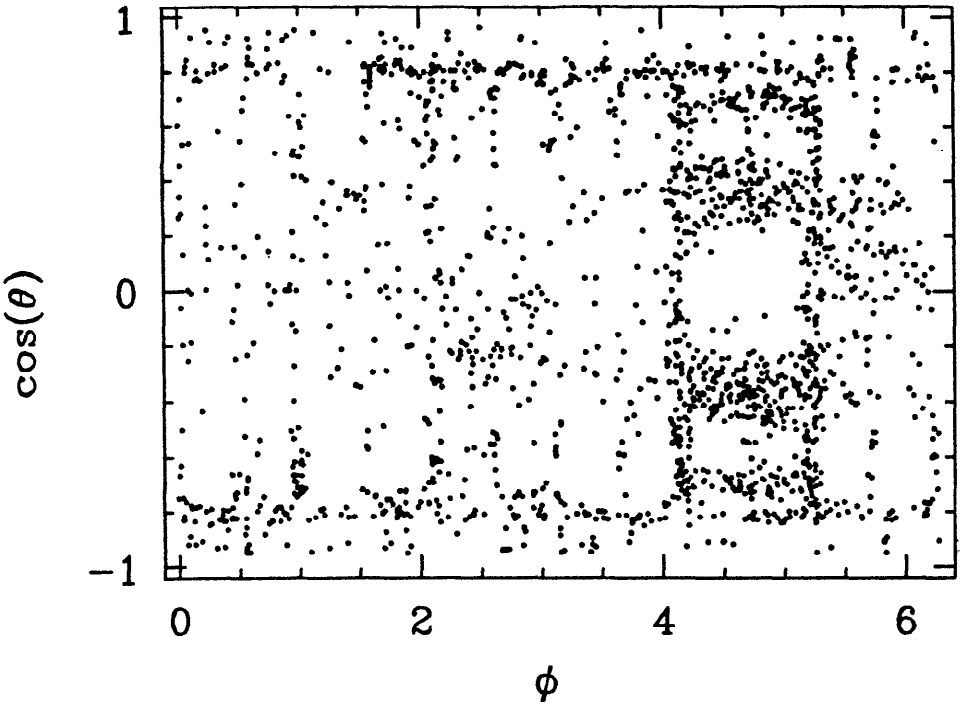

Figure 4.7 Inefficiencies in the OD-HD System. Tracks that are found in the central tracking system, fire a scintillator within 1 ns of the beam, leave < 4 GeV in the MAC calorimeters, but are *not* not found in the OD-HD system are plotted. The dominant inefficiencies are seen to be at the bottom of the detector, where the supports for the detector are, and at the overlap between the hex boxes and the endplugs, near $|cos(\theta)| \approx 0.9$.

in these analyses; 2) calorimeter tracks are not required in those analyses. The lack of hadronic background in those studies justifies the looser cuts.

In multihadron events, OD-HD tracks due to leakage from hadronic showers and decays in flight may fail to link to central tracks. The three matching variables, ϕ, θ, and particularly $1/p$ will mismatch in such cases to a degree larger than they mismatch for prompt muons from heavy flavors. Therefore, the efficiency for OD-HD tracks to link to central tracks in multihadron events is not a measure of central tracking efficiency, but more a reflection of the amount of mismatch from background processes. However, our Monte Carlo simulation should portray leakage from hadronic showers and decays in flight. The efficiency for OD-HD tracks to link to central tracks tests the accuracy of the Monte Carlo modeling. In Figure 4.8 we show this efficiency for both Monte Carlo and data, for a variety of χ^2_m values, and as a function of both polar angle θ, and the angle

of the muon from the thrust axis, θ_j. The agreement between the two is excellent. Some loss of efficiency occurs near the core of the jet, for small θ_j, but in fact study in the Monte Carlo shows this is entirely due to the greater incidence of leakage from hadronic showers there, and *not* due to tracking inefficiency.

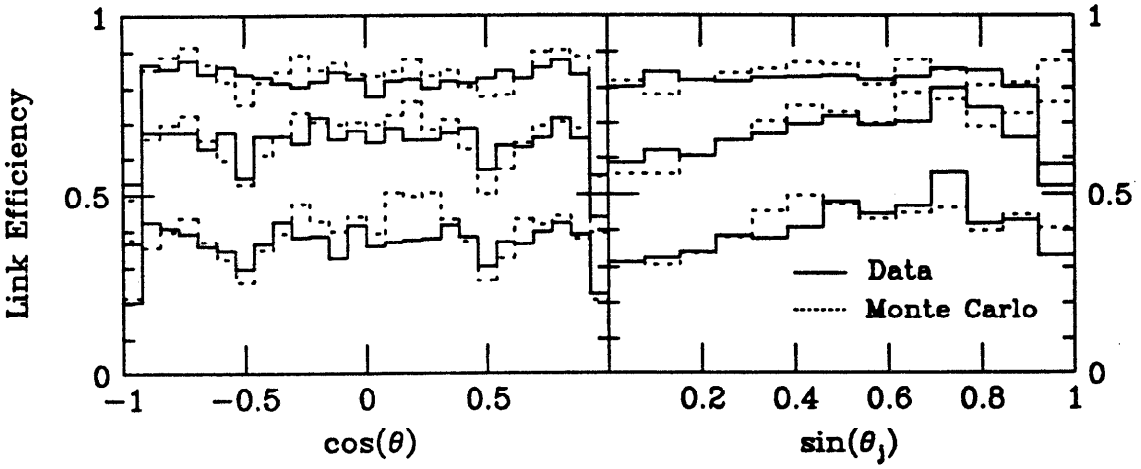

Figure 4.9 Efficiency for OD-HD Tracks to Link to Central Tracks. Versus polar angle from the beam axis, θ, and angle from the thrust axis, θ_j. The three cases are $\chi^2_m < 100$, 25, and 5. The primary reason for an OD-HD track not to link to a central track is that the OD-HD track originates from the leakage of a hadronic shower, and therefore fails to match well to any central track. The good agreement between Monte Carlo and data for the linking efficiency shows that the Monte Carlo is portraying this process accurately.

4.3.4 *Studies of Background*

We have performed two studies to test the modeling of backgrounds by the Monte Carlo. In general, we have confidence in the modeling of the decay in flight of pions and kaons, and of the incidence of non-interacting hadrons, or punch-through. The leakage of hadronic showers is more difficult to model. Our first study is directed toward this phenomena. The second study utilizes the clean source of pions provided by $\tau \rightarrow 3$ charged pions.

When leakage from hadronic showers results in an OD-HD track, the variables θ_{OD}, ϕ_{OD}, and signed $1/p_{OD}$ determined for a track will tend not to match any central track, but will occasionally do so by chance. The probability to do so is arguably independent of the sign of $1/p_{OD}$; this is *not* true for OD-HD tracks that result from true muons. Let N_m denote the number of links between OD-HD tracks and central tracks where the measured sign of $1/p_{OD}$ has been retained in determining χ^2_m, and N_f denote the number of links that occur when the sign of $1/p_{OD}$ has been flipped. Then it is easy to show that $N_f/(N_m - N_f)$ is an *upper* bound on the fraction of links from hadronic showers among N_m. This limit is shown in Figure 4.10 as a function of a cut on the track momentum transverse to the thrust axis, $p_\perp$. Also shown is the prediction of the Monte Carlo for the fraction of tracks from misidentified hadrons, *including* non-interacting hadrons. At low $p_\perp$, wrong sign links from true muons probably keep the upper bound well above the true shower leakage rate. At high $p_\perp$, the upper limit actually dips *below* the Monte Carlo prediction, indicating the Monte Carlo overestimates hadronic shower leakage in that region. Other evidence, described in the next section, suggests that the Monte Carlo underestimates the background to muons. We will use the difference between data and Monte Carlo observed here as a systematic error estimate.

We have also studied the rate of apparent muon reconstruction among the tracks resulting from $\tau \to 3$ charged particles. The charged particles are dominantly pions, with a mean momentum of 3.3 GeV and standard deviation in momentum of 2.6 GeV. Only central tracks with momentum sufficient to overcome ionization losses and penetrate to the outer drift system are considered candidates for misidentification, and there are 2.2 such tracks among the 3 τ decay products per event. The pion momentum spectrum is harder than that in multihadron events, and there are far fewer kaons in 3 prong tau decay than in multihadrons. The misidentification probabilities determined in this study are therefore not directly transferable to multihadrons, but they provide a useful test of the Monte Carlo. The results are summarized in Table 4.3. The agreement between data and Monte Carlo is excellent. For the loosest muon identification criteria, the OD-HD match, the Monte Carlo estimates $\approx$ 20% of the events result from decays in flight, and $\approx$ 80% from hadron misidentification. For the nominal $\chi^2_m < 25$, the Monte Carlo estimates $\approx$ 40% decays and $\approx$ 60% hadron

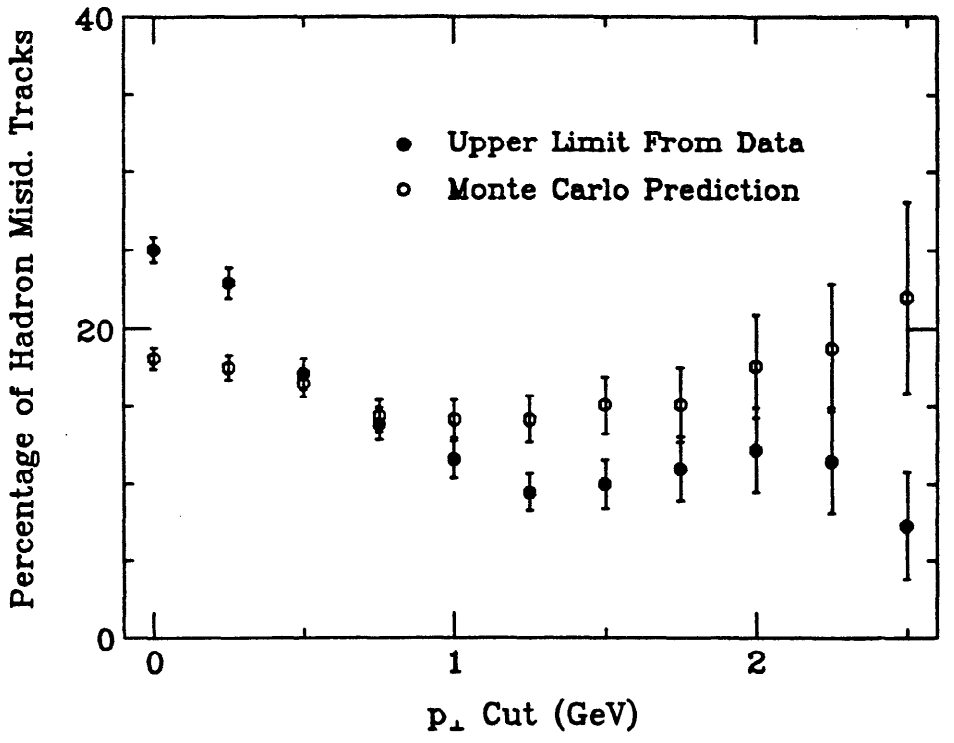

Figure 4.10 Upper Bound on Leakage from Hadronic Showers from Wrong Sign Links. Versus lower cut on momentum transverse to the thrust axis. An upper bound on leakage from hadronic showers in the inclusive muon sample is inferred from the data, as discussed in the text, from the fraction of wrong sign links between the OD-HD and central tracking systems. Also shown is the fraction of tracks from misidentification of hadrons, as predicted from the Monte Carlo. In the region $p_\perp > 1GeV$, the Monte Carlo overestimates the hadronic shower leakage by $\approx 5\%$; this will ultimately be used in a systematic error estimate.

misidentification. The misidentification probabilities versus polar angle in the detector are shown in Figure 4.11.

4.3.5 *Flavor Enrichment*

In this section, we detail the final criteria used to select the sample enriched in B-hadrons, and discuss the purity of that sample. First, some miscellaneous cuts will be described, then, the cuts on momentum and momentum transverse to the thrust axis will be discussed. The cut on transverse momentum, or $p_\perp$, produces most of the flavor enrichment.

Recall that the cuts described in section 1.3.2 lead to the selection of 4205 events containing 4306 linked muon tracks in 311 pb^{-1} of data. In order to

	Data		*Monte Carlo*	
cut	$\#\mu$ i.d.'s	mis i.d./track	$\#\mu$ i.d.'s	mis i.d./track
OD-HD	196	$1.80 \pm .13\%$	842	$1.76 \pm .06\%$
and punch rej.	86	$0.79 \pm .09\%$	417	$0.87 \pm .04\%$
and CD, $\chi^2_m < 100.$	76	$0.70 \pm .08\%$	346	$0.72 \pm .04\%$
and CD, $\chi^2_m < 25.$	54	$0.50 \pm .07\%$	216	$0.45 \pm .03\%$

Table 4.3 Muon Misidentification in $\tau \rightarrow$ 3 *prongs*. Four levels of the muon id cuts are shown. The data were taken from 311 pb^{-1} containing 4959 1-3 τ events, and the Monte-Carlo from 990 pb^{-1} containing 21728 1-3 τ events.

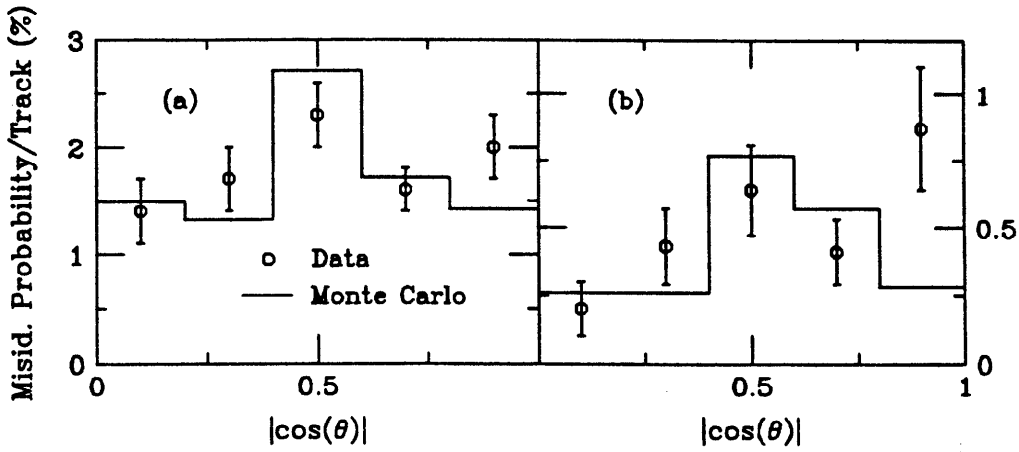

Figure 4.11 Polar Angular Distribution of Muon Misidentification in $\tau \rightarrow$ 3 *prongs*. (a) loosest muon identification, requiring only a match between the OD and the hadronic calorimeter. (b) nominal, requiring the track to pass cuts designed to reject punch-through and to link to the CD with $\chi^2_m < 25$.

eliminate some background originating in rare 2γ processes, we require that no hemisphere in the event contain fewer than two central tracks. These mild cuts remove only 117 events, bringing the linked track raw cross section to $13.5 \pm .2$pb, to be compared with the Monte Carlo prediction of 15.2 ± 0.2pb.

We demand that the linked track have momentum greater than 2 GeV. This cut reduces background, in particular leakage from hadronic showers, which tends to cluster at low momentum. This leaves a sample of 3179 events containing 3243 linked tracks, a raw cross section of 10.4 ± 0.2pb compared with the

	ρ(GeV)	ν	α	β
$b \rightarrow \mu$	1.70	1.219	0.967	7.60
$b \rightarrow c \rightarrow \mu$	0.594	$\equiv \infty$	0.819	$\equiv 2$
$c \rightarrow \mu$	0.351	5.42	1.184	$\equiv 2$
background	0.424	3.88	0.914	$\equiv 2$

Table 4.4 Parameterization of Monte Carlo $p_\perp$ Spectra. The most general form of ([4.3]) was found to be necessary for the primary $b \rightarrow \mu$, which has a very steep edge in the $p_\perp$ distribution. The simplification $\beta = 2$ was found adequate for primary c and background, and $\nu \rightarrow \infty$ for cascade b.

12.1 ± 0.2pb predicted by the Monte Carlo.

We cut on the linked track momentum transverse to the thrust axis to achieve most of the b-flavor enrichment. We use two methods to estimate the fraction of $b\bar{b}$ events in the sample. In the first, we fit the $p_\perp$ spectrum of the data with a set of functions, whose shape is determined from the Monte Carlo. This method allows the data itself to determine the b-purity, thereby accounting for actual fluctuations and allowing for the constraint of systematic errors. We take the fit value as the most accurate purity estimate. In the second, we take the purity directly from the Monte Carlo.

The Monte Carlo $p_\perp$ spectra for linked tracks originating from a primary $b \rightarrow \mu$ decay, a cascade $b \rightarrow c \rightarrow \mu$ decay, a primary $c \rightarrow \mu$ decay, and background tracks are fit with functions or the form,

$$f(x) \propto \frac{x^\alpha}{(1 + x^\beta/\nu)^{\frac{\nu+1}{2}}} \qquad [4.3]$$

$$x = \frac{p_\perp}{\rho},$$

where ρ, ν, α, and β are free parameters. The simplification $\beta = 2$, $\nu \rightarrow \infty$ leads to a chi-squared distribution, and if this leads to a sufficiently good representation of the Monte Carlo, it is employed. Table 4.4 shows the typical fitted parameters.

The data is fit as a sum of these functions. The cascade b, primary c, and background functions have very similar shapes, so the relative normalization of primary c to background and cascade b to primary b is fixed, leaving two normalizations free in the fit. The fit to the data is shown in Figure 4.12. Using these normalizations, we obtain Figure 4.13, which exhibits the percentage of $b\bar{b}$ events as a function of $p_\perp$ cut. The small percentage of $b\bar{b}$ events that produce linked tracks from background processes, typically 3%, are included in the figure.

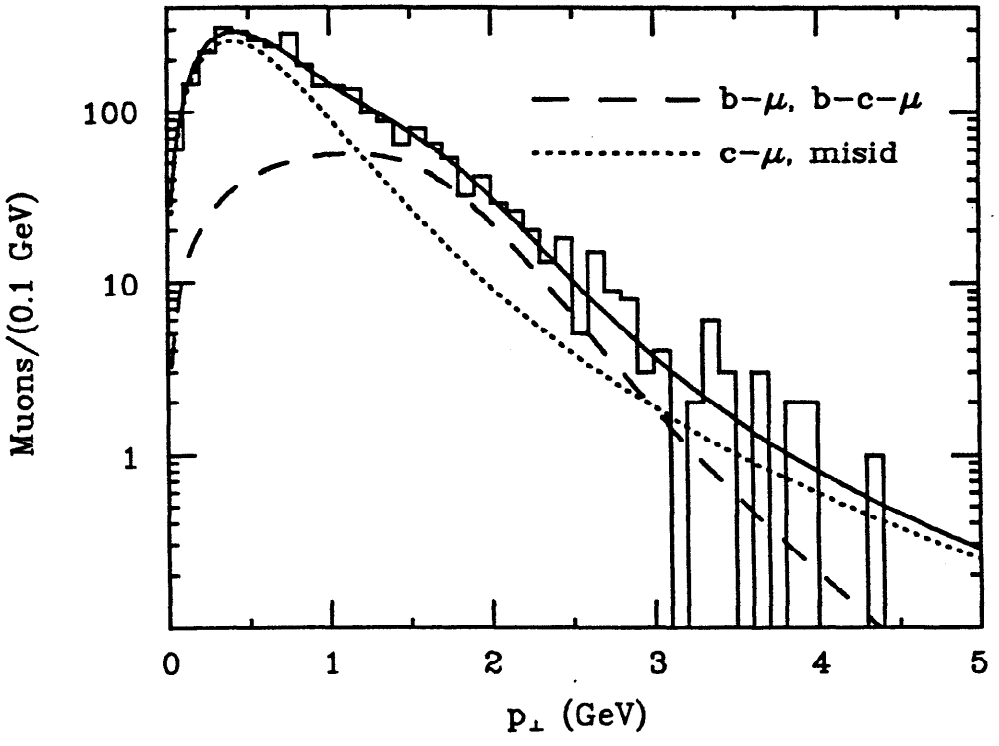

Figure 4.12 Fit to Inclusive Muon $p_\perp$ Spectrum. The data is binned into 100 MeV bins. The goodness of fit χ^2 is 56 for 47 degrees of freedom. Note that the $c \rightarrow \mu$ and background dominate for both very low and exceedingly high $p_\perp$. The bulge in the midrange, due to primary b, is evident

From Figure 4.13, it is apparent that the maximum $b\bar{b}$ event purity is obtained for a lower $p_\perp$ cut of 1.5 GeV. Due to the proximity of an extremum in purity, we expect general insensitivity to systematic errors. With this cut, 453 events containing 458 linked tracks remain in the data, a raw cross section of 1.47 ± 0.07pb, compared with a Monte Carlo prediction of 1.62 ± 0.07pb.

The $b\bar{b}$ purity of this sample, estimated from the fit to the data, is $60.3 \pm 2.6\%$, while the Monte Carlo predicts $62.8 \pm 1.6\%$. In section 1.3.4, the data indicated

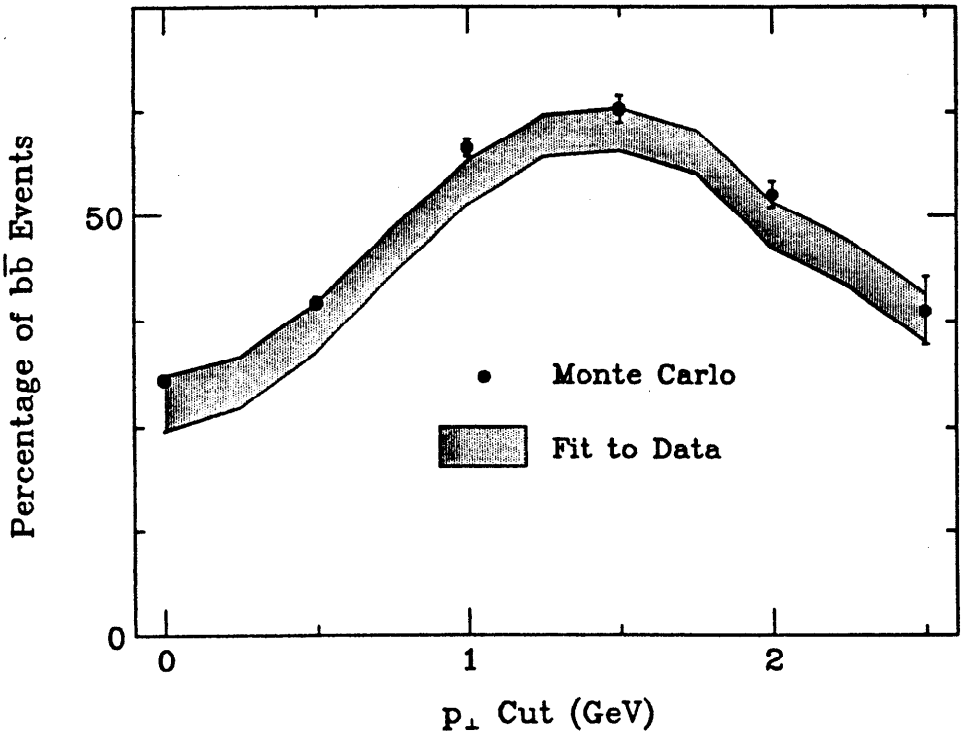

Figure 4.13 Percentage of Bottom Events as a Function of $p_\perp$. The ± 1 standard deviation errors of the fit to the data are shown. The agreement with the Monte Carlo is good.

that the Monte Carlo may be overestimating background from hadronic showers by 5%, which would lead to an increase in estimated $b\bar{b}$-purity of 3%. We find that variation of the shapes and relative normalizations of the primary c and background functions change the fitted $b\bar{b}$ purity by 2%. Variation of the bottom and charm fragmentation functions lead to $< 1\%$ change in the fitted $b\bar{b}$ purity. Combining these systematic errors in quadrature with the statistical error, we arrive at an estimated fraction of $b\bar{b}$-events in the final muon sample of $60 \pm 4.5\%$. We estimate the fraction $c\bar{c}$ events to be 22%, where 6% enter from misidentification, and 16% from primary $c \rightarrow \mu$ decays. The remaining 18% comes from light quark production.

We now perform a simple check of the number of $b\bar{b}$ events in the final sample. We start with 150,845 events, of which 97% are multihadrons from 1γ annihilation, and $\approx 1/11$ of which contain 2 b-quarks. The requirement that the thrust axis have $\theta > 30°$ retains $\approx 81\%$ of the $1 + \cos^2(\theta)$ distribution; the cuts on thrust itself and against 2γ background retain 95% each. For the muon itself,

the CD covers 93% of the $1+\cos^2(\theta)$ distribution, and the muon identification is 59% efficient. The cuts on $p > 2\,\mathrm{GeV}$ and $p_\perp > 1.5\,\mathrm{GeV}$ retain 23% of $b \to \mu$, and we take the b semileptonic branching ratio to be 12%. Hence, we expect:

$$150,845 \times 0.97 \times \frac{2}{11} \times 0.81 \times 0.95^2 \times 0.93 \times 0.59 \times 0.23 \times 0.12 = 295$$

$b\bar{b}$ events. There are 453 events in the final sample, of which 55%, or 249 come from $b - \mu$. The data thereby has 18% less events than this simple prediction, 14% of which is explained by the discrepancy between the data and Monte Carlo in the description of the punch cuts.

4.4 Selection of Electron Sample

Electrons are identified in the MAC detector by their shower profile in the central shower chamber. The algorithms to do so were not developed for this work and are described elsewhere, although a brief summary will be provided in this section.[75] As in the case of muon identification, these algorithms are more stringent than those used in MAC analyses of electrons in τ or Bhabha scattering events, because of larger background in multihadron events.[76] In particular, no identification of electrons in the MAC endcaps is made for this dissertation, but is in those analyses.

A new feature of this work is an analysis of background from the process $e^+e^- \to e^+e^-q\bar{q}$, where at least one electron is scattered at large angle into the shower chamber. This process has an effective cross section for survival through the MAC multihadron selection and electron identification of $\approx$ 1pb, and possesses a very flat spectrum in $p_\perp$, so survives the flavor enrichment cut.

4.4.1 *General Discussion*

Electrons initiate a cascade of bremmstrahlung in the nuclear field followed by pair conversion in the nuclear field when they enter matter. The depth of this cascade, or electromagnetic shower, is very dependent on the atomic number of the target matter, Z, and is $\propto 1/Z^2$. In contrast, hadrons and muons do not initiate electromagnetic showers, because their masses are at least hundreds of times greater than that of the electron. Hadrons induce cascades that are

primarily due to collisions mediated by the strong interaction. The depth of hadron showers decreases only as $\approx 1/Z^{\frac{2}{3}}$. Therefore, for materials of high Z, it is possible to distinguish electron-initiated showers because they develop much more quickly in depth than do hadron-initiated showers. In the MAC detector, we distinguish electrons in the central shower chamber, which has lead ($Z = 82$) absorbers.

As discussed in Chapter 2, the SC consists of 32 layers of alternating layers of lead and wire chambers. These layers are ganged into three groups, of 2.7, 5.0, and 4.7 X_0. Electrons deposit the great majority of their energy in the SC, and their energy is typically measured with a resolution $\approx 24\%/\sqrt{E}$; hadrons typically deposit only one-half of their energy in the SC, and the remainder is deposited in the surrounding HC and ECs. Hence, a match between the energy deposited in the SC and the momentum measured in the CD is required for electron identification. A match in direction from the interaction point, shower development in depth consistent with an electromagnetic cascade, and lack of energy in the HC are required as well. The probability that a well isolated hadron will mimic an electron is typically 1/200, and the irreducible phenomena allowing hadrons to fake electrons being π^0 production in an early hadronic collision.

However, it is not the direct faking of an electron by a hadron that dominates the misidentification probability in multihadron events. The overlap of the electromagnetic shower, often from a prompt π^0 decay, with a charged hadron is more likely. The $p_\perp$ cut, which is made primarily for flavor enrichment, also tends to reduce this background. In addition, real electron pairs come from processes other than the prompt decay heavy hadrons: stiff pairs from photon conversion, as well as Dalitz decays of π^0s are two such sources. In contrast to the situation for muons, there are not direct decays to single electrons analogous to $\pi^+ \to \mu^+ \nu_\mu$.

4.4.2 *Specific Implementation*

All tracks found in the central tracking system having momentum $p >$ 1.8 GeV are projected into the SC, and the one or two hit(s) closest to the track in each SC layer, but within $\delta\phi = 4.5°, 3.0°$, and $2.2°$ in azimuth in the three layers, respectively, and within $\delta\theta = 5.5°, 4.0°$, and $4.0°$ in polar angle of

the track is associated with that track. In a similar manner, the one hit closest to the track in each of the three HC layers, but within $\delta\phi = 5.0°, 4.5°$, and $4.0°$ in the three layers, respectively are associated with that track. Let E_I, E_{II}, E_{III}, and $E_{\rm hc}$ denote the energies of the hits associated with the track in the three SC layers and all the HC layers, respectively. Then the identification of the track and associated calorimeters hits as due to an electron is made if:

1. The track does not come from a *very* loosely defined primary vertex.
2. $\frac{E_I}{p} > 0.1$ and $\frac{E_{II}}{p} > 0.3$.
3. $\frac{E_I+E_{III}}{E_I} > 0.2$.
4. $0.4 < \frac{E_I+E_{II}+E_{III}}{p} < 1.8$.
5. $E_{\rm hc} < 0.5\,\text{GeV}$ and $\frac{E_{\rm hc}}{p} < 0.12$.

The electron sample is taken from 137018 multihadron events from $297\,\text{pb}^{-1}$ of integrated luminosity, $205\,\text{pb}^{-1}$ before installation of the VC, and $92\,\text{pb}^{-1}$ subsequently. Fewer multihadron events are used for the electron sample than for the muon sample because of technical problems with the SC. In these multihadron events, some 210721 tracks pass (1), and 7469 pass (2). Of these, 5902 pass (3) and (4), and 4027 tracks in 3914 events survive the final hadron calorimeter cuts.

4.4.3 *Efficiency*

As noted in the discussion of the muon sample selection, knowing the efficiency is not critical for the B-lifetime measurement. Nevertheless, some knowledge of the electron identification efficiency is useful for comparing data and Monte Carlo.

Studies with the Monte-Carlo of clean electrons lead to an estimate of 0.80 ± 0.03 for the efficiency to averaged over 2 and 10 GeV, and $|cos(\theta)| < 0.7$. A similar study of clean electron pairs from 2γ processes in the MAC data leads to an estimate 0.68 ± 0.02.

The efficiency in multihadron events, as estimated by the Monte Carlo, is ≈ 0.50. This is less than for clean electrons, because 1) tracks fail the hadron calorimeter cuts, due to overlap of hadrons; 2) overlap of hadrons causes some of the SC cuts, in particular (2) and (3) of the last section, to be failed; and

3) the central tracking is less efficient in the crowded multihadron environment. The efficiency as a function of $p_\perp$ is shown in Figure 4.14b. Scaling the Monte Carlo estimate by the ratio of data to Monte Carlo for clean electron events, we estimate the electron efficiency to be ≈ 0.43 for data multihadrons. This is most likely an overestimate.

4.4.4 *Background*

We estimate backgrounds with our Monte Carlo simulations. The dominant background is due to hadron misidentification, induced by the overlap of photons with hadrons. The effect of these overlaps dominates at low $p_\perp$, because the density of particles is greater near the thrust axis. At larger $p_\perp$, the fluctuation of hadronic showering is responsible for misidentification. Figure 4.14a shows the misidentification probability as a function of $p_\perp$.

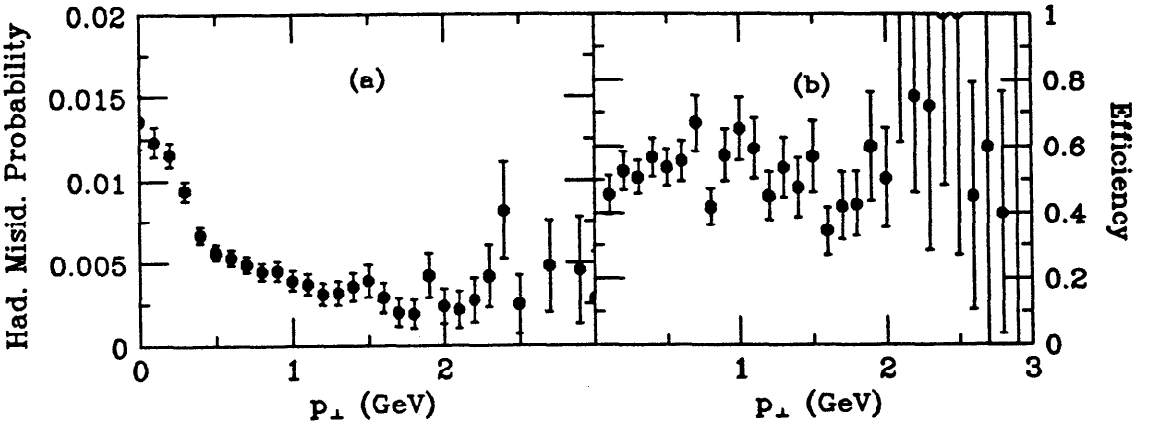

Figure 4.14 Hadron Misidentification and Electron Identification Efficiency vs. $p_\perp$. As estimated by our Monte Carlo. (a) Hadron misidentification probability per track. (b) Electron identification efficiency.

4.4.5 *Sample Composition*

For flavor enrichment we employ the same cuts on the value of thrust and polar angle as in the muon sample, as well as the came cuts on momentum p and momentum transverse to the thrust axis $p_\perp$, namely $> 2\,\text{GeV}$ and $> 1.5\,\text{GeV}$. Our motivations differ somewhat in this case, however. The momentum cut

ensures that the electromagnetic shower typically penetrates to the third layer of the shower chamber, and peaks in the second. The $p_\perp$ cut enriches the sample in b-quark events, but also reduces background from hadron-photon overlap, and sensitivity to imperfect modeling of this phenomena. In the data, 364 tracks in 358 events pass these cuts.

Inspection of the 358 passing events reveals a substantial background from $O(\alpha^4)$ $e^+e^- \to e^+e^- q\bar{q}$ processes. In previous MAC analysis of inclusive electrons in multihadron events, this background was removed by scanning. For this dissertation, we have formalized this background rejection to definite cuts implemented in software. We have also estimated the remaining background using the most complete $O(\alpha^4)$ $e^+e^- \to e^+e^- q\bar{q}$ Monte Carlo available. The dominant such background is from multiperipheral 2γ processes, where one electron is scattered at large angle into the SC, the other escapes down the beam pipe, and the photon pair couples to hadrons. This process tends to produce isolated electrons with large momentum and $p_\perp$. The presence of this process is qualitatively evident from Figure 4.15, the distribution of the electron tracks in $p_\perp$. There is a clear excess of large $p_\perp$ tracks when compared with the same distribution for the muon sample, Figure 4.12. This observation leads to our first cut intended to reject the 2γ background: events containing tracks with $p_\perp > 3$ GeV are rejected. 299 events remain after this cut.

The remaining 2γ events tend to have a very unbalanced appearance, both in the density of charged track and in momentum along the beam direction, and a low multiplicity. In a large number, the scattered electron appears to recoil against a jet of hadrons. In these events, the projection of the thrust axis in the plane perpendicular to the beam, or x–y plane, tends to be parallel to the scattered electron. Most of the scattered electron's $p_\perp$ is along the beam axis. To eliminate such events, we demand the x-y component of $p_\perp$, or $p_{\perp xy}$, to exceed 0.5 GeV. This cut tends to reduce hadron misidentification due to overlap as well. Figure 4.16a exhibits the distribution of $p_{\perp xy}$ and the cut location. 207 events remain after this cut. Some unbalanced events remain even after the $p_{\perp xy}$ cut. We make the following additional requirements:

1. A quantity, C, is constructed that characterizes the isolation of the most isolated track in the event. For each track reconstructed from our central tracking, the relative direction cosines of all tracks is computed, and the

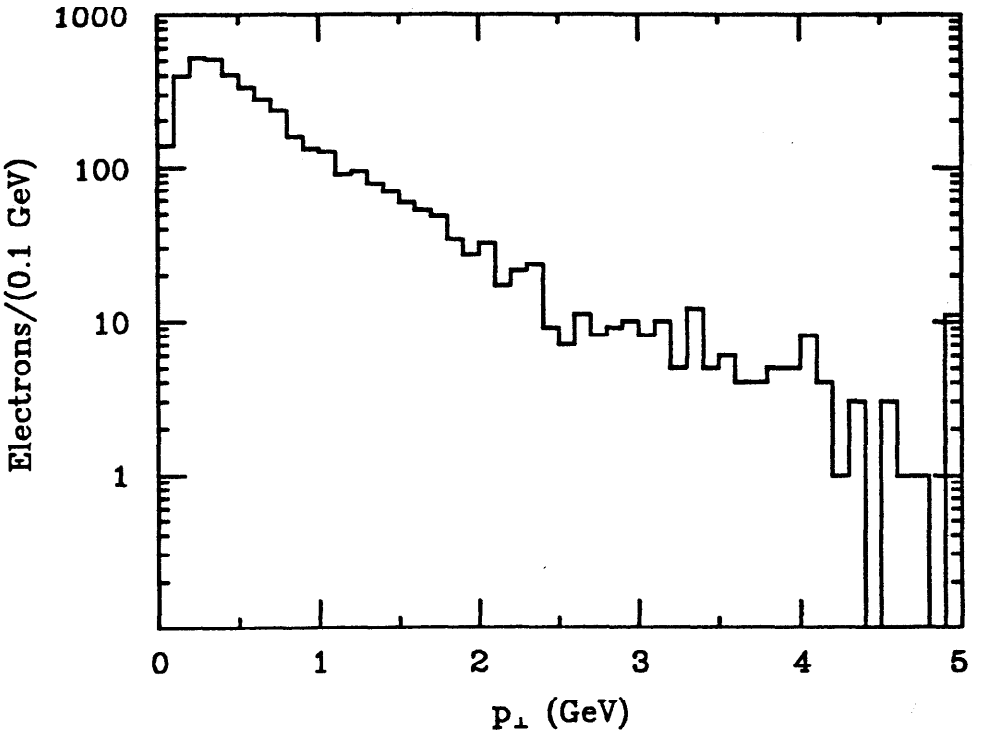

Figure 4.15 Distribution of $p_\perp$ for Electron Tracks. The distribution has a tail at high $p_\perp$ due to 2γ background, which motivates the cut described in the text of $p_\perp < 3.0\,\mathrm{GeV}$. Comparison with Figure 4.12 for the muon sample reflects the higher misidentification probability at low $p_\perp$ for the electron sample, as well as the lower absolute detection efficiency.

sum of all positive direction cosines is made. This quantity is at least 1, because the direction cosine of a track with respect to itself is retained in the sum. C is then the minimum of these sums over all reconstructed tracks. We require $C > 1.1$. The distribution or this quantity is shown in Figure 4.16b. C_e is the sum for the identified electron track; we additionally require $C_e > 2.1$.

2. At least six tracks containing ≥ 6 hits in the CD are required.

147 events survive these final cuts. Scanning these shows that only 5 of these would have failed the earlier scanning criteria.

We have used the generator of Berends, Daverveldt, and Kleiss (BDK) to estimate the remaining 2γ background in the sample[77] . This computer program generates events of the type $e^+e^- \to e^+e^- XX$, where XX can be $e^+e^-, \mu^+\mu^-, q\bar{q}$ according to a nearly complete $O(\alpha^4)$ calculation. We have checked this pro-

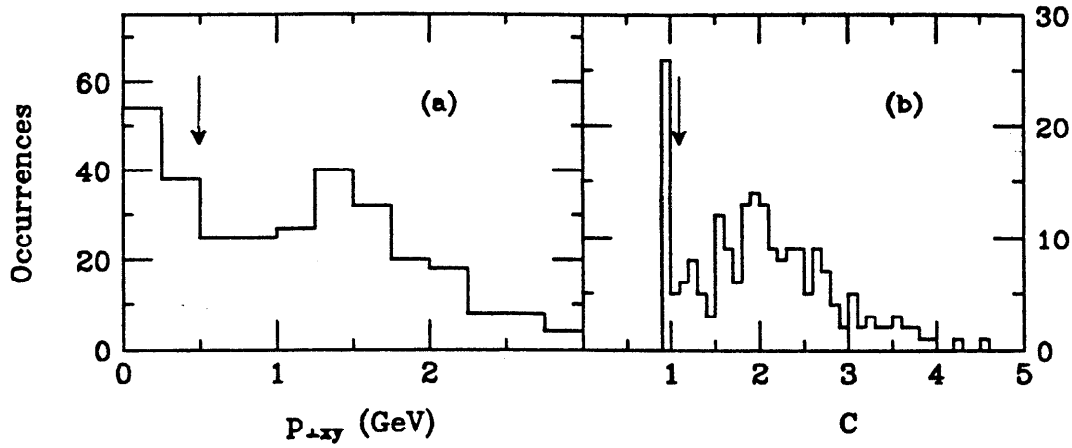

Figure 4.16 Distributions for Two of the 2γ Rejection Cuts. (a) Distribution of $p_{\perp xy}$, the component of $p_\perp$ in the x–y plane. The peak at low $p_{\perp xy}$ results from e-jet type 2γ events. (b) distribution of the isolation variable C. Events with only one track in a hemisphere have $C = 1$. The cut values are shown by the arrows.

gram's calculation for $e^+e^- \to e^+e^-\mu^+\mu^-$, where one electron is scattered into the SC, with the MAC data, and find agreement to better than 25%.[78] We use the Lund hadronization Monte Carlo to evolve quarks into hadrons for the process $e^+e^- \to e^+e^-q\bar{q}$, and ignore resonance phenomena. The mean center of mass energy of the $q\bar{q}$ when one electron scatters into our SC is $\approx 10\,\text{GeV}$, so we expect the Lund approximation to be good. Table 4.5 summarizes the Monte Carlo estimate of the cross section for 2γ to enter the inclusive electron sample.

The effect of the cuts beyond the $p > 2.0\,\text{GeV}$ and $p_\perp > 1.5\,\text{GeV}$ cuts are summarized in Table 4.6. The agreement between the data and Monte Carlo is good, with the exception that the number of data events removed by the $p_{\perp xy} > 0.5\,\text{GeV}$ is slightly greater than the number in the Monte Carlo. This is may be because the 2γ cuts are more efficient in the data, or because there are more 2γ events in the data than in the Monte Carlo. However, the latter possibility is limited by the agreement of data and Monte Carlo for $e^+e^- \to e^+e^-\mu^+\mu^-$, where the data actually contain $18\% \pm 9\%$ *fewer* events than the Monte Carlo predicts. We use the former and latter possibilities to estimate systematic errors on the flavor composition of the data sample.

We estimate that in the final sample of 147 electron tagged events, $59 \pm 5\%$ come from $b\bar{b}$ production, where the error contains contributions from statistics and Monte Carlo statistics. The systematic error in the 2γ background raise

Flavor	σ_0	ϵ_{mh}	ϵ_e	σ_{eff}
$u\bar{u}$	2.98 pb	0.37	0.65	0.69 ± 0.05 pb
$d\bar{d}$	0.29 pb	0.46	0.52	0.070 ± 0.008
$s\bar{s}$	0.19 pb	0.53	0.52	0.052 ± 0.006
$c\bar{c}$	0.41 pb	0.80	0.65	0.21 ± 0.01
total	3.87 pb	0.43	0.61	1.02 ± 0.05

Table 4.5 Two Photon Cross Section to Enter the Inclusive Electron Sample. The first column designates the quark flavor for $e^+e^- \to e^+e^- q\bar{q}$. The second column contains the cross section for at least one electron with momentum > 2 GeV to scatter at an polar angle from the beam having $\cos(\theta) < 0.7$. The second column contains the efficiency for events, after Lund hadronisation and detector simulation, to pass our multihadron identification, and the third column contains the efficiency (in the Monte Carlo) for electron identification. The final column is the effective cross section for these events to enter our inclusive electron sample, prior to thrust axis, thrust, $p_\perp$, etc., cuts.

Cut	Data	Monte Carlo		
	(Events)	Total	1γ	2γ
$p_\perp > 1.5$ GeV, $p > 2.0$ GeV	358	339	204	135
$p_\perp < 3.0$ GeV	299	288	197	91
$p_{\perp xy} > 0.5$ GeV	207	233	170	63
$C > 1.1$	176	209	162	47
$C_e > 2.1$	153	189	153	36
$n_g > 5$	147	182	151	31

Table 4.6 Effect of Additional Cuts in the Electron Sample. Events must pass the thrust axis, thrust, and $p > 2.0$ GeV and $p_\perp > 1.5$ GeV cuts to be counted at the beginning of the table. For 297 pb^{-1} of integrated luminosity. The Monte Carlo estimates have been scaled by the ratio of electron identification efficiencies between data and Monte Carlo for clean events, $\approx 85\%$. The agreement between data and Monte Carlo is excellent with the exception of the cut on $p_{\perp xy}$, which removes some 38 more events in the data than in the Monte Carlo. We use this discrepancy to estimate a systematic error in the composition of the electron sample.

the total error to ±7%. Our Monte Carlo predicts the remaining 41% comes 9.4% from $c\bar{c}$ production, 15% from light quark production, and 17.1% from 2γ production. If we lowered the $p_\perp$ to 1.0 GeV, the we estimate that the resulting sample of 391 events would come $56 \pm 7\%$ from $b\bar{b}$, 17% from $c\bar{c}$, 18% from light quarks, and 9% from 2γ. A smaller fraction of the 1γ events are from $b\bar{b}$ than for the $p_\perp > 1.5$ GeV cut, but the relative fraction of 1γ to 2γ events increases so that the $b\bar{b}$ fraction changes little. Hence the systematic error from the 2γ estimate is less important, but a new systematic error from discrepancies between the data and Monte Carlo for hadron misidentification at lower $p_\perp$ compensate this, making the total error the same.

Chapter 5

B-Lifetime Determination

In this chapter we describe the use of the events enriched in $e^+e^- \rightarrow b\bar{b}$ to measure the B-hadron lifetime. This measurement has several components. First, an estimate of the $b\bar{b}$ production point must be made. In previous MAC B-lifetime measurements, the centroid of the beam spot, determined on a run by run basis, was used. In this analysis, the improved resolution provided by the VC has enabled us to make a better estimate on an event by event basis by combining beam and tracking information. Second, an estimate of the B-hadron flight direction must be made, for which we use the thrust axis, described in the previous chapter. Third, a parameter sensitive to the B-hadron flight path must be measured for some group of tracks in the event. We take this to be the impact parameter, or distance of closest approach, with respect to the $b\bar{b}$ production point of all tracks passing certain quality requirements. We do not require the track to come from an identified lepton, as in previous MAC analyses. The *sign* given the impact parameter is crucial, and in the convention we use *positive* accumulation is indicative of a non-zero lifetime. Negative impact parameters result from errors in tracking, and occasionally from backward decays. Finally, the accumulated parameters must be converted to a lifetime. We use the trimmed mean of the impact parameter distribution for this purpose. The trimmed mean retains the statistical precision claimed by the maximum likelihood method, but is less sensitive to assumptions concerning the shape of the resolution function. We convert the trimmed mean to a lifetime, accounting for the B momentum, background, and charmed particle lifetimes. There are several major points that bear emphasis. The tracking system is precise only in the plane transverse to the beam axis, so we make no use of the z component of

tracks. See Appendix A for a discussion of the MAC tracking convention. We analyze the entire MAC data set, including the data taking prior to the installation of the vertex detector, although some emphasis will be placed on the sample taken with the VC. We will refer to the data taken prior to VC installation as the 'CD' data, and that taken with the VC as 'VC' data. The very large number of inclusive multihadron events will be used as a control sample.

5.1 Beam Position Determination

We determine beam positions on a run by run basis with Bhabha scattering events. The duration of a typical run is 2 hours, and corresponds to one fill of PEP from the LINAC. Usually 100 Bhabha scattering events were used for the determination of the beam centroid, (x_b, y_b, z_b). The co-ordinates in the plane transverse to the beam are found by minimizing

$$\chi^2_b = \sum_{i=1}^{N} \frac{(\delta_{0i} - (y_b \cos(\phi_i) - x_b \sin(\phi_i))^2}{\sigma^2_{\delta i}(\phi_i)}$$

$$\sigma^2_{\delta i}(\phi_i) = \sigma^2_{mi} + \sigma^2_b(\phi_i)$$

$$\frac{1}{\sigma^2_b(\phi_i)} = \frac{\sin^2(\phi_i)}{\sigma^2_x} + \frac{\cos^2(\phi_i)}{\sigma^2_y} + \frac{\sin^2(\phi_i)\cos^2(\phi_i)(\frac{1}{\sigma^2_x} - \frac{1}{\sigma^2_y})^2}{\frac{\cos^2(\phi_i)}{\sigma^2_x} + \frac{\sin^2(\phi_i)}{\sigma^2_y}}.$$

Here $\{\delta_1, \ldots, \delta_N\}$ and $\{\phi_1, \ldots, \phi_N\}$ are the track parameters, from a momentum constrained fit; $\{\sigma_1, \ldots, \sigma_N\}$ are the errors on the δ_0's from the fit covariance matrix, and are typically $300\mu m$ for data taken prior to VC installation, and $50\mu m$ for data with the VC; $\sigma_b(\phi)$ is the spatial standard deviation of the beam as seen from the angle ϕ, which depends on σ_x and σ_y, the spatial standard deviations of the beam in the horizontal and vertical. As we discuss below, these are $350 \pm 5\mu m$ and $55 \pm 5\mu m$. The (x_b, y_b) as a function of run number for the data taken with the vertex chamber are displayed in Figure 5.1. For a typical run, the error in x_b is $40\mu m$ and that in y_b is $20\mu m$.

The impact parameters with respect to (x_b, y_b) for horizontal and vertical tracks are shown in Figure 5.2, and show one determination of σ_x and σ_y. The fitted gaussians have $\sigma_x = 351 \pm 7\mu m$ and $\sigma_y = 63 \pm 2\mu m$, but these include the

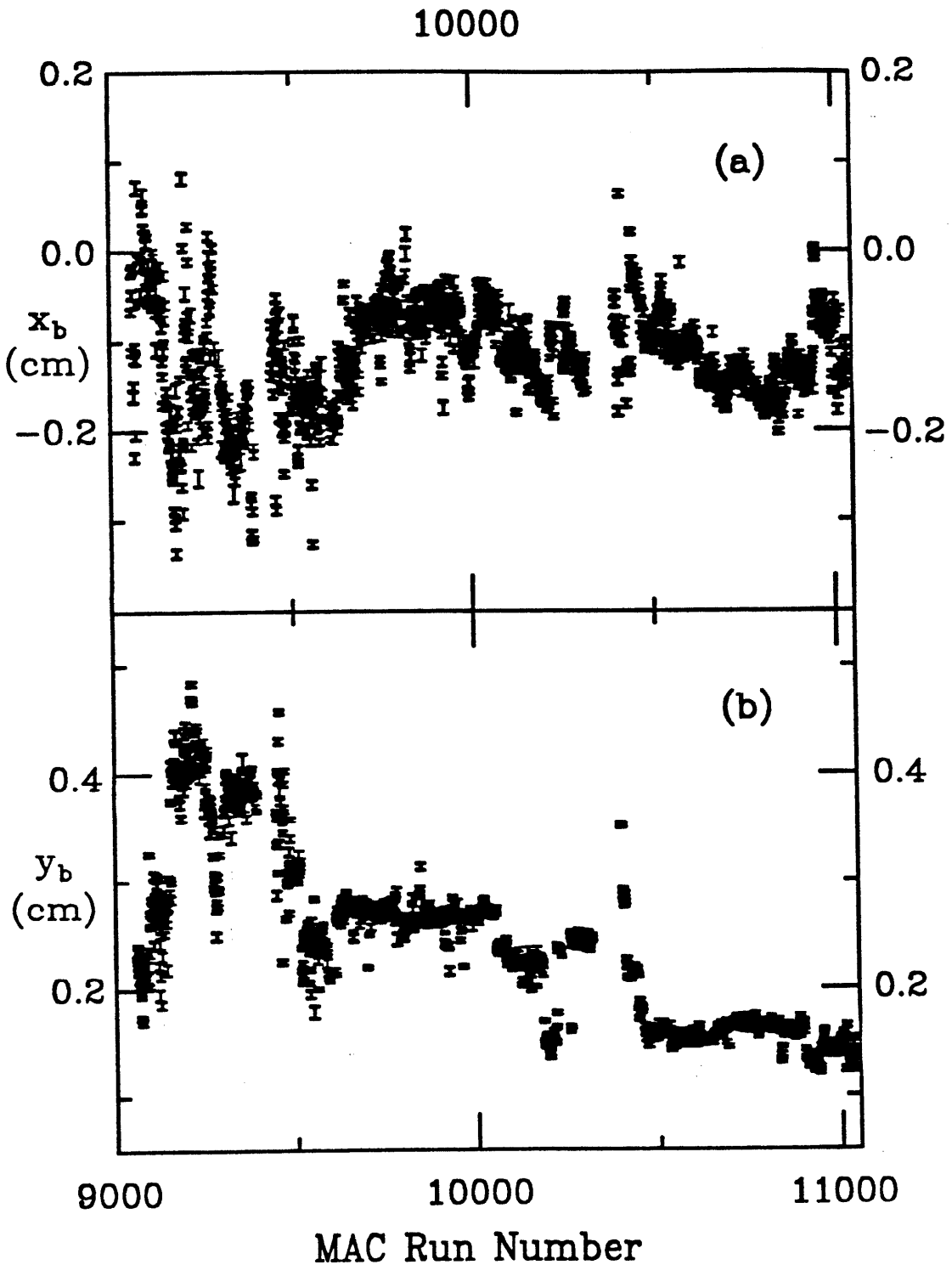

Figure 5.1 Beam Positions for Data Taken with the Vertex Chamber. (a) x_b, horizontal beam position; (b) y_b, vertical. The error bars are typically $40\mu m$ in x_b, and $20\mu m$ in y_b.

smearing due to the resolution of the tracking system, as discussed in Chapter 3. Deconvolution of this smearing, which we determine empirically from the Bhabha miss distribution, leads to the estimates quoted above. These data were taken with the VC installed.

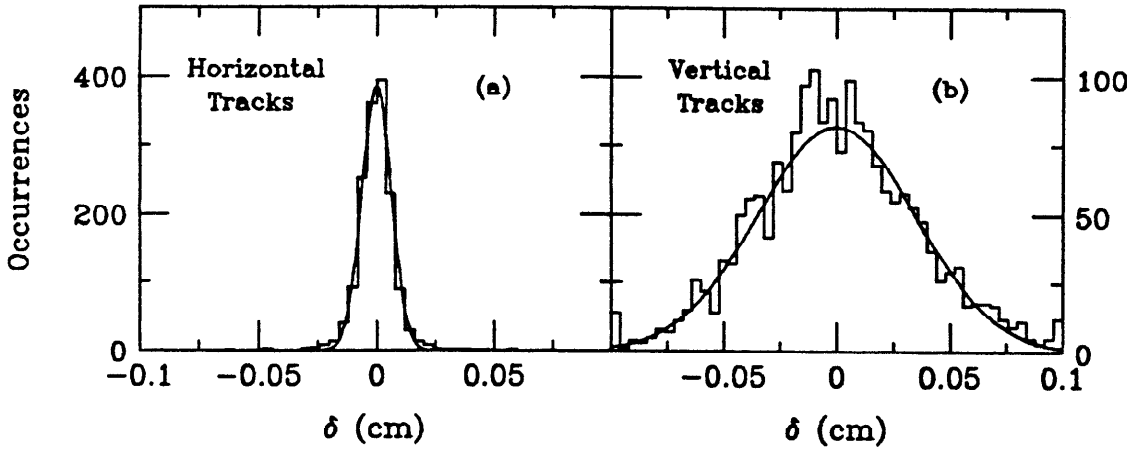

Figure 5.2 Impact Parameters for Horizontal and Vertical Tracks. (a) within ±0.45° of horizontal and (b) within ±0.45° of vertical, from the totality or data taken with the VC. The fitted gaussians have $\sigma_x = 351 \pm 7\mu m$ and $\sigma_y = 63 \pm 2\mu m$ respectively.

The horizontal beam size, σ_x, is must larger than σ_y, because of horizontal oscillations in the beams due to synchrotron radiation. Presumably very detailed machine effects determine σ_y. These sizes include any contribution from instability of the beam during the run, which we have in general found to be small. We exhibit the widths σ_x and σ_y as determined on a run by run basis are shown in Figure 5.3. The statistical error in determining σ_x and σ_y dominates these histograms, but only $\approx 3\%$ of runs have $\sigma_x > 500\mu m$ or $\sigma_y > 200\mu m$.

5.2 Primary Vertex Position in Multihadron Events

The horizontal width of the beam of some $350\mu m$ is somewhat larger than the resolution in impact parameter δ for data in which the VC is present. It is therefore possible to make an estimate of the position where the $e^+e^- \rightarrow q\bar{q}$ occurred, the primary vertex, on an event by event basis in these data. In this section, we describe the procedure we use to make the improved estimate. First, we describe the cuts we apply to obtain the tracks used, then we discuss

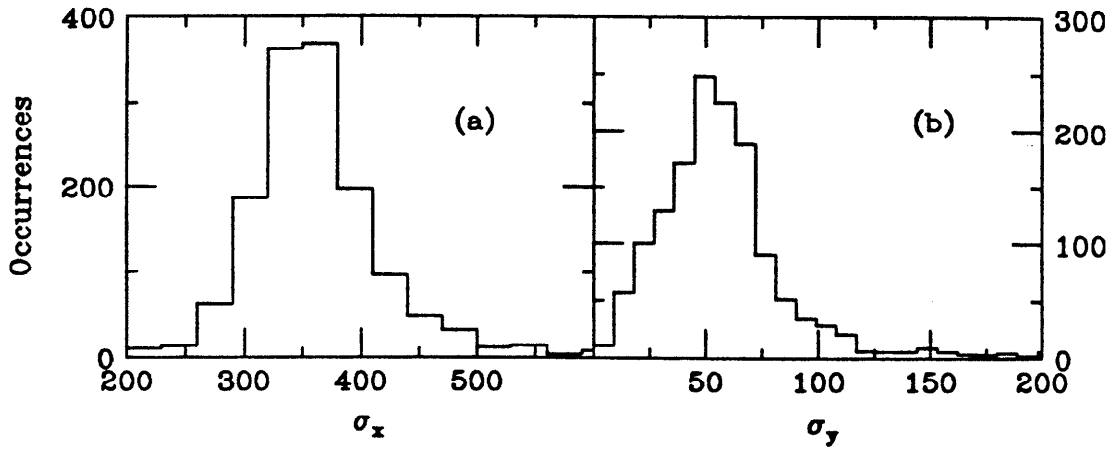

Figure 5.3 Horizontal and Vertical Beam Widths. Determined on a run by run basis, in (a) horizontal and (b) vertical.

our procedure for combining the track and beam information to arrive at the improved estimate.

We use tracks that satisfy the following requirements to improve the estimate of the primary vertex:

1. At least 7 hits in the CD, and in data where the VC is present, at least 3 hits in the VC.
2. Momentum $p > 0.5\,\mathrm{GeV}/c$.
3. Distance of closest approach from the beam centroid $< 1500\mu m$ in data taken with the CD alone, and $< 1000\mu m$ in data taken with the VC in addition.

The first two requirements are 'quality' cuts, in the sense we observe that tracks that fail these cuts tend to contain more false tracks from pattern recognition mistakes. In addition, the momentum cut eliminates tracks with large errors in extrapolation from multiple scattering. Tracks that pass these cuts, which we refer to as 'quality' tracks, as well as two additional cuts to be described in subsequent sections, will be used to measure the B-lifetime. The third requirement is made only for tracks used to improve the primary vertex estimate, and is also intended to reduce the effect of pattern recognition mistakes. In the control sample of inclusive multihadron events, these cuts select 6.10 ± 0.02 tracks per event in the CD data, and 4.33 ± 0.02 in the VC data. The loss of efficiency in the VC data is only slightly due to the requirement of 3 VC

hits; the remainder originates in the use of HRS gas in the CD while the vertex chamber was present. In Figure 5.4, we show the multiplicity distributions for the CD and VC inclusive multihadron samples.

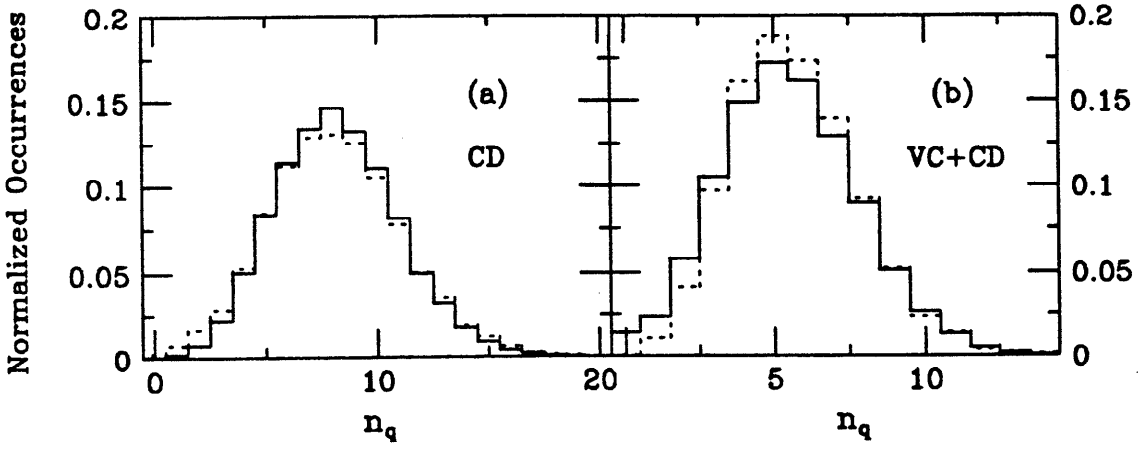

Figure 5.4 Multiplicity of Quality Tracks in Multihadron Events. For (a) CD data and (b) VC data. Solid-data; dots-fast Monte Carlo, where LUND generated particles have tracking parameters smeared, and efficiencies as a function of p, θ, ϕ, and overlap are accounted for.

Given N of the tracks in an event, we find our improved estimate of the primary vertex, (x_v, y_v), by minimizing the simple quadratic loss function, χ^2_v:

$$\chi^2_v = \sum_{i=1}^{N} \frac{(\delta_{0i} - (y_v \cos(\phi_i) - x_v \sin(\phi_i))^2}{\sigma^2_{\delta i}} + \frac{(x_v - x_b)^2}{\sigma^2_x} + \frac{(y_v - y_b)^2}{\sigma^2_y}. \qquad [5.1]$$

Here $\{\delta_1, \ldots, \delta_N\}$ and $\{\phi_1, \ldots, \phi_N\}$ are the track parameters, $\{\sigma_1, \ldots, \sigma_N\}$ are errors on the δ's from the covariance matrix from the track fitting procedure, (x_b, y_b) is the beam position, and (σ_x, σ_y) describe the beam cloud. We refer to (x_v, y_v) as the 'average' vertex.

In general we measure the distance of closest approach of tracks to (x_v, y_v) to measure the B-lifetime, as we will discuss in great detail in Section 5.3. If we were to include the track for which we measure the impact parameter in the computation of (x_v, y_v), the measured impact parameter would be smaller than the true value, because of the influence or 'pull' of the track in [5.1]. In principle this effect could be calibrated, but in practice substantial systematic errors arise

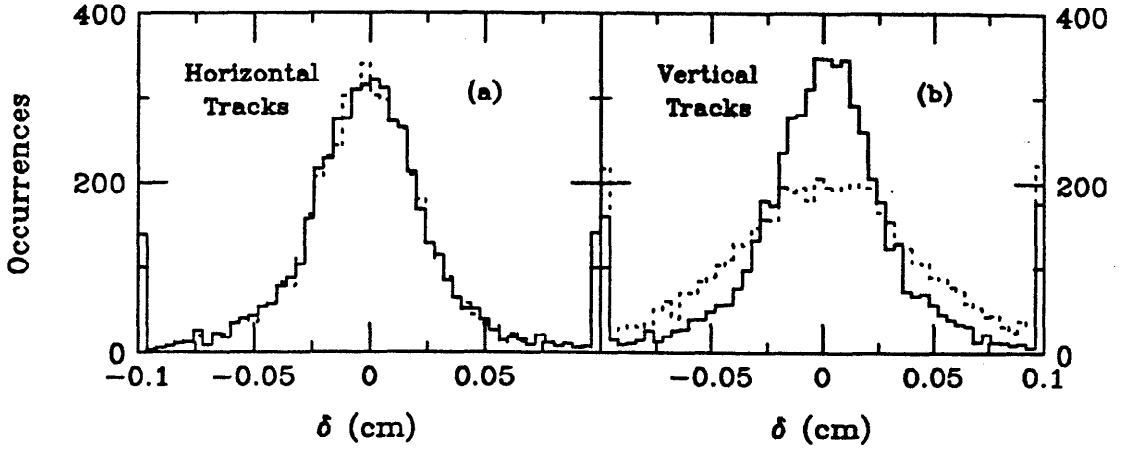

Figure 5.5 Primary Vertex Improvement in Multihadron Events. Impact parameters for tracks within ±1.8° of (a) horizontal and (b) vertical in multihadron events. Solid-with respect to the average vertex; dots-with respect to the beam centroid. Considerable improvement is seen for vertical tracks.

from non-gaussian tails. Therefore, we *exclude* the track for which we measure the impact parameter from [5.1]. Then we cycle through the tracks, defining a new (x_v, y_v) for each, and accumulate the set of impact parameters for the event. We show the effect of this procedure for the inclusive VC multihadron sample in Figure 5.5. Little improvement is observed for horizontal tracks, due to the tiny beam size in y; considerable improvement is seen for vertical tracks.

The improvement displayed in Figure 5.5 is substantial, but one might wonder if the average vertex procedure destroys information or introduces false information about non-zero impact parameters. A more detailed discussion of this point will follow in Section 5.6, but the typical impact parameter is small enough compared to our impact parameter resolution that little bias is introduced.

5.3 Sign Determination

Given helix parameters for a track and the estimated primary vertex, (x_v, y_v), the magnitude of the distance of closest approach, or impact parameter, is easily found. However, the sign of the impact parameter is a matter of convention, and we describe in this section the particular convention we use to measure lifetimes. We also motivate a final cut we require tracks to pass in order to be used to measure the B-lifetime.

We start by discussing the sign convention utilized for all impact parameter

distributions presented so far. This is the convention of Appendix A, and we refer to it as the 'geometric' convention. If one imagines two vectors in the plane transverse to the beam, the first, $\hat{\delta}$, from (x_v, y_v) to the point of closest approach along the track, and the second, $\hat{p}$, pointing in the direction of the particle motion along the track, the geometric sign convention is based on the cross product of these. In the MAC convention, positive $\hat{p} \times \hat{\delta}$ points in the positive z direction, along the e^+ beam. In this case the geometric sign, $s_g = +1$. Systematic biases in the geometry of the drift chambers, or in the various drift chamber constants tend to accumulate with this sign convention.

To define the 'lifetime' sign convention, one needs an estimate of the flight direction of the parent particle that has decayed to the observed daughter track. We use the thrust axis, discussed in Section 4.2, for this estimate. The result of our Monte Carlo study, which agrees very well with cross checks in the data, is that the B direction is reconstructed to 5.6° in the x–y plane by the thrust axis. However, we have no knowledge of which way along the thrust axis the parent travelled. We assume the parent proceeded into the hemisphere that contains the daughter track. This assumption allows us to construct the unit vector $\hat{t}_p$ from the thrust axis but now with the direction ambiguity resolved. We are in error when decay products go in the opposite direction of the parent; for the parent moving at velocity β_p, and if the decay product has velocity $\beta^\star$ in the parent rest frame, and if the decay is isotropic in the rest frame, this occurs $\frac{1}{2}(1 - \beta_p/\beta^\star)$ of the time. This is typically 0.04 of the time for daughters of Bs. We note that although the $\hat{t}_p$ and $\hat{p}$ share the same hemisphere, they do not necessarily share the same semicircle in the x–y plane.

We attribute a positive sign if the track intersects the thrust axis in forward of the primary vertex, where 'forward' is defined by the x–y projection of $\hat{t}_p$. We take this lifetime sign from the sign of the cross product of the x–y projections of $\hat{t}_p$ and $\hat{p}$. Call this sign s_t; then the lifetime sign, $s_l = s_g s_t$. An example appears in Figure 5.6a. Biases may effect the average s_g, but s_t will randomize these, resulting in merely a broader distribution of lifetime impact parameters. It is not easy to conceive of biases in the lifetime sign, and one concludes that the impact parameter method of measuring lifetimes has fundamental robustness.

The dominant source of sign errors is the resolution in extrapolation. This subject will be discussed at some length in Section 5.5. Such sign errors cannot

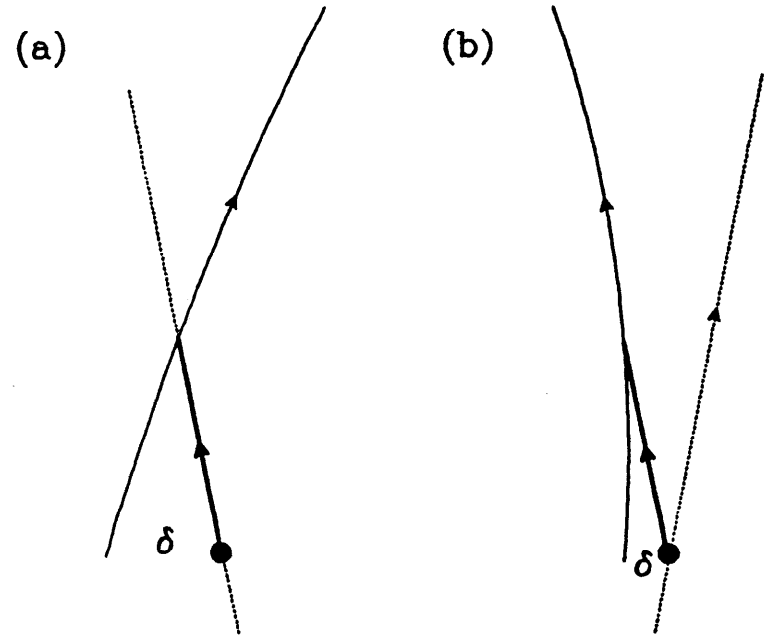

Figure 5.6 The Lifetime Sign Convention. Shown are the primary vertex, the solid circle; the path of the parent particle, the heavy arrow; the thrust axis, dots; the reconstructed trajectory, the impact parameter, δ. (a) shows the case where the situation is properly reconstructed, with the thrust axis matching the parent direction. Here, the sign conventions described in the text lead to a positive geometric sign s_g, where the positive z axis is going out of the page. s_t is positive as well, so $s_l = s_g s_t$ is positive, as it should be. Note that if the track where reflected about the thrust axis, both s_g and s_t change sign. In (b), the thrust axis has been inaccurately reconstructed. s_g is the same as in (a), but s_t has flipped sign, leading to a negative s_l. This phenomenon clearly happens most often for tracks nearly parallel to the thrust axis, which also tend to have small impact parameters.

destroy the average positive impact parameter from a non-zero lifetime, whereas sign errors from thrust axis errors can. Sign errors from thrust misreconstruction tend to occur for tracks close in azimuth to the thrust axis, as examination of Figure 5.6b shows. The error in thrust axis azimuth is approximately $\propto 1/\sin(\theta_t)$, where θ_t is the thrust polar angle; hence, to reduce our sensitivity to our modeling of the thrust axis we require tracks for the B lifetime measurement to be separate in azimuth by at least $0.2/\sin(\theta_t)$ (radians) from the thrust axis. This is approximately 2 standard deviations of the thrust error. Figure 5.7 shows the fraction of wrong signs as a function of this variable. Thrust type sign errors that remain tend to come from backward decays, at least for B parents. We note that tracks from K^0 and Λ decays, as well as those from $\pi^-, K^- \to \mu^- \overline{\nu}$

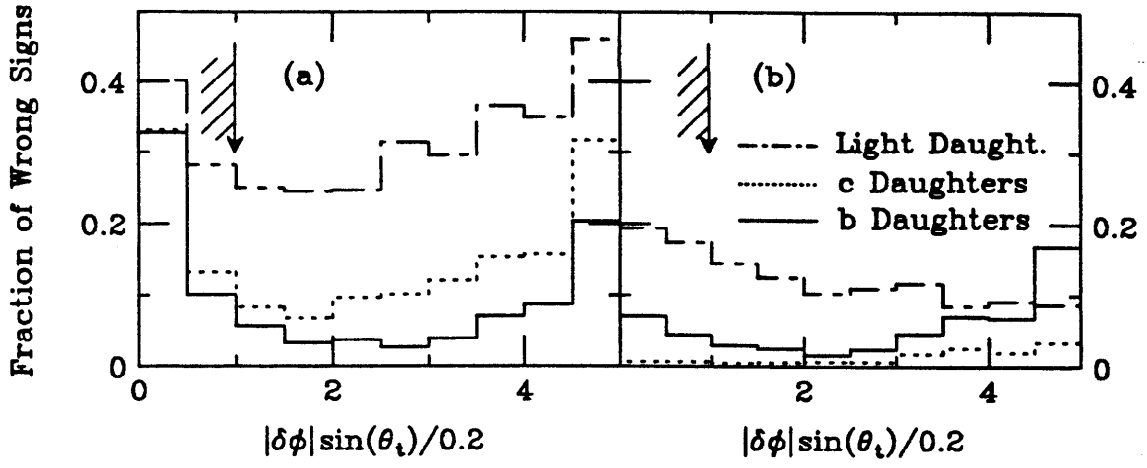

Figure 5.7 Sign Errors as A Function of Azimuth from Thrust Axis. From Monte Carlo simulation. $\delta\phi$ is the difference in azimuth between the thrust axis and the track, θ_t the polar angle of the thrust axis. (a) includes tracking and thrust errors, as well as backward decay errors; (b) shows just the contribution from backward decays. Light daughters are tracks from K^0, Λ, $\pi^\pm$, and $K^\pm$ decays; c daughters from the decay of c-flavored hadrons in $c\bar{c}$ events; b daughters include the cascade $b-c$ decays. Note that light daughters suffer a high sign error rate, while for $\delta\phi\sin(\theta_t)/0.2 > 1$ most sign errors for heavy decays come from backward decays.

tend to be subject to a far higher sign error rate than tracks from heavy quark decays. This is because the light parent's direction is not nearly as correlated with the thrust axis as the heavy parent's. We also note that our cut about the thrust axis increases sensitivity to the B life, because tracks separated from the thrust axis see a larger component of the B flight path.

5.4 Data and Central Value Estimation

In this section we describe the reduction of the lifetime signed impact parameters for the B enriched data samples. We keep the CD and VC samples separate, but combine muon tagged and electron tagged samples in these respective categories. Our objective is to characterize whatever positive displacement the signed impact parameter distribution has. We have chosen the trimmed mean to do so, because of its good statistical efficiency but lack of sensitivity to

the shape of the resolution function. We leave to the next section the conversion of the trimmed mean to a mean B hadron lifetime.

Sample	Events	μ Events	e Events	Quality Tracks	Lifetime Tracks	Passing δ Cut
B enriched CD	439	336	103	2810	1763	1694
Control CD	17425	-	-	106206	64433	59412
B enriched VC	161	117	44	709	463	453
Control VC	8323	-	-	36004	21811	21477

Table 5.1 Events and Tracks in the B-enriched and Control Samples. Quality tracks must have at least 7 hits in the CD, as well as at least 3 in the VC when the VC is present, and momentum $> 0.5\,\mathrm{GeV}/c$. Lifetime tracks in addition differ in azimuth from the thrust axis $> 0.2/\sin(\theta_t)$, where θ_t is the thrust polar angle. Finally, we make a mild cut on the absolute value of the impact parameter, $\delta < 4\,\mathrm{mm}$ in CD data and $\delta < 3\,\mathrm{mm}$ in VC data, to reduce fluctuation from long lived light particles.

Table 5.1 summarizes the numbers of events and tracks in the B-enriched data sample. In the CD sample, 2810 tracks survive the quality cuts enumerated in Section 5.2. Of these, 1763 are sufficiently separated in azimuth from the thrust axis to pass the cut discussed in the previous section. We refer to this subset as 'lifetime' tracks. In the VC sample, there are 709 quality tracks, and 463 of these are lifetime tracks. Event selection is the same for the control sample as for the B-enriched sample, except that no lepton tag is required for the track with $p > 2\,\mathrm{GeV}/c$ and $p_\perp > 1.5\,\mathrm{GeV}/c$. We plot the signed impact parameter distributions for the CD and VC samples of lifetime tracks in Figures 5.8a and d, respectively. The CD distribution shows a clear positive shift. The VC distribution is approximately 4 times narrower than the CD sample, due to the superior vertex resolution, and shows not only a clear positive shift but an exponential-like tail. Also shown in Figure 5.8 are the impact parameter distributions of lepton tracks for the respective samples, as well as the distributions for the control samples of tracks from untagged multihadrons. The control samples show markedly less positive shift.

We use the data in Figures 5.8a and d, the signed impact parameters from all lifetime tracks in B-enriched events to obtain the mean B-hadron lifetime.

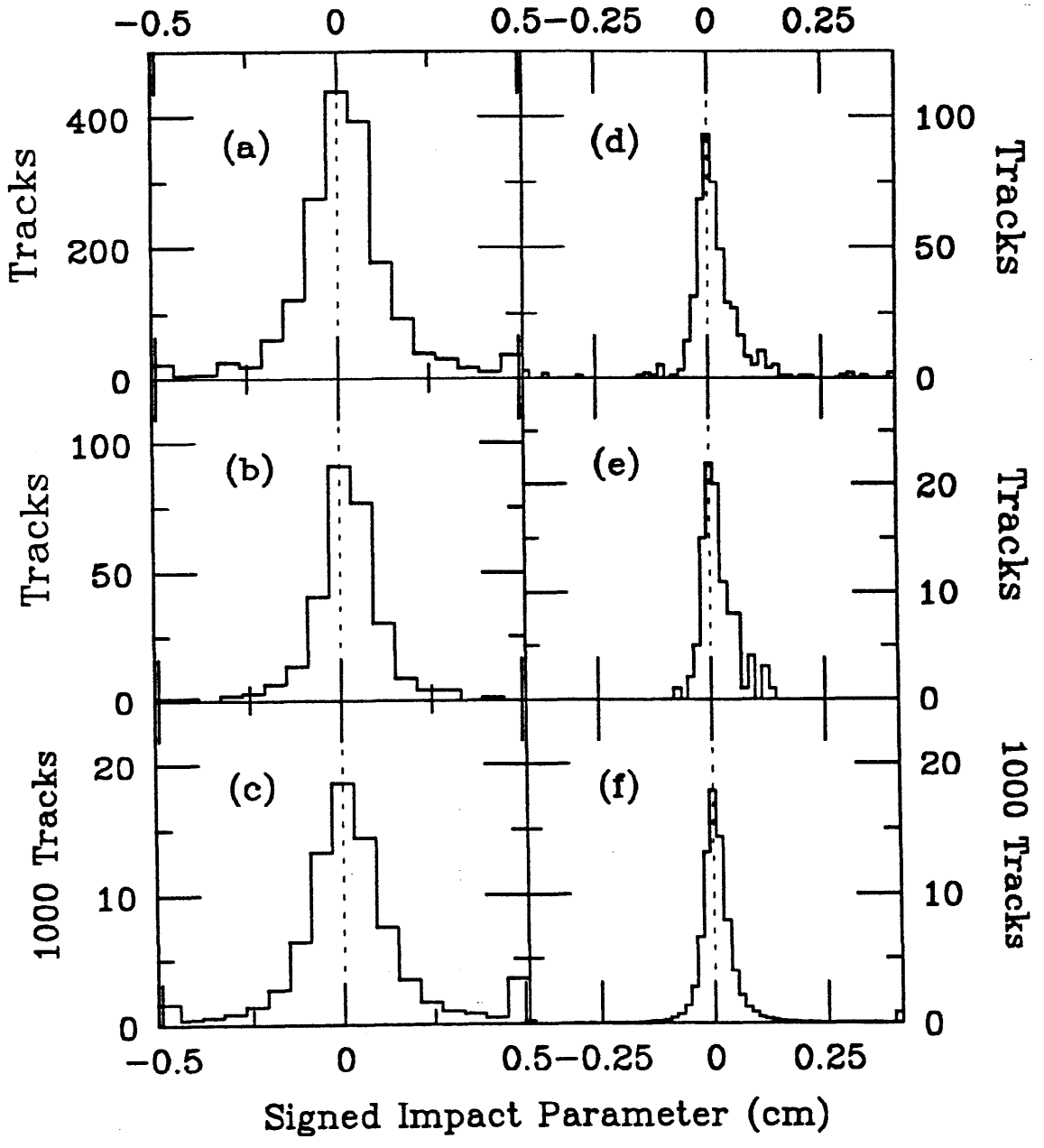

Figure 5.8 Signed Impact Parameter Distributions. (a) Lifetime tracks in the B-enriched CD sample. (b) Lepton (μ and e) tracks in the B-enriched CD sample. (c) Tracks in a control sample of untagged CD multihadrons. (d) Lifetime tracks in the B-enriched VC sample. (e) Lepton (μ ad e) tracks in the B-enriched VC sample. (f) Tracks in a control sample of untagged VC multihadrons.

In this way we obtain a higher statistic than the previous MAC measurement, which used only the impact parameters of the leptons, in particular those of Figure 5.8b. A higher fraction of leptons tracks actually come from the B or subsequent decay than all lifetime tracks. This results in a smaller possible *systematic* error if we employed just the lepton tracks. However, leptons constitute only $\approx \frac{1}{4}$ of all lifetime tracks. We would pay for the smaller systematic error with a larger statistical error. Further, if the B lifetime is a truly non-zero, a positive displacement should be evident in non-lepton tracks. Finally, the non-lepton tracks can have a momentum as low as $0.5\,\mathrm{GeV}/c$, while leptons are required to have momentum $> 2.0\,\mathrm{GeV}/c$. Kinematics therefore force the non-lepton tracks from B-decay to be somewhat more sensitive to the B-lifetime than the lepton tracks.

The use of all tracks, as opposed to just lepton tracks, introduces a higher fraction of tracks from long lived light species, such as K^0_ss and Λs. Tracks from these species, which can have impact parameters up to several centimeters, are picked up somewhat sporadically by our pattern recognition. To reduce fluctuations from this phenomena, we impose the final cut for tracks to be used to obtain the B-lifetime: $|\delta| < 4\,\mathrm{mm}$ for CD data, and $|\delta| < 3\,\mathrm{mm}$ for VC data. In the CD B-enriched sample, 1694 tracks survive this cut, and 453 do so in the VC data.

We reduce the surviving data in Figures 5.8a and d to two numbers, namely, a mean B-hadron lifetime, and a statistical error on that lifetime. 'Mean' in this context implies not just the average lifetime as opposed to the another measure of lifetime, for example the half-life, but also implies the average over all hadron species produced at PEP that contain b-quarks. We have considered two methods of reducing the data: 1) taking an estimate of the central value of the signed impact parameter distributions, then converting this estimate into a lifetime and 2) performing a maximum likelihood fit to the signed impact parameter distribution.[79] In choosing between these, our concern was uncertainty in the exact tracking resolution function. Figure 5.8 represents the convolution of an 'exact' impact parameter distribution with the tracking resolution function of our drift chambers. If we had complete knowledge of this resolution function, a maximum likelihood fit would, at least in the limit of large statistics, achieve the smallest statistical error possible. However, uncertainty in the shape of the

resolution function can produce quite substantial systematic errors in the lifetime found from the fit. In the typical case, the width of the resolution function is underestimated, and a bias toward longer lifetimes is produced.[80] In contrast, central estimators such as the mean, median, or our preferred estimator, the trimmed mean, are more immune to biases from imperfect knowledge of the resolution function. Further, a trimmed mean usually has high efficiency, meaning its statistical error is nearly as small as the maximum likelihood estimator. Finally, we appreciate the directness and simplicity of central estimators.

To contrast several aspects of central estimators and the maximum likelihood fit, consider the case of samples drawn from a parent distribution obtained from the convolution of an exponential, $e^{-x/\lambda}$, with a gaussian, $e^{-x^2/2\sigma^2}$. This problem is similar to the B-lifetime estimation, where the exponential is similar to the true distribution of signed impact parameters, and the gaussian to the smearing caused by non-zero tracking resolution. The mean is an *efficient* estimator of λ in the limiting cases $\sigma \gg \lambda$ and $\sigma \ll \lambda$, meaning the statistical error from no estimator, including a maximum likelihood fit, is smaller than that of the mean. This result obtains by comparison the variance of the mean with the 'information' of the two limiting distributions. In the regime $\sigma \sim \lambda$, the mean is not efficient. In Figure 5.9 we show the ratio of the lower bound on the statistical error from the information, to the standard deviation of the mean, as a function of λ/σ. One sees that at worst, for $\lambda \sim \sigma/2$, the lower bound is only 11% below the standard deviation of the mean. We conclude that this is the most a maximum likelihood fit could gain in estimating λ. However, the regime $\lambda \sim \sigma$ is also precisely where the most sensitive to knowledge of σ in the maximum likelihood fit; the correlation between λ and σ is nearly unit. In contrast, the mean does not suffer this disadvantage. Hence, the smaller statistical error in λ provided by the maximum likelihood fit must be paid back with a systematic error from ignorance of σ.

In practice, very few experimental resolution functions are truly gaussian, and most have some sort of non-exponential tail. These tails compromise the statistical efficiency of the mean. In fact, for the Cauchy distribution, $f(x,\sigma) = 1/\sigma\pi(1 + (x/\sigma)^2)$, the variance of the mean is *infinite*. Therefore, we have explored the use of other central estimators that retain more statistical efficiency in the presence of tails than the mean. In the previous MAC analysis of the B-

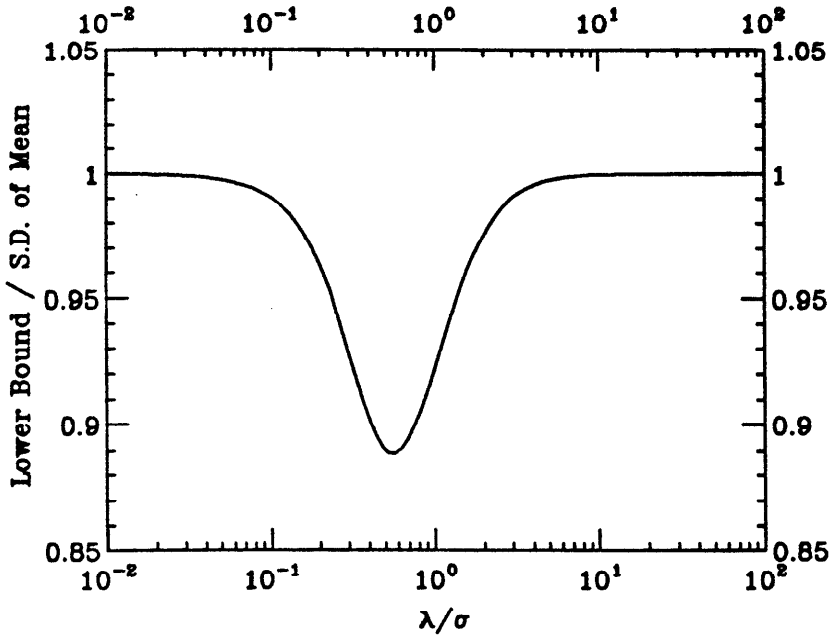

Figure 5.9 **Efficiency of Mean for the Convolution of a Gaussian with an Exponential. The lower bound is computed from $I_\lambda^{-1/2}$, where the information $I_\lambda = \int(\partial \ln f(x,\lambda,\sigma)/\partial\lambda)^2 f(x,\lambda,\sigma)dx$, where $f(x,\lambda,\sigma)$ is the convolution of the exponential characterised by λ and the gaussian by σ. A maximum likelihood fit asymptotically approaches the lower bound for large statistics, but only improves by 11% at best on the mean.**

lifetime, the median was used. For N samples drawn from a parent distribution $f(x)$ with median x_m, the standard deviation of the median s_m is:

$$s_m = \frac{1}{2\sqrt{N} f(x_m)} \qquad [5.2]$$

For example, for a Cauchy distribution, s_m is within 10% of the lower bound computed from the information. Before the introduction of the vertex chamber, the tracking resolution is fairly large compared to the typical impact parameter from a B decay, and the median provides a good estimator of the non-zero displacement of Figure 5.8b. However, since introduction of the VC, the tracking resolution is comparable to the typical impact parameter. As is discussed in the Section 5.5, a number of tracks from a parent distribution with zero impact parameter are present in Figure 5.8a and d. The presence of these tracks makes the median insensitive to the tracks with non-zero impact parameter, if the resolution is good. One can imagine the limiting case of zero tracking resolution:

if greater that 50% of the tracks have zero impact parameter, the median would be zero, regardless of the non-zero impact parameters of the remainder of the distribution. So, we use a central estimator that is in a sense 'in between' the mean and median, namely the trimmed mean.

Given a set of measurements $\{x_1,\ldots,x_N\}$, the trimmed mean $\bar{x}_t$ for trim factor t, $0.0 < t < 1.0$, is found by

1. Sorting the measurements $\{x_1,\ldots,x_N\}$.
2. Eliminating the smallest $t/2$ and largest $t/2$ measurements. Call the smallest remaining measurement x_L and the largest x_R.
3. Taking the mean of the remaining $N \times (1-t)$ measurements.

Note that the limiting cases $t = 0$ and $t = 1$ correspond to the mean and median, respectively. Note also that although the smallest and largest $t/2$ measurements are eliminated from last step of the computation of the mean, they still have influence in the location of x_L and x_R, so have influence on the value of $\bar{x}_t$. Calculation of the standard deviation of the trimmed mean can proceed from trinomial statistics, or Poisson statistics. Formulas extent in the literature are in general for symmetric parent distributions, that is, when $x'_L \equiv \bar{x}_t - x_L = x_R - \bar{x}_t \equiv x'_R$.[81] For the distributions of Figure 5.8, especially those for data taken with the VC, this is not strictly true, so we have derived the result for this case,

$$s_{\bar{x}_t} = \left\{ \frac{1}{N(1-t)} \left[s^2 + \frac{t}{4} \left(\frac{(x'_R - x'_L)^2}{1-t} + (x'_R + x'_L)^2 \right) \right] \right\}^{1/2} \qquad [5.3]$$

$$s^2 = \frac{1}{N} \sum_{i=Nt/2}^{N(1-t)/2} (x_i - \bar{x}_t)^2$$

The term containing $x'_R + x'_L$ enters only for asymmetric distributions. Note that for $t = 0$, the second term in the square brackets in [5.3] vanishes, and this is just the error on the mean. In the limit $t \to 1$, the first term in the curved brackets contributes $((x'_R - x'_L)/(1-t))^2 \to 1/f^2(x_m)$, and the other terms vanish, giving the result for the error on the median.

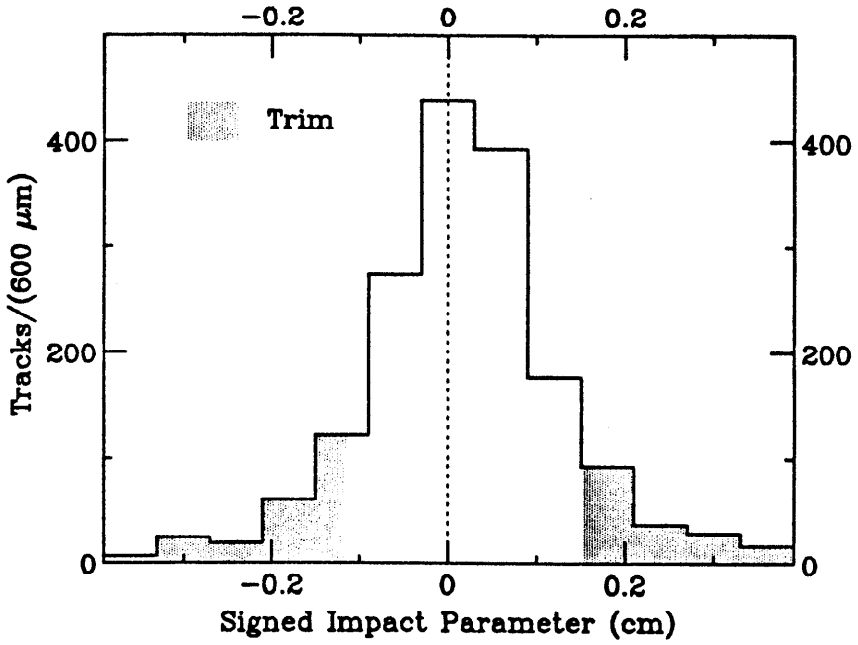

Figure 5.10 Signed Impact Parameter Distribution for CD B-Enriched Data, Showing Trim. The trim factor, $t = 0.2$. The shaded region is trimmed; the trimmed mean is $162.1 \pm 24.9\mu m$. $x_L = -1147\mu m$, $x_R = 1530\mu m$, $s = 627\mu m$. The terms from the x'_L and x'_R contribute $669\mu m$, to be added in quadrature to s, then divided by $\sqrt{.8 \times 1694}$ to get the statistical error of $24.9\mu m$.

The literature indicates that $t \approx 0.7$ gives a standard deviation within $\sim 10\%$ of the lower bound from the information for a variety of parent distributions.[81] For our distributions, such a hard trim degrades sensitivity to the tracks with non-zero impact parameters, and ultimately to the B-hadron lifetime. Studies with our Monte Carlo show good statistical sensitivity to the lifetime for trims from $0.05 - 0.5$; in this range, there is no sharp maximum in sensitivity. We choose a trim of 0.2. The locations of this trim on the distributions of Figure 5.8a and d are shown in Figures 5.10 and 5.11. In Table 5.2, we give the trimmed means for the B-enriched samples and the control samples. For both CD and VC data samples, there are statistically very significant differences between the B enriched samples and the control samples. In the next section we take up the conversion of these numbers and errors to a B lifetime and error.

Before doing so, we would like to comment on weighting schemes. We have chosen equal weighting: all points in Figures 5.8a and d, that pass the cut on absolute value of impact parameter, are weighted equally. We have some knowledge of the error on each impact parameter from the covariance matrix

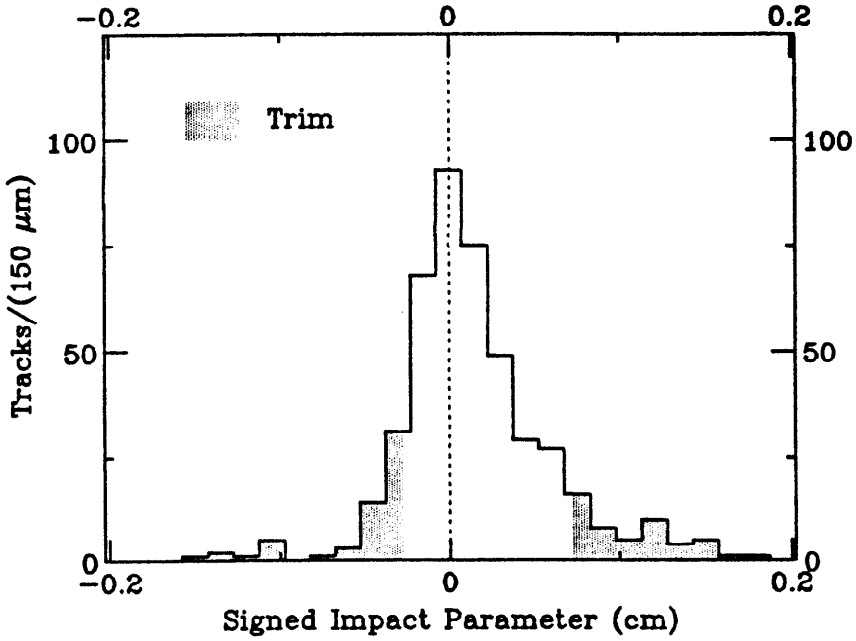

Figure 5.11 Signed Impact Parameter Distribution for VC B-Enriched Data, Showing Trim. The trim factor, $t = 0.2$. The shaded region is trimmed; the trimmed mean is $130.2 \pm 18.5\mu m$. $x_L = -275\mu m$, $x_R = 726\mu m$, $s = 244\mu m$. Terms from the x'_L and x'_R contribute $250\mu m$, to be added in quadrature to s, then divided by $\sqrt{.8 \times 453}$ to get the statistical error of $18.5\mu m$.

Sample	Tracks	Trimmed Mean
B enriched CD	1694	$162.1 \pm 24.9\mu m$
Control CD	59412	$71.2 \pm 4.3\mu m$
B enriched VC	453	$130.2 \pm 18.5\mu m$
Control VC	21477	$29.2 \pm 2.0\mu m$

Table 5.2 Trimmed Means. For the B enriched and untagged multihadron samples. In both the VC and CD data, there is a very significant difference between the B-enriched and control samples.

of the track fit, however: it might seem that by using this error in a $1/\sigma^2$ type weighting might give better statistical efficiency. In truth, this is not entirely clear: a major contribution to the computed impact parameter error comes from multiple coulomb scattering, which is larger for low momentum tracks. Thus low momentum tracks would be de-weighted; but as discussed previously, these

tracks tend to have higher sensitivity to the B-lifetime. Instead of separately accounting for both effects, we choose equal weighting.

5.5 Conversion of Impact Parameter to Lifetime

There are primarily four factors that influence the conversion of the impact parameters to an average B-hadron lifetime:

1. The momenta of the B's in the lab, and the momenta of the B descendants in the B rest frame.
2. The composition of tracks in the B enriched sample.
3. The tracking resolution function.
4. Systematic bias from pattern recognition and fitting.

We account for the first two factors through the use of the Lund Monte Carlo, described earlier, which models b-quark hadronization and subsequent B-hadron decay. We will make some qualitative comments about these factors. We have studied the tracking resolution function, and use it in a fast, non-simulation Monte Carlo of the detector effect on the Lund output. We compare the results from this fast Monte Carlo to results from our full detector simulation, and thus are able to test for systematic biases: we find no such biases in the VC data, and a slight bias in the CD bias. Taking this into account, we are able to construct the relationship between the trimmed mean impact parameter and the B-hadron lifetime.

The B-hadron retains about 80% of the beam energy at PEP, or about 12 GeV, or a Lorentz factor $\gamma_p \approx 2.4$. For a mean lifetime $\tau_b = 1ps$, $c\tau_b \approx 300\mu m$, and in the lab frame $\gamma_p c\tau \approx 740\mu m$. Decay products emitted in the rest frame of the B at angle θ^* with respect to the B lab direction and speed β^* appear in the lab at θ_l given by

$$\tan(\theta_l) = \frac{\sin(\theta^*)}{\gamma_p(\cos(\theta^*) + \beta_p/\beta^*)} \qquad [5.4]$$

The magnitude of the impact parameter $\gamma_p c\tau \sin(\theta_l)$ tends to a constant for $\gamma_p \to \infty$, since $\sin(\theta_l) \sim 1/\gamma_p$. All impact parameters are positive for $\beta^* < \beta_p$; negative impact parameters become possible for $\beta^* > \beta_p$ from backward decays.

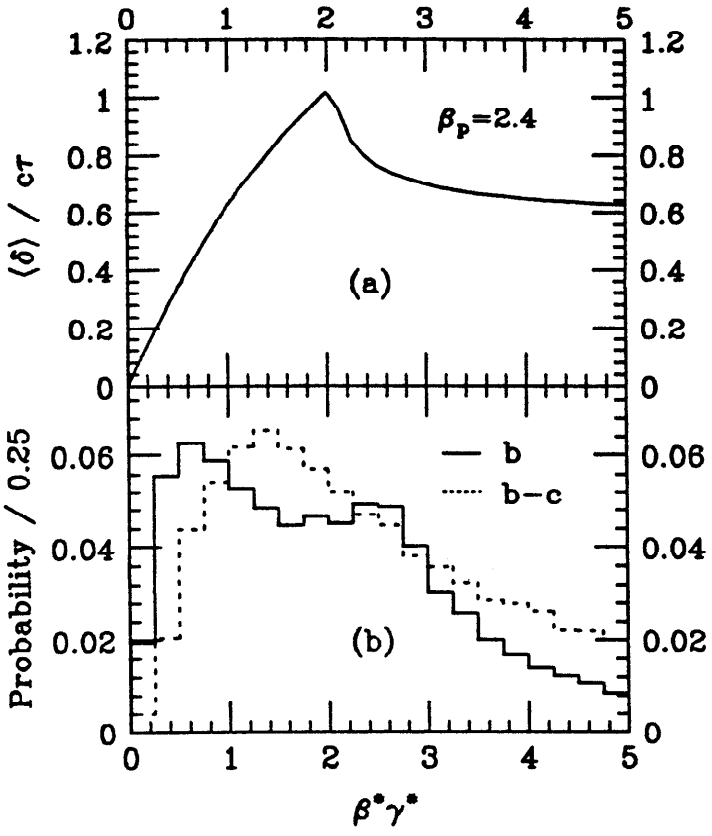

Figure 5.12 Kinematical Effects on the Average Impact Parameter. (a) impact parameter averaged over θ_l. Negative impact parameters occur for $\beta^* > \beta_p$, causing the decrease in the average impact parameter. (b) spectra of reduced momenta in the B rest frame of B decay products. The b products have a long positive tail, not shown, from leptons. No cuts, such as $p > 0.5\,\mathrm{GeV}/c$ have been applied.

In Figure 5.12a we plot the impact parameter, averaged over θ_l, as a function of $\beta^*\gamma^*$ for the PEP conditions. In Figure 5.12b, we plot the $\beta^*\gamma^*$ spectra from the Lund Monte Carlo for direct B stable daughters, and cascade $b-c$ daughters as well. One sees that $\langle\delta\rangle \approx 0.6c\tau \approx 180\mu m$ is to be expected for decay products, and a 1 ps lifetime.

We do not measure γ_p on an event by event basis, and in fact, there is substantial uncertainty in the mean value of γ_p. This causes systematic error in the B-lifetime value, but the error for this all tracks analysis is different than that for analyses of the lepton tracks exclusively. Leptons usually have $\beta^* > \beta_p$ at PEP, so, for a given B lifetime, their average impact parameter increases as β_p increases, because less backward decays are produced. Hadrons from B

decay are significantly softer than leptons, and in many cases have $\beta^* < \beta_p$, where the mean impact parameter decreases as β_p increases. Therefore hadrons are less sensitive to β_p than leptons, since some cancellation of increases for $\beta^* > \beta_p$ against decreases for $\beta^* < \beta_p$ occurs. However, a systematic error from uncertainty in β_p of a different origin arises for this all tracks analysis, namely the uncertainty in the fraction of primary tracks in $b\bar{b}$ events.

In Chapter 4 we discussed the flavor composition of the B-enriched event sample. However, to convert the impact parameter to a B-lifetime, we need *track* content of the sample. We use the Lund Monte Carlo, processed through our detector simulation, to do so. The results from this simulation are summarized in Table 5.3.

Category	$b\bar{b}$	$c\bar{c}$	$u\bar{u}$, $d\bar{d}$, $s\bar{s}$	all
Events	0.6	0.2	0.2	1.0
Tracks: all	0.68	0.17	0.15	1.0
primary	0.21	0.11	0.15	0.47
c	0.0	0.06	0.0	0.06
b	0.23	0.0	0.0	0.23
$b-c$	0.22	0.0	0.0	0.22
K_s^0, etc.	0.02	0.005	0.005	0.03

Table 5.3 Track Content of B Enriched Sample Fraction of total events and tracks in various categories is listed. The event fractions are for the mix of muon and electron B-enriched samples: the 2γ component of the electron sample has been placed with the light quarks. c refers to the fraction of tracks from charmed hadron decays, b from B hadron decays, and $b-c$ from bottom-charm cascade.

We do not have as strong a cross check in the data of the Monte Carlo for the track fractions as we have from the lepton $p_\perp$ spectra for the event fractions. Nevertheless, we have some checks. The multiplicity of lifetime tracks in untagged multihadrons is 3.13 ± 0.01 for CD data and 2.17 ± 0.01 for VC data, while the result of the Lund Monte Carlo and detector simulation for untagged multihadrons is 3.17 ± 0.01 for CD and 2.17 ± 0.01 for VC. Admittedly, some

tuning of the parameters of the Lund Monte Carlo and the detector simulation was performed to achieve this agreement, although the tuning was not performed on the number of lifetime tracks. However, for the B-enriched samples, there are 3.86 ± 0.02 lifetime tracks per event in the CD sample, and 2.8 ± 0.1 in the VC sample, while the Monte Carlo predicts 3.80 ± 0.04 and 2.87 ± 0.03, in excellent agreement that is not particularly the result of tuning. A check on the contribution of tracks from light, long lived sources, such as K^0_ss and Λs, comes from the fraction of tracks removed by the impact parameter cut of 4 mm in CD data and 3 mm in VC data. In the CD data, 0.039 ± 0.005 of the B-enriched tracks are removed by this cut, while the Monte Carlo predicts 0.032 ± 0.002; for the VC data, 0.022 ± 0.007 are removed, while the Monte Carlo predicts 0.012 ± 0.001. There is agreement within errors.

Our Monte Carlo assumptions regarding charmed particle species content and lifetimes are summarized in Table 5.4

Species	Continuum	B-decay	Lifetime
D^0	0.50	0.59	0.44 ps
D^+	0.33	0.22	1.06 ps
D_s	0.12	0.13	0.48 ps
Λ_c, etc.	0.05	0.06	0.20 ps
mean lifetime	0.64 ps	0.57 ps	-

Table 5.4 Charmed Particle Summary. From our implementation of the Lund Monte Carlo. The continuum column constrain the assumed fractions of the various species, while the B-decay column contains the number of each species *per* B. The lifetimes are from the recent results of the E-691 experiment.[82]

We have used our large sample of untagged multihadrons to study our tracking resolution function. To do so, we fit the negative side of the distribution of signed impact parameters with respect to the average vertex to a Student's t distribution:

$$f(x) \propto (1 + (x/s)^2/\nu)^{\frac{-(\nu+1)}{2}} \qquad [5.5]$$

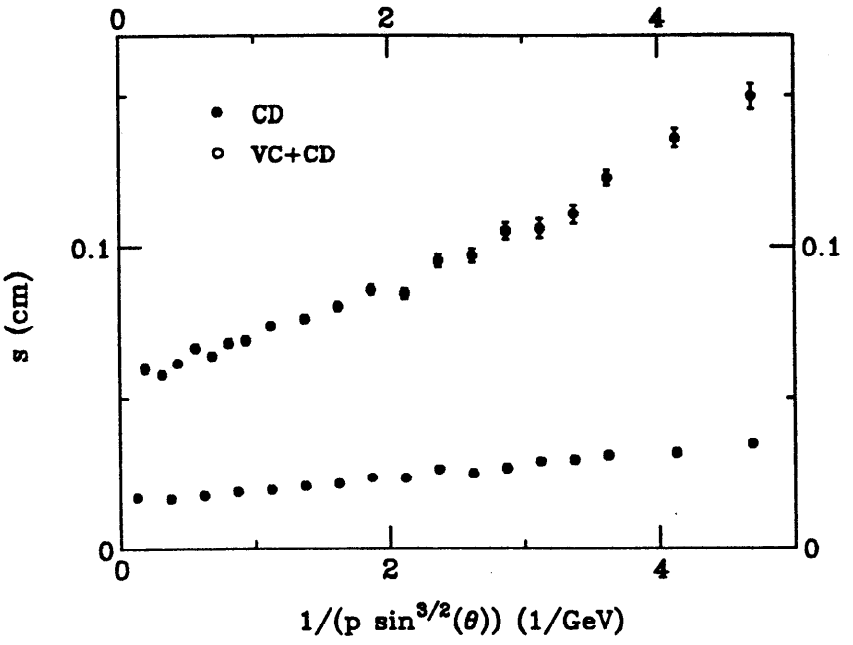

Figure 5.13 Width Parameter of Tracking Resolution Function. From the fit to a Student's t distribution, as described in the text, of impact parameters with respect to the average vertex.

The parameter s describes the width of the distribution, and ν the tails. We perform the fit as a function of $1/p\sin^{3/2}(\theta)$, to include the effect of multiple scattering. The resulting s as a function of this variable appears in Figure 5.13. From these plots, we find for the CD data, for $\rho = 1/p\sin^{3/2}(\theta)$ GeV/c^{-1},

$$s = 565 + 158\rho + 338\rho^2 \ \mu m$$

and in the VC data,

$$s = 150 + 44\rho \ \mu m$$

We find that the tail parameter ν is momentum independent, and is 2.0 for the CD data and 3.5 for the VC.

We use this tracking resolution function in a fast, non-simulation Monte Carlo. In this Monte Carlo, we take the momentum vectors output by Lund and with a few simple parameters model the effect of the MAC tracking system. We include the acceptance of the tracking system, loss of efficiency for overlapping tracks, momentum resolution, and smearing in the impact parameter from the

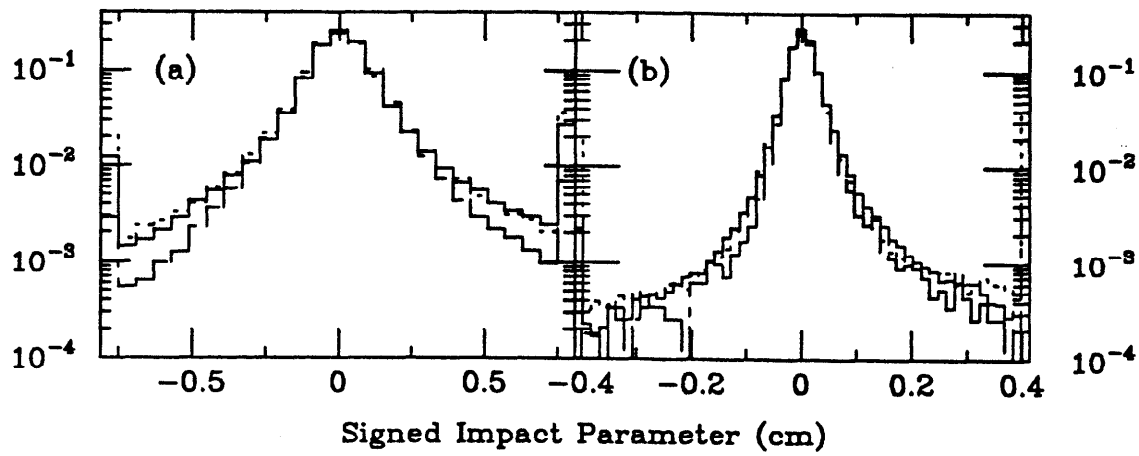

Figure 5.14 Comparison of Impact Parameter Distributions for Multihadron Data, Full Monte Carlo, and Fast Monte Carlo. *Solid* - data; *Dotdash* - Full Monte Carlo; *Dots* Fast Monte Carlo. Both the full and fast Monte Carlos use the output of Lund event generation. Hit generation in the drift chambers, pattern recognition, and tracking are done for the full Monte Carlo, while a fast characterization of the tracking system is done in the fast Monte Carlo.

tracking resolution function. We actually utilize a large database of events that have had their shower development in the MAC calorimeters already modeled; in this way we obtain the calorimetric thrust axis. In Figure 5.14, we compare the signed impact parameter distributions for multihadrons from the control sample, multihadrons modeled with the full detector simulation, and those from the fast Monte Carlo. We use this fast Monte Carlo to explore sensitivities to various parameters that would be take a large amount of computer time to examine with the detector simulation. For example, with the fast Monte Carlo we have found that the trimmed mean impact parameter for a given B-hadron lifetime is insensitive to the losses of efficiency do to overlapping tracks.

We generate calibration curves for the trimmed mean signed impact parameter as a function of the input average B-Hadron lifetime with both the full detector simulation and the fast Monte Carlo. The results are given in Figure 5.15. For the VC data, agreement between full and fast Monte Carlos is very good. We conclude that the pattern recognition, track fitting, and average vertex procedure is unbiased at the level of $5\mu m$ for these data. For the CD data, the full reconstruction appears to add a slight bias to the mean impact parameter of $\approx 23\mu m$. This is to be compared with a typical resolution in impact parameter in CD data of $800\mu m$.

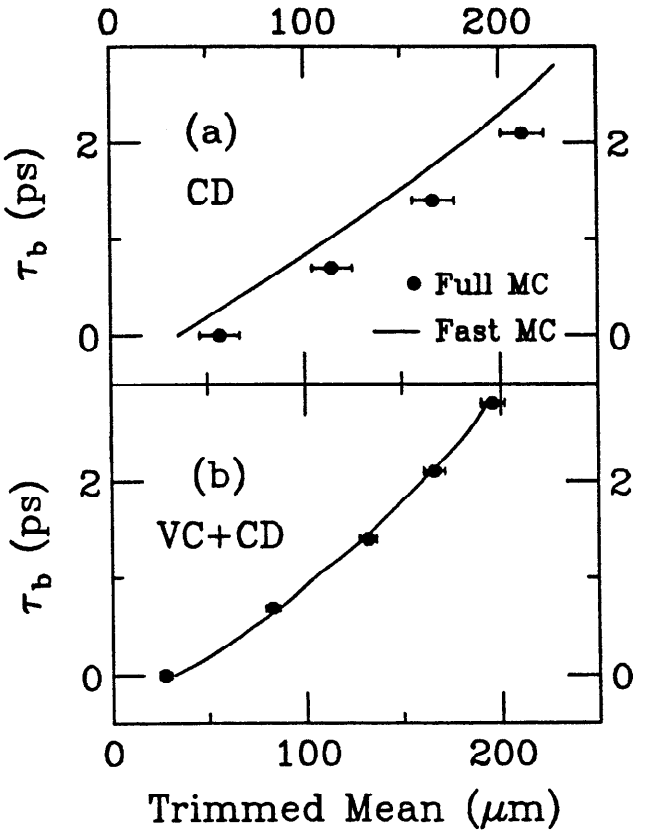

Figure 5.15 Calibration of Trimmed Mean Impact Parameter. (a) for CD data. A slight bias is evident in the full Monte Carlo. (b) for VC data. No bias is evident.

We have undertaken a number of studies of this bias, with negative results. It clearly appears in the data in the CD multihadron control sample, in the form of the difference between the trimmed mean for the CD and VC samples in Table 5.2. Comparison of CD and VC trimmed means for a variety of samples leads to Table 5.5. We conclude that its origin is in our pattern recognition or track fitting algorithm. It is not caused by the dense environment of multihadrons, since it is present for $1-1$ τs. However, we have set the resolution with which hits are generated in our detector simulation to a very small value, and the bias vanishes, so it seems to scale with resolution. We note it is only 5% of the impact parameter resolution in the CD data. We accept its presence, and account for it in our calibration curve of B-hadron lifetime versus trimmed mean impact parameter. Based on Table 5.5, we will attribute an additive systematic error of $8\mu m$ to the bias. It would clearly be enlightening to understand the origin of this bias, particularly how it survives the lifetime sign convention.

Sample	Data	Full M.C.	Fast M.C.
Multihadrons	$37 \pm 3\mu m$	$23 \pm 6\mu m$	$15 \pm 3\mu m$
τ: all	$33 \pm 5\mu m$	$38 \pm 6\mu m$	$2.4 \pm 1\mu m$
1-1	$30 \pm 7\mu m$	$33 \pm 4\mu m$	$1.9 \pm 1.5\mu m$
1-3	$48 \pm 13\mu m$	$42 \pm 7\mu m$	$5.3 \pm 3.5\mu m$
1-3	$17 \pm 10\mu m$	$45 \pm 7\mu m$	$-2.4 \pm 2.4\mu m$

Table 5.5 CD Bias in Various Samples. The entries are the differences between the CD and VC trimmed mean impact parameters for identically selected samples, in the data, full Monte Carlo, and fast Monte Carlo. A larger sample of multihadrons is used here than is used for the control samples. The τ lepton sample is split into $1-1$ events, and $1-3$ events. The $1-3$ events are further broken down according to the origin of the track on the **1** or **3** side of the event.

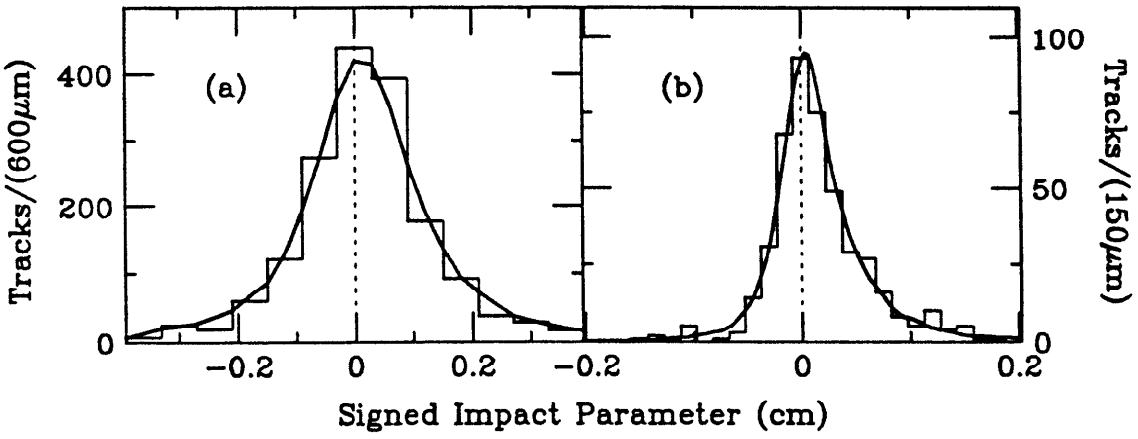

Figure 5.16 Comparison of Monte Carlo with B-enriched Data. (a) for signed impact parameters in the CD data, and (b) for signed impact parameters in the VC data.

The calibration yields an average B-hadron lifetime of $1.35^{+0.31}_{-0.29}$ps for CD data and $1.40^{+0.33}_{-0.27}$ps for VC data. The errors are statistical only. Both data sets combined give $1.37^{+0.22}_{-0.19}$ps. If we combine the CD and VC muon samples, we find $1.36^{+0.30}_{-0.28}$ps, while the electron samples give $1.18^{+0.36}_{-0.35}$ps. Figure 5.16 shows the overlay of the fast Monte Carlo results on the data for the determined lifetimes.

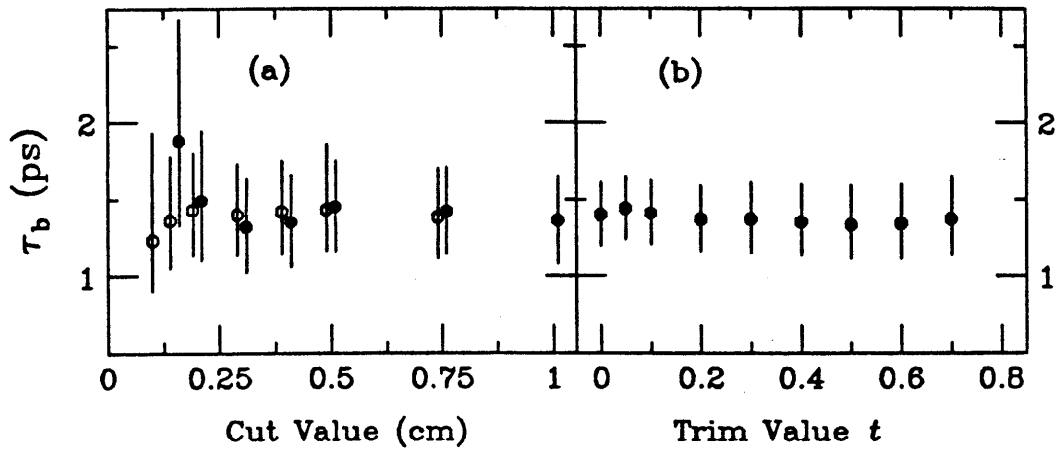

Figure 5.17 Sensitivity of the B-lifetime to Variation in Cut and Trim. (a) change in τ_b with the cut on absolute value of the impact parameter, with solid circles CD and open circles VC data, and (b) change in τ_b with trim factor t, VC and CD data combined.

The next section is devoted to the systematic errors of this measurement. However, of particular concern is the effect of our cuts and trims on the B lifetime result. We present the B-lifetime as a function of cuts and trims in Figure 5.17, where it can be seen that the result is insensitive to variations in these parameters.

5.6 Systematic Errors

We group systematic errors into two broad categories: first, errors in the definition or measurement of the trimmed mean impact parameter, and second, errors in the interpretation of the trimmed mean due to errors in the measured or assumed properties of the event sample.

5.6.1 *Errors in the Trimmed Mean*

The first type of error in this category we address is pedestal and scale of length. That is, how well do we know the location of $0\mu m$, and for non-zero trimmed mean, how well do we know that what we call $1\mu m$ is the same measure that the rest of the world calls $1\mu m$?

Since we have performed calibration of the central tracking system, as discussed in Chapter 3, we have some feeling of the accuracy of our location of $0\mu m$ from that work. We observed in that work drifts in the Bhabha scattering

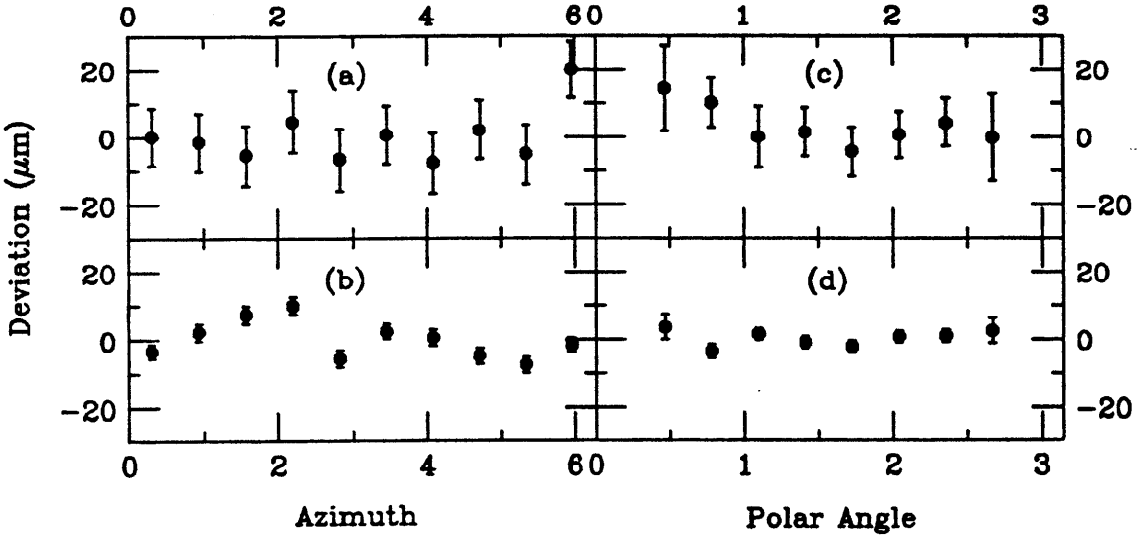

Figure 5.18 Trimmed Mean Variation with ϕ and θ. (a) CD untagged multihadron data versus ϕ; (b) VC data; (c) CD untagged multihadron data versus θ; (d) VC data. The VC data show some significant variation with ϕ, with an rms of $\approx 5\mu m$. However, this washes out when averaged over ϕ, as the θ data show. Hence, we believe $5\mu m$ to be a conservative systematic error.

miss distribution of the order of $5\mu m$. With further study, such drifts could be suppressed, but we have not expended the effort.

We can bring the very large sample of untagged multihadrons events to bear on this issue. In Figure 5.18a-d, we plot the deviation from the trimmed mean for this sample as a function of azimuth and polar angle. These data support an assignment of $\approx 5\mu m$ systematic error, which we refer to as the 'instrumental' pedestal systematic. Our image is that the physical instrument might produce biases at this level. Another indication is the trimmed mean of the untagged multihadron data, taken with the geometric sign convention from Section 5.4, instead of the lifetime sign convention. This yields $2.1 \pm 2.0\mu m$ for CD data, and $8.1 \pm 0.7\mu m$ for VC data. Some dilution of the slight VC bias certainly occurs when the lifetime sign convention is employed, so the $5\mu m$ systematic is reasonable.

As for an instrumental systematic error in the definition of $1\mu m$, what we refer to as an instrumental scale error, ultimately our definition of $1\mu m$ is traceable to the drilling of the endplates of our drift chambers. This drilling was good to at most $20 - 40\mu m$ per 10 cm, limiting this systematic to well less than 0.05%, which is truly negligible on the scale of the errors that follow. We note

that the software calibration of our drift chambers did not allow them to stretch or shrink.

As we discussed in the previous section, we believe that there is a systematic effect in the CD data that produces an offset of $\approx +23\mu m$, where the lifetime sign convention is used. We do not refer to this as 'instrumental' because it appears in the Monte Carlo, and vanishes when the drift chamber resolution in the Monte Carlo is set to 0. We refer to this as the 'pattern recognition/fitting bias', reflecting our suspicion as to its origin, and we assign it a systematic error of $8\mu m$, based upon the comparison of multihadron and τ data. All indications are that this is negligible for VC data.

One might imagine the average vertex procedure to generate some distortion of the impact parameter distribution. In fact, we can find no such effect. If we use the beam centroid rather than the average vertex, we find the trimmed mean impact parameter in the B enriched samples to be $164.2 \pm 24.9\mu m$ rather than $162.1 \pm 24.9\mu m$ for CD data, and $130.4 \pm 21.4\mu m$ rather than $130.2 \pm 18.5\mu m$ for the VC data. These are negligible differences, and seem somewhat against the intuition, so we have conducted some further studies. The average vertex procedure has the greater effect in the VC data, to which we confine our attention. In general, semileptonic decay of B mesons produces fewer charged tracks than hadronic decay, 3.8 ± 0.4 as opposed to 6.0 ± 0.3?[83] At PEP energies, $\approx 5 \pm 1$ additional charged tracks are emitted from the primary vertex by the hadronization process?[84] One might expect some 'pulling' of the average vertex to the hadronic side of the event. However, for the VC data, the tracks on the hadronic side of the event yield a trimmed mean of $122.2 \pm 31.1\mu m$, consistent with the $135.5 \pm 23.9\mu m$ on the semileptonic side of the event. We have conducted a Monte Carlo study of the average vertex procedure. A large sample of $b\bar{b}$ events with a very long B lifetime of 5.6 ps was produced, and in Figure 5.19a we show the impact parameter with respect to the average vertex plotted versus the true impact parameter. We have performed a linear fit, and find an intercept of $14 \pm 7\mu m$ and a slope of 0.981 ± 0.004. Repeating the fit on impact parameter with respect to the beam centroid rather than the average vertex results in an intercept of $11 \pm 6\mu m$, and a slope of 0.980 ± 0.004. It is extremely difficult to escape the conclusion that the average vertex procedure produces a systematic error well below $5\mu m$ in offset and 2% in scale, which are negligible.

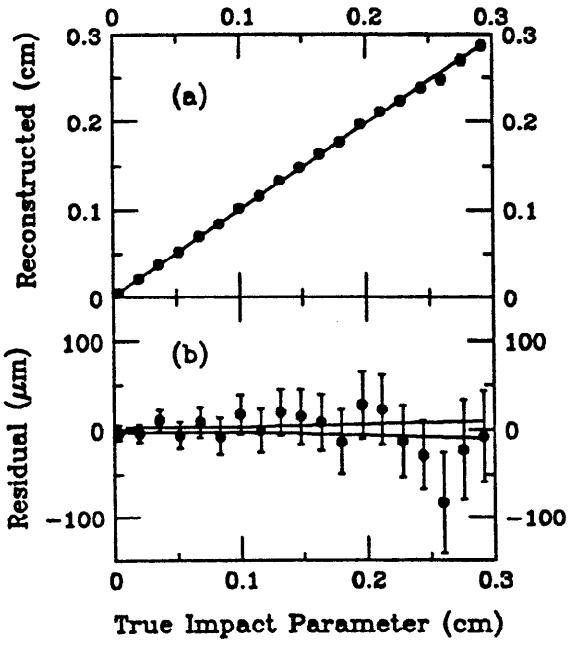

Figure 5.19 Test of Average Vertex.. (a) Signed impact parameter with respect to the average vertex versus the true signed impact parameter, with a linear fit. (b) Residuals from the fit, on an expanded scale, and with the fit's error envelope. The fit has slope 0.980 ± 0.004, and intercept $14 \pm 7 \mu m$.

5.6.2 *Errors in the Interpretation of the Trimmed Mean.*

Imperfect knowledge of the tracking resolution function can result in the wrong calibration of B-lifetime as a function of trimmed mean. We use the fast Monte Carlo to estimate our sensitivity to the width parameter, s, of the student distribution, and the power ν, that controls the tails. We give the results in Figure 5.20. The fit to multihadron data gives s to better than 5%, and ν to 10%. Based on these variation, the systematic error in the B lifetime is less than 0.03 ps.

Error in the fragmentation function of b-quarks effects the calibration of τ_b as a function of the trimmed mean in two ways, both of which lead to smaller τ_b for a given trimmed mean impact parameter for harder fragmentation. First, the more of the initial b quark energy that is retained by the B hadron, the fewer the number of tracks from the primary vertex, which have zero impact parameter. Second, the higher the energy of the B hadron, the larger the impact parameter of the B's daughters, from kinematics. As mentioned in Section 4.1.1, the world data permit variation of the Peterson variable of $\epsilon_b = 0.012^{+0.019}_{-0.009}$,

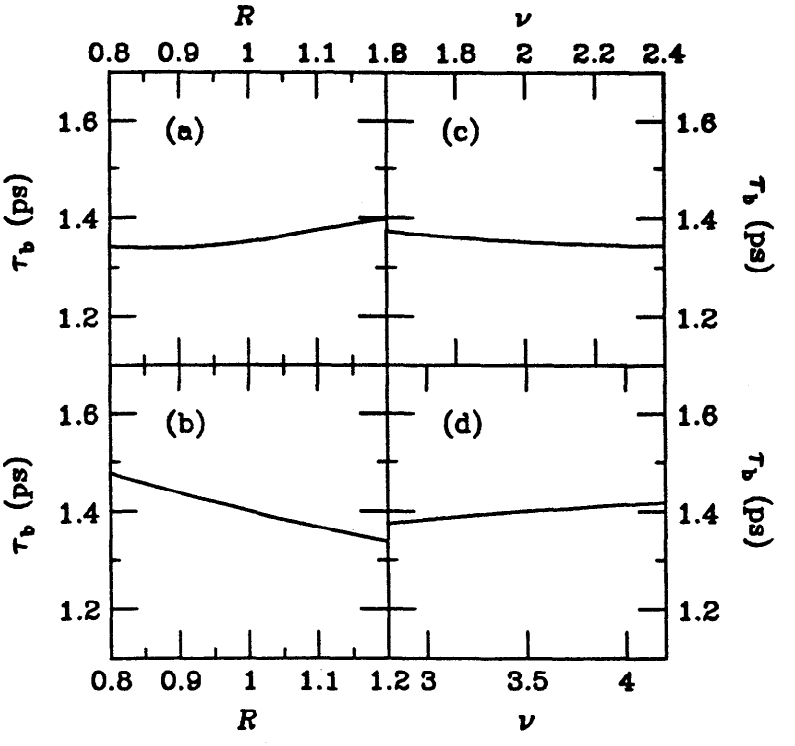

Figure 5.20 Variation of B lifetime with Shape of Resolution Function. (a) For CD data, if the width parameter used in the Student's t distribution is scaled by R, the variation in the resulting B lifetime is shown. (b) similar, for VC data. (c) variation of B lifetime with ν, which describes the tails of the student's t resolution function. The fit to multihadron data gives 2.0 ± 0.2 for the CD, shown here. (d) similar, for VC data, where $\nu = 3.5 \pm 0.3$ from the fit to multihadron data. These four plots show the general insensitivity of the trimmed mean to the shape of the resolution function. The variation of B-lifetime with width of the resolution function is typically four times greater than in (b) when a maximum likelihood fit is employed

which corresponds to a variation in the beam energy retained by the B hadron, corrected for initial state radiation, of 0.78 ± 0.05. This variation changes the *slope* of our calibration curve of τ_b as a function of the trimmed mean by $\pm 10\%$. However, the intercept of the curve, that is the trimmed mean for 0 B lifetime, is insensitive to this variation, and varies by only ± 0.01 ps.

The results of the inclusive lepton analysis of Chapter 4 were somewhat insensitive to variations in the fragmentation function, because the shape of the $p_\perp$ spectrum is nearly Lorentz invariant. Those results are also insensitive to changes in the branching ratio of B into leptons. Hence, we can take the b purity of the muon event sample of $60 \pm 4.5\%$ and the electron event sample of $59 \pm 7\%$

without more detailed consideration of the errors. These errors in purity lead to a systematic error in the slope of the τ_b calibration curve of $\pm 8.5\%$, and a systematic error of the intercept at zero lifetime of ± 0.03 ps.

We have considered errors in our track purities, as opposed to event purities, that is, the entries in Table 5.3. We note that our data and Monte Carlo agree in the result that the B enriched sample has a higher multiplicity of lifetime tracks than the untagged multihadron sample, as we mentioned previously. From study of the data on multiplicity in heavy quark events;[83,84] we assign a systematic error to the B lifetime calibration of $\pm 7\%$ in slope and ± 0.03 ps in intercept from possible errors in the b and $b-c$ track fractions in Table 5.3. We feel this is a very conservative assignment, as we are in some part double counting errors in the fraction of tracks from the primary vertex that have been included in the systematic from b fragmentation.

Because we have chosen to use all tracks, as opposed to just lepton tracks in this analysis, we are somewhat more sensitive to the effects of light, long lived particles, such as K^0_ss, Λs, and decays in flight of charged pions and kaons. Consistency was noted in the previous section between the number of tracks with very large impact parameters between our data and Monte Carlo, indicating no serious discrepancy. We have, however, artificially increased the abundance of light, long lived species in our Monte Carlo, and show the effect on the B-lifetime result in Figure 5.21. A pessimistic variation of a full factor of 2 in the light, long lived abundance would produce a systematic error of ± 0.05 ps in the B-lifetime. We assign a more realistic error of ± 0.03 ps.

Finally, we consider the systematic error from errors in the lifetimes of charmed particles. Due to the success of experiment E-691, the lifetimes of the dominant charmed hadron species are known with great accuracy. If we assume the abundances in Table 5.4 are correct, there is an error of only ± 0.03 ps in the mean charmed lifetime in our sample. However, the abundances are themselves subject to considerable uncertainty, and this in fact dominates. Our study of results from CLEO and Argus[85] indicate that these uncertainties produce and error of ± 0.06 ps in the mean charmed lifetime in our sample. This error produces a systematic error of only ± 0.02 ps in the B-lifetime.

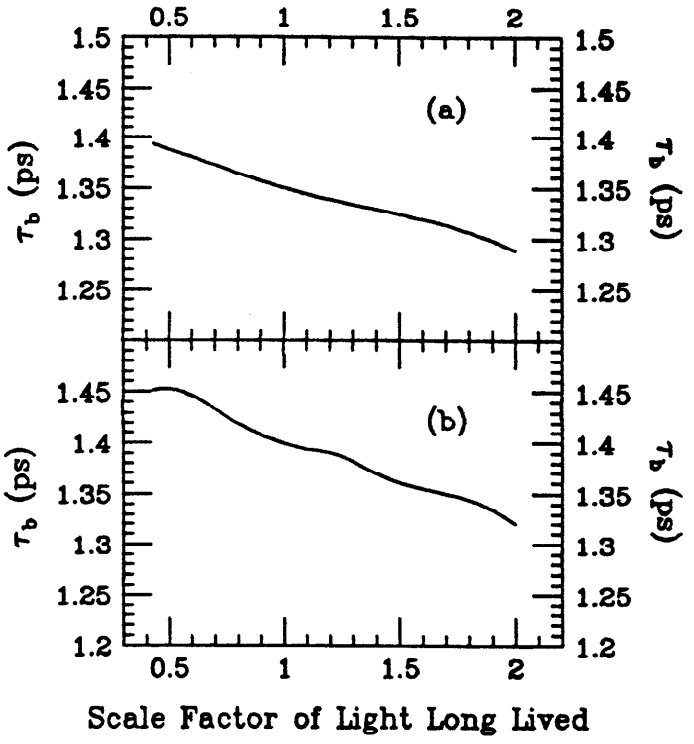

Figure 5.21 Variation of B Lifetime with Level of Light, Long Lived Species. (a) is for CD data, (b) is for VC data. The fraction of light, long lived species is scaled by the factor along the horizontal; the calibration of τ_b as a function of trimmed mean is then reevaluated and a new B-lifetime computed. We note that the trimmed mean is a good deal less sensitive to the level of light, long lived species than the untrimmed mean. However, some bias would be created if there was an extremely long lived but uncommon species of B hadron.

5.6.3 *Other Checks*

The τ lepton lifetime has been measured with both CD data,[86] and VC data.[87] The measurement using VC data actually employed 3 different techniques to extract the τ life. The result utilizing the average vertex technique is $0.297 \pm 0.026 \pm 0.014$ps.

The CD biases in Table 5.5 are found from the difference of CD and VC trimmed mean impact parameters. We note here that the values for the trimmed means of untagged multihadrons are $72.8 \pm 2.8\mu m$ for CD data and 67.1 ± 6.4 for the equivalent full Monte Carlo sample. In the VC data, the untagged multihadrons yield $36.3 \pm 1.1\mu m$, while the full detector simulation yields $34.1 \pm 3.2\mu m$.

Source	Error in Impact Parameter	Error in Offset	Error in Slope
Instrumental	$\pm 5\mu m$	± 0.07 ps	-
CD Bias	$\pm 8\mu m$	± 0.06 ps	-
Resolution	-	± 0.03 ps	-
Fragmentation	-	± 0.01 ps	$\pm 10\%$
Event Purity	-	± 0.03 ps	$\pm 8.5\%$
Track Purity	-	± 0.03 ps	$\pm 7\%$
Light, Long Lived	-	± 0.03 ps	-
Charmed Lifetime	-	± 0.02 ps	-
All in Quadrature	$\pm 6.5\mu m$	± 0.11 ps	$\pm 15\%$

Table 5.6 Summary of Systematic Errors.

5.6.4 *Summary of Systematic Errors*

We summarize the systematic errors in Table 5.6

Chapter 6

Conclusions

6.1 Summary of Results

6.1.1 *Vertex Chamber*

We have described the design, construction, and operation of a vertex chamber used with the MAC detector. This device consists of aluminized mylar tubes, or straws, and has operated reliably only 4.6 cm from colliding beams at PEP. An average spatial resolution of $45\mu m$ has been achieved, and the resolution is $35\mu m$ over much of the drift distance. The resolution in extrapolation to the vertex, as measured with Bhabha scattering events, is $87\mu m$.

6.1.2 *B Hadron Lifetime*

The B hadron lifetime, averaged over the species produced in e^+e^- annihilations at $\sqrt{s} = 29\,\mathrm{GeV}$, has been measured. A sample of events enriched in $b\bar{b}$ production has been obtained by the requirement of either a muon or electron with large momentum transverse to the thrust axis. The impact parameters of all tracks in these events that pass certain cuts have been employed to measure the lifetime. Data from $214\,\mathrm{pb}^{-1}$ taken without the vertex chamber and $94\,\mathrm{pb}^{-1}$ with the vertex chamber has been employed to obtain the result:

$$\tau_b = \left[1.37\,^{+0.22}_{-0.19}\,\text{stat.}\pm 0.11\ \text{sys.}\right] \times (1 \pm 0.15)\ \text{psec.}$$

The final factor is the systematic error in the scale, and is stated separately to emphasize the fact that it does not degrade the statistical significance of the difference of this result with 0.

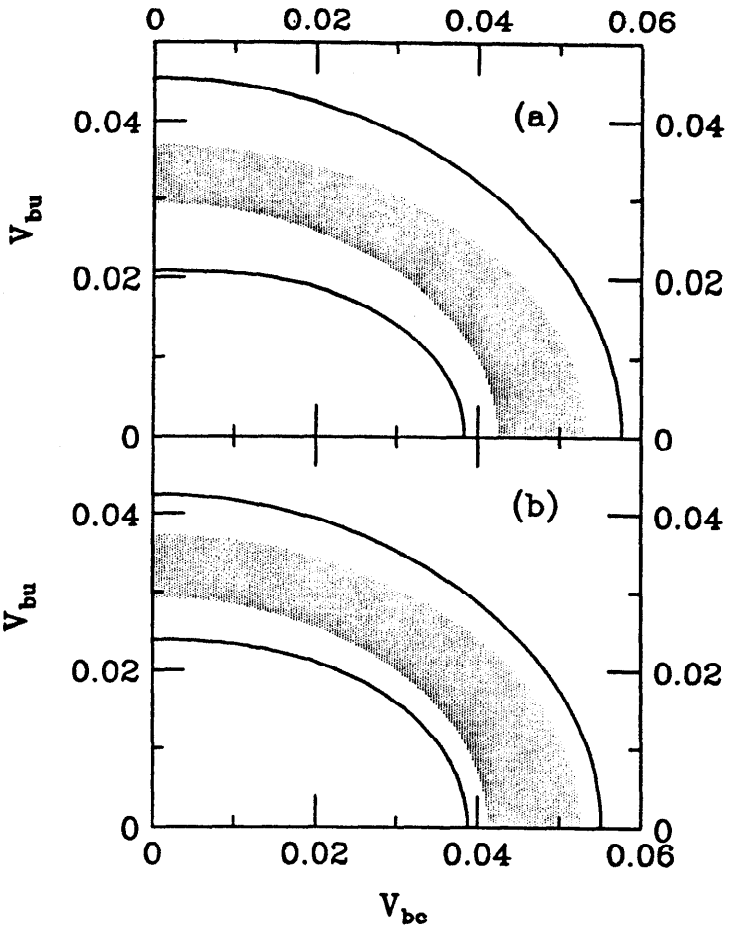

Figure 6.1 Restrictions on V_{bu} and V_{bc} from this Measurement. The ± one standard deviation allowed region without inclusion of estimated theoretical error is hatched. Inclusion of theoretical error leads to the region between the solid lines. then reevaluated and a new B-lifetime computed. (a) the B lifetime has been used, with equation 1.3; (b) the partial rate to electrons, taking the branching ratio to be $12 \pm 1\%$, has been used.

6.2 Constraints on the Quark Mixing Matrix

Using the expressions from Section 1.2.5, in particular [1.3] and [1.4], we are able to compute a bounded region in the elements of the KM quark mixing matrix, V_{bu} and V_{bc}, from our B lifetime measurement, assuming the naive spectator model. These results are given in Figure 6.1, where we have made an effort to distinguish our experimental error from theoretical errors in the relationships between τ_b and the KM quark mixing matrix elements.

6.3 Comparison with Other B Lifetime Measurements

In Figure 6.2 and Table 6.1, we detail other measurements of the B-lifetime. All but one come from e^+e^- experiments, and the one fixed target experiment has only two B decays, although they are extremely well reconstructed. We have made a strong effort to make this compilation complete, so that systematic differences between experiments and trends may be observed. This means that a great many of these measurements do not come from refereed journals. We list 26 measurements other than ours.

The B-lifetime measurements made at e^+e^- colliders are distinguished by technique to achieve a B enriched sample, method of estimation at the vertex, and resolution in extrapolation to the vertex. These qualities are tabulated in Table 6.1. We have employed semileptonic decays of Bs to obtain an enriched sample, while some groups at PETRA have attempted to exploit the spherical shape of hadronic decays of Bs to obtain enriched samples. We emphasize that semileptonic enrichment has undergone far more study with data than has hadronic enrichment. Recently, the PETRA experiments have given up enrichment altogether, and have used the inclusive multihadron samples to estimate the B-lifetime. The sensitivity of such techniques to the B-lifetime is low, but the large statistic allows a significant measurement to be made. However, we believe the surrender of sensitivity allows high susceptibility to systematic errors. For example, the $5\mu m$ systematic error in impact parameter we assign from instrumental phenomena would become more prominent if we did not enrich our sample.

Among measurements that do use semileptonic enrichment, our measurement is distinguished by the highest value of the cut on $p_\perp$, and by the predominance of muons. We emphasize the redundancy and solid angle coverage of the MAC muon system.

At the vertex, we utilize the signed impact parameter of all tracks to estimate the lifetime. By using all tracks instead of just lepton tracks we gain statistics, at some expense of systematic error. However, a number of experiments utilize vertex fitting or other measures or the B decay length. These are inherently more susceptible to systematic errors in fragmentation and track composition than the signed impact parameter.

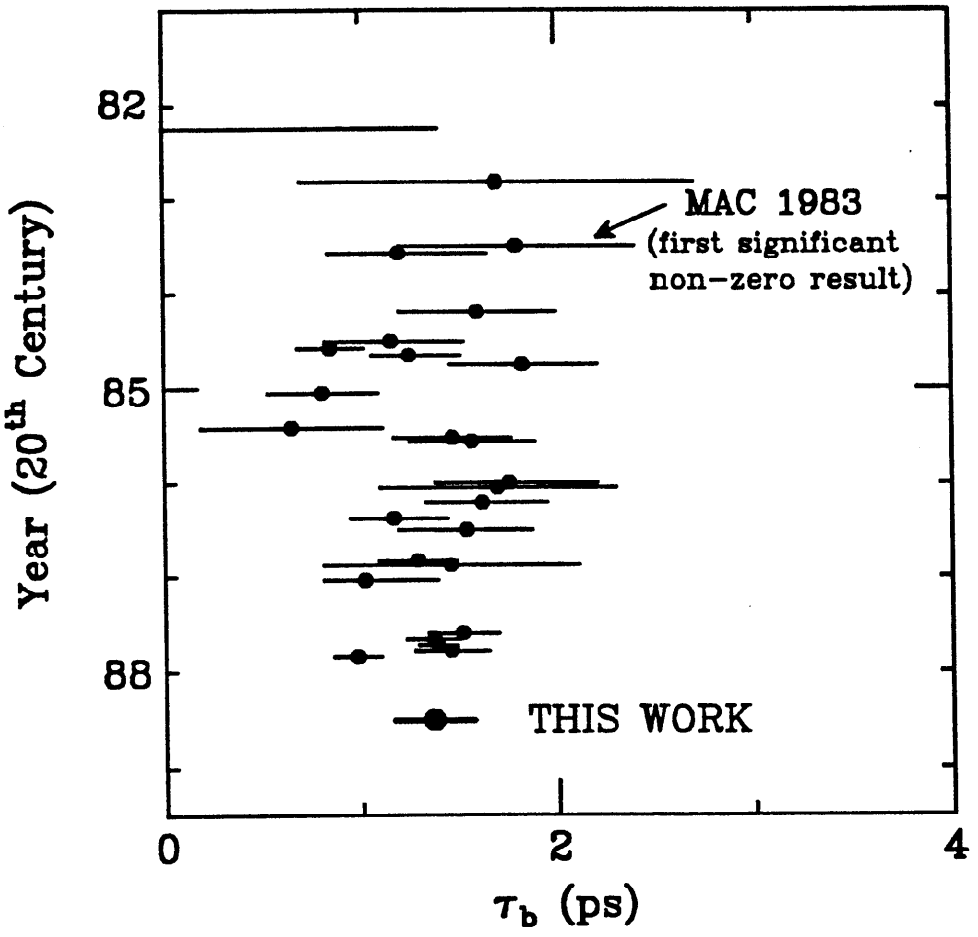

Figure 6.2 World B-lifetime Measurements over Time. Only statistical errors are shown, in part because a sizeable fraction of the systematic errors are known to be common to all experiments. Systematic errors due to fragmentation are one such example. Note that we have not put this measurement quite in its chronological place, for emphasis.

Finally, we have good resolution in extrapolation to the vertex, particularly considering we allow tracks with momenta as low as 500 MeV into our sample.

Table 6.1 **Measurements of the B lifetime. References to results published in refereed journals are in boldface, others are in italics. The Tags l, h, and ϕ refer to semileptonic tagging, hadronic tagging, and no tagging. Among fractions, b includes cascade b-c, bk means events with leptons from misidentification of decay, lt refers to light quark events, and o to tracks from the primary vertex of light, long lived species. 'Entries' are entries in the distribution used to derive the lifetime, where δ refers to impact parameters, and v to vertices; the dipole method of TASSO, which is somewhere between these alternatives, is labelled 'dip.' The resolution σ is that of the distribution of entries. The JADE(82) upper limit may have contained an error of a factor of 1.3, and we have placed the corrected value in parenthesis.** ***(Next Four Pages)***

Experiment	Reference	$\mathcal{L}$ pb^{-1}	Tag l, h, ϕ	Events	Fractions	Entries δ, v	Fractions	$\langle\delta\rangle$ (μm)	σ	τ_b picoseconds
JADE(82)	(88) 3/18/82	—	l, h $p > 1.4$ $T_1 > 0.2$	27μ	0.47b 0.38c 0.15bk	δ 27μ	0.47b 0.38c 0.15bk	10 ± 87	450	< 1.4 95% CL (1.8)
MAC(82)	(22) 10/30/82	30	l, h $p > 2$ $p_\perp > 1$ $M_{jet} > 6$	23μ	0.55b 0.28c 0.17bk	δ, v 23μ	—	—	600	1.7 ± 1.0
MAC(83)	(23) 6/30/83	106μ 92e	l $p > 2$ $p_\perp > 1.5$	155μ 133e	0.68b 0.13c 0.19bk	δ 155μ 133e	0.68b 0.13c 0.19bk	$158 \pm 81\,\mu$ $174 \pm 75\,e$	600	$1.8 \pm 0.6 \pm 0.4$
MARK-II(83)	(24) 8/02/83	80	l $p > 2$ $p_\perp > 1$ $\sigma_\delta < 350$	104 μ+e	0.64b 0.16c 0.20bk	δ 104	0.64b 0.16c 0.20bk	106 ± 29	200	$1.20^{+0.45}_{-0.36} \pm 0.3$
MAC(84)	(89) 3/12/84	160μ 120e	l $p > 2$ $p_\perp > 1.5$ $\sigma_\delta < 1$ mm	238μ 160e	0.52b 0.18c 0.30bk	δ 238μ 160e	0.52b 0.18c 0.30bk	$159 \pm 39\,\mu$ $83 \pm 42\,e$	600	$1.6 \pm 0.4 \pm 0.3$
DELCO(84)	(90) 7/27/84	118	l $p > 1$ $p_\perp > 1$	60 e	0.83b 0.11c 0.06bk	δ 60 e	0.83b 0.11c 0.06bk	215 ± 81	400	$1.16^{+0.37}_{-0.34} \pm 0.23$
MARK-II(84a)	(91) 8/3/84	220	l $p > 2$ $p_\perp > 1$ $\sigma_\delta < 350$	270 μ+e	0.64b 0.16c 0.20bk	δ 270	0.64b 0.16c 0.20bk	80 ± 17	200	$0.85 \pm 0.17 \pm 0.21$

Table 6.1

Experiment	Reference	$\mathcal{L}$ pb^{-1}	Tag l, h, ϕ	Events	Fractions	Entries δ, v	Fractions	$\langle\delta\rangle$ (μm)	σ	τ_b picoseconds
MARK-II(84b)	(92) 8/24/84	209	l $p>2$ $p_\perp>1$	270 $\mu+e$	$0.64b$ $0.16c$ $0.20bk$	v 551	–	413 ± 43	400	$1.25^{+0.26}_{-0.19} \pm 0.5$
TASSO(84)	(93) 10/9/84	79 CD 14 VC	h $S_1 \cdot S_2 > 0.1$	2354 CD 204 VC	$0.32b\bar{b}$ $0.35c\bar{c}$ $0.33lt$	δ 7526 CD 716 VC	–	105 ± 17 CD 109 ± 23 VC	1100 CD 380 VC	$1.83^{+0.38+0.37}_{-0.37-0.34}$
MAC(85)	(94) 1/18/85	210	l $p>2$ $p_\perp>1.5$ $\sigma_\delta<1$ mm	505	$0.52b$ $0.18c$ $0.30bk$	δ 505	$0.52b$ $0.18c$ $0.30bk$	70 ± 22	530	$0.81 \pm 0.28 \pm 0.17$
WA75(85)	(95) 6/5/85	10^{-4}	l -	2	$1.00b\bar{b}$	v 2	$1.00b\bar{b}$	2433 ± 2.5	5	0.65 ± 0.46
DELCO(85)	(96) 85	214	l $p>1$ $p_\perp>1$	118 e	$0.79b$ $0.17c$ $0.04bk$	δ 118 e	$0.79b$ $0.17c$ $0.04bk$	–	400	$1.47 \pm 0.30 \pm 0.29$
TASSO(85)	(97) 7/24/85	79 CD 25 VC	h $S_1 \cdot S_2 > 0.1$	2354 CD – VC	$0.32b\bar{b}$ $0.35c\bar{c}$ $0.33lt$	δ 7526 CD – VC	–	105 ± 17 CD – VC	1100 CD 380 VC	$1.57 \pm 0.32^{+0.37}_{-0.34}$
JADE(86a)	(98) 1/9/86	63	l, h $p>1.8\mu$ $p>1.5e$ $p_\perp>0.9$ *3-jet* cuts	74μ $34e$	$0.76b$ $0.09c$ $0.15bk$	δ 74μ $34e$	$0.76b$ $0.09c$ $0.15bk$	$282 \pm 78\,\mu$ $457 \pm 107\,e$	570	$1.76^{+0.45}_{-0.38} \pm 0.38$

Table 6.1 *(continued)*

Experiment	Reference	$\mathcal{L}$ pb^{-1}	Tag l, h, ϕ	Events	Fractions	Entries δ, v	Fractions	$\langle\delta\rangle$ (μm)	σ	τ_b picoseconds
JADE(86b)	(98) 1/9/86	63	l, h $p > 1.8\mu$	293μ	$0.19b\bar{b}$ $0.47c\bar{c}$ $0.34lt$	δ 9233a	$0.2b\bar{b}$	$195 \pm 62\,\mu$	850	$1.7 \pm 0.6 \pm 0.4$
TASSO(86d)	(100) 3/16/86	47	ϕ	–	–	–	dip.	328 ± 28	750	$1.62^{+0.33}_{-0.29} \pm 0.25$
DELCO(86)	(99) 6/86	214	l $p > 1$ $p_\perp > 1$	113 e	$0.79b$ $0.17c$ $0.04bk$	δ 113 e	$0.79b$ $0.17c$ $0.04bk$	259 ± 49	400	$1.16^{+0.27+0.17}_{-0.22-0.16}$
TASSO(86v)	(101) 86	33	ϕ	3586	$0.11b\bar{b}$ $0.35c\bar{c}$ $0.54lt$	v 2119	$0.12b\bar{b}$ $0.35c\bar{c}$ $0.53lt$	140 ± 21	500	$1.54^{+0.38}_{-0.35} \pm 0.29$
MAC(86)	(102) 10/27/86	220 CD 94 VC	l $p > 2$ $p_\perp > 1.5$	410 CD 152 VC	$0.64b\bar{b}$ $0.19c\bar{c}$ $0.17lt$	δ 1558a CD 441a VC	$0.47b$ $0.05c$ $0.48o$	154 ± 26 CD 129 ± 19 VC	800 CD 200 VC	$[1.29 \pm 0.20 \pm 0.11]$ $\times(1.00 \pm 0.15)$
TASSO(86l)	(103) 11/86	47	l $p > 2$ $p_\perp > 1.1$	68μ $31e$	$0.39b$ $0.22c$ $0.39bk$	δ 68μ $31e$	$0.39b$ $0.22c$ $0.39bk$	138 ± 47	280	$1.46 \pm 0.65 \pm 0.34$
HRS(87)	(104) 1/87	200	l $p > 2$ $p_\perp > 1.1$	312 e	$0.53b$ $0.22c$ $0.25bk$	δ 312 e	$0.53b$ $0.22c$ $0.25bk$	80 ± 27	325	$1.02^{+0.41}_{-0.37}$

Table 6.1 *(continued)*

Experiment	Reference	$\mathcal{L}$ pb^{-1}	Tag l, h, ϕ	Events	Fractions	Entries δ, v	Fractions	$\langle\delta\rangle$ (μm)	σ	τ_b picoseconds
TASSO(87)	(*105*) 9/5/87	157	h $S_1 \cdot S_2 > 0.18$	–	$0.34 b\bar{b}$	δ –	–	86.8 ± 6.2	380	$1.52 \pm 0.18 \pm 0.24$
TASSO(87d)	(*105*) 9/5/87	157	ϕ	–	–	dip.	–	305 ± 13	750	$1.37 \pm 0.14 \pm 0.32$
TASSO(87v)	(*105*) 9/5/87	157	ϕ	–	$0.12 b\bar{b}$	v –	–	83.7 ± 5.1	380	$1.39 \pm 0.10 \pm 0.25$
JADE(87)	(*105*) 9/5/87	115	ϕ $S_1 \cdot S_2$ weight	15111	–	v	–	1008 ± 80	1300	$1.46 \pm 0.19 \pm 0.3$
MARKII(87)	(*106*) 9/87	206	l $p > 2$ $p_\perp > 1.0$	231μ $386e$	$0.64b$ $0.19c$ $0.17bk$	δ 231μ $386e$	$0.64b$ $0.19c$ $0.17bk$	$112 \pm 16e$ $118 \pm 21\mu$	130	$0.98 \pm 0.12 \pm 0.13$
This Work	10/87	220 CD 94 VC	l $p > 2$ $p_\perp > 1.5$	439 CD 161 VC	$0.60 b\bar{b}$ $0.22 c\bar{c}$ $0.18lt$	δ 1694a CD 453a VC	$0.45b$ $0.06c$ $0.49o$	162 ± 25 CD 130 ± 19 VC	800 CD 200 VC	$[1.37^{+0.22}_{-0.19} \pm 0.11]$ $\times (1.00 \pm 0.15)$

Table 6.1 *(continued)*

Appendix A

Tracking Parameterization

Five parameters describe the helical trajectory of charged particles in the axial magnetic field of MAC. Three of these describe the circular projection of the trajectory in the plane perpendicular to the beam axis: κ, the reciprocal of the radius of curvature; δ_0 the (signed) distance of closest approach of the circle to the geometric center of the MAC coordinate system; and ϕ_0, the azimuth of the trajectory at closest approach. The sign of δ_0 is determined from the cross product of the direction of the particle trajectory at closest approach taken with the direction from the geometric center to the point of closest approach. Figure A.1 exhibits the definition of κ, δ_0, and ϕ_0. The remaining two parameters describe the particle trajectory out of the plane perpendicular to the beam. θ is the angle with respect to the beam axis of the trajectory, and z_0 its intercept with the axis, viewed along the azimuth containing the distance of closest approach. In the MAC track fitting routines, multiple coulomb scattering is described by 'kinks' at the radii of matter concentrations, such as the boundary between the VC and CD. Several kink angles are fit, but with a constraint by the r.m.s. angle predicted by multiple coulomb scattering. This procedure quite naturally incorporates errors from multiple coulomb scattering into the covariance matrix of $\kappa, \delta_0, \phi_0, \theta$, and z_0.

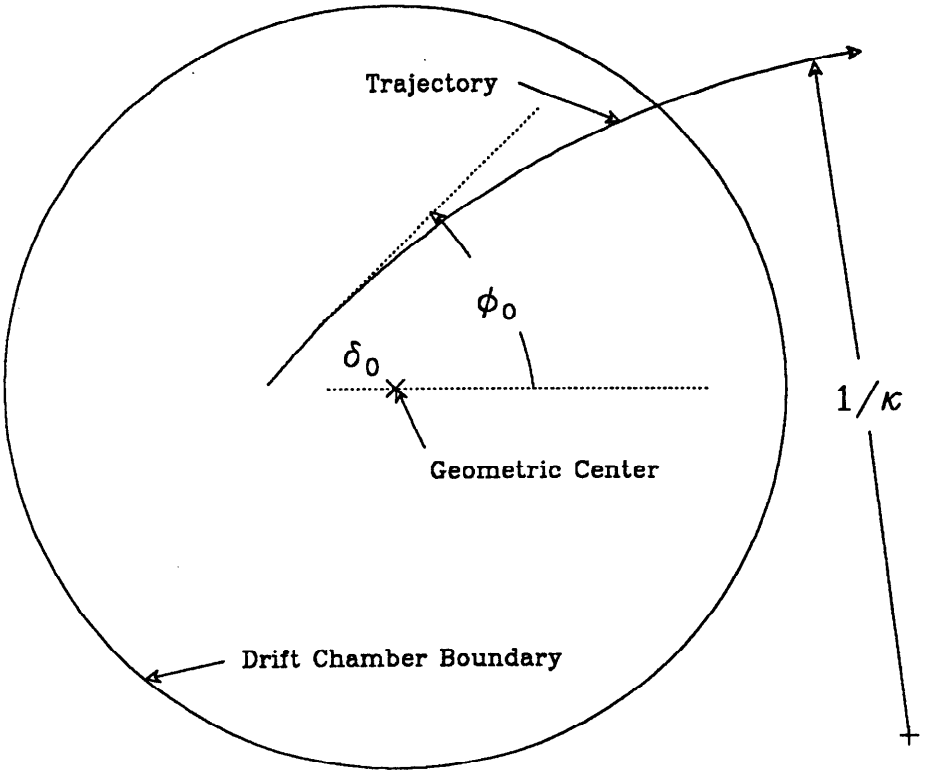

Figure A.1 Parameters Describing a Particle Trajectory. The figure is in the plane perpendicular to the beam. The outer circle schematically represents a boundary in the drift chamber system. δ_0 is given a sign based upon the cross product of a vector pointing along the particle trajectory taken with a vector from the geometric center to the perihelion of the trajectory.

References

1) A minimal list is: 3 dimensionless coupling constants (2 for the electroweak interaction, one for the strong interaction); 3 charged lepton masses, 6 quark masses (including the as yet unobserved top quark); 3 real quark mixing angles and one CP violating phase; 2 electroweak masses, *e.g.*that of the W and of the Higgs. Gravity, formally not included in the Standard Model, would contribute 1 dimensionless coupling constant. We acknowledge that some interrelationships between these parameters may exist from loop corrections, and that some things are not considered 'parameters': the number of dimensions of spacetime (4), the number of colors in QCD (3); quark electric charges (1/3 or 2/3). Numbers consistent with zero, such as the neutrino masses, a photon mass, are parameters, but are also assumed to *be* zero in this list, so are not free to be varied.

2) A good reference on the theory of the Standard Model is: C. Quigg, *Gauge Theories of the Strong, Weak, and Electromagnetic Interactions* (Benjamin/Cummings, Menlo Park, 1983). The experimental development of the Standard Model is technical, elusive, and often impenetrable to the layman or anyone uninitiated into the practice of Experimental High Energy Physics. See, for example: A. Pickering, *Constructing Quarks*, (Univ. of Chicago Press, Chicago, 1984); R. P. Crease, *The Second Creation*, (Macmillan, New York, 1986); G. Taubes *Nobel Dreams*, (Random House, New York, 1986). A good textbook is: D. H. Perkins, *Introduction to High Energy Physics*, (Addison Wesley, Menlo Park, 1987).

3) M. Aguilar-Benitez *et al.*, *Phys. Lett.* **170B**, 1, (1986) (Review of Particle Properties).

4) M. Kobayashi, and T. Maskawa, *Prog. Theor. Phys.* **49**, 652 (1973).

5) H. Harari and M. Leurer, *Phys. Lett.* **181B**, 123 (1986).

6) R. Ruckl, *Weak Decays of Heavy Flavors*, CERN PRINT 83-1063, October 1983 (Unpublished). This contains an excellent overview of the subject. The assumptions of the Naive Spectator Model are discussed on p. 51.

7) J. L. Cortes, X. Y. Pham, and A. Tounsi *Phys. Rev.* **D25**, 188 (1982).

8) M. Wirbel, B. Stech, and M. Bauer, *Z. Physik C, Particles and Fields* **29**, 637 (1985).

9) B. Grinstein, M. Wise, and N. Isgur, *Phys. Rev. Lett.* **56**, 298 (1986); CALT-68-1311 (unpublished).

10) T. Altomari and L. Wolfenstein, CMU-HEP-86-17 (unpublished).

11) M. K. Gaillard and B. W. Lee, *Phys. Rev. Lett.* **33**, 108 (1974); G. Altarelli and L. Maiani *Phys. Lett.* **52B**, 351 (1974).

12) G. Altarelli *et al.*, *Phys. Lett.* **99B**, 141 (1981); *Nucl. Phys.* **B187**, 461 (1981).

13) N. Cabibbo and L. Maiani, *Phys. Lett.* **70B**, 109 (1974).

14) R. E. Behrends *et al.*, *Phys. Rev.* **101**, 866 (1956); S. Berman, *Phys. Rev.* **112**, 866 (1958); T. Kinoshita and A. Sirlin, *Phys. Rev.* **113**, 1652 (1959). The effective weak Hamiltonian for muon decay can be rearranged to $[\bar{e}\gamma_\lambda(1-\gamma_5)\mu][\overline{\nu_\mu}\gamma^\lambda(1-\gamma_5)\nu_e]$, identical in form to that describing $b\to ce^-\overline{\nu_e}$.

15) A. Bean *et al.*, *Phys. Rev. Lett.* **58**, 183 (1987).

16) B. Guberina *et al.*, *Phys. Lett.* **89B**, 111 (1979).

17) M. Bander *et al.*, *Phys. Rev. Lett.* **44**, 7;962(E) (1980).

18) A. Soni, *Phys. Rev. Lett.* **53**, 1407 (1984).

19) I. Bigi, *Phys. Lett.* **169B**, 101 (1986);also in *Proceedings of the Fourteenth SLAC Summer Institute on Particle Physics, Stanford, 1986*, edited by Eileen C. Brennan (Stanford Linear Accelerator Report No. 312, Stanford, 1987).

20) T. Altomari and L. Wolfenstein, *Phys. Rev. Lett.* **58**, 1583 (1987).

21) E. H. Thorndike, in *Proceedings of the 1985 International Symposium on Lepton and Photon Interactions at High Energy, Kyoto, Japan, 1985*, edited by M. Konuma and K. Takahashi. (Kyoto University, Kyoto, Japan, 1986).

22) R. Weinstein, *P*roceedings of the American Physical Society Division of Particles and Fields Meeting, College Park, October 1982, edited by W. Caswell and G. Snow. (AIP, New York, New York 1983).

23) E. Fernandez *et al.*, Phys. Rev. Lett. **51**, 1022 (1983).

24) N. S. Lockyer *et al.*, Phys. Rev. Lett. **51**, 1316 (1983).

25) B. M. Anand, Proc. Roy. Soc. (London) **A220**, 183 (1953); G. Harris, J. Orear, and S. Taylor, Phys. Rev. **106**, 327 (1957); P. Stamer *et al.*, Phys. Rev. **151**, 151 (1966); H. W. Atherton *et al.*, Phys. Lett. **158B**, 81 (1985).

26) D. B. MacFarlane lecture presented at the Fifteenth SLAC Summer Institute on Particle Physics, Stanford, 1987.

27) S. Stone, CLNS-87-56, March 1987 (unpublished); Plenary talk presented at DPF meeting at Salt Lake City, January 1987.

28) R. M. Baltrusaitis, *et al.*, *Phys. Rev. Lett.* **56**, 2140 (1986).

29) P. H. Ginsparg, S. L. Glashow, M. B. Wise, *Phys. Rev. Lett.* **50**, 1415 (1983); *Phys. Rev. Lett.* **51**, 1395 (1983) (E).

30) P. Langacker in *Proceedings of the 1985 International Symposium on Lepton and Photon Interactions at High Energies, Kyoto, 1985*, edited by M. Konoma and K. Takahashi (Kyoto University, Kyoto, 1986).

31) F. J. Gilman and M. B. Wise, *Phys. Rev.* **D20**, 2392 (1979).

32) T. Inami and C. S. Lim, *Prog. Theor. Phys.* **65**, 297 (1981).

33) ϵ': FNAL-731, Spokesperson B. Winstein; CERN-NA-31, Spokesperson H. Wahl. $K^- \to \pi^- \nu\overline{\nu}$: BNL-787, Spokespersons T. F. Kycia, A. J. S. Smith.

34) C. Albajar *et al.*, *Phys. Lett.* **186B**, 247 (1987); H. Albrecht *et al.*, DESY-87-029 April 1987; R. Hurst, contribution to the 22nd Moriond Meeting on Perspectives in Electroweak Interactions and Unified Theories, Les Arcs, France, March 1987.

35) J. Ellis, J. S. Hagelin and S. Rudaz, CERN-TH-4679/87; L. L. Chau, W. Y. Keung, UCD-87-02; T. Morimitsu, EMU-04-87; V. Barger, T. Han, D. V. Nanopoulos, and R. J. N. Philips, MAD/PH/341, MAD/TH/87-12.

36) Stanford Linear Accelerator Center, *A Proposal for an Electron-Positron Colliding- Beam Storage Ring Project*, SLAC-171 (1974); *PEP Design Handbook*, edited by H. Weidemann, (1977).

37) D. Ritson, 'A Lepton-Missing Mass Detector,' Talk presented at PEP Conference, June 23-25, 1976 (unpublished); R. L. Anderson, D. B. Gustavson, J. R. Johnson, R. P. Prepost, D. M. Ritson, and D. E. Wiser, 'A Proposal for a Lepton-Total Energy Detector at PEP,' PEP Proposal PEP-6, December 1976 (unpublished).

38) The doctoral dissertations written from MAC data provide the best detailed reference on the detector and data processing: S. Kaye, Ph. D. Thesis, SLAC Report No. 262, 1983; Hoyun Lee, Ph. D. Thesis, University of Utah, 1983; S. Clearwater, Ph. D. Thesis, SLAC Report No. 264, 1983; B. Heltsley, Ph. D. Thesis, University of Wisconsin-Madison Report WISC-EX-83/233, 1983; L. Rosenberg, Ph. D. Thesis, SLAC Report No. 289, 1985; M. Delfino, Ph. D. Thesis, University of Wisconsin-Madison Report WISC-EX-85/263, 1985; G. Goderre, Ph. D. Thesis, Northeastern University Report NUB-2687, 1985; A. L. Read, Ph. D. Thesis, University of Colorado-Boulder Report COLO-HEP-122, 1986.

39) R. Anderson *et al.*, IEEE Trans. Nucl. Sci. **NS-25**, 340 (1978).

40) E. Cisneros *et al.*, *IEEE Trans. Nucl. Sci.* **NS-24**, 413 (1977).

41) M. Breidenbach *et al.*, *IEEE Trans. Nucl. Sci.* **NS-25**, 706 (1978).

42) B. Gottschalk *Nucl. Instrum. Meth.* **196**, 447 (1982); B. Gottschalk, SLAC-TN-81-006, August 1981 (unpublished).

43) F. Berends, R. Kleiss and S. Jadach, Nucl. Phys. **B202**, 63 (1982).

44) The $O(\alpha_s^2)$ matrix elements used are those of R. Ellis, D. Ross and A. Terrano, Nucl. Phys. **B178**, 421 (1981).

45) B. Andersson, G. Gustafson and B. Soderberg, Z. Phys. **C20**, 317 (1983); We use a modified form of the Lund JETSET version 5.2 code.

46) C. Peterson, D. Schlatter, I. Schmitt and P.M. Zerwas, Phys. Rev. **D27**, 105 (1983).

47) R. Ford and W. Nelson, SLAC report SLAC-210, 1978 (EGS code)

48) T. W. Armstrong, in *Computer Techniques in Radiation Dosimetry*, edited by W. R. Nelson and T. M. Jenkins (Plenum Press, New York, 1980)(HETC code).

49) The MAC collaboration consists of: W. W. Ash, H. R. Band, T. Camporesi, G. B. Chadwick, M. C. Delfino, R. De Sangro, W. T. Ford, M. W. Gettner, G. P. Goderre, D. E. Groom, R. B. Hurst, J. R. Johnson, K. H. Lau, T. L. Lavine, R. E. Leedy, T. Maruyama, R. L. Messner, J. H. Moromisato, L. J. Moss, F. Muller, H. N. Nelson, I. Peruzzi, M. Piccolo, R. Prepost, J. Pyrlik, N. Qi, A. L. Read, Jr., D. M. Ritson, F. Ronga, L. J. Rosenberg, W. D. Shambroom, J. C. Sleeman, J. G. Smith, J. P. Venuti, P. G. Verdini, E. von Goeler, H. B. Wald, R. Weinstein, D. E. Wiser, and R. W. Zdarko, *University of Colorado, INFN-Laboratori Nazionali di Frascati, University of Houston, Northeastern University, Stanford Linear Accelerator Center, Stanford University, University of Utah, and University of Wisconsin.*

50) M. Kobayashi and K. Maskawa, Prog. Theor. Phys. **49**, 652 (1973); P. H. Ginsparg, S. L. Glashow, and M. B. Wise, Phys. Rev. Lett. , **50**, 1415, (1983) and **51**, 1395, (1983).

51) D. Rust in *Proceedings of the Third International Conference on Instrumentation for Colliding Beam Physics, Novosibirsk, 1984*, (USSR Academy of Sciences, Siberian Division, Institute of Nuclear Physics, Novosibirsk, 1984); P. Baringer, C.K. Jung, H.O. Ogren, D.R. Rust, Nucl. Instrum. Meth. **A254**, 542 (1987).

52) R. Bouclier *et al.*, CERN-EP/87-89, May 1987, to appear in Proceedings of the Fourth International Conference on Instrumentation for Colliding Beam Physics, SLAC, 1984; R. Bouclier *et al.*, CERN-EP/87-14, Jan. 1987, Presented at the Workshop on Vertex Detectors, Erice, Italy, Sept. 21-26, 1986; R. Bouclier *et al.*, Nucl. Instrum. Meth. **A252** 373 (1986).

53) G. Battistoni *et al.*, Nucl. Instrum. Meth. **A235**, 91 (1985).

54) E. Fernandez *et al.*, SLAC-PUB-3390, Aug. 1984, in *Proceedings of the Twelfth SLAC Summer Institute on Particle Physics, Stanford, 1984* edited by P.M. McDonough (Stanford Linear Accelerator Center, Stanford, 1984); W. Ash *et al.*, SLAC-PUB-4311, Apr. 1987, submitted to Nucl. Instrum. Meth.

55) G. Chadwick and F. Muller, MAC Internal Memo No. 683: this study employed the model described in J. Va'Vra, Nucl. Instrum. Meth. **225**, 445 (1984).

56) M. Breidenbach, F. Sauli, and R. Tirler, Nucl. Instrum. Meth. **108**, 23 (1973).

57) G.L. Godfrey "Proportional Tube Lifetimes (Magic Gas, A-CO_2, DME)," in *Workshop on Radiation Damage in Wire Chambers, Berkeley, CA*, edited by J. Kadyk (Lawrence Berkeley Laboratory, Berkeley, CA, 1986).

58) H.N. Nelson "Lifetime Tests for MAC Vertex Chamber," SLAC-PUB-4017, Jul. 1986, in *Workshop on Radiation Damage in Wire Chambers, Berkeley, CA*, edited by J. Kadyk (Lawrence Berkeley Laboratory, Berkeley, CA, 1986).

59) G. Baldini, Phys. Rev. **128**, 1562 (1962).

60) W.T. Ford *et al.*, Phys. Rev. **D33**, 3472 (1986).

61) D.E. Groom, Nucl. Instrum. Meth. **219**, 141 (1984).

62) E. Fernandez *et al.*, SLAC-PUB-4048 (in preparation), and to be published.

63) F. Solmitz, Ann. Rev. Nucl. Sci. **14**, 375 (1964).

64) M. Althoff *et al.*, *Phys. Lett.* **149B**, 524 (1984); R. Marshall *et al.*, *Z. Physik C, Particles and Fields* **25**, 291 (1984); W. Bartel *et al.*, *Phys. Lett.* **146B**, 437 (1984).

65) M. Suzuki, *Phys. Lett.* **71B**, 139 (1977); J. D. Bjorken, *Phys. Rev.* **D17**, 171 (1978).

66) C. Peterson, D. Schlatter, I. Schmitt, and P. Zerwas, *Phys. Rev.* **D27**, 105 (1983).

67) E. Fernandez *et al.*, *Phys. Rev. Lett.* **54**, 1624 (1985).

68) S. Bethke, *Z. Physik C, Particles and Fields* **29**, 179 (1985); a useful summary or world *b*-fragmentation data, published after our analysis is W. Bartel *et al.*, *Z. Physik C, Particles and Fields* **33**, 339 (1987).

69) An exception is the thesis of H. S. Kaye, Ph. D. Thesis, Stanford Linear Accelerator Report SLAC-262, 1983; for PETRA work see ref. 64.

70) L. J Rosenberg, private communication.

71) E. Farhi, Phys. Rev. Lett. **39**, 1587 (1977).

72) *Handbook of Mathematical Functions*, edited by M. Abramowitz and I. Stegun (National Bureau of Standards, Applied Mathematics Series 55, Washington D.C., 1972), p. 948. The Student's *t*-distribution has the form $f(x) \propto (1 + (x/s)^2/\nu)^{\frac{-(\nu+1)}{2}}$. The parameter ν controls the tails of the distribution; for $\nu \to \infty$ the distribution becomes gaussian.

73) E. Fernandez *et al.*, *Phys. Rev. Lett.* **54**, 1624 (1985); W. Ash *et al.*, *Phys. Rev. Lett.* **55**, 1831 (1986).

74) The outer drift chambers are usually 4 layers within a space of 90 cm, each with 2 mm resolution, $\sigma_{OD} \approx 0.2 \times 3.5/(90 \times 2) = 0.013$, although detailed consideration raises this 35% to 0.018.

75) M. Piccolo in *Proceedings of the Eleventh Annual SLAC Summer Institute, Stanford, 1983*, edited by P. McDonough (SLAC, Stanford, 1984; SLAC Report No. 267).

76) E. Fernandez *et al.*, *Phys. Rev. Lett.* **54**, 1624 (1985); E. Fernandez *et al.*, *Phys. Rev.* **D35**, 10 (1987).

77) F. A. Berends, P. H. Daverveldt, and R. Kleiss *Nucl. Phys.* **B253**, 441 (1985).

78) H. N. Nelson, MAC-Note 761.

79) W. T. Eadie, D. Drijard, F. E. James, M. Roos, and B. Sadoulet, *Statistical Methods in Experimental Physics* (North-Holland, New York,

1971). Discussion of the maximum likelihood method, as well as the information and the lower bound on the statistical error that follows from the information, known as the Cramér-Rao inequality, can be found in Chapter 7. Central estimators, in particular the trimmed mean, are discussed in Chapter 8, section 7.

80) Discussion of this effect seems to be confined to Ph. D. Theses: D. Amidei, Ph. D. Thesis, LBL-17795, May 1984; C. K. Jung, Ph. D. Thesis, IUHEE-98, May 1986; D. Klem, Ph. D. Thesis, SLAC-0300, June 1986.

81) Among a variety of possible references contained in (79) to articles on robust statistics, E. L. Crow and M. M. Siddiqui, *J. Amer. Stat. Ass.* **353**, 62 (1967) is by far the most useful.

82) J. C. Anjos *et al.*, *Phys. Rev. Lett.* **58**, 311 (1987); J. C. Anjos *et al.*, *Phys. Rev. Lett.* **58**, 1818 (1987); M. S. Witherell, Print 87-0024, March 1987.

83) R. Giles *et al.*, *Phys. Rev.* **D30**, 2279 (1984).

84) J. Chrin, DESY 87-040, May 1987 reviews PEP and PETRA heavy flavor multiplicity measurements.

85) See, for example, R. H. Schindler, SLAC-PUB-4417, Sept. 1987, Invited Talk Presented at the International Europhysics Conference on High Energy Physics, Uppsala, July, 1987.

86) W. T. Ford *et al.*, *Phys. Rev. Lett.* **49**, 106 (1982).

87) H. Band *et al.*, *Phys. Rev. Lett.* **59**, 415 (1987).

88) W. Bartel *et al.*, *Phys. Lett.* **114B**, 71 (1982).

89) W. T. Ford, in *Flavor Mixing in Weak Interactions*, Proceedings of the Europhysics Topical Conference, Erice, Italy, edited by L. L. Chau (Plenum Press, New York, 1984).

90) D. E. Klem *et al.*, *Phys. Rev. Lett.* **53**, 1873 (1984).

91) J. A. Jaros, in *Proceedings of the Summer Institute on Particle Physics, SLAC, 1984*, edited by P. M. McDonough (SLAC Report No. 281, January 1985); also appears as SLAC-PUB-4569, February 1985.

92) J. A. Jaros, in *Proceedings of Physics in Collision 4, Santa Cruz, 1984*, edited by A. Seiden (Gif-sur-Yvette, France, Editions Frontieres, 1984).

93) M. Althoff *et al.*, *Phys. Lett.* **149B**, 524 (1984).

94) W. T. Ford, *Ann. New York Acad. Sci.* **461**, 529 (1986).

95) J. P. Albanese *et al.*, *Phys. Lett.* **158B**, 186 (1985).

96) D. E. Klem, private communication to E. H. Thorndike, in *Proceedings of the 1985 International Symposium on Lepton and Photon Interactions at High Energy, Kyoto, Japan, 1985*, edited by M. Konuma and K. Takahashi. (Kyoto University, Kyoto, Japan, 1986).

97) G. J. Baranko in *Proceedings of the European Physical Society Meeting on High Energy Physics, Bari, 1985* edited by L. Nitti and G. Preparata (Laterza Bari, Bari, Italy, 1985).

98) W. Bartel *et al.*, *Z. Physik C, Particles and Fields* **31**, 349 (1986).

99) D. E. Klem, Ph. D. Thesis, SLAC Report No. 300, 1986; also D. E. Klem *et al.*, SLAC-PUB-4025, September 1986, submitted to Phys. Rev. **D**.

100) A. C. Caldwell in *Proceedings of the 21st Rencontre de Moriond: Progress in Electroweak Interactions, Les Arcs, 1986* edited by J. Tran Thanh (Gif-sur-Yvette, France, Editions Frontieres, 1986).

101) A. C. Caldwell, Ph. D. Thesis, RX-1180(Wisconsin), 1987.

102) W. W. Ash *et al.*, *Phys. Rev. Lett.* **58**, 640 (1987).

103) D. J. Mellor, Ph. D. Thesis, Rutherford Appleton Laboratory Report RAL-T-036, November 1986.

104) D. Blockus, *et al.*, Argonne National Laboratory Report ANL-HEP-PR-86-144, January 1987.

105) D. Muller in Proceedings of International Symposium on the Production and Decay of Heavy Flavors, Stanford, 1987 edited by E. Bloom (Stanford, 1987).

106) R. A. Ong, Ph. D. Thesis, SLAC Report No. 320, 1987.